Computational Modelling of the Coastal Protection Function of Salt Marshes with Flexible Vegetation Cover

by

Thomas Johannes van Veelen

Submitted to Swansea University
in fulfilment of the requirements for the Degree of

Doctor of Philosophy

at

Swansea University

2020

Abstract

Salt marshes are intertidal coastal wetlands that are typically found in sheltered locations such as estuaries. They exhibit a diverse vegetation cover with flexible grasses and rigid shrubs. This vegetation provides coastal protection by attenuating currents and waves. Unlike traditional hard defences, they offer co-benefits by stabilising shorelines and enhancing natural habitats. However, it has remained unclear how salt marshes with a flexible vegetation cover contribute to coastal protection under storms with surge and wave components.

In this thesis, I have developed a new coupled current-wave-vegetation model which includes the effect of vegetation flexibility on wave attenuation. The wave-vegetation model builds on novel laboratory experiments using artificial vegetation in the Swansea University Wave Flume, where wave damping, water velocity fields, and plant motion were measured simultaneously for the first time. A new work factor is introduced to explicitly account for vegetation flexibility in computational models. Furthermore, a momentum sink term parameterisation is found to best resemble current-vegetation interactions. The advanced coupled model is successfully applied to simulate flood risk in the Taf Estuary under six contrasting vegetation scenarios.

My results highlight how the vegetation cover affects the coastal protection provided by salt marshes. All modelled vegetation species constrain flood currents to the main estuary channel and damp incoming waves. Although flexible grasses are 50% less effective in wave damping than rigid shrubs in the Taf Estuary. The wave conditions, wind conditions and local topography further affect the protection provided. Additionally, rigid species can amplify orbital velocities above the canopy by inducing wave-averaged currents, but flexible species do not.

It is recommended that the biomechanical properties of vegetation, including the flexibility, are included when modelling the coastal protection by salt marshes. My new computational modelling framework provides evidence to support the continuing uptake of salt marshes as sustainable coastal defences.

Declarations

This work has not previously been accepted in substance for any degree and is not being concurrently submitted in candidature for any degree.

Signed: .....

Date: .....

This thesis is the result of my own investigations, except where otherwise stated. Other sources are acknowledged by footnotes giving explicit references. A bibliography is appended.

Signed: .....

Date: .....

I hereby give my consent for my work, if relevant and accepted, to be available for photocopying and for inter-library loans **after expiry of a bar on access approved by the University**.

Signed: .....

Date: .....

In loving memory of
Fred van Veelen
Civil engineer, enthusiast of the British Isles, and loving grandfather.

"Wave after wave
Wave after wave
I'm slowly drifting
drifting away"

From: Waves – Mr. Probz

Contents

Abstract iii

Declarations v

Acknowledgements xiii

List of Figures xvii

List of Tables xxi

Nomenclature xxiii

Main text

1 Introduction 1
- 1.1 Research context . . . 2
- 1.2 Scope . . . 3
- 1.3 Outline . . . 4

2 Literature review 7
- 2.1 Introduction . . . 8
- 2.2 The salt marsh ecosystem . . . 9
  - 2.2.1 General description . . . 9
  - 2.2.2 Salt marsh vegetation . . . 11
  - 2.2.3 Creek networks . . . 15
- 2.3 Current-vegetation interaction . . . 16
  - 2.3.1 Drag resistance by rigid vegetation on unidirectional currents 16
  - 2.3.2 Drag resistance by flexible vegetation on unidirectional currents . . . 18
  - 2.3.3 Effect of salt marsh vegetation on tidal flow and storm surges 21
- 2.4 Wave-vegetation interaction . . . 24
  - 2.4.1 General description of wave damping . . . 24
  - 2.4.2 Wave damping over rigid vegetation . . . 26

2.4.3 Wave damping over flexible vegetation 28
2.4.4 Wave-driven velocity structure within vegetation 37
2.5 Computational modelling tools 38
2.5.1 Governing equations 38
2.5.2 Current-vegetation parameterisations 40
2.5.3 Wave-vegetation parameterisations 42
2.5.4 Computational modelling applications to salt marshes . . . 46
2.6 Conclusions 48

3 Modelling current-vegetation interaction 51
3.1 Introduction 52
3.2 Model setup 53
3.2.1 Model description 53
3.2.2 Vegetation parameterisations 56
3.3 Results 60
3.3.1 Depth-averaged modelling 60
3.3.2 3D modelling 61
3.4 Comparison of vegetation parameterisations 63
3.5 Conclusions 65

4 Experiments on vegetation flexibility 67
4.1 Introduction 68
4.2 Theoretical background 71
4.3 Experimentation 73
4.3.1 Flume setup 73
4.3.2 Wave conditions 75
4.3.3 Experiment similarity 75
4.3.4 Wave attenuation measurements 79
4.3.5 Water particle velocity measurements 80
4.4 Results 83
4.4.1 Drag coefficient for wave attenuation 83
4.4.2 Sensitivity of the drag coefficient to hydrodynamic parameters 86
4.4.3 Water Particle Velocities 87
4.5 Discussion 93
4.5.1 Impact of plant flexibility on wave attenuation 93
4.5.2 Wave-induced circulation 95
4.5.3 Orbital velocity structure 96
4.5.4 Length of the vegetation field 98
4.5.5 Implications for nature-based coastal defences 100
4.6 Conclusions 101

5 Modelling wave attenuation by vegetation 103
5.1 Introduction . . . 104
5.2 Theoretical background . . . 106
5.2.1 Coordinate system . . . 106
5.2.2 Wave-vegetation interaction . . . 108
5.2.3 Wave damping . . . 110
5.3 Wave attenuation under observed plant motion . . . 111
5.3.1 Laboratory experiments . . . 111
5.3.2 Key mechanisms in the wave-vegetation interaction . . . 112
5.4 Model for wave damping over flexible vegetation . . . 118
5.4.1 Model assumptions . . . 118
5.4.2 Solution of plant motion . . . 120
5.4.3 Work Factor . . . 122
5.4.4 Wave damping . . . 123
5.4.5 Wave damping under linear wave theory . . . 123
5.5 Model validation . . . 124
5.5.1 Validation of the velocity transfer function (G) . . . 124
5.5.2 Validation of the damping coefficient . . . 125
5.6 Implications for nature-based coastal defences . . . 128
5.6.1 Plant and wave parameters that control wave damping . . . 128
5.6.2 Model application for nature-based coastal defences . . . 130
5.6.3 Model limitations . . . 131
5.7 Conclusions . . . 131

6 Modelling random wave attenuation 133
6.1 Introduction . . . 134
6.2 Random wave model . . . 135
6.3 Experiments . . . 137
6.4 Validation . . . 138
6.5 Conclusions . . . 141

7 Taf Estuary computational model 145
7.1 Introduction . . . 146
7.2 Study area: Taf Estuary . . . 148
7.2.1 Salt marshes . . . 150
7.3 Model setup . . . 153
7.3.1 Model domain . . . 154
7.3.2 Storm conditions . . . 156
7.3.3 Vegetation parameterisation . . . 160
7.3.4 Model validation . . . 163
7.4 Vegetation scenarios . . . 166

7.5 Results . . . 169
7.5.1 Impact of salt marshes on water depth . . . 170
7.5.2 Impact of salt marshes on currents . . . 174
7.5.3 Impact of salt marshes on waves . . . 177
7.6 Comparison against the full flexible model . . . 178
7.7 Conclusions . . . 185

8 Conclusions **187**
8.1 Synthesis . . . 188
8.2 Main outcomes . . . 188
8.3 Visual summary . . . 193
8.4 Suggested improvements in methodology . . . 194
8.5 Future Research . . . 195

Appendices

A Data collection in South Wales estuaries **197**
A.1 Plant Data . . . 197
A.2 Wave Properties . . . 198

B Linear velocity estimation **199**

C Derivation of plant motion **201**

D Description of the spatial modes **209**

E Proof of a unique velocity transfer function **211**

F Flexible model validation data **213**

G Research outcomes **219**
G.1 Journal publications . . . 219
G.2 Conference papers . . . 220
G.3 Conference presentations . . . 220

Bibliography **223**

Acknowledgements

This thesis would not have been possible without the continuous support of my colleagues, funders, friends and family. First of all, I would like to thank my first supervisor Prof. Harshinie Karunarathna for providing me with the opportunity to undertake this research. You have encouraged me to delve into the topics that I found most interesting, allowing me to try, fail, and try again until it eventually all worked out. Your supervision has been kindly supported by Prof. Dominic Reeve, who has provided useful feedback on key outputs of my PhD.

To my colleagues in the CoastWEB project and the Energy and Environment Research group, it has been a pleasure working with all of you. We have undertaken many interesting cross-disciplinary projects that have supported my research (and hopefully yours too). In particular, I would like to thank Dr. Tom Fairchild for providing essential data of vegetation, bathymetry and current velocities in the Taf estuary, as well as providing positive energy during fieldwork. Whilst I have been leading the design, execution, and analysis of the experiments in this thesis, the assistance of Dr. Jose Horrillo-Caraballo, Stephen Orimoloye and Dr. Ali Zuhaira has been invaluable. The have made suggestions to optimise the design, and have lend a helping hand in setting up and as a safety cover during the experiments. I am grateful to Dr. Simon Read for his illuminating research into the history of the Taf estuary. Callum Jackson has kindly assisted as the second controller during the analysis of vegetation motion. The collection of vegetation in the Neath estuary was kindly supported by Dr. William Bennett, who has also provided modelling results on which the wave conditions in my experiments were based, and extreme storm scenarios for the case study. Dr. Sue Alston is deeply thanked for providing equipment and assistance during the stem bending tests. Last but not least, I would like to express my gratitude to Dr. Jasper Dijkstra of Deltares for providing valuable feedback on the development of the current-wave-vegetation model in Delft3D.

I would also like to thank the people in the Port and Airport Research Institute (PARI) in Yokosuka, Japan, whom I had the honour of visiting for one week during my PhD to support their mangrove experiments. It was a fantastic experience in a fascinating country. Thank you for the amazing opportunity.

I am grateful for the funding provided by Swansea University, which has allowed me to undertake this academic journey. Furthermore, I am grateful to the Great-Britain Sasakawa Foundation, who have supported my research visit to PARI. The British Society of Geomorphology (BSG), Wiley-Blackwell and the MARID VI committee have generously funded me to attend the MARID VI conference in Bremen, Germany. Finally, this research forms part of the Valuing Nature Programme, which is supported by the UK Research Councils under Natural Environment Research Council award NE/N013573/1.

Essential data for my research, and in particular for the case study of the Taf estuary, has kindly been provided by several people and organisations. I would like to thank Dr. Suzie Jackson of Bangor University for providing ADCP data inside the Taf estuary. Digital elevation and salt marsh maps contain Natural Resources Wales information © Natural Resources Wales and Database Right. All rights Reserved. The bathymetry used in this study contains public sector information, licensed under the Open Government Licence v3.0, from the UK Hydrographic Office (UKHO).

Swansea has been a long way from my home in the Netherlands, where distances are small and everyone lives relatively nearby. Leaving the comfort of my home soil has not always been easy, but thanks to so many amazing people, I have found a new home in Wales. It is a country with a great outdoors, which was explored by foot from the first weekend to the last with Emilio and Sky. Your incredible kindness, seemingly limitless positive energy and fabulous food has always been most welcoming during the chaos of my PhD. Also, Omar, Ross, Ieuan, and Irfan often joined during these trips, all of whom are incredible friends who made Swansea feel like home. Apart from hiking, chess has been a favourite activity to relax my mind. Countless hours were filled behind the chessboard with Donovan and other members of the chess society with or without glasses of wine. Many other exciting activities have been undertaken with more great friends than I can write down here. Thank you all.

Despite the distance, many friends from the Netherlands have remained close. I have been overwhelmed by the vast number of visits over the years, which helped to keep my spirits up. Ivo, Mick, Lars, Niels, Annet, Bas, Roy, Wietse and Astrid have all crossed the waters to reach Swansea. I hope you all enjoyed these trips as much as I did. When I was in the Netherlands, Hans, Justin, Maaike, Maarten and Martin were always happy to free some time for a cup of tea and a chat. The Netherlands has never been far away thanks to all of you.

Last but not least, I would like to thank my family for their continuous love and support. My loving parents Marcel and Winfried who have nurtured and encouraged me to expand my mind from a young age; my dear brother Wouter who is amazing in so many ways; my grandmother who has written countless kind

cards and a visit to her was always on my schedule for trips to the Netherlands; and my grandfather who always had a smile on his face when I came to see him. The distance to all of you has been far, but the heart is close.

Three years is a long period, and I am forever grateful for all of you who have supported me along the way, during the highs and the lows. Thank you.

— Thomas

List of Figures

1.1 Thesis Outline 5

2.1 The global distribution of salt marshes 9
2.2 Sketch of a typical salt marsh topography 10
2.3 Laugharne South Marsh, Carmarthenshire, UK, at high water . . 11
2.4 Samples of five common salt marsh species 12
2.5 Definition sketch of a salt marsh canopy 13
2.6 Definition sketches of the plant-scale dynamics 19
2.7 Current velocity structure 22
2.8 Turbulence production by vegetation 23
2.9 Water level on a salt marsh at high and low water 24
2.10 Definition sketch of the canopy-scale coordinate system with waves 25
2.11 Reduction of the relative wave height H_0/H as function of βx . . 27
2.12 Swaying of flexible vegetation under wave motion 29
2.13 Comparison of $C_{Dw,ref}$ against EI_v 35
2.14 C_{Dw} as function of Re for salt marsh vegetation in three studies . 36
2.15 Wave-induced current circulations as identified by *Pujol et al.* (2013) 38

3.1 Idealised model domain 54
3.2 Depth-averaged current velocity magnitude 58
3.3 Direction of the depth-averaged currents 59
3.4 Vertical distribution of the current velocity magnitude and turbulent energy 62
3.5 Time series of water level and bed shear stress 63

4.1 Schematisation of wave attenuation over vegetation 72
4.2 Sketch of the experimental set-up 74
4.3 Example fit of wave attenuation parameter β 79
4.4 Comparison of the PIV-derived particle velocity measurements . . 81
4.5 Transformation of a PIV output signal 82
4.6 Empirical relations for drag coefficient C_{Dw} 84
4.7 Comparison of drag coefficient relations 85
4.8 Sensitivity of the drag coefficient to five predictors 87

4.9 Normalized horizontal particle velocity fields 88
4.10 Normalized horizontal particle velocity structure at transect T1 . 90
4.11 Normalized horizontal particle velocity structure at transect T2 . 91
4.12 Normalized horizontal particle velocity structure at transect T3 . 92
4.13 Vertical profile of wave-averaged net velocities 94
4.14 Comparison of the wave-averaged mean velocity fields in *Pujol et al.* (2013) and this study 97
4.15 Difference in horizontal particle velocities between rigid vegetation and no vegetation 99

5.1 Coordinate system of the wave-vegetation interface 106
5.2 Schematisation of the data collection 114
5.3 Schematisation of the derivation of the plant position 115
5.4 Correlation between β_{for} and β_{exp} 115
5.5 Root-mean-square magnitude of the wave forces 116
5.6 Average rate of energy dissipation versus the along-stem coordinate 117
5.7 Individual contributions of stem reconfiguration and stem velocity 119
5.8 Validation of the velocity transfer function G 126
5.9 The three real vegetation species used in model validation 127
5.10 Validation of the modelled wave damping coefficients 129

6.1 Distributions of the measured wave heights and frequencies 139
6.2 Validation of the modelled random wave damping coefficients $\hat{\beta}_{model}$ 142

7.1 Topography of the Taf Estuary 149
7.2 Salt marshes in the Taf Estuary 151
7.3 The computational model domain of the Taf model 155
7.4 Bathymetry of the Taf model 156
7.5 Modelled wave heights under south-westerly and easterly storm directions 158
7.6 A sample water level curve 160
7.7 Flowchart of the three-step methodology to simulate flexible vegetation in SWAN 162
7.8 Example application of our three-step methodology 164
7.9 Model validation of the water depth and current velocity 167
7.10 Bottom profile and location of transects T1, T2 and T3 170
7.11 Modelled water depths in the Taf Estuary under six scenarios . . 172
7.12 Modelled water depths relative to the no vegetation scenario . . . 173
7.13 Modelled current velocities in the Taf Estuary under six scenarios 175
7.14 Modelled current velocity magnitudes relative to the no vegetation scenario 176

7.15 Modelled wave height in the Taf Estuary under six scenarios . . . 179
7.16 Modelled wave height relative to the no vegetation scenario 180
7.17 Comparison of the wave damping capacity along three transects . 181
7.18 Comparison between the Taf model and the full flexible model . . 182
7.19 Comparison between the Taf model without wind and the full flexible model 184

8.1 Visual summary of selected outcomes 193

C.1 Plant posture model 202
C.2 Flexible stem identification under condition R11 205
C.3 Flexible stem identification under condition R23 206
C.4 Stem posture of flexible vegetation over time 207

D.1 The first four spatial modes ψ_n 210

List of Tables

2.1 List of salt marsh species and their biomechanical properties . . . 14
2.2 List of studies that derived relations for C_{Dw} 33
2.3 List of drag coefficient relations in the form of $C_{Dw} = (a/\text{predictor})^b + c$ 34
2.4 List of wave models grouped with respect to governing equations . 44
2.5 List of publications that have investigated the impact of salt marshes on coastal environments 47

4.1 List of tested wave conditions 76
4.2 List of parameter values for field and experiment conditions . . . 78
4.3 List of fitted coefficients in Eq. 4.6 in literature 84

5.1 List of tested wave conditions and damping coefficients 113
5.2 List of vegetation species used for model validation 128

6.1 List of observed random wave dynamics 138
6.2 List of model validation data 143

7.1 List of vegetation species per NVC-type 152
7.2 Cover and plant parameters of the five dominant species 153
7.3 List of parameters of south-westerly and easterly storm conditions 158
7.4 List of model parameters 165
7.5 List of vegetation scenarios 169
7.6 Modelled wave height by the full flexible model and the Taf model 183

A.1 Plant data as measured on South Wales salt marshes 198

F.1 Validation data rigid mimics 214
F.2 Validation data flexible mimics 215
F.3 Validation data *P. Maritima* 216
F.4 Validation data *S. Anglica* 217
F.5 Validation data *E. Athericus* 217

Nomenclature

A list of parameters, which are used in this thesis, is provided below. Modified versions of the parameters may appear in text. An asterisk next to a parameter denotes that the parameters is scaled. Subscript $_p$ denotes that a parameter is associated with the peak wave period. Accent $\hat{}$ denotes that a parameter is associated with random wave conditions. A bold font denotes vector notation, e.g. $\boldsymbol{u} = (u, v, w)$.

A_p	Solid volume fraction per unit water depth
A_w	Wave excursion length
B	Buoyancy number
C_A	Added mass coefficient
C_F	Friction coefficient
C_M	Inertia coefficient
C_b	Chézy coefficient of the bare bed
C_w	Wind drag coefficient
C_z	Chézy coefficient
$C_{Dw,ref}$	Wave drag coefficient under reference field conditions
C_{Dc}	Current drag coefficient
C_{Dw}	Wave drag coefficient
C_{SD}	Sectional drag coefficient
Ca	Cauchy number
D	Water depth to wave excursion ratio

E Wave energy

EI_v Vegetation flexural rigidity

E_v Vegetation Young's modulus

F_A Added mass force

F_B Buoyancy force

F_D Drag force

F_F Skin friction force

F_W Total wave force

F_c Canopy drag force

F_r Froude number

F_s Shear stress

F_x Horizontal force component

F_z Vertical force component

F_{FK} Froude-Krylov force

F_{rms} Root-mean-square force magnitude

G Transfer function between water and vegetation velocity

H Wave height

H_0 Offshore wave height

H_r Relative wave height

H_s Significant wave height

H_{max} Peak wave height

$H_{rms,0}$ Offshore root-mean-square wave height

H_{rms} Root-mean-square wave height

K Horizontal eddy viscosity

KC	Keulegan-Carpenter number
K_r	Reflection coefficient
L	Wave excursion ratio
L_D	Canopy drag length
L_v	Length of vegetation patch
L_{wave}	Wavelength
M	Momentum source
N_w	Action density spectrum
P	Pressure
Q	Scaled flexibility
Q_r	River discharge
Q_{KC}	Keulegan-Carpenter number modified by the submergence ratio
R	Transfer function between water and relative velocity
Re	Reynolds number
Re_D	Reynolds number modified by the deflected plant height
S_v	Vegetation spacing
S_{veg}	Vegetation-induced dissipation of the wave energy spectrum
T	Wave period
T_p	Peak wave period
T_{max}	Maximum wave period
T_{storm}	Storm duration
U	Complex flow velocity
U^*	Normalized orbital velocity scale
U_f	Complex water velocity coefficient in physical space

U_n Spatiotemporal complex water velocity coefficient

U_r Complex relative velocity

U_s Complex flow velocity at a stem

U_{net} Wave-averaged velocity

U_{veg} Complex vegetation velocity

VC Vogel coefficient

V_f Complex vegetation velocity coefficient in physical space

V_n Spatiotemporal complex vegetation velocity coefficient

W Work

W_{net} Vertical orbital velocity amplitude

W_{rig} Work on rigid vegetation

X Stem position

X_n Spatiotemporal complex plant position coefficient

X_{cp} Complex centre point of vegetation bending

Δt Time step

Δt_{flow} Time step D-FLOW

Δt_{wave} Time step D-WAVE

α Submergence ratio

α_n Eigenvalue of spatial mode ψ_n

β Wave damping coefficient

β_{exp} Experimentally derived wave damping coefficient

β_{for} Force-derived wave damping coefficient

β_{model} Modelled wave damping coefficient

χ Work factor

ϵ_v	Wave energy dissipation per stem
η	Water surface elevation
γ_j	JONSWAP peak enhancement factor
κ	von Kármán constant
λ	Wave steepness
λ_a	Frontal area per unit water volume
λ_f	Relative frontal area
λ_p	Plant volume per unit ground area
λ_s	Solid volume fraction
ν	Kinematic viscosity
ν_T	Eddy viscosity due to vegetation-induced turbulence
ω	Wave frequency
ϕ_G	Phase of transfer function G
ϕ_R	Phase of transfer function R
ϕ_u	Phase of the water velocity
ϕ_v	Phase of the vegetation velocity
ψ_n	Spatial modes of a cantilever beam
ρ	Mass density of water
ρ'	Relative vegetation bulk density
ρ_v	Mass density of vegetation
σ	Standard deviation
τ	Shear stress
τ_b	Bed shear stress
θ	Vegetation bending angle

θ_a	Vegetation arc angle
θ_v	Vegetation rotation
θ_w	Wave directional spectrum
θ_{cp}	Bending angle of X_{cp}
θ_{wave}	Wave direction
θ_{wind}	Wind direction
a_G	Amplitude of transfer function G
a_R	Amplitude of transfer function R
a_u	Amplitude of the water velocity
a_v	Amplitude of the vegetation velocity
b_v	Vegetation diameter
c_g	Wave group velocity
d	Chord length
d_{grid}	Grid resolution
f	Coriolis parameter
g	Gravitational acceleration
h	Water depth
h_r	Relative water depth
h_v	Vegetation height
h_{max}	Peak water level
k	Wave number
l_D	Deflected vegetation length
l_e	Effective vegetation length
n_m	Manning's coefficient

n_p	Canopy porosity
n_v	Vegetation density
r^2	Coefficient of determination
s	Axis in the along-stem direction
t	Time
t_{ini}	Spin-up time
u	Flow velocity in the direction of the x-axis
u_0	Velocity based on linear wave theory
u_b	Peak backward velocity
u_c	Velocity scale
u_f	Peak forward velocity
u_n	Stem-normal velocity
u_p	Stem-parallel velocity
u_r	Horizontal relative velocity
u_s	Horizontal flow velocity at a stem
u_α	Velocity at reference water depth
u_{amp}	Horizontal orbital velocity amplitude
u_{rn}	Stem-normal component of the relative velocity
u_{rp}	Stem-parallel component of the relative velocity
u_{veg}	Horizontal vegetation velocity
u_{wind}	Peak wind speed
v	Flow velocity in the direction of the y-axis
w	Flow velocity in the direction of the z-axis
w_r	Vertical relative velocity

w_s	Vertical flow velocity at a stem
w_{amp}	Vertical orbital velocity amplitude
w_{veg}	Vertical vegetation velocity
x	Axis parallel to the dominant flow direction
x_v	Horizontal axis at the plant scale
y	Axis perpendicular to the dominant flow direction
z	Axis in upward vertical direction
z_v	Vertical axis at the plant scale

Chapter 1

Introduction

1.1 Research context

Coastal flooding is a significant hazard in the UK and around the globe. During the coastal storm events in the winter of 2013 to 2014, 11,000 properties were flooded across England and Wales alone (*Environment Agency*, 2018). The economic damages of these floodings were estimated at £1.3 billion. The risk of coastal flooding is expected to further increase in the next decades due to global climate change (*IPCC*, 2019). As a result, traditional hard coastal defences are increasingly challenged by frequent storms, land subsidence and sea level rise, but cannot adapt to the worsening conditions (*Temmerman et al.*, 2013). Therefore, coastal management specialists are searching for alternative sustainable coastal defence solutions.

Recent studies have demonstrated that salt marshes can be a sustainable coastal defence solution. Salt marshes are intertidal wetlands that are typically found in sheltered coastal areas such as estuaries. They exhibit salt-tolerant vegetation species that range from rigid shrubs to flexible grasses. The interaction of the vegetation with currents and waves provides benefits to coastal protection by attenuating storm surges (*Paquier et al.*, 2017) and waves (*Möller et al.*, 2014). Unlike traditional hard defences, they provide co-benefits by stabilising shorelines, enhancing natural habitats, acting as natural carbon storage, and are capable of adapting to a moderate rise of the sea level (*French*, 1993; *Borsje et al.*, 2011; *Bouma et al.*, 2014; *Nordstrom*, 2014; *Leonardi et al.*, 2018).

Computational models have been developed to quantify the contributions of salt marshes to coastal protection. These models simulate coastal processes, including the interaction between currents, waves and vegetation during storm events, which enable them to provide detailed information on water levels, current velocities and wave climates over large spatial scales (*Hu et al.*, 2018). Recently, a growing body of studies has applied computational models to simulate storm surge (e.g. *Loder et al.*, 2009) and wave attenuation (e.g. *Garzon et al.*, 2019b) by salt marshes, and have provided additional support for their capacity to contribute to coastal protection.

However, current computational models may provide limited insight into the coastal protection provided by salt marshes due to their simplified parameterisations of vegetation. The diversity of natural salt marsh vegetation is not included in computational models which are typically restricted to a single rigid vegetation type (*Tempest et al.*, 2015). Yet, the range of flexibilities that is exhibited by natural salt marsh species (*Chatagnier*, 2012) affects their interaction with waves (*Paul et al.*, 2016). Unlike rigid vegetation, flexible plants bend over during a wave cycle which reduces their capacity to attenuate waves. Several models (*Mullarney and Henderson*, 2010; *Luhar and Nepf*, 2016; *Maza et al.*, 2013) have been

developed to quantify the impact of plant motion by flexible vegetation on wave attenuation, but these are restricted to vegetation species with limited flexibility or are computationally too expensive for field-scale application. Furthermore, the coastal protection by salt marshes has been investigated under surge-dominated or wave-dominated conditions, but rarely under storm conditions where surge and wave dynamics are both important.

To further the uptake of salt marshes as sustainable coastal defences, a better understanding of the coastal protection provided by salt marshes with vegetation of arbitrary flexibility is called for, using improved computational models. These models should be applicable to storm conditions with surge and wave components, and include the effect of vegetation flexibility on the wave-vegetation interaction. Therefore, I have investigated the interaction of currents and waves with vegetation, focussing on the impact of plant flexibility on wave attenuation. My research culminated into a new current-wave-vegetation interaction model that was applied to quantify the coastal protection by salt marshes in the Taf Estuary, Carmarthenshire, United Kingdom. These salt marshes exhibited a diverse cover of vegetation species that varied in flexibility.

1.2 Scope

The main objective of this research is to better understand how salt marshes with a flexible vegetation cover contribute to coastal protection under storm conditions with surge and wave components, and how the vegetation cover affects the level of protection that is provided. I have employed computational modelling at the plant and estuary scales, and laboratory experiments in the Swansea University Wave Flume to improve our understanding of the current-vegetation and wave-vegetation interactions. A prime focus of this thesis is how vegetation flexibility affects the wave-vegetation interaction, which was identified as a potentially important mechanism that is currently omitted in computational models. The insights gained in the current-vegetation and wave-vegetation interactions contributed towards a new computational model, which was applied to simulate flood risk in a case study site, in order to achieve the main objective.

Insights in the current-vegetation interaction were gained by computational modelling of the hydrodynamics in an idealised estuary with salt marshes. Whilst it is well-accepted that vegetation reduces current velocities (*Baptist et al.*, 2007), there is little agreement on how the current-vegetation interaction should be included in computational models. Four fundamentally different parameterisations have been used, but it is unclear how these affect the simulated hydrodynamics. Therefore, I have investigated the uncertainty of the estuary hydrodynamics to each parameterisation with the aim of improving our understanding of the

current-vegetation dynamics in the context of estuarine environments and their uncertainty due to model parameterisations.

Insights in the wave-vegetation interaction were obtained by laboratory experiments and plant-scale modelling. Building on prior experimental studies (e.g. *Sánchez-González et al.*, 2011; *Jadhav et al.*, 2013; *Hu et al.*, 2014; *Ozeren et al.*, 2014; *Losada et al.*, 2016) that have primarily focussed on quantifying wave damping over specific plant species, I have measured, for the first time, the wave damping, the wave velocity field and the plant motion simultaneously around two artificial vegetation fields that differed in flexibility. The combined experimental observations have provided new physical evidence to identify the key wave-vegetation interactions for wave attenuation over rigid and flexible plants. Based on the identified interactions, I have developed a new physics-based model for wave damping over vegetation of arbitrary flexibility. As the wave damping in the new model depends on wave and vegetation parameters only, it is applicable across coastal vegetation species without plant-specific calibration as is required in current wave damping models (*Tempest et al.*, 2015).

A new coupled current-wave-vegetation model was applied to quantify the contribution of salt marshes with a flexible vegetation cover to coastal protection under storm conditions with surge and wave components. A selected current-vegetation parameterisation and the new wave damping model were combined with the coastal modelling suite Delft3D (*Lesser et al.*, 2004) to develop a coupled current-wave-vegetation model, which was applied to simulate flood risk in the Taf Estuary. Six contrasting vegetation scenarios were selected to understand the sensitivity of flood risk to variations in the vegetation cover on the salt marshes.

1.3 Outline

This thesis is organised as follows (Fig. 1.1): Chapter 2 provides the necessary theoretical background by reviewing existing literature. This chapter aims to identify and provide the detail on current knowledge gaps. Chapter 3 investigates the uncertainty of estuary hydrodynamics to four current-vegetation parameterisations. A computational model of an idealised estuary is set up to compare the currents, water levels, turbulent intensities and bed shear stresses induced by each parameterisation.

Chapter 4 describes the wave-vegetation experiments in the Swansea University Wave Flume. Two artificial vegetation canopies that differed in flexibility are placed in the wave flume with the aim of quantifying the impact of vegetation flexibility on wave damping and the wave-driven velocity structure. The water surface elevation and water particle velocity fields are measured simultaneously. The velocity fields are measured using particle image velocimetry (PIV).

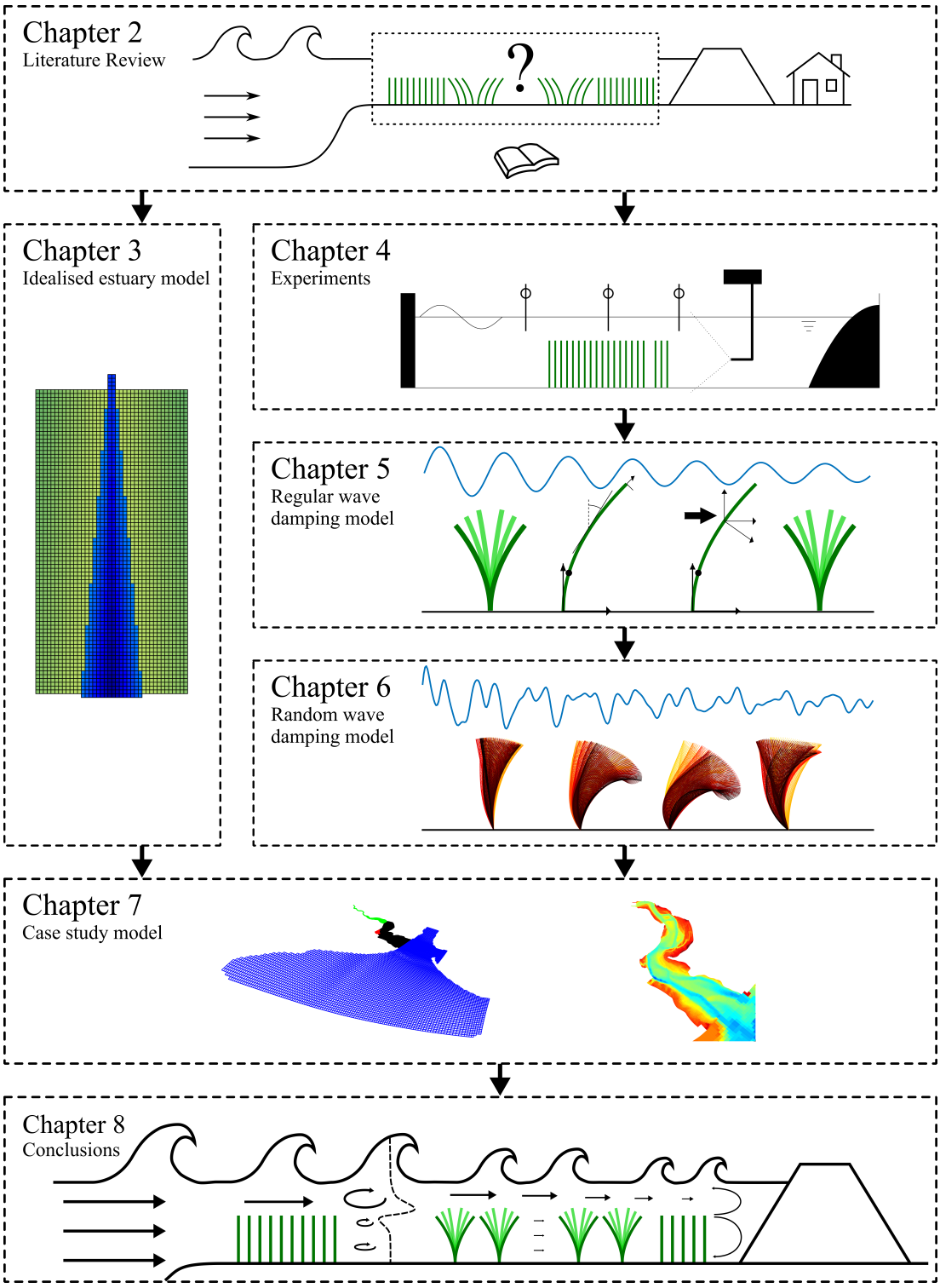

Figure 1.1: Thesis outline. See text for further explanation.

The experimental results are used to derive new empirical relations for the drag coefficient, to identify wave-driven current structures, and to identify regions of amplified and reduced orbital velocities.

Chapter 5 presents the development of a new model for wave damping over flexible coastal vegetation. The experimental data of water surface elevation and water particle velocity fields is combined with simultaneous observations of plant motion. The key wave-vegetation interactions in the context of wave attenuation over flexible vegetation are derived from the experimental data and justify my modelling assumptions. The velocity transfer between water and plant motion under regular waves is solved via the Euler-Bernoulli beam equations. Its solution is linked to a new work factor, which describes the reduction in wave dissipation over flexible vegetation relative to rigid vegetation. The model is validated against observed wave damping over five vegetation species that differ in flexibility. The wave damping model is expanded to random waves under a Rayleigh spectrum in Chapter 6.

Chapter 7 investigates the coastal protection provided by salt marshes with flexible vegetation in the Taf Estuary. A selected wave-current parameterisation (based on Chapter 4) and the new random wave damping model (Chapter 6) are combined with Delft3D to set up a novel current-wave-vegetation model. The model is applied to simulate the water depth, currents and waves under a 1 in 100 year storm event. Six contrasting vegetation scenarios are used to quantify the impact of the vegetation cover on the coastal protection provided by salt marshes in the Taf Estuary.

Finally, Chapter 8 details the overarching conclusions of this thesis. It also highlights potential avenues of future research in this field.

Chapter 2

Literature review

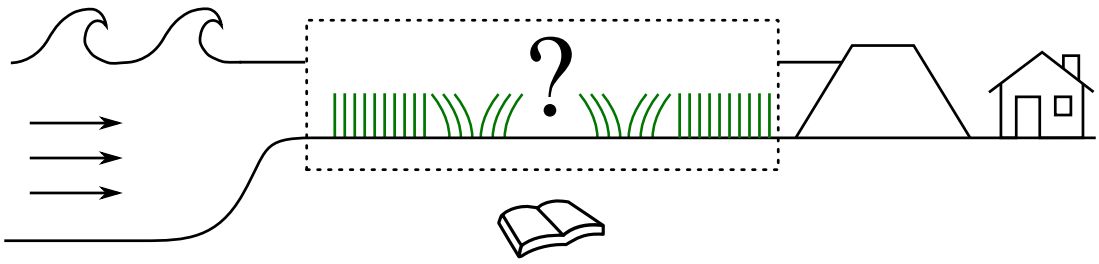

2.1 Introduction

Salt marshes provide coastal protection services through the interaction of their vegetation with currents and waves, but their uptake as coastal defence solutions has been hampered by uncertainties in the level of protection they provide. The coastal protection by salt marshes depends on three elements: (i) the properties of the salt marsh ecosystem, (ii) the interaction between salt marsh vegetation and currents, and (iii) the interaction between salt marsh vegetation and waves. Understanding how these elements contribute to coastal protection is key to improving computational models and reducing uncertainties in flood risk simulations.

Vegetation is increasingly included in computational models which quantify the flood defence function by salt marshes in large-scale coastal areas under storm-driven surges and waves. These models simulate the effect of salt marsh vegetation on the hydrodynamics over complex bathymetries and in relation to other coastal processes such as tide propagation and wave generation. However, they employ simplified parameterisations of the complex interactions between hydrodynamics and vegetation (*Tempest et al.*, 2015). Therefore, the quality of flood risk simulations does not only rely on our understanding of the underlying current-vegetation and wave-vegetation dynamics but also on their parameterisation in computational models.

Here we will systematically review the growing body of experimental, analytical and computational modelling studies that have been devoted to improving our understanding of the coastal protection function of salt marshes. We will address the salt marsh ecosystem, its interaction with currents and waves, and the parameterisations in computational models. The aim of this review is two-fold: (i) to summarize the current state-of-the-art in research, and (ii) to identify knowledge gaps in our understanding of the coastal defence function of salt marshes.

This review is structured along four review questions that relate to the physical and computational components of modelling coastal protection by salt marshes.

1. What characterizes the salt marsh ecosystem? (Section 2.2)
2. How do currents and vegetation interact? (Section 2.3)
3. How do waves and vegetation interact? (Section 2.4)
4. How can computational models improve our understanding of the coastal defence function of salt marshes? (Section 2.5)

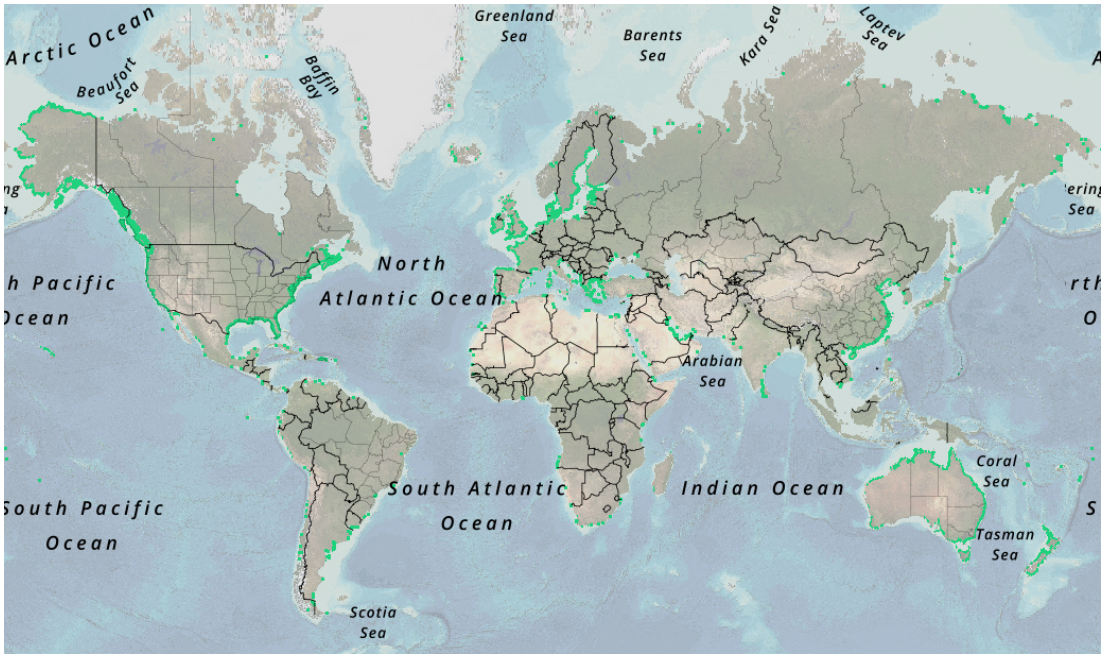

Figure 2.1: The global distribution of salt marshes. The green dots denote known salt marsh locations. Source: *Mcowen et al.* (2017).

2.2 The salt marsh ecosystem

2.2.1 General description

Salt marshes are intertidal coastal wetlands with salt-tolerant vegetation, which are typically found in sheltered environments within temperate climate zones (*Fagherazzi et al.*, 2012; *Mcowen et al.*, 2017). Although they have been found worldwide, salt marshes are most frequently located in low-lying, ice-free coasts, bays and estuaries of the North Atlantic (*Mcowen et al.*, 2017) (Fig. 2.1). Salt marshes are defined by two criteria (*Allen*, 2000): (i) they are regularly flooded by the sea; (ii) they exhibit salt-tolerant vegetation. These properties are also satisfied by mangrove vegetation to which salt marshes are closely related. However, salt marsh vegetation is typically herbaceous or low shrubby, whereas mangroves are populated by trees (*Chmura*, 2009).

Salt marshes are located in the intertidal zone between the marine and terrestrial zone. The seaward edge is typically a saltwater body with calm hydrodynamic conditions, such as a sheltered sea, bay or estuary (*Bouma et al.*, 2014). Salt marshes may border the water body directly, but they may also be separated by a mudflat. On the landward side, the border between the salt marsh and terrestrial land is defined by the line of highest astronomical tide (*Foster*

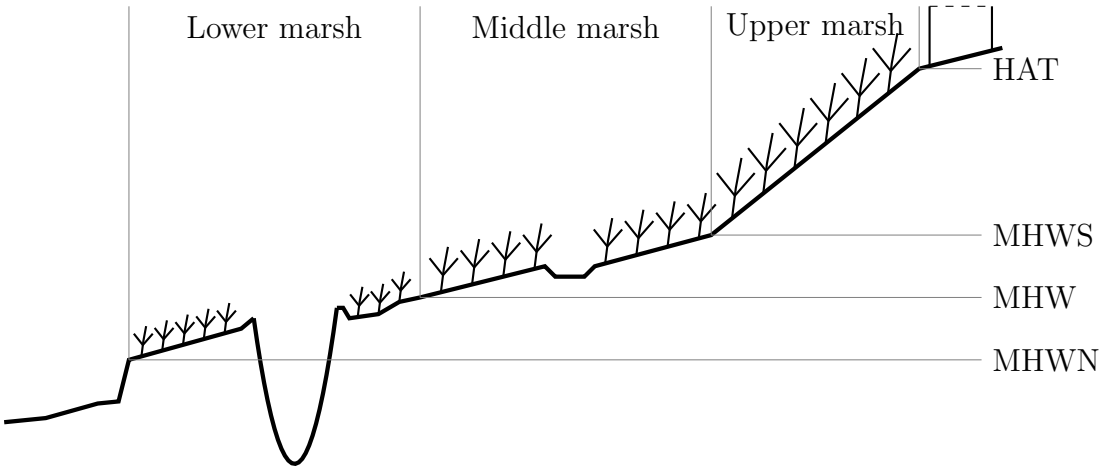

Figure 2.2: A typical salt marsh can be divided into three zones (from left to right): lower marsh, middle marsh and upper marsh. Each area can be identified by its elevation with respect to tidal level and exhibits vegetation and creeks. HAT: Highest Astronomical Tide; MHWS: Mean High Water at Spring tide; MHW: Mean High Water; MHWN: Mean High Water at Neap tide (MHWN). After: *Foster et al.* (2013).

et al., 2013). Due to their location in the intertidal zone, salt marshes are wholly or partially flooded at high water and dry at low water.

The salt marsh topography can be divided into three zones by their elevation with respect to the tidal levels (Fig. 2.2). The zone between the seaward edge, which is found at mean high water neap (MHWN), and mean high water level (MHW) is the lower marsh. This zone is flooded twice-daily with the exception of neap tide. Further inland, the middle marsh is located between MHW and the mean high water level at spring tide (MHWS). This zone is only flooded during the spring half of the spring-neap cycle. Finally, the upper marsh is the area between MHWS and the highest astronomical tide (HAT). This zone only floods during very high tides or storm events.

The salt marsh habitat is a combination of vegetated platforms and creeks (*Fagherazzi et al.*, 2012) (Fig. 2.3). The vegetated platforms exhibit a diverse range of salt-tolerant vegetation, which includes grasses, bushes and reeds. The platforms are dissected by a creek network, which routes the incoming and outgoing tides through the salt marsh. The creeks may also a discharge river flow when connected to the landward boundary of the marsh.

Figure 2.3: Laugharne South Marsh, Carmarthenshire, UK, at high water.

2.2.2 Salt marsh vegetation

Salt marsh platforms exhibit typical vegetation types in each zone due to the variations in inundation frequency. The height of the vegetation tends to increases with elevation as stresses by inundation and waves reduce at higher elevations (*Pennings and Callaway*, 1992; *Foster et al.*, 2013). The lower marsh is commonly populated by succulent species such as those belonging to *Spartina* and *Salicornia* genus (*Foster et al.*, 2013). *Atriplex* and *Aster* can be found along the creeks in this zone. The vegetation of the middle marsh is diverse with bushes and grasses that can have leaves and flowerheads. Typical genera are *Juncus*, *Festuca* and *Agrostis*. Finally, the upper marsh often exhibits grasses such as *Elymus* and *Puccinellia*. The exact distribution of species depends on a complex interaction between environmental conditions, soil and species competition (*Pennings and Callaway*, 1992). Photos of selected common salt marsh vegetation species are presented in Fig. 2.4.

It is commonly assumed that the geometry of a salt marsh field can be simplified as an array of cylinders (*Mullarney and Henderson*, 2018). The individual plants are described by their height h_v, stem diameter b_v, and stem flexural rigidity EI_v (Fig. 2.5a). Vegetation is classified as rigid when its rigidity is sufficiently high to prevent stem bending under current and wave forces. Alternatively, a plant is classified as flexible when it bends over under current or wave forcing. Furthermore, plant density n_v and spacing $S_v = n_v^{-1/2}$ are used to describe veg-

Figure 2.4: Samples of five common salt marsh species. The black and white squares are 0.25×0.25 m in size.

etation fields (Fig. 2.5b). These parameters are referred to as the biomechanical properties of vegetation. Throughout this thesis, the Cartesian coordinate system is defined such that the x-axis is parallel to the main flow direction, the y-axis is normal to the main flow direction, and the z-axis is in the upward direction with $z = 0$ at the free surface and $z = -h$ at the bed. Herein, h is the water depth.

The biomechanical properties vary significantly within and between salt marsh species with the largest variation observed in the stem density and flexural rigidity. We compared the biomechanical properties of six common vegetation species in Table 2.1. The reported vegetation heights and diameters differed by up to one order of magnitude across species. The vegetation heights are in the range of 200–1100 mm and the stem diameters are in the range of 1–11 mm. Alternatively, the reported stem densities and flexural rigidities differed by up to three orders of magnitude. In addition to differences between species, the reported stem density and flexural rigidity also differed strongly within a specie.

The variation in biomechanical plant properties can be related to natural causes, but a full understanding is limited due to a lack of data. First, environmental and genetic factors strongly impact plant properties (*Anderson and Treshow*, 1980; *van Hulzen et al.*, 2007) and can vary significantly between salt marsh sites. Second, seasonal variations may strongly impact the observed plant density and flexural rigidity (*Schulze et al.*, 2019). Specifically, flexural rigidity, due to a lower Young's modulus, may reduce by 75% and biomass by 33% in winter compared to summer conditions. However, it should be noted that data sets are scarce. In particular, stiffer shrubs such as *A. Portulacoides* and *A. Tripolium* (not included in Table 2.1 due to lack of data) are underrepresented which prevents a reliable inter-species comparison.

Building on the fundamental biomechanical properties, we can define addi-

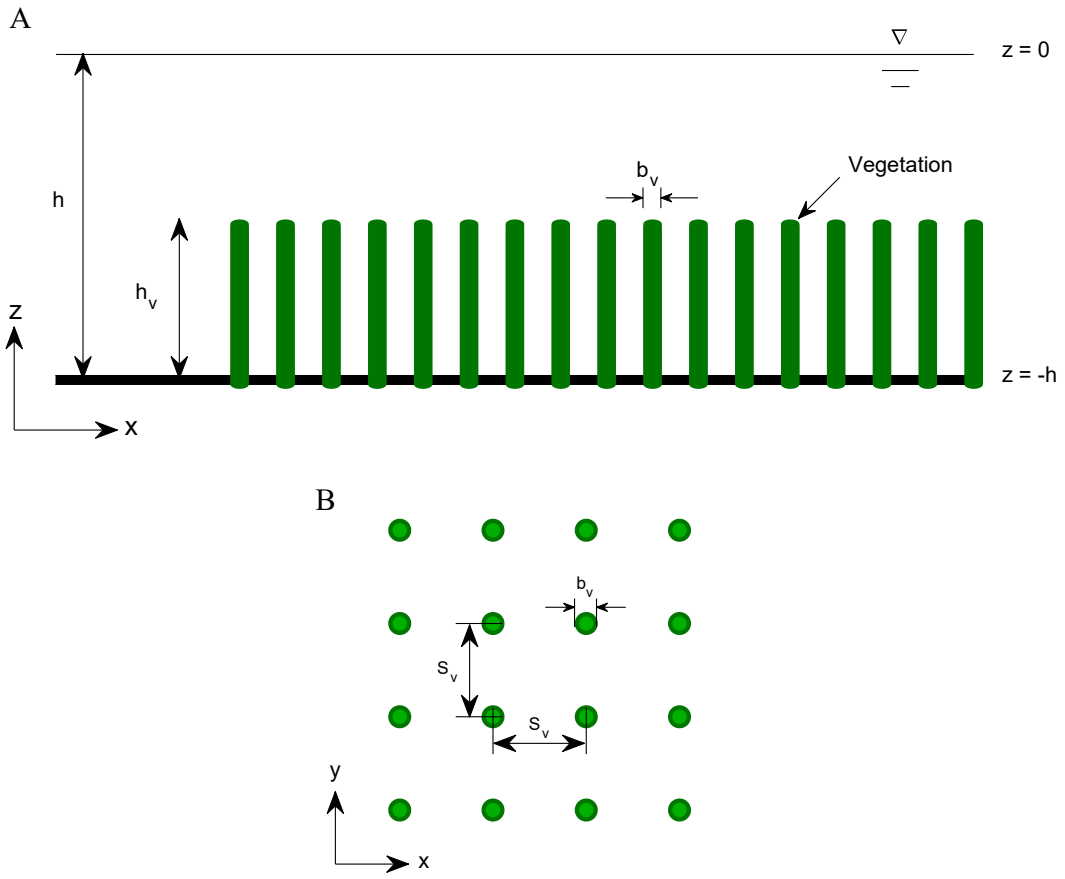

Figure 2.5: Definition sketch of a salt marsh canopy. (a) Side view of submerged vegetation; (b) top view of a canopy. Plants are denoted by cylindrical stems.

Table 2.1: List of salt marsh species and their biomechanical properties. The range given is between the lowest and highest reported value. n denotes the number of studies available per specie.

Specie	h_v **[mm]**	b_v **[mm]**	n_v **[m^{-2}]**	EI_v **[Nm^2]**	λ_f **[-]**	**n**	
Spartina Anglica	270-580	2-6	16-3500	9.6×10^{-4}-1.8×10^{-2}	1-5	6	[1]
Puccinellia Maritima	200-470	1-3	2500-14000	1.2×10^{-5}-4.5×10^{-4}	1-6	4	[2]
Elymus Athericus	460-700	1-2	835-1700	6.1×10^{-4}-4.6×10^{-3}	2.2	3	[3]
Spartina Alterniflora	220-1100	4-11	88-420	7.4×10^{-3}-5.4×10^{-2}	0.78	5	[4]
Atriplex Portulacoides	359	2	220	-	0.15	1	[5]

[1] *van Hulzen et al.* (2007); *Widdows et al.* (2008); *Bouma et al.* (2013); *Rupprecht et al.* (2015); *Lara et al.* (2016); *Schulze et al.* (2019); [2] *Bouma et al.* (2013); *Möller et al.* (2014); *Rupprecht et al.* (2015); *Lara et al.* (2016); [3] *Möller et al.* (2014); *Rupprecht et al.* (2015); *Schulze et al.* (2019); [4] *Christiansen et al.* (2000); *Feagin et al.* (2011); *Ysebaert et al.* (2011); *Chatagnier* (2012); *Jadhav et al.* (2013); [5] *Feagin et al.* (2011).

tional parameters to classify vegetation fields on the canopy scale. First, the relative water depth $h_r = \min(h_v/h, 1)$ represents the part of the water column that is covered by vegetation. $h_r < 1$ indicates that vegetation is submerged and $h_r = 1$ indicates that vegetation is emergent. The submergence ratio $\alpha = \max(h/h_v, 1) = 1/h_r$ is used as an alternative ratio (e.g. *Mendez and Losada*, 2004). Second, the relative frontal area $\lambda_f = h_v b_v n_v$ is a dimensionless parameter that expresses the plant frontal area per unit ground area as a measure of the density of a canopy (*Lowe et al.*, 2005). The relative frontal area varies strongly between salt marsh sites, but typically lies between 0.1 and 6 (Table 2.1). The plant volume per unit area $\lambda_p = \pi b_v^2 h_v n_v/4$ (*Lowe et al.*, 2005), the solid volume fraction $\lambda_s = \pi b_v^2 h_r n_v/4$ (*Tanino and Nepf*, 2008) and the frontal area per unit water volume $\lambda_a = h_r b_v n_v$ (*Mullarney and Henderson*, 2018) are alternative measures of the canopy density.

Salt marsh vegetation contributes to coastal protection through sediment capture, root binding, and its interaction with currents and waves. The presence of vegetation captures suspended sediment from the water column (*Mudd et al.*, 2010; *Fauria et al.*, 2015) and plant roots bind the soil to prevent erosion (*De Battisti et al.*, 2019). The root binding effect remains effective under high energy wave conditions (*Möller et al.*, 2014). Sediment capture and root binding promote sediment accretion on salt marshes and allow them to potentially keep up with a moderate pace of sea level rise (*French*, 1993; *Best et al.*, 2018). The interaction with currents and waves is explored in detail in Sections 2.3 and 2.4 respectively.

2.2.3 Creek networks

Creeks form branching sinuous networks that dissect the vegetation platforms. Their primary function is to route the tidal in- and outflow, which carries seeds and sediments that are essential for the growth and expansion of the vegetation cover. In fact, elevated marsh areas with vegetation flood perpendicularly from the creeks, when the water level exceeds the creek levels, rather than by sheet flow from the estuary channel itself (*Temmerman et al.*, 2005; *Ashall et al.*, 2016). They are connected to the seaward water body at their mouth and may also connect to a river inflow at the landward side when present.

Creek networks are controlled by the topography and vegetation cover throughout their evolution. They are initiated by flow convergence over an intertidal surface due to vegetation or small perturbations in local bottom elevation (*Temmerman et al.*, 2007; *Fagherazzi et al.*, 2012). The flow concentrates around the edges of the vegetation and in local bed level minima. In particular, denser vegetation canopies generate more drag and enhance flow concentration. Tidal currents will continue to converge due to the increased cross-sectional area and depth at the incisions, which provide lower flow resistance (*Fagherazzi and Fur-*

bish, 2001). This positive feedback loop promotes the development of a channel. The roots of vegetation bind sediment on steep creek banks, enabling the development of deep narrow channels (*D'Alpaos et al.*, 2006). Besides cross-sectional growth, a creek may initiate a network via extension and tributary branching. Headward erosion can extend a channel when the critical shear stress is exceeded (*Fagherazzi et al.*, 2012). Similarly, tributary branching may occur when lateral incisions are carved out by local flow concentrations.

The developing creek network supplies the adjacent vegetated platforms with seeds and sediment which promotes their accretion (*D'Alpaos et al.*, 2006) but also initiates an asymptotic evolution towards an equilibrium. The increased platform elevation decreases the water volume that flows over a salt marsh during a tidal cycle and, subsequently, dampens flow convergence. As a result, the platforms are supplied with fewer sediments, which slows down further accretion. This process continues until the net sediment fluxes vanish and an equilibrium is reached between the platform elevation, creek morphology and tidal water volume (*D'Alpaos et al.*, 2006; *Fagherazzi et al.*, 2012). It is expected that areas with a high degree of flow concentration develop the most extensive and deepest networks. This hypothesis is supported by *Temmerman et al.* (2007), who argues that marshes that are colonized by dense vegetation trigger networks with higher drainage densities.

A single salt marsh may display several creek networks with different sizes. *D'Alpaos et al.* (2009) describe how competition between multiple inlets results in branching creek networks. These dynamics resemble the drainage of watersheds by meandering rivers. Indeed, tidal creeks are highly sinuous, but lack scale invariance features as observed in their fluvial counterparts (*Rinaldo et al.*, 1999; *Marani et al.*, 2003). This means that geometrical properties may not only vary between different salt marshes, but also within hundreds of meters of a particular marsh or network.

2.3 Current-vegetation interaction

2.3.1 Drag resistance by rigid vegetation on unidirectional currents

When currents travel through vegetation fields, they exercise drag force and skin friction on plant stems (*Abdelrhman*, 2007). We consider unidirectional currents that travel through a vegetation field such that the x-z coordinate system defined in Fig. 2.5a is valid. The current field is expressed as $U(x, z, t) = u + iw$, where the real part denotes flow in x-direction (u) and the complex part denotes flow in z-direction (w). The currents can vary in both spatial directions and in time

(t). The drag force typically dominates the skin friction in the current-vegetation interaction (*Luhar and Nepf*, 2011). The drag force on a rigid upright stem per unit length is given by (*Dijkstra and Uittenbogaard*, 2010)

$$F_D(x,z,t) = \frac{1}{2}\rho C_{Dc} b_v u|u|. \tag{2.1}$$

Herein, ρ is the water density which is set at 1025 kg/m^3 for seawater and C_{Dc} is the drag coefficient induced by currents. C_{Dc} is a function of the canopy density λ_s and Reynolds number $Re = ub_v/\nu$ with $\nu = 10^{-6}$ m^2/s as the kinematic viscosity of water. C_{Dc} increases for denser canopies and higher Reynolds numbers (*Tanino and Nepf*, 2008). $C_{Dc} = 1$ is typically a representative value for field conditions (*Ashall et al.*, 2016; *Hu et al.*, 2018). Most natural canopies are sufficiently sparse such that interactions between stems may be ignored (*Mullarney and Henderson*, 2018). Then, the drag force of a vegetation canopy area per unit ground area and per unit stem length is given by

$$F_c(x,z,t) = n_v F_D = \frac{1}{2}\rho C_{Dc} b_v n_v u|u| \tag{2.2}$$

with F_c as the canopy drag force.

The vegetation-induced drag manipulates the current dynamics through the horizontal momentum balance. Given that salt marshes are located in the intertidal zone where water depths are shallow and that vegetation drag dominates bottom drag for natural vegetation types (*Mullarney and Henderson*, 2018), the canopy drag can be implemented in the shallow-water equations. Following *Dijkstra and Uittenbogaard* (2010) and including advection, the horizontal momentum equation in the flow direction is given by

$$\underbrace{\frac{\partial u}{\partial t}}_{\text{inertia}} + \underbrace{u\frac{\partial u}{\partial x} + w\frac{\partial u}{\partial z}}_{\text{advection}} + \underbrace{g\frac{\partial \eta}{\partial x}}_{\text{pressure gradient}} + \underbrace{\frac{F_c}{\rho(1-A_p)}}_{\text{vegetation drag}} = \underbrace{\frac{1}{1-A_p}\frac{\partial}{\partial z}\left((1-A_p)\left(\nu+\nu_T\right)\frac{\partial u}{\partial z}\right)}_{\text{turbulent mixing}} \tag{2.3}$$

where $g = 9.81$ m/s^2 is the gravitational acceleration, $\eta(x,t)$ is the water surface elevation, $\nu_T(x,z,t)$ is the eddy viscosity due to vegetation-induced turbulence (*Dijkstra and Uittenbogaard*, 2010), and $A_p(z) = n_v \pi b_v^2/4$ is the solid volume fraction per unit water depth. When steady ($\partial/\partial t = 0$) and depth-uniform flow ($\partial/\partial z = 0$) is assumed, Eq. 2.3 reduces to

$$u\frac{\partial u}{\partial x} + g\frac{\partial \eta}{\partial x} + \frac{F_c}{\rho(1-A_p)} = 0 \tag{2.4}$$

which shows that vegetation drag causes a reduction in the horizontal flow velocity or a negative water level gradient in the flow direction.

2.3.2 Drag resistance by flexible vegetation on unidirectional currents

Flexible plants bend in the flow direction when forced by currents of sufficient magnitude, which reduces their frontal area. Therefore, the drag force produced by a flexible stem will be lower than by a rigid stem. Two methods have been proposed to include the effect of plant bending on the drag force: (i) the Vogel coefficient; (ii) solving plant bending.

The Vogel coefficient An empirical formulation for the reduction in drag through streamlining of flexible vegetation is obtained by relating the drag force to the Vogel coefficient (*Vogel*, 1996), according to

$$F_D \propto u^{2+VC} \tag{2.5}$$

where VC is the Vogel coefficient. $VC = 0$ for rigid vegetation and VC decreases with increasing stem flexibility. Experimental studies have proposed $-0.3 > VC \geq -1$ for a range of flexible floodplain vegetation species (*Albayrak et al.*, 2012; *Aberle and Järvelä*, 2013). The Vogel coefficient has been particularly successful in simulating flow resistance by leafy vegetation with complex geometries that differ significantly from the rigid cylindrical stems that are commonly assumed. However, this method relies on plant-specific calibration.

Solving plant bending In order to solve the plant bending of flexible vegetation, we introduce a plant-scale coordinate system (Fig. 2.6a) in addition to the canopy-scale coordinate system (Fig. 2.5). x_v is the horizontal axis in the flow direction relative to the plant root and z_v is the vertical axis relative to the plant root. Furthermore, s is the along-stem axis. The root of the stem is located at $x_v = z_v = s = 0$ and the the stem tip is located at $s = h_v$. The stem shape is defined by stem position $X(x, s, t) = x_v + iz_v$ and local stem bending angle $\theta(x, s, t)$. The velocities and forces acting on a stem are expressed in terms of the plant-scale coordinate system (Fig. 2.6b). $U_s(x, s, t) = u_s + iw_s$ is the projection of the ambient velocity on a stem and $u_n = \Re\left(U_s e^{i\theta}\right)$ is the velocity component in a direction normal to the stem. The plant position and velocity at the stem are a function of canopy-scale coordinate x as the current magnitude changes over a vegetation field.

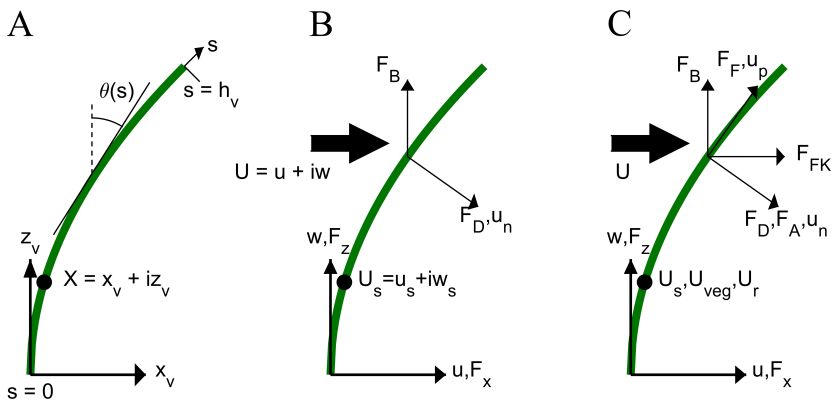

Figure 2.6: Definition sketches of the (a) plant-scale coordinate system; (b) velocities and forces under unidirectional flow; (c) velocities and forces under wave forcing.

The bending of a flexible stem can be obtained through a solution of the force balance between the drag force and the restoring forces (*Dijkstra and Uittenbogaard*, 2010; *Luhar and Nepf*, 2011). It is assumed that stems are inextensible, move in the vertical plane only, do not fold around themselves, have homogeneous cylindrical cross-sections, have homogeneous flexural rigidity and do not interact with other stems (*Dijkstra and Uittenbogaard*, 2010; *Luhar and Nepf*, 2011, 2016). The drag force is generated by the current-vegetation interaction in a direction normal to the stem. Due to bending of flexible vegetation, the stem-normal direction varies over the stem length and cannot be assumed parallel to the x-axis as was the case with rigid vegetation. Therefore, Eq. 2.1 changes to

$$F_D(x,s,t) = \frac{1}{2}\rho C_{Dc} b_v u_n |u_n| e^{-i\theta}. \tag{2.6}$$

The term $e^{-i\theta}$ denotes that the drag force acts in the stem-normal direction. The stem buoyancy force results from the density difference between vegetation and water. It acts in a direction parallel to the z-axis and is given by (*Luhar and Nepf*, 2016)

$$F_B(s,t) = i\frac{1}{4}\pi(\rho - \rho_v) g b_v^2 \tag{2.7}$$

with ρ_v as the mass density of the vegetation. Finally, the stem stiffness represents the internal shear resistance of the vegetation against bending and acts in a direction normal to the stem (*Luhar and Nepf*, 2011). The shear stress at any

point on the stem is given by

$$F_s(x,s,t) = -EI_v \frac{\partial^2 \theta}{\partial s^2} e^{-i\theta}. \tag{2.8}$$

Then, the force balance between drag forces and restoring forces at any location along the stem s' is given by (*Luhar and Nepf*, 2011)

$$\int_{s'}^{h_v} F_D ds + \int_{s'}^{h_v} F_B ds + F_s(s') = 0 \tag{2.9}$$

where the real part denotes the horizontal force balance and the complex part denotes the vertical force balance. The integrals denote that the drag and buoyancy forces are exerted over the full stem section $s \geq s'$. Substitution of Eq. 2.6-2.8 in Eq. 2.9, taking the spatial derivative $\partial/\partial s$, and multiplication with $e^{i\theta}$, leads to a new expression for the force balance, according to

$$\frac{1}{2}\rho C_{Dc} b_v u_n |u_n| + i\frac{1}{4}\pi(\rho - \rho_v) g b_v^2 e^{i\theta} - EI_v \left(\frac{\partial^3 \theta}{\partial s^3} - i \frac{\partial \theta}{\partial s} \frac{\partial^2 \theta}{\partial s^2} \right) = 0 \tag{2.10}$$

where the real part is in the stem-normal direction and the complex part in the stem-parallel direction. As θ is the only unknown in Eq. 2.10, the plant position can be solved as a function of the current velocity. Solutions have been obtained using computational models with the buoyancy force omitted (*Dijkstra and Uittenbogaard*, 2010) and with the buoyancy force included (*Luhar and Nepf*, 2011). Specifically, *Luhar and Nepf* (2011) showed the relative importance of each term in Eq. 2.10 through a scaling analysis. Substitution of the dimensionless parameters $s_* = s/h_v$ and $U_* = U/u_c$, where u_c is the flow velocity scale, in Eq. 2.10 gives

$$\frac{1}{2} C_{Dc} Ca \, u_{n*} |u_{n*}| + iBe^{i\theta} - \frac{\partial^3 \theta}{\partial s_*^3} + i \frac{\partial \theta}{\partial s_*} \frac{\partial^2 \theta}{\partial s_*^2} = 0 \tag{2.11}$$

with

$$B = \frac{(\rho_v - \rho)\, \pi g b_v^2 h_v^3}{4EI_v} \tag{2.12}$$

as the Buoyancy number, and

$$Ca = \frac{\rho b_v u_c^2 h_v^3}{EI_v} \tag{2.13}$$

as the Cauchy number. The buoyancy number represents the ratio between restoring forces due to buoyancy and stiffness. The Cauchy number represents the ratio between the drag force as the bending force and vegetation stiffness as the restoring force. The here presented formulations for the Buoyancy and Cauchy numbers

differ in two ways from those defined in *Luhar and Nepf* (2011). First, we consider cylindrical instead of rectangular vegetation. Second, the drag coefficient is left out of the Cauchy number as it is a function of flow conditions (*Tanino and Nepf*, 2008).

Luhar and Nepf (2011) define an effective vegetation length l_e such that a rigid stem of length l_e produces an equal drag force as would be produced by a flexible stem of length h_v. They find three regimes for plant bending based on B and Ca. In case of buoyancy dominated flow $B \gg Ca$, $l_e \approx h_v$ for $B < 1$ and scales with $le/h_v \sim (B^{-1}Ca)^{-2/3}$ for $B > 1$. In case of stiffness-dominated flow $B \ll Ca$, $l_e \approx h_v$ for $Ca < 1$ and scales with $le/h_v \sim Ca^{-1/3}$ for $Ca > 1$. In case of general flow where $B \approx Ca$, $l_e \approx h_v$ for $B^{-1}Ca < 1$ and scales with $le/h_v \sim Ca^{-1/3}$ for $B^{-1}Ca > 1$.

2.3.3 Effect of salt marsh vegetation on tidal flow and storm surges

Tides and storm surges drive water level gradients and currents over salt marshes. In addition to reducing current magnitudes, the presence of salt marsh vegetation modifies the vertical velocity structure, produces turbulence, redirects currents, and lowers water levels.

Implications for velocity structure

We find through the momentum balance (Eq. 2.4) that vegetation-induced drag reduces flow velocities within vegetation which modifies the vertical structure of the velocity. Four velocity zones can be defined (*Baptist et al.*, 2007) (Fig. 2.7).

1. Zone 1, directly above the substrate, is dominated by bed friction and the velocity structure follows the logarithmic bottom boundary layer.

2. Zone 2 covers the vegetated region that is unaffected by the top and bottom. The velocity structure is uniform and controlled by the vegetation.

3. Zone 3 is located near the top of the vegetation and forms a transitional profile between the vegetated and unvegetated zones. It can be approximated by an exponential profile.

4. Zone 4 ranges from the top of zone 3 to the water surface. A logarithmic profile is observed, similar to flow over an unvegetated bed.

Zones 2 and 4 can be viewed as the vegetation-dominated and free flow zones respectively. Alternatively, zones 1 and 3 can be viewed as transitional zones near

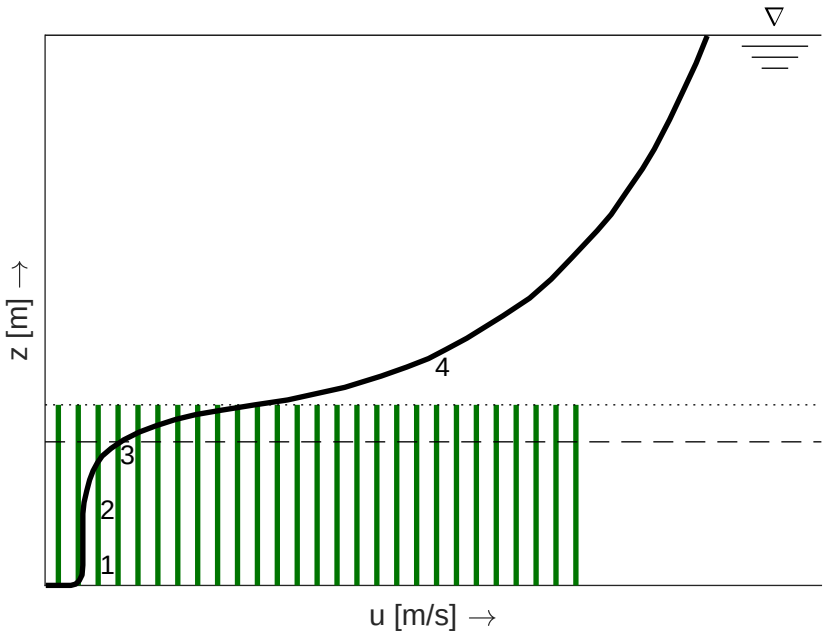

Figure 2.7: Vertical velocity profile of unidirectional currents that travel through and over vegetation. The profile is divided into four zones (see text). The dotted line denotes the height of the vegetation and the dashed line denote the zero-plane displacement of the logarithmic velocity profile over the vegetation (zone 4). After: *Baptist et al.* (2007).

the bottom and around the top of the vegetation. Zones 3 and 4 are only present when the vegetation is sufficiently submerged. When vegetation is emergent, the vertical velocity profile is uniform (zone 2) with the exception of the bottom boundary layer near the seabed (zone 1). Finally, when vegetation would be removed, only the free flow zone (4) remains.

Implications for turbulence

Current-vegetation interactions produce turbulence at the plant and canopy scales. Plant-scale turbulence is produced in the wake downstream of vegetation (*Nepf*, 1999). Alternatively, canopy-scale turbulence results from the high shear stress at the top of the vegetation canopy (*Nepf*, 2012b). The canopy-scale turbulent energy peaks at the top of the vegetation and dissipates in the free flow zone above the vegetation and within vegetation towards the bottom (*Dijkstra and Uittenbogaard*, 2010). The turbulence production by vegetation is vital for sediment accretion as it keeps fine sediment longer in suspension (*Furukawa et al.*,

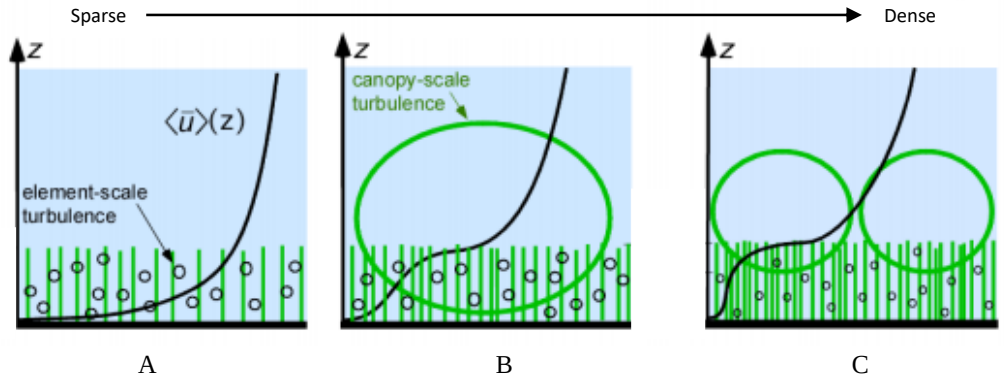

Figure 2.8: Turbulence production by vegetation at (a) the plant scale in sparse canopies and (b,c) the canopy scale in denser canopies. Source: *Nepf* (2012b).

1997).

Implications for current direction

The drag that is generated by salt marsh vegetation can redirect tidal currents and storm surges. As vegetated areas induce a greater momentum loss than unvegetated areas (Eq. 2.4), the discharge over salt marshes decreases, whereas it increases over unvegetated zones. For example, vegetation platforms are flooded from a direction perpendicular to the nearest creek rather than through sheet flow (*Temmerman et al.*, 2005; *Ashall et al.*, 2016; *Wu et al.*, 2017). Furthermore, the presence of salt marsh vegetation on the banks of estuaries amplifies the flow through the main estuary channel and reduces along-channel flow over the salt marshes (*Ashall et al.*, 2016; *Wu et al.*, 2017)

Implications for water levels

The simplified momentum balance (Eq. 2.4) demonstrates that the momentum lost due to drag by vegetation can be compensated by a negative water level gradient. As a result, the water level that is driven by tides or storm surges may decrease over salt marshes (Fig. 2.9). Salt marshes of at least 100 m in length have been found to reduce water levels by 0–700 mm/km marsh length (see reviews by *Stark et al.*, 2015; *Paquier et al.*, 2017). Conversely, vegetated platforms drain at a slower rate than unvegetated areas due to the vegetation-induced drag (*Furukawa and Wolanski*, 1996). Additionally, salt marshes may contribute to along-channel reductions of the tidal and storm surge levels through water storage (*Smolders et al.*, 2015) in a way that is similar to managed realignment.

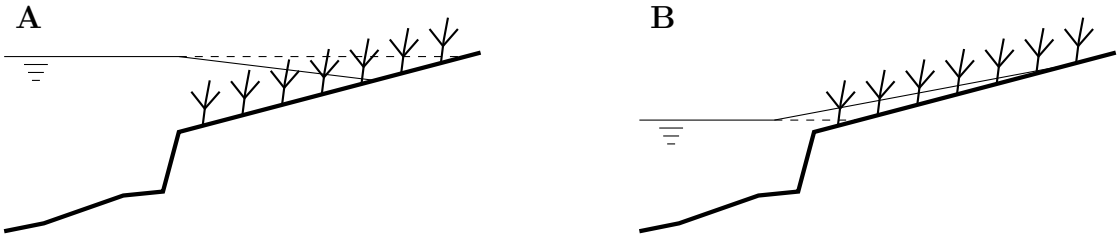

Figure 2.9: Water levels on a salt marsh at (a) high and (b) low water. The thin solid line denotes the water surface, and the dashed line is the water surface without vegetation present.

2.4 Wave-vegetation interaction

When waves travel over vegetation fields, the interaction between waves and vegetation modifies the wave dynamics around vegetation. The waves reduce in height due to energy dissipation over vegetation (*Dalrymple et al.*, 1984) and the shear forces produced by the wave-vegetation interaction may induce phase-averaged currents around vegetation (*Luhar et al.*, 2010).

2.4.1 General description of wave damping

We include waves with spatially variable height $H(x)$ in the canopy-scale coordinate system (Fig. 2.10), and define vegetation velocity $U_{veg}(s,t) = \partial X/\partial t$ and the four wave-induced forces $F_D(s,t)$ $F_F(s,t)$, $F_A(s,t)$, $F_{FK}(s,t)$ at the plant scale (Fig. 2.6c). The waves propagate in a direction parallel to the x-axis. As a key difference with steady current flow, waves exhibit periodic orbital motion with velocities that vary in magnitude and direction over a wave cycle. Velocities and forces are a function of space and time under these conditions, i.e. $U(x,z,t)$, $U_s(x,s,t)$ and $F(x,s,t)$.

The definition of the four wave-induced forces are (*Zeller et al.*, 2014; *Luhar and Nepf*, 2016): the drag force in stem-normal direction;

$$F_D(x,s,t) = \frac{1}{2}\rho C_{Dw}|u_{rn}|u_{rn}e^{-i\theta}, \tag{2.14}$$

the skin friction in stem-parallel direction;

$$F_F(x,s,t) = \frac{1}{2}\rho C_F|u_{rp}|u_{rp}ie^{-i\theta}, \tag{2.15}$$

the added mass force in stem-normal direction;

$$F_A(x,s,t) = \frac{1}{4}\pi\rho C_A b_v^2 \frac{\partial u_{rn}}{\partial t}e^{-i\theta}, \tag{2.16}$$

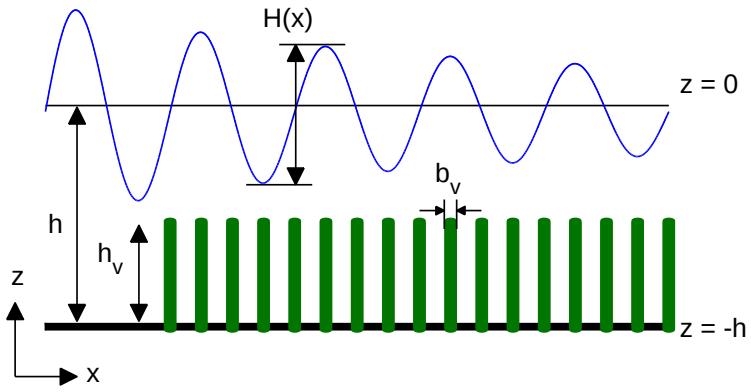

Figure 2.10: Definition sketch of the canopy-scale coordinate system with waves.

and the Froude-Krylov force in the flow direction;

$$F_{FK}(x,s,t) = \frac{1}{4}\pi\rho b_v^2 \frac{\partial U_s}{\partial t_*}. \tag{2.17}$$

Herein, C_{Dw} is the drag coefficient induced by waves. C_F and C_A are coefficients for the friction and the added mass force respectively. $u_{rn} = \Re\left(U_r e^{i\theta}\right)$ and $u_{rp} = \Im\left(U_r e^{i\theta}\right)$ are the stem-normal and stem-parallel components of the relative velocity between water and stem $U_r = U_s - U_{veg}$. All forces are given per unit stem length. We note that the definition of the wave-induced drag force (Eq. 2.14) reduces to the definition of the current-induced drag force for rigid vegetation (Eq. 2.1) when the stem position is steady ($U_{veg} = 0$) and upright ($\theta = 0$). Alternatively, the drag force reduces to the definition of the current-induced drag force for flexible vegetation (Eq. 2.6) when only the stem position is steady but not upright. Furthermore, it is noted that drag coefficient C_{Dw} under wave conditions differs from the drag coefficient C_{Dc} under current conditions. Although both are in the order of unity and a function of Re, the drag coefficient induced by waves appears to be more sensitive to variations in Re. The velocity is steady under current forcing, but changes in magnitude and direction over short time scales under wave motion. The hydrodynamic forcing and associated Re change over a wave cycle but, typically, a phase-averaged C_{Dw} is defined for simplicity. Furthermore, the wave drag coefficient C_{Dw} often acts as a calibration parameter, which affects its value. Additional research is needed to further clarify why C_{Dc} and C_{Dw} may differ.

The full wave force is given by

$$F_W(x,s,t) = F_D + F_F + F_A + F_{FK}. \tag{2.18}$$

Wave energy dissipation over vegetation is controlled by the conservation of wave power (*Dalrymple et al.*, 1984). In case of a flat bed, it is given by

$$c_g \frac{\partial E}{\partial x} = -n_v \epsilon_v \tag{2.19}$$

where $E(x) = \frac{1}{8}\rho g H^2$ is the wave energy, $c_g = \frac{\omega}{2k}\left(1 + \frac{2kh}{\sinh 2kh}\right)$ is the wave group velocity with ω as the wave frequency and k as the wave number, and

$$\epsilon_v(x) = \int_{s=0}^{h_v} \overline{F_W \cdot U_s} ds \tag{2.20}$$

is the energy dissipation per stem. Here the overbar $\bar{}$ denotes phase-averaging and $\cdot$ denotes a dot-product. Wave damping over a vegetation field can be described when a solution for Eq. 2.19 is found. A direct solution can be found in case of rigid vegetation when vegetation motion is absent. Alternatively, plant swaying by flexible vegetation will induce a two-way interaction between wave forces and plant motion for which several solution methods have been trialled.

2.4.2 Wave damping over rigid vegetation

Rigid vegetation remains upright over a wave cycle. Therefore, $\theta = 0$, $U_{veg} = 0$ and the s-axis is parallel to the z-axis such that $s = z - h$. The energy dissipation over rigid vegetation is dominated by the work done by the horizontal component of the drag force (*Mendez and Losada*, 2004). Whilst the added mass and Froude-Krylov forces may be significant in magnitude, their total work done is net zero as they are 90° out of phase with the wave velocity (*Hu et al.*, 2014). Furthermore, the work done in horizontal direction by the drag force dominates the work done in vertical direction by the friction force (*Kobayashi et al.*, 1993; *Mendez and Losada*, 2004). Under these conditions, the wave force simplifies to

$$F_W = F_D = \frac{1}{2}\rho C_{Dw} b_v u_s |u_s|. \tag{2.21}$$

An analytical solution can be obtained if it can further be assumed that linear wave theory is valid within the vegetation field. The velocity field under linear wave theory is given by (*Dean and Dalrymple*, 1991)

$$u = \frac{Hgk \cosh k(h+z)}{2\omega \cosh kh} \cos(kx - \omega t). \tag{2.22}$$

Then, the velocity field at the stem is given by

$$u_s = \frac{Hgk \cosh ks}{2\omega \cosh kh} \cos(kx - \omega t) \tag{2.23}$$

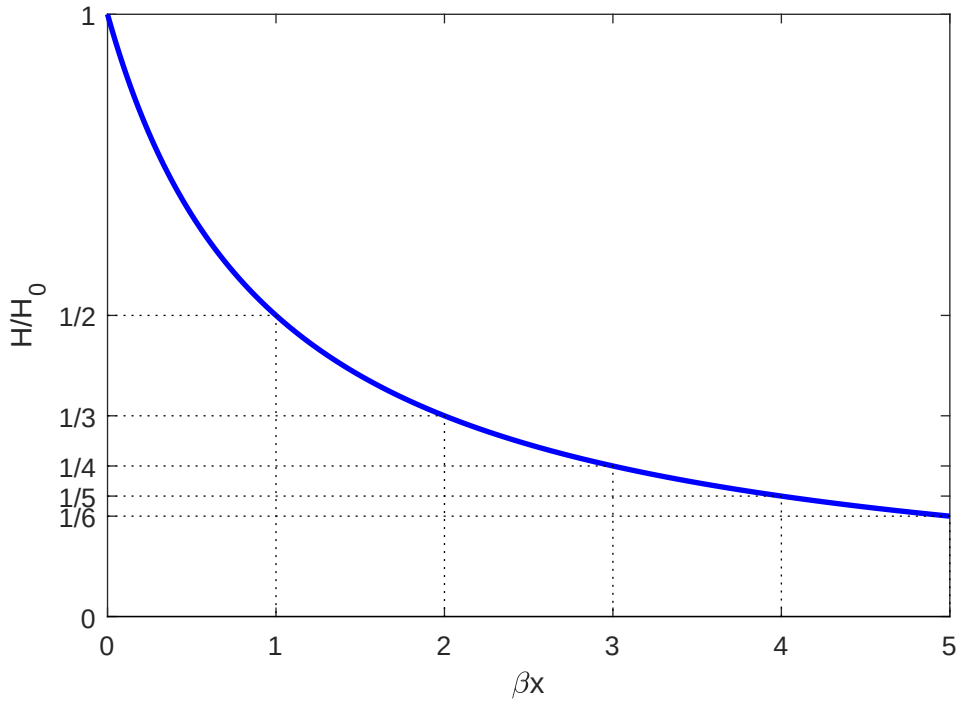

Figure 2.11: Reduction of the relative wave height H_0/H as function of βx.

Substitution of Eq. 2.21, 2.23 in Eq. 2.20 results in a direct equation of the energy dissipation according to

$$\epsilon_v = \frac{1}{12\pi}\rho C_{Dw} b_v \left(\frac{kg}{\omega}\right)^3 \frac{\sinh^3 kh_v + 3\sinh kh_v}{3k\cosh^3 kh} H^3. \tag{2.24}$$

Dalrymple et al. (1984) show that the solution of Eq. 2.19, obtained through substitution of Eq. 2.24, describes wave damping in the direction of wave propagation according to

$$H = \frac{H_0}{1+\beta x} \tag{2.25}$$

where H_0 is the wave height at the upstream edge of the vegetation field and

$$\beta = \frac{4}{9\pi} C_{Dw} b_v n_v H_0 k \frac{\sinh^3 kh_v + 3\sinh kh_v}{(\sinh 2kh + 2kh)\sinh kh} \tag{2.26}$$

is the wave damping coefficient. Figure 2.11 shows how the wave height reduces over vegetation as function of βx.

The wave damping solution provided by Eq. 2.25 and 2.26 is valid for regular waves. *Mendez and Losada* (2004) showed that a similar solution approach can

be adopted to solve damping under a Rayleigh wave distribution. In this case, waves damp according to

$$H_{rms} = \frac{H_{rms,0}}{1 + \tilde{\beta} x} \tag{2.27}$$

with H_{rms} as the root-mean-square wave height, $H_{rms,0}$ as the offshore root-mean-square wave height, and

$$\hat{\beta} = \frac{1}{3\sqrt{\pi}} \hat{C}_{Dw} b_v n_v H_{rms,0} k_p \frac{\sinh^3 k_p h_v + 3 \sinh k_p h_v}{(\sinh 2k_p h + 2kh) \sinh k_p h} \tag{2.28}$$

as the random wave damping coefficient. The accent $\hat{}$ denotes that the parameter is for random waves specifically and k_p is the wave number associated with the peak wave period T_p.

2.4.3 Wave damping over flexible vegetation

Flexible vegetation sways over a wave cycle which modifies the magnitude and direction of the wave forces (*Luhar and Nepf*, 2016) (Fig. 2.12). This reduces the wave damping potential of flexible vegetation in two ways. First, the orbital velocities are maximum in the horizontal direction in shallow water (*Dean and Dalrymple*, 1991). When vegetation is upright, the horizontal velocities align with the stem-normal direction, which enhances the drag and added mass forces. However, when stems bent, the horizontal velocities no longer align with the stem-normal component which reduces the drag and added mass forces (*Luhar and Nepf*, 2016). This is referred to as the stem reconfiguration effect. Second, when the vegetation follows the water motion, the velocity difference between the water and the stem reduces, lowering the magnitude of the drag, friction and added mass forces (*Méndez et al.*, 1999; *Mendez and Losada*, 2004). This is referred to as the stem velocity effect. In absence of simultaneous data on wave damping, water velocity fields, and plant motion, which can be used to separate the two mechanisms, it remains unclear what the relative contributions of the stem reconfiguration and the stem velocity effects are.

The wave-vegetation interaction is controlled by the force balance given by

$$\frac{1}{4}\pi \rho_v b_v^2 \frac{\partial^2 X}{\partial t^2} + EI \left(\frac{\partial^3 \theta}{\partial s^3} - i \frac{\partial \theta}{\partial s} \frac{\partial^2 \theta}{\partial s^2} \right) e^{-i\theta} = F_W + F_B. \tag{2.29}$$

Compared to the force balance for current-vegetation interaction (Eq. 2.10), the drag force is replaced by the wave force and a term for plant inertia is added to the left-hand side. The plant inertia term emerges as the vegetation moves over a wave cycle as opposed to unidirectional flow where the stem is continuously bent in downstream direction. The solution of Eq. 2.29 describes the vegetation

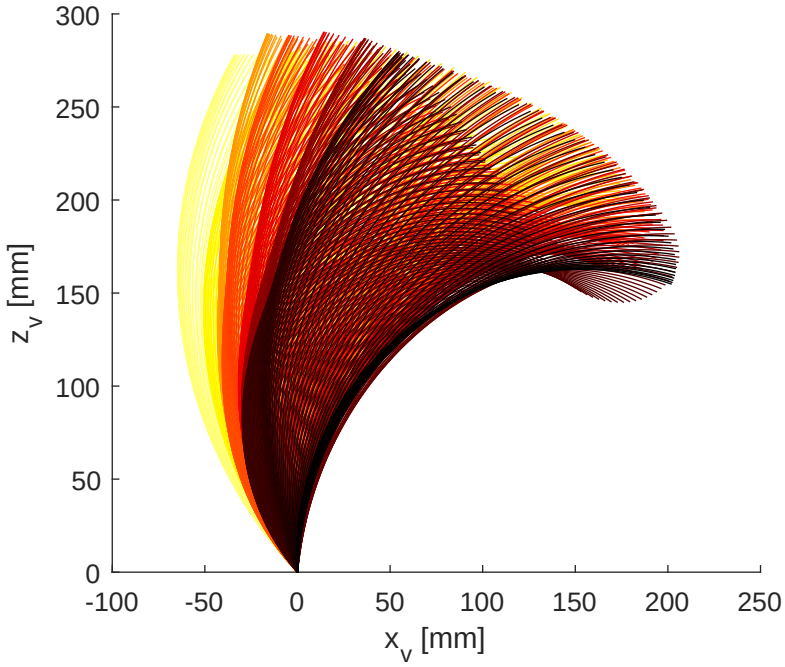

Figure 2.12: Swaying of flexible vegetation under wave motion. Solid lines denote the stem position and the colouring denotes the time. The plant position at the start of the observation period is yellow and the plant position at the end is black.

motion and wave forces over a wave cycle, which are required to solve wave damping over flexible vegetation. However, as the wave forces (Eq. 2.14-2.18) are both a driver and a function of plant motion, solving Eq. 2.29 is complex. Four solution methods have been developed to derive wave damping over flexible vegetation fields: (i) complex computational modelling; (ii) beam theory; (iii) scaling analysis; and (iv) drag coefficient calibration.

Complex computational modelling Eq. 2.29 has been solved computationally at the plant scale using finite difference schemes (*Luhar and Nepf*, 2016), and at canopy-scale using Reynolds Averaged Navier-Stokes (RANS) solvers with Volume of Fluid (VOF) surface capture (*Maza et al.*, 2013; *Chen and Zou*, 2019). Whilst these models have successfully reproduced plant motion and wave dynamics, their computational cost is significant, which makes them impractical for large-scale coastal applications.

Beam theory Solutions based on beam theory rely on simplifications of the wave-vegetation force balance. In it most basic form, it is assumed that (i) stem deflections during the swaying motion are small, (ii) wave forces are dominated by the horizontal component of the drag force, (iii) the drag force can be linearised, (iv) stem stiffness is the dominant restoring force, and (v) stem inertia is negligible. Under these conditions, the force balance simplifies to a balance between stem stiffness and the linearised drag force (*Mullarney and Henderson*, 2010), according to

$$EI\frac{\partial^4 x_v}{\partial z_v^4} = \frac{1}{2}\rho C_{Dw} b_v |u_r| \frac{\partial (u - u_{veg})}{\partial t}. \tag{2.30}$$

Eq. 2.30 represents an Euler-Bernoulli beam equation. This type of equation can be solved as a cantilever under uniform loading (*Méndez et al.*, 1999) or through a spatiotemporal expansion of the water and vegetation motion (*Mullarney and Henderson*, 2010). Both solution methods provide a transfer function that relates the vegetation motion directly to wave motion, based on which the wave forces and, subsequently, wave damping are computed. The advantage of a spatiotemporal expansion is that it can account for vertical variations in the wave velocity and in the plant biomechanical properties. Eq. 2.30 has been expanded to include plant inertia, added mass forces and buoyancy forces to obtain solutions under more complex conditions (*Méndez et al.*, 1999; *Henderson*, 2019), but all solutions assume small plant deflections. The solutions based on beam theory are computationally efficient but are restricted by the assumption of limited plant deflection.

Scaling analysis A related but more general method of simplifying the force balance is through a scaling analysis. We introduce

$$t_* = t\omega, \quad s_* = \frac{s}{h_v}, \quad U_* = \frac{U}{u_c}, \quad X_* = \frac{X}{h_v}, \quad KC = \frac{u_c T}{b_v} \tag{2.31}$$

as the dimensionless time coordinate, along stem coordinate, velocity, plant position and Keulegan-Carpenter number (*Keulegan and Carpenter*, 1958) respectively as well as wave period T. When $KC \gg 1$ the drag force dominates the force balance (Eq. 2.29) (*Luhar and Nepf*, 2016) which reduces to

$$\left(\frac{\partial^3\theta}{\partial s_*^3} - i\frac{\partial\theta}{\partial s_*}\frac{\partial^2\theta}{\partial s_*^2}\right) = \frac{1}{2}Ca\Re\left(\left(U_* - L\frac{\partial X_*}{\partial t_*}\right)e^{i\theta}\right)\left|\Re\left(\left(U_* - L\frac{\partial X_*}{\partial t_*}\right)e^{i\theta}\right)\right| \tag{2.32}$$

where

$$L = \frac{h_v}{A_w} \tag{2.33}$$

is the wave excursion ratio with $A_w = u_c/\omega$ as the wave excursion length. *Luhar and Nepf* (2016) identify two plant motion regimes depending on the wave excursion ratio, for which they define an effective vegetation length of equivalent wave damping. First, when the wave excursion is much larger than the plant length ($L \ll 1$), the plants will bend over during the first part of the wave cycle up to their maximum excursion, after which they cannot sway further until the flow reverses. The relative velocity is controlled by the water motion and the dynamics will be similar to steady current conditions (Section 2.3.2). Following the scaling analysis of vegetation under unidirectional currents, the effective length scales as $l_e/h_v \sim Ca^{-1/3}$ under drag-dominated conditions. Alternatively, when the wave excursion is much larger than the plant length ($L \gg 1$), the vegetation remains relatively vertical such that the Eq. 2.32 reduces to a dimensionless equivalent of the Euler-Bernoulli beam equation (Eq. 2.30). Here *Luhar and Nepf* (2016) show that the effective vegetation length scales as $l_e/h_v \sim (CaL)^{-1/4}$. The scaling relations have been successfully extended to develop relations for the effective vegetation length for flexible vegetation canopies (*Luhar et al.*, 2017; *Lei and Nepf*, 2019). However, as scaling does not provide an exact solution for plant motion, plant-specific calibration is required to fit the scaling relations. Furthermore, the scaling analysis does not provide a solution at the interface between the two regimes, i.e. at $L \approx O(1)$.

Drag coefficient calibration Rather than solving plant motion directly, its effect on wave damping may be included by calibration of the drag coefficient C_{Dw} in Eq. 2.26 or $\hat{C}_{Dw}$ in Eq. 2.28 (*Méndez et al.*, 1999; *Mendez and Losada*, 2004). The drag coefficient is fundamentally a function of the hydrodynamic conditions and object shape (*Keulegan and Carpenter*, 1958). However, as the drag coefficient cannot be measured a priori and the geometry of real vegetation is complex, it has been identified as a calibration parameter to account for model simplifications. These typically include simplified stem geometries, no vegetation motion, no interaction between stems (*Dalrymple et al.*, 1984), and, in order to fit Eq. 2.26 or Eq. 2.28, also a velocity profile inside vegetation that satisfies linear wave theory.

Empirical relations which predict the drag coefficient have been successfully developed for a range of aquatic vegetation species (Table 2.2). Most studies find that Reynolds number $Re = u_c b_v/\nu$ is the best predictor for the drag coefficient, but some find that the Keulegan-Carpenter number $KC = u_c T/b_v$ is a better predictor. Re and KC are both related to the flow regime and increase with higher orbital velocities. Both predictors have been successfully applied for a range of vegetation types that includes salt marshes, seagrass, real vegetation, artificial vegetation, blade-shaped leaf-dominated vegetation and cylindrical stem-dominated vegetation (see Table 2.2 for a full overview of test setups). Hence, Re and KC are applicable across a wide range of vegetation types. Yet, two alternative predictors have been developed. *Mendez and Losada* (2004) identified that a better fit for C_{Dw} was obtained using $Q_{KC} = KC/\alpha^{0.76}$ which includes the submergence ratio α. *Garzon et al.* (2019a) also found that Q_{KC} was an important predictor for wave damping in combined wave-current flows but raised α to the power 9 instead of 0.76, suggesting that Q_{KC} relies on an additional calibration. Finally, $Re_D = l_D u_c/\nu$ is a predictor based on the deflected plant height l_D (*Losada et al.*, 2016) but requires data on plant motion before it can be defined which reduces its predictive value.

Empirical relations commonly take the form of

$$C_{Dw} = \left(\frac{a}{KC}\right)^b + c \tag{2.34}$$

where a, b and c are fitted empirical coefficients (relation first proposed by *Kobayashi et al.*, 1993). A list of proposed sets of coefficients for studies where Re or KC was used as the best predictor is provided in Table 2.3. Furthermore, a reference drag coefficient $C_{Dw,ref}$ is given to compare values at $Re = 1000$ or $KC = 120$ provided these are covered by the range of a proposed relation. $Re = 1000$ is a typical regime for salt marshes under storm conditions (*Vuik et al.*, 2016). $KC = 120$ provides equivalent hydrodynamic conditions when $b_v = 5$ mm and $T = 3$ s. Fig. 2.13 shows that $C_{Dw,ref}$ values differ by up to two

Table 2.2: List of studies that derived relations for C_{Dw}. Pred. = Predictor and Type = Study Type. The references in the comments denote the data sources.

No	Pred.	Type	Vegetation material	Comments
[1]	Re	LABMG	polypropylene strips	(Data by) [17]
[2a]	Re	LABMG	polypropylene strips	Orbital velocity [17]
[2b]	Re	LABMG	polypropylene strips	Relative velocity [17]
[3]	Q_{KC}	LAPIG	Artificial *L. Hyperborea*	Exponential relation [18]
[4a]	KC	LACIH	Wooden dowels	Scatter plot
[4b]	KC	LACIS	Polyethylene foam	Scatter plot
[5a]	Re	FRBIG	Mainly *T. Testudinum*	Orbital velocity
[5b]	Re	FRBIG	Mainly *T. Testudinum*	Relative velocity
[6a]	Re	FRBIG	*Z. Noltii*	All data
[6b]	Re	FRBIG	*Z. Noltii*	Only $H_s > 0.1$ m
[7a]	KC	LABMG	Polyethylene blades	
[7b]	KC	LABIG	Polyethylene blades	
[8]	KC	FRCIS	*S. Alterniflora*	
[9]	Re	LAPIG	PVC blades in stiff rod	
[10a]	Re	LAPIG	PVC blades in stiff rod	Orbital velocity [19]
[10b]	Re	LAPIG	PVC blades in stiff rod	Relative velocity [19]
[11]	Re	LACIS	Polyolefin rods	
[12]	Re	LACMH	Wooden rods	Wave-only and wave-current conditions
[13a]	Re	LRCMS	Mainly *E. Athericus*	
[13b]	Re	LRCIS	Mainly *E. Athericus*	
[14a]	KC	LACMS	Birch dowels	
[14b]	KC	LACMS	Ethylene Propylene cords	
[14c]	KC	LRCMS	*S. Alterniflora* (dormant)	
[14d]	KC	LRCMS	*S. Alterniflora* (green)	
[14e]	KC	LRCMS	*J. Roemerianus*	
[15a]	Re_D	LRPMS	*P. Maritima* & *S. Anglica*	
[15b]	Re_D	LRPIS	*P. Maritima* & *S. Anglica*	
[16a]	Re	LRPMS	*S. Foliosa*	Stem and leaves
[16b]	Re	LRCIS	*S. Pacifica*	Stem only

Study types: L = Laboratory study; F = Field observational study; A = Artificial vegetation; R = Real vegetation; B = Blade-shaped vegetation; C = Cylindrical vegetation; P = Plant-like vegetation with stem and leafs; M = Monochromatic (regular) waves; I = Irregular (random) waves.

References: [1] *Kobayashi et al.* (1993); [2] *Méndez et al.* (1999); [3] *Mendez and Losada* (2004); [4] *Augustin et al.* (2009); [5] *Bradley and Houser* (2009); [6] *Paul and Amos* (2011); [7] *Sánchez-González et al.* (2011); [8] *Jadhav et al.* (2013); [9] *Koftis et al.* (2013); [10] *Maza et al.* (2013); [11] *Anderson and Smith* (2014); [12] *Hu et al.* (2014); [13] *Möller et al.* (2014); [14] *Ozeren et al.* (2014); [15] *Losada et al.* (2016); [16] *Foster-Martinez et al.* (2018); [17] *Asano et al.* (1988); [18] *Dubi* (1997); [19] *Stratigaki et al.* (2011).

Table 2.3: List of drag coefficient relations in the form of $C_{Dw} = (a/\text{predictor})^b + c$. $C_{Dw,ref}$ is a reference value of the drag coefficient at $Re = 1000$ or $KC = 120$.

No	**a**	**b**	**c**	**Range**	$\boldsymbol{C_{Dw,ref}}$	$\boldsymbol{EI_v}$ [$\mathbf{Nm^2}$]
[1]	2200	2.4	0.08	$2200 < Re < 18000$	6.71	$1.2 \times 10^{-9\ddagger}$
[2a]	2200	2.2	0.08	$200 < Re < 15500$	5.75	$1.2 \times 10^{-9\ddagger}$
[2b]	4600	2.9	0.4	$2300 < Re < 20000$		$1.2 \times 10^{-9\ddagger}$
[5a]	925	$3.16^\dagger$	0.1	$200 < Re < 800$		
[5b]	925	$3.52^\dagger$	0	$200 < Re < 800$		
[6a]	97.9	4.02	0.34	$100 < Re < 1000$	0.34	
[6b]	153	1.45	0.06	$100 < Re < 1001$	0.13	
[7a]	30.1	1.08	0	$15 < KC < 425$	0.22	$4.0 \times 10^{-7\ddagger}$
[7b]	13.5	0.73	0	$15 < KC < 425$	0.20	$4.0 \times 10^{-7\ddagger}$
[8]	139.8	0.86	0	$25 < KC < 135$	1.14	1.5×10^{-2}
[9]	2400	0.77	0	$1000 < Re < 3200$	1.96	
[10a]	2200	0.88	0.87	$2000 < Re < 7000$		
[10b]	4600	1.9	1.61	$2000 < Re < 7000$		
[11]	744.2	1.27	0.76	$500 < Re < 2300$	1.45	$1.4 \times 10^{-2\ddagger}$
[12]	730	1.37	1.04	$300 < Re < 4700$	1.69	Stiff
[13a]	305.5	0.977	−0.046	$100 < Re < 1100$	0.27	$5.0 \times 10^{-4\ddagger}$
[13b]	227.3	1.615	0.159	$100 < Re < 1100$	0.25	$5.0 \times 10^{-4\ddagger}$
[14a]	7.995	1.22	1.28	$15 < KC < 95$		Stiff
[14b]	12.07	2.25	0.683	$15 < KC < 35$		$1.5 \times 10^{-3\ddagger}$
[14c]	65.72	1.07	0.036	$5 < KC < 75$		
[14d]	79.64	1.48	1	$15 < KC < 150$	1.55	
[14e]	126.2	0.828	0.15	$15 < KC < 350$	1.19	
[16a]	22.2	1.14	0.187	$76 < Re < 511$		
[16b]	11.9	1.53	0.402	$10 < KC < 170$		

† The −-sign as reported by *Bradley and Houser* (2009) is removed because it is at odds with the curves displayed in their work and is inconsistent with other literature.

‡ Calculated from the reported biomechanical properties.

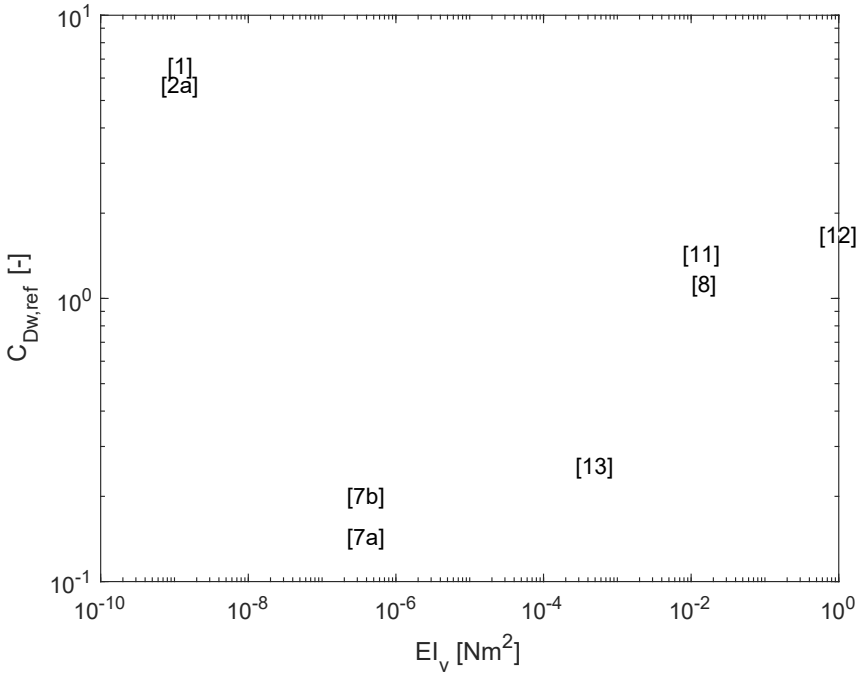

Figure 2.13: Comparison of $C_{Dw,ref}$ against EI_v. The data points and their labels refer to Tables 2.2-2.3. Studies [13a] and [13b] have been merged into [13] for clarity. The stiff vegetation of [12] has been set at $EI_v = 1$ Nm^2 to allow comparison.

orders of magnitude. Studies 7-8, 11-13 suggest that $C_{Dw,ref}$ correlates positively with flexural rigidity EI_v, i.e. when C_{Dw} is calibrated to include plant motion lower C_{Dw} values are found for flexible vegetation. This correlation agrees with the concept that plant swaying by flexible vegetation reduces energy dissipation. On the other hand, studies 1-2 rank highest for $C_{Dw,ref}$ and lowest for EI_v. Also, *Augustin et al.* (2009) found no difference in damping rates between stiff and flexible artificial vegetation. A possible explanation of these contradictions could be found in the wide range of vegetation geometries, materials and test conditions (Table 2.2) which impedes the comparison of individual parameters across studies. Even for the smaller subset of cylindrical stem-dominated salt marsh vegetation, which is the focus of this study, the variation in drag coefficients is significant (Fig. 2.14). Given the strong variability of drag coefficients found under different study conditions, the predictive value of C_{Dw}-relations is currently limited, and plant- and site-specific calibration is often required (*Tempest et al.*, 2015). This is particularly relevant when vegetation properties vary or in case of new salt marshes (e.g. managed realignment).

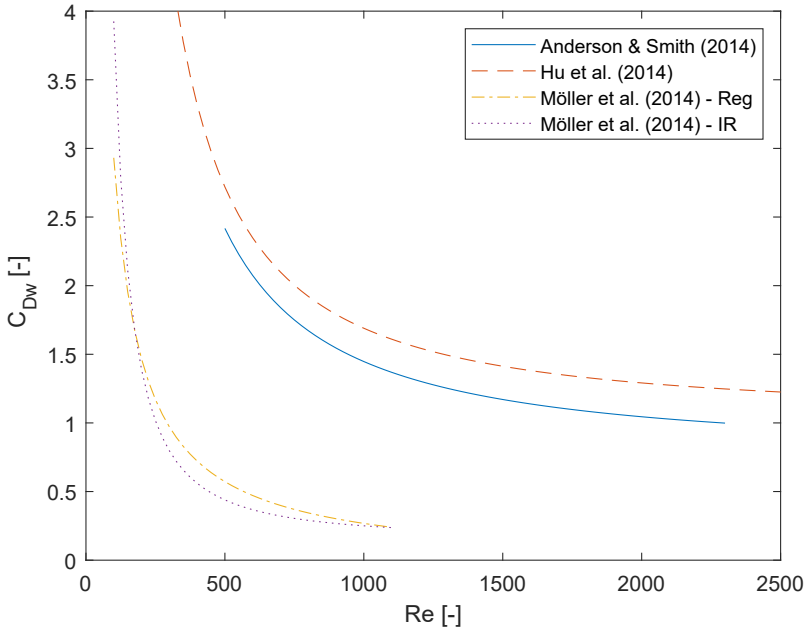

Figure 2.14: C_{Dw} as function of Re as derived for salt marsh vegetation in three studies. *Möller et al.* (2014) tested both regular (Reg) and random (IR) waves.

Comparison of solution methods for wave damping over flexible vegetation The four methods differ in complexity, the included physics and applicability, but it remains unclear which method is most suited for practical use. Complex computational modelling includes the most physics and is applicable across vegetation species, but its computational cost is very high. Beam theory provides a solution for vegetation motion for simplified hydrodynamic conditions but is limited to vegetation with small deflections. Scaling analysis relates the effective length of a flexible stem to the key processes in the wave-vegetation interface under different regime buts requires plant-specific calibration and does not provide a solution for the transitional regime. Finally, plant motion can be accounted for indirectly through calibration of the drag coefficient in the equations that govern wave damping over rigid vegetation. Whilst it is a simple method, it requires plant- and site-specific calibration. Currently, the drag coefficient calibration is the most common method. The calibration can be carried out for any field site but a significant spread in calibrated values for the drag coefficient has been identified which is a source for uncertainty in the predicted wave damping. Given the contrasting methods, test conditions and results, it remains unclear how vegetation flexibility contributes to wave damping and which solution method is preferred for practical use.

2.4.4 Wave-driven velocity structure within vegetation

The interaction of waves with vegetation may impact the vertical velocity structure in two ways. It was observed in experimental studies that the orbital velocities were preferentially attenuated within meadows of wide rigid cylinders (*Lowe et al.*, 2005; *Pujol et al.*, 2013; *Abdolahpour et al.*, 2017) and flexible vegetation (*Luhar et al.*, 2010; *Rupprecht et al.*, 2017). Furthermore, wave-driven phase-averaged currents were observed around artificial rigid (*Pujol et al.*, 2013; *Hu et al.*, 2014; *Abdolahpour et al.*, 2017) and flexible (*Luhar et al.*, 2010; *Abdolahpour et al.*, 2017) vegetation patches, and reproduced by computational modelling (*Chen et al.*, 2019). Hence, the wave-driven velocity structure within vegetation may differ significantly from linear wave theory. This affects predictions of wave damping through methods that assume the validity of linear wave theory. In particular, Eq. 2.26, 2.28 rely on the validity of linear wave theory as modifications in the velocity structure directly impact the magnitude of the drag force and the work done by it. Therefore, the velocity structure induced by wave-vegetation interactions could potentially be an explaining factor of why a wide range of calibrated drag coefficients was found in literature (Table 2.3).

Vegetation flexibility appears to control the magnitude of the attenuation of orbital velocities and the direction and position of the wave-driven currents. In a comparative experiment with artificial rigid and flexible vegetation under identical wave conditions, *Pujol et al.* (2013) identified velocity attenuation by rigid vegetation but not by flexible vegetation. Yet, velocity attenuation within flexible meadows has been reported in other experiments which focussed solely on flexible vegetation (*Luhar et al.*, 2010; *Rupprecht et al.*, 2017). Furthermore, rigid vegetation induces net currents in the direction of wave propagation through the top of the vegetation (*Pujol et al.*, 2013; *Hu et al.*, 2014; *Abdolahpour et al.*, 2017) with return flows over or within the vegetation depending on the submergence ratio (*Pujol et al.*, 2013) (Fig. 2.15). Flexible vegetation may induce wave-driven currents in the direction of wave propagation near the seabed (*Luhar et al.*, 2010; *Rupprecht et al.*, 2017) but, on the other hand, no wave-driven currents were observed in *Pujol et al.* (2013).

The role of vegetation stiffness on the wave-driven velocity structure remains unclear in the absence of high-quality comparative data. Rigid and flexible vegetation with identical shapes have not yet been tested in the context of the wave-driven velocity structure. Cylinders were used to mimic rigid vegetation (*Lowe et al.*, 2005; *Pujol et al.*, 2013; *Hu et al.*, 2014; *Abdolahpour et al.*, 2017) as opposed to blades (*Luhar et al.*, 2010; *Pujol et al.*, 2013; *Abdolahpour et al.*, 2017) or real grasses (*Rupprecht et al.*, 2017) for flexible vegetation. Furthermore, measurements have been restricted to points (*Hu et al.*, 2014) or cross-sections (*Lowe et al.*, 2005; *Luhar et al.*, 2010; *Pujol et al.*, 2013; *Abdolahpour et al.*, 2017). Full

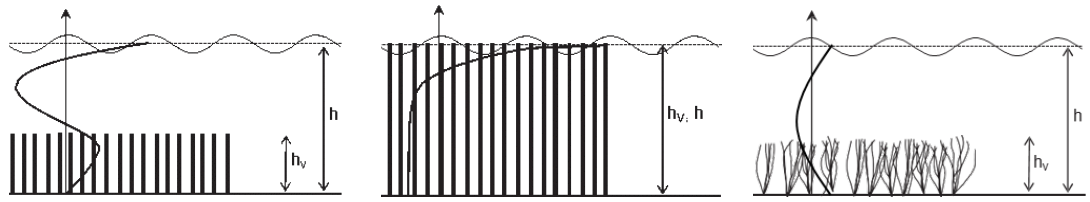

Figure 2.15: Wave-induced current circulations as identified by *Pujol et al.* (2013). Positive wave-averaged velocities denote currents in the direction of wave propagation and negative wave-averaged velocities denote currents opposite to the direction of wave propagation. Submerged rigid vegetation induces a counter-clockwise circulation (left); emergent rigid vegetation induces a clockwise circulation (middle); Flexible vegetation does not induce circulation (right). The observed velocity structure is equal to the velocity structure without vegetation (not shown here). Source: *Pujol et al.* (2013) (adapted).

velocity fields within and around vegetation patches have not been measured yet.

2.5 Computational modelling tools

Process-based computational modelling tools are widely used to evaluate the hydrodynamics induced by real-world salt marshes. Computational models are valuable tools because they can couple the current-vegetation and wave-vegetation interactions with other coastal processes such as — but not limited to — tidal propagation, wave generation by wind, wave refraction, and river flow. Furthermore, they can be applied to the complex bathymetries found in coastal zones. Here we discuss how vegetation is parameterised in computational models and which salt marsh models have successfully been applied for real-world case studies.

2.5.1 Governing equations

The hydrodynamics in computational models are governed by the continuity and momentum equations. These are commonly derived from the Navier Stokes equations for incompressible fluids and under the shallow water and Boussinesq assumptions in most large-scale models, e.g. ADCIRC (*Luettich et al.*, 1992), Delft3D (*Lesser et al.*, 2004), and TELEMAC (*Galland et al.*, 1991). The three-dimensional continuity equation is given by

$$\frac{\partial u}{\partial x} + \frac{\partial v}{\partial y} + \frac{\partial w}{\partial z} = 0, \tag{2.35}$$

and the momentum equations are given by

$$\frac{\partial u}{\partial t} + u\frac{\partial u}{\partial x} + v\frac{\partial u}{\partial y} + w\frac{\partial u}{\partial z} - fv = \frac{1}{\rho}\left(-\frac{\partial P}{\partial x} + \frac{\partial \tau_{xx}}{\partial x} + \frac{\partial \tau_{yx}}{\partial y} + \frac{\partial \tau_{zx}}{\partial z}\right) + M_x, \tag{2.36}$$

$$\frac{\partial v}{\partial t} + u\frac{\partial v}{\partial x} + v\frac{\partial v}{\partial y} + w\frac{\partial v}{\partial z} + fu = \frac{1}{\rho}\left(-\frac{\partial P}{\partial y} + \frac{\partial \tau_{xy}}{\partial x} + \frac{\partial \tau_{yy}}{\partial y} + \frac{\partial \tau_{zy}}{\partial z}\right) + M_y, \tag{2.37}$$

$$\frac{\partial P}{\partial z} = -\rho g. \tag{2.38}$$

Herein, we have introduced v as the horizontal flow velocity parallel to the y-axis, f as the Coriolis parameter, P as the pressure, τ as the shear stress, and M_x and M_y are momentum sources (or sinks). The left-hand side of the horizontal momentum equations (Eq. 2.36, 2.37) describes the acceleration, advection, and Coriolis effects. The right-hand side describes forcing due to pressure, shear stresses and external forcing. The vertical momentum equation (Eq. 2.38) has reduced to the hydrostatic pressure balance under the shallow water assumption. The corresponding boundary condition at the free surface is defined as (*Luettich et al.*, 1992)

$$w|_{z=\eta} = \frac{\partial \eta}{\partial t} + u\frac{\partial \eta}{\partial x} + v\frac{\partial \eta}{\partial y}, \tag{2.39}$$

where η is the free surface elevation, and the boundary conditions at the bed are defined as (*Luettich et al.*, 1992; *Lesser et al.*, 2004)

$$w|_{z=-h} = -\left(\frac{\partial h}{\partial t} + u\frac{\partial h}{\partial x} + v\frac{\partial h}{\partial y}\right), \tag{2.40}$$

$$\frac{\nu}{h}\frac{\partial u}{\partial z}\bigg|_{z=-h} = \frac{\tau_{bx}}{\rho}, \qquad \frac{\nu}{h}\frac{\partial v}{\partial z}\bigg|_{z=-h} = \frac{\tau_{by}}{\rho}, \tag{2.41}$$

with $\boldsymbol{\tau_b} = (\tau_{bx}, \tau_{by})$ as the bed shear stress. The here presented set of governing equation forms the basis of most process-based computational models. Yet, the exact forms varies and depends on the purpose, assumptions and solution method of the specific model.

2.5.2 Current-vegetation parameterisations

The effect of vegetation on unidirectional currents is typically parameterised through one of four ways: (i) fixed bed roughness; (ii) depth-dependent bed roughness; (iii) trachytope model; (iv) momentum sink balance.

Fixed bed roughness Vegetation is considered an bottom roughness element under this parameterisation. The energy dissipation due to drag by vegetation is implemented as an equivalent equivalent bottom roughness. Vegetated areas are assigned a rougher bed than non-vegetated areas. The bed roughness is typically expressed through a Chézy coefficient C_z (e.g. *Marciano et al.*, 2005) or a Manning's coefficient n_m (e.g. *Loder et al.*, 2009). The Chézy and Manning's coefficients are related through $C_z = h^{1/6}/n_m$. The Chézy coefficient is related to the bottom shear stress, according to

$$\boldsymbol{\tau_b}(x, y, t) = \frac{\rho g}{C_z}\boldsymbol{u} \tag{2.42}$$

where $\boldsymbol{u} = (u, v, w)$ is the velocity vector. $\boldsymbol{\tau_b}$ manipulates the flow through Eq. 2.41. The bed roughness value can be set at different levels to account for different vegetation types (*Loder et al.*, 2009; *Wamsley et al.*, 2009) but it is typically set constant over large salt marsh areas and over time. Hence, the effect of bed roughness on flow is exerted preferentially in shallow water conditions. Furthermore, empirical functions are required to relate the bed roughness value to vegetation conditions. This method can be applied in all computational models, including ADCIRC, Delft3D, and TELEMAC.

Depth-dependent bed roughness Here the equivalent bottom friction by vegetation is a function of the vegetation height h_v and the water depth h (*Baptist et al.*, 2007). The bottom friction is a function of the submergence ratio. If the vegetation is emergent ($h_v > h$), the bottom friction depends on the frontal area of the vegetation only. If vegetation is submerged, the relative contribution of vegetation-induced bottom drag diminishes as a free flow zone develops over the vegetation. *Baptist et al.* (2007) defined the depth-dependent Chézy coefficient as

$$\begin{aligned} C_z(x, y,t) &= \sqrt{\frac{1}{1/C_b^2 + C_{Dc} n_v b_v h/(2g)}} && \text{if } h < h_v \\ C_z(x, y,t) &= \sqrt{\frac{1}{1/C_b^2 + C_{Dc} n_v b_v h_v/(2g)}} + \frac{\sqrt{g}}{\kappa} \ln\left(\frac{h}{h_v}\right) && \text{if } h > h_v \end{aligned} \tag{2.43}$$

Herein, C_b is the Chézy coefficient of an unvegetated bed, and $\kappa = 0.41$ is the von Kármán constant. The Chézy coefficient is updated every time step in accordance with local water depth. The depth-dependent method is included in Delft3D (*Al-Asadi and Duan*, 2017).

Trachytope model Delft3D provides a modified implementation of the depth-dependent bed roughness parameterisation, which is known as the trachytope model. The vegetation is considered a roughness element to the flow but partially implemented via the momentum equations to reduce the simulated bottom shear stress (*Deltares*, 2018). The effect of vegetation on flow is partially modelled via bed roughness

$$C_z(x,y,t) = \begin{cases} C_b & \text{if } h < h_v \\ C_b + \dfrac{\sqrt{g}}{\kappa} \ln\left(\dfrac{h}{h_v}\right) \sqrt{\dfrac{1}{C_{Dc} n_v b_v h_v/(2g)}} & \text{if } h > h_v \end{cases} \tag{2.44}$$

and partially via a sink term in the momentum equations $M_x = -\frac{\lambda_m}{2} u|u|$ (Eq. 2.36) in which

$$\begin{aligned} \lambda_m(x,y,t) &= C_{Dc} b_v n_v && \text{if } h < h_v, \\ \lambda_m(x,y,t) &= C_{Dc} b_v n_v \frac{h}{h_v} \frac{c_b^2}{C_z^2} && \text{if } h > h_v. \end{aligned} \tag{2.45}$$

The combined roughness via bottom friction (Eq. 2.44) and momentum sink (Eq. 2.45) is equivalent to water depth-dependent bed roughness (Eq. 2.43) and has been defined such that the ratio u/C_z^2 remains constant when the water level rises or falls.

Momentum sink term This parameterisation considers vegetation an object in the flow field rather than a bottom roughness element. The vegetation-induced drag force (Eq. 2.2) can be parameterised in the horizontal momentum equations (Eq. 2.36, 2.37) in a way similar to Eq. 2.3, i.e.

$$M_x(x,y,z,t) = -\frac{F_c}{\rho} = -\frac{1}{2} C_{Dc} b_v n_z u|u|. \tag{2.46}$$

This parameterisation includes the vegetation characteristics stem diameter, density, and height explicitly — note M_x is a function of z — and can account for spatial variations therein. It has been successfully implemented for rigid cylindrical stems in Delft3D (*Temmerman et al.*, 2005) and Wu's subgrid model (*Wu et al.*, 2017). Additionally, COAWST (*Beudin et al.*, 2017) and sECOM (*Marsooli*

et al., 2016) can account for flexible vegetation through an effective vegetation length given plant dimensions and flexural rigidity. Finally, the effect of plant motion on the drag force was included in OpenFoam (*Chen and Zou*, 2019) but at high computational cost.

Comparison of current-vegetation implementations The four available parameterisations differ in included physics and required data. The fixed bed roughness parameterisation is the simplest and only requires information on the habitat type but relies on empirical relations to select an equivalent roughness value. The depth-dependent bed roughness and trachytope model introduce stem diameter, height and density in the formulation of bed roughness coefficient. They include additional physics but also require more data on vegetation. The momentum sink term parameterisation relates the vegetation-induced drag to vegetation characteristics based on plant characteristics. As it considers vegetation as objects rather than a bottom roughness element, the momentum sink parameterisation is physically more intuitive. This comparison would suggest that the fixed bed roughness is a useful parameterisation when few data is available whereas the momentum sink term may be applied when high-quality vegetation data is available and accurate modelling of hydrodynamics is required.

However, there is limited insight into the uncertainty of the modelled hydrodynamics to the selected parameterisations. *Ashall et al.* (2016) compared parameterisations via bottom friction and momentum sink over rigid cylinders for a large macro-tidal estuary. They found that both parameterisations reproduced current magnitudes for most of the tidal cycle, but the dynamics under submerged vegetation could only be captured via a momentum sink term over rigid cylinders. Alternatively, *Al-Asadi and Duan* (2017) found that a plant submergence term in bed roughness formulations was key to reproduce velocities on freshwater marshes. As both studies focussed on reproducing currents under specific field site conditions and selected parameterisations, our broader understanding of the uncertainty to all parameterisations in coastal environments is limited.

2.5.3 Wave-vegetation parameterisations

The parametrisation of the effect of vegetation fields on wave propagation depends on the governing model equations. Wave models (Table 2.4) can be divided into models that are governed by (i) a spectral wave action balance, (ii) Boussinesq equations, (iii) Reynolds-averaged Navier Stokes (RANS) equations, and (iv) nonlinear shallow water equations. The spectral wave action balance is governed by the conservation of energy, whereas the other three equation sets govern wave motion through the continuity and momentum balances.

Spectral wave action balance The evolution of a wave spectrum is controlled by the action balance given by (*Hasselmann et al.*, 1973)

$$\frac{d}{dt}N_w + \frac{d}{dx}c_x N_w + \frac{d}{dy}c_y N_w + \frac{d}{d\omega}c_\omega N_w + \frac{d}{d\theta_w}c_\theta N_w = -\frac{S_{veg}}{\omega} + \frac{S_{other}}{\omega} \quad (2.47)$$

where $N_w(\omega, \theta_w) = E(\omega, \theta_w)/\omega$ is the action density spectrum with frequency ω and direction θ_w. Furthermore, c_x and c_y represent wave group velocity in x and y-direction respectively. c_ω and c_θ are the propagation velocities in spectral space. S_{veg} is the energy dissipation due to vegetation and S_{other} are energy sources and sinks due to other wave processes such as wind growth and breaking. The energy dissipation by vegetation S_{veg} is typically derived from wave dissipation over a rigid stem (Eq. 2.24). It can be shown that the equivalent energy dissipation of a directional wave spectrum over a vegetation field reads (*Suzuki et al.*, 2012)

$$S_{veg}(x, y, t) = \sqrt{\frac{2}{\pi}} g^2 \hat{C}_{Dw} b_v n_v \left(\frac{k_p}{\omega_p}\right) \frac{\sinh^3 k_p h_v + 3\sinh k_p h_v}{(\sinh 2k_p h + 2kh)\sinh k_p h} \sqrt{E_{tot}} E(\omega, \theta_w) \quad (2.48)$$

This formulation has been implemented in SWAN (*Suzuki et al.*, 2012), STWAVE (*Anderson and Smith*, 2015), XBeach (*Van Rooijen et al.*, 2015), and MDO (*Marsooli et al.*, 2017). The solution of the spectral wave action balance has a low computational cost but is restricted to phase-averaged energy dissipation.

Boussinesq equations The propagation of nonlinear waves in shallow water can be described using the Boussinesq equations (*Liu*, 1995). They include a depth-averaged continuity equation and a momentum balance. Here they are given in the direction of wave propagation, according to

$$\frac{\partial \eta}{\partial t} + \frac{\partial}{\partial x}\left[(\eta + h)u_\alpha\right] + \text{H.O.T.} = 0 \quad (2.49)$$

$$\frac{\partial u_\alpha}{\partial t} + g\frac{\partial \eta}{\partial x} + \frac{1}{2}\frac{\partial}{\partial x}|u_\alpha^2| + S_{veg} + S_{other} + \text{H.O.T.} = 0 \quad (2.50)$$

Herein, u_α is the velocity evaluated at a reference water depth and H.O.T. is used as a short-hand notation for the higher order terms that follow from the Boussinesq approximation (see e.g. *Liu*, 1995). The effect of vegetation is considered through the momentum balance with (*Chakrabarti et al.*, 2017)

$$S_{veg}(x, y, t) = \frac{C_{Dw} n_v b_v}{2(h + \eta)} \min(h_v, h)|u_\alpha|u_\alpha. \quad (2.51)$$

Alternatively, a friction factor can be used to replace $1/2 C_{Dw} n_v b_v \min(h_v, h)$ (*Augustin et al.*, 2009). The Boussinesq equations with dissipation by vegetation have

Table 2.4: List of wave models grouped with respect to governing equations.

Wave models	**Governing equations**	**Temporal resolution**	**Vegetation type**	**Cost**[†]
MDO, STWAVE, SWAN, Xbeach	Spectral action balance	Phase-averaging	Rigid	Low
COULWAVE, FUNWAVE	Boussinesq	Phase-resolving	Rigid	Medium
IH-2VOF, OpenFoam	RANS	Phase-resolving	Rigid and Flexible	High
SWASH	Nonlinear shallow water	Phase-resolving	Rigid	Medium

[†] Based on *Suzuki et al.* (2019).

been implemented in FUNWAVE (*Chakrabarti et al.*, 2017) and COULWAVE (*Augustin et al.*, 2009; *Yang et al.*, 2018). The advantage of the Boussinesq equations is that they are phase-resolving but the solution procedure is computationally more expensive than the spectral wave balance.

RANS equations The RANS equations describe water motion under wave forcing in three dimensions. The continuity and momentum equations are given in tensor notation by (*Maza et al.*, 2013)

$$\frac{\partial u_i}{\partial x_i} = 0, \tag{2.52}$$

$$\frac{\partial u_i}{\partial t} + u_j \frac{\partial u_i}{\partial x_j} = -\frac{1}{\rho}\frac{\partial P}{\partial x_i} + g_i + \frac{1}{\rho}\frac{\partial \tau_{ij}}{\partial x_j} - \frac{\partial u_i' u_j'}{\partial x_j} - F_{D,i}, \tag{2.53}$$

where subscripts i references to the components of the respective quantity in x, y and z-directions. The drag force induced by the vegetation, F_D, is given by Eq. 2.14 and may include vegetation motion and stem bending. The RANS equations solve the wave and vegetation dynamics simultaneously, and have been successfully applied for wave dissipation over flexible vegetation (*Maza et al.*, 2013; *Chen and Zou*, 2019) but the computational demand for solving the RANS equations is very high. The RANS equations have been implemented in IH-2VOF (*Maza et al.*, 2013) and OpenFoam (*Chen and Zou*, 2019).

Nonlinear shallow water equations A formulation of the effect of vegetation in the nonlinear shallow water equations has been developed for SWASH in *Suzuki et al.* (2019). They consider the effect of the drag, added mass and Froude-Krylov forces on rigid vegetation directly through the momentum balance and include the porosity effect by vegetation. The governing continuity and momentum equations in the direction of wave propagation are given by

$$\frac{\partial \eta}{\partial t} + \frac{\partial hu}{\partial x} = 0, \tag{2.54}$$

$$\left[1 + C_m(1-n_p)\right] \frac{\partial u/n_p}{\partial t} + n_p \frac{\partial \left(u/n_p\right)^2}{\partial x} + n_p \left(g\frac{\partial \eta}{\partial x} + \frac{\partial P}{\partial x} \right) + \frac{1}{2} C_{Dw} \alpha b_v n_v \left| \frac{u}{n_p} \right| \frac{u}{n_p} = 0. \tag{2.55}$$

Here n_p is the porosity which is defined as ratio fluid volume relative to the total volume. The nonlinear shallow water equations can be extended to include horizontal vegetation elements in addition to vertical vegetation elements (*Suzuki et al.*, 2019).

Comparison of wave-vegetation parameterisations Table 2.4 lists wave models with respect to their governing equations, temporal resolution, vegetation type and computational cost. It is shown that models based on the spectral action balance are computationally most efficient but cannot resolve the phases of different spectral frequencies. On the other hand, models based on RANS equations can resolve wave phases and solve swaying of flexible vegetation simultaneously but at a high computational cost. Models based on Boussinesq or nonlinear shallow water equations can resolve phases at a medium computational cost but have only been developed for rigid vegetation. Currently, no wave model is available that includes flexible vegetation at a computational cost that is acceptable for field-scale applications.

2.5.4 Computational modelling applications to salt marshes

The effect of salt marshes on coastal dynamics is a topic that has recently experienced a surge of attention. Table 2.5 provides a selection of recent key computational modelling studies in this topic to assess the current state-of-the-art modelling practice for large-scale coastal areas with salt marsh vegetation. The preferred modelling suites are ADCIRC, Delft3D and TELEMAC. These three modelling suites have been primarily developed for current dynamics, but ADCIRC and Delft3D have been successfully coupled with wave models STWAVE and SWAN respectively. Although currently relatively few studies consider the current-vegetation and wave-vegetation interactions simultaneously.

The current-vegetation interaction is parameterised in different ways across studies. The fixed bed roughness, the trachytope model and the momentum sink parameterisations are all used across the reviewed studies. Out of the three most used modelling suites, ADCIRC and TELEMAC can only account for vegetation through a fixed enhanced bottom roughness whereas Delft3D also includes parameterisations of vegetation through a depth-dependent bed roughness, trachytope model and a momentum sink term. sECOM and the subgrid model also include vegetation through a momentum sink term but have not yet been coupled with a wave model.

Alternatively, all reviewed studies that include wave-vegetation interactions are based on the spectral action balance. This is likely due to its low computational cost which is important for large-scale applications. However, with the computational power increasing and the recent developments in wave-vegetation parameterisations (Section 2.5.3) it is likely that a broader range of wave models will be applied to large-scale coastal areas with salt marshes in the near future.

Finally, plant swaying by flexible vegetation is often omitted in large-scale computational modelling. Out of the reviewed studies, only *Marsooli et al.* (2016) have included the effect of plant flexibility on the current-vegetation interaction in a field-scale salt marsh study. No study had included vegetation flexibility in the wave-vegetation interaction at field-scale. Instead, most studies rely on a calibration of the drag coefficient (*Tempest et al.*, 2015). When all vegetation species are considered rigid, salt marshes cannot be diversified based on plant flexibility but only on dimensions.

Our review shows that (i) few studies consider the current-vegetation and the wave-vegetation interaction simultaneously; (ii) there is no agreement in the optimal current-vegetation interaction parameterisation; (iii) the spectral wave action balance is most commonly used to parameterise the wave-vegetation interaction; (iv) there is a lack of studies that include the swaying effect of flexible vegetation.

Table 2.5: List of publications that have investigated the impact of salt marshes on coastal environments.

Publication	**Modelling suite**	**Current-veg method**	**Wave-veg method**	**Flexible veg?**	**Study context**
Temmerman et al. (2005)	Delft3D	Momentum sink	-	No	Morphodynamics
Loder et al. (2009)	ADCIRC	Fixed bed roughness	-	No	Surge attenuation
Wamsley et al. (2009)	ADCIRC-STWAVE	Fixed bed roughness	Spectral action balance	No	Surge and wave attenuation
Barbier et al. (2013)	ADCIRC	Fixed bed roughness	-	No	Surge attenuation
Hu et al. (2015)	Delft3D	Fixed bed roughness	-	No	Surge attenuation
Smolders et al. (2015)	TELEMAC	Fixed bed roughness	-	No	Surge attenuation
Haddad et al. (2016)	ADCIRC-SWAN	Fixed bed roughness	-	No	Surge attenuation
Marsooli et al. (2016)	sECOM	Momentum sink	-	Yes	Surge attenuation
Ashall et al. (2016)	Delft3D	Momentum sink	-	No	Tidal hydrodynamics
Stark et al. (2016)	TELEMAC	Fixed bed roughness	-	No	Surge attenuation
Mariotti and Canestrelli (2017)	Delft3D-SWAN	Fixed bed roughness	Spectral action balance	No	Idealised evolution
Wu et al. (2017)	Subgrid model	Momentum sink	-	No	Tidal hydrodynamics
Best et al. (2018)	Delft3D	Trachytope model	-	No	Idealised evolution
Hu et al. (2018)	Delft3D-SWAN	Fixed bed roughness/ Trachytope model	Spectral action balance	No	Morphodynamics
Siverd et al. (2019)	ADCIRC-SWAN	Fixed bed roughness	-	No	Surge attenuation
Garzon et al. (2019b)	XBeach	-	Spectral action balance	No	Wave attenuation

2.6 Conclusions

We have systematically reviewed the salt marsh ecosystem, the current-vegetation interaction, the wave-vegetation interaction, and large-scale computational models of coastal environments. Let us now answer the review questions posed in Section 2.1.

1. **What characterizes the salt marsh ecosystem?**
   Salt marshes are vegetated coastal wetlands that can be found in the intertidal zone. They are regularly flooded by the sea and exhibit salt-tolerant tolerant vegetation platforms. Their vegetation cover is typically diverse with a strong spatiotemporal variation. Salt marsh species range from woody shrubs such as *Atriplex Portulacoides* to flexible grasses such as *Puccinellia Maritima*. All plant species contribute to sediment capture and root binding, which promotes sediment accretion on vegetated platforms. This allows the bed to potentially keep up with moderate levels of sea level rise and protects the bed from erosion during storms. Furthermore, salt marsh vegetation platforms are often dissected by a creek network. The creeks are essential to route tidal flow with fresh sediments through the marsh, which is essential for salt marsh accretion.

2. **How do currents and vegetation interact?**
   When currents travel over vegetation fields, they reduce in magnitude due to the vegetation-induced drag force. The magnitude of the drag force is a function on the frontal area of vegetation and plant stiffness. Rigid vegetation does not move under current forcing and produces the largest drag force. Bending by flexible vegetation reduces the frontal area, which lowers the drag force that is produced. Therefore, currents are preferentially attenuated by rigid vegetation. The reduction in drag force due to stem bending can be included through the Vogel coefficient or by solving the force balance that controls the current-vegetation interaction. Furthermore, the drag produced by vegetation modifies the velocity structure. Current velocities are constant over the water depth inside the vegetation field, and a free flow zone develops above the canopy when the vegetation is submerged. The current-vegetation interaction produces turbulence at the plant and canopy scale. Finally, the current-vegetation interaction can enhance sediment transport, redirect currents, and lower flood water levels.

3. **How do waves and vegetation interact?**
   When waves travel over vegetation fields, energy is dissipated due to the work done by wave forces on plants. Laboratory experiments have shown

that the wave height lowers when travelling over salt marsh vegetation. Vegetation is often simplified to rigid cylindrical stems that do not modify the ambient velocity field. Under these assumptions, the work done by waves on vegetation is dominated by the drag force. In case of flexible vegetation, plants sway under wave motion which reduces their frontal area and the velocity difference water and vegetation. Both mechanisms reduce the work done by waves on vegetation. It is accepted that plant swaying may reduce wave damping, but there is a lack of physical evidence to quantify its impact on the wave dynamics. Four computational solutions have been proposed to include the impact of vegetation swaying: (i) plant-scale computational modelling of the full wave-vegetation interface; (ii) beam theory; (iii) an effective plant length; and (iv) a calibrated drag coefficient. (i) solves plant and wave motion simultaneously using complex computational schemes but is computationally expensive. (ii) solves plant motion efficiently but is only valid for small plant deflections. (iii) and (iv) are simple but rely on plant-specific calibration. Currently, no method exists to solve wave damping over flexible vegetation efficiently for large-scale coastal areas. Furthermore, the wave-vegetation interactions may induce wave-driven currents over vegetation. The magnitude and location of wave-driven currents may also depend on plant flexibility, but this is unclear due to contrasting experimental results.

4. **How can computational models improve our understanding of the coastal defence function of salt marshes?**
   Salt marshes may protect against coastal flooding in complex coastal systems, which feature a combination of storm surges, wave dynamics, vegetation, and river flows. Large-scale computational models are widely considered a powerful tool for flood risk simulations over complex domains. The Delft3D, ADCIRC and TELEMAC coastal modelling suites have all been successfully applied to simulate the contribution of salt marsh vegetation to coastal protection and have supported its potential to attenuate storm surges and waves across various case study sites. The current-vegetation and wave-vegetation interactions can each be implemented by four different parameterisations, which differ in the included physics, data requirement and computational cost. Currently, most studies select simplified parameterisations of vegetation, such as a bed roughness coefficient, or are restricted to rigid vegetation. It is unclear how these simplifications affect the predicted coastal protection function by salt marshes. Furthermore, there is a lack of studies that simulate flood risk on vegetated coastlines under storm conditions with surge and wave components or include multiple vegetation species that differ in flexibility.

Our review shows that salt marsh vegetation contributes to coastal protection in multiple ways. The vegetation stabilises the shoreline, and it interacts with currents and waves. The interaction with currents can potentially reduce water levels and storm surge impacts on the coastline. The interaction between vegetation and waves can reduce the height of the waves, lowering the impact on coastal defence structures. These benefits have been shown in laboratory experiments and reproduced in computational models.

However, our review also highlights that current computational flood risk models employ simplified parameterisations of the interaction between salt marshes and hydrodynamics. As a major simplification, salt marsh vegetation is often assumed to be rigid, but we found that salt marshes exhibit a diverse vegetation cover of stiff shrubs and flexible grasses, challenging the rigid vegetation assumption. In particular, flexible vegetation sways during a wave cycle, which potentially reduces its capacity to damp waves. Due to a lack of physical evidence, it remains unclear to what extent swaying plants affect the wave-vegetation interactions, and to what extent the rigid vegetation assumption induces model errors in simulated wave damping. Furthermore, four current-vegetation are currently in use but have not been compared under identical hydrodynamic forcing. Finally, there is a lack of computational models that consider the effect of salt marshes on currents and waves simultaneously to fully evaluate the potential of salt marshes to contribute to coastal protection in complex real-world environments.

To address these knowledge gaps, we will investigate the uncertainty of estuary hydrodynamics to current-vegetation interactions (Chapter 3) and the effect of vegetation flexibility on the wave-vegetation interactions (Chapters 4-6). Based on the outcomes of these investigations, a new coupled current-wave-vegetation model will be developed to quantify the coastal protection function by salt marshes with a diverse vegetation cover under storm conditions with surge and wave components (Chapter 7)

Going forward, the Delft3D model is selected as the preferred computational modelling suite. Delft3D includes all four current-vegetation parameterisations that are currently used, which allows for a direct comparison of the four parameterisations. Second, Delft3D can be coupled with the wave model SWAN, such that storms with surge and wave components can be studied, which is a main objective of this thesis. Third, Delft3D and SWAN are open-source. Both models can be modified to improve how vegetation is included in either model. Finally, Delft3D has been successfully applied previously to study the coastal protection services of salt marshes (Table 2.5), which provides confidence in utilising Delft3D for new applications in this field.

Chapter 3

The impact of the uncertainty in current-vegetation parameterisations on estuary hydrodynamics

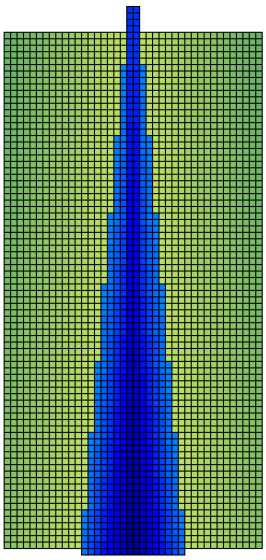

3.1 Introduction

Salt marshes are intertidal coastal wetlands that form green buffer zones between land and sea. They are frequently found in sheltered areas such as estuaries in temperate climate zones (*Allen*, 2000). Salt marshes exhibit salt-tolerant vegetation that alleviates coastal flood risk. The vegetation-induced drag attenuates currents and waves, lowers flood water levels and can expand the sediment budget (*Bouma et al.*, 2014; *Mullarney and Henderson*, 2018). Additionally, they provide co-benefits such as carbon storage, grazing area for cattle, ecosystem enhancement and recreational opportunities (*Sutton-Grier et al.*, 2015; *Leonardi et al.*, 2018).

The interaction between currents and vegetation is vital for sediment accretion and storm surge attenuation over salt marshes. As salt marshes are located in the intertidal zone, they are subjected to ebb and flood tidal flows. The tide carries sediments which are essential for the sediment budget on the vegetated platforms and its function as a coastal buffer zone. Furthermore, the loss of momentum of currents due to the drag force balances the forcing by the pressure gradient, which can reduce storm surge levels over longer distances (*Zhang et al.*, 2012). Therefore, modelling current patterns over salt marshes is essential to investigate their function as a natural flood defence.

Current fields over salt marshes are typically solved using computational models for which four parameterisations have been proposed. Under the first parameterisation, drag by vegetation is modelled via a fixed elevated bottom roughness coefficient for vegetated areas (e.g. *Mariotti and Canestrelli*, 2017). Second, *Baptist et al.* (2007) noted that a fixed bottom roughness coefficient could not account for variations in the drag force due to changes in water level, which affect the part of the water column that is populated by vegetation. Therefore, they formulated a depth-dependent bottom roughness, which has been successfully applied for vegetated channel flow (e.g. *Verschoren et al.*, 2016), but may overestimate bed shear stress (*Hu et al.*, 2015), which affects sediment erosion. As a computational solution, it has been proposed to consider vegetation as a roughness element but include it partially as a sink term in the momentum balance. This parameterisation is known as the trachytope model. Finally, vegetation is considered a rigid cylindrical object in the water column that generates drag and turbulent energy over its length. The impact of the drag force is fully implemented as a sink term in the momentum balance (e.g. *Temmerman et al.*, 2005).

The four parameterisations have been applied successfully in separate studies with aquatic vegetation, but there is limited insight in the uncertainty of modelled hydrodynamics to the selected parameterisations. *Ashall et al.* (2016) compared parameterisations via a bottom friction and a momentum sink term over rigid

cylinders for a large macro-tidal estuary. They found that both parameterisations reproduced current magnitudes for most of the tidal cycle, but the dynamics under submerged vegetation could only be captured via a momentum sink term. Alternatively, *Al-Asadi and Duan* (2017) found that a plant submergence term in the bed roughness formulation was required to reproduce velocities on freshwater marshes. As both studies focussed on reproducing currents under specific field site conditions and selected parameterisations, our general understanding of the uncertainty of estuary hydrodynamics as a function of all four parameterisations is limited.

In this study, we set up a model of an idealised estuary to investigate the impact of the four parameterisations of the current-vegetation interaction on hydrodynamics. Rather than reproducing field site conditions, our interest lies in the qualitative impact of the parameterisations on hydrodynamic parameters, such as current velocity, velocity structure, turbulence and water level. Understanding of the model uncertainty in response to the four parameterisations highlights the advantages and disadvantages of each parameterisation. Furthermore, it lays the foundation for a preferred parameterisation of the current-vegetation interaction in computational models, which can be applied to study the effect of salt marsh vegetation on storm surges (as is done in Ch. 7).

This chapter is organised as follows. Section 3.2 describes the model setup, including the four current-vegetation parameterisations. Then, Section 3.3 presents the modelled hydrodynamics under each parameterisation. A comparison between all parameterisations is made in Section 3.4 based on the model results. Finally, conclusions are drawn in Section 3.5.

3.2 Model setup

3.2.1 Model description

Modelling suite The computational coastal and river model Delft3D (*Lesser et al.*, 2004) was selected to investigate the interaction between vegetation and tidal currents. Delft3D uses a finite-difference scheme to solve the horizontal momentum equation numerically. It calculates water levels, currents and turbulence based on forcing at the boundary (i.e. tides and river flow). It is an open-source software package and includes different parameterisations for modelling vegetation. The modelling suite has been successfully applied to model hydrodynamics over salt marshes in two and three dimensions (e.g. *Ashall et al.*, 2016; *Wu et al.*, 2017).

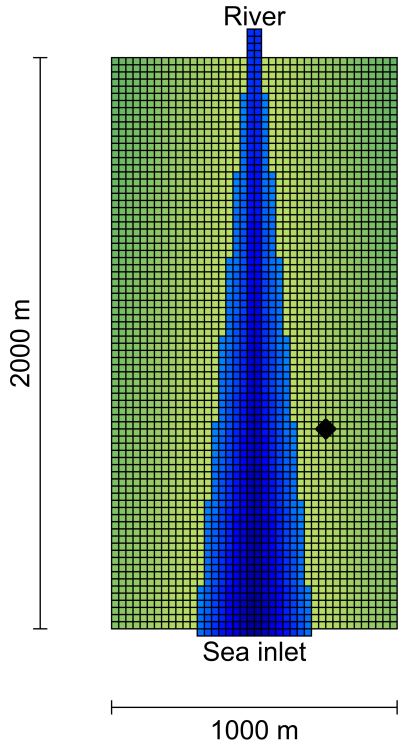

Figure 3.1: The model domain represents an idealised funnel-shaped estuary with back-barrier marshes. Blue grid cells denote the channel and green cells denote salt marshes. The river continues 3 km outside the displayed domain. The black diamond denotes the selected location for the comparison of local hydrodynamics.

Model domain Our model represents an idealised funnel-shaped estuary with back-barrier salt marshes (Fig. 3.1) which is a common estuary type in northwest Europe (*Allen*, 2000). The estuary is 2000 m in length and 1000 m in width and connects to a sea at its mouth and a river at its head. The river dynamics are modelled up to the tidal limit, which is 3000 m upstream of the head of the estuary. Furthermore, a channel runs along the central axis of the estuary and connects to the sea and the river. Its cross-section is triangular with a minimum bed level of 2.5 m below mean sea level at the mouth and 1.5 m below mean sea level at the head. The width of the channel decreases linearly from 600 m at the mouth to 50 m at the head. The remaining area is covered by salt marshes with a uniform vegetation cover. They are on an uphill slope of 2×10^{-3} m/m in cross-estuary direction (channel to land) and 1.25×10^{-4} m/m in along-channel direction (mouth to head). The marsh elevation is 0.80 m above mean sea level at the channel edge and between 1.25 m (mouth) and 1.5 m (head) at its landward edge. The vegetation is inspired by the common salt marsh shrub *Atriplex Portulacoides* with height $h_v = 300$ mm, stem diameter $b_v = 2.5$ mm and stem density $n_v = 2000$ stems/m^2.

The model domain is represented by a rectangular grid of 25×25 m cells with refinement around the central axis of the estuary. The deeper channel and river are projected on a 10×25 m grid (cross-estuary×along-estuary) due to the expected high flow velocities along this axis. The grid has been extended towards the sea by 500 m at the mouth to create a relaxation zone between the boundary and the area of interest. We run the model both in depth-averaged mode and in three dimensions. For the latter case, the model is expanded to 50 vertical layers which adjust with the water depth.

Boundary conditions We model a tide-dominated estuary for which we assume that the effect of the river inflow on the hydrodynamics is negligible. We apply an M_2-tide with amplitude 1.5 m on the seaward boundary. The tidal amplitude has been selected to inundate the salt marshes fully. The highest tidal level exceeds the salt marsh elevation by 0.7 m at its seaward edge and matches the bottom elevation at the landward edge. Under these conditions, the current-vegetation interaction is modelled for variable submergence ratios across the salt marshes.

Time frame The model is run for two and a half tidal cycles. The first one and a half cycle act as a spin-up and the final cycle is used to study the dynamics. Sensitivity analysis showed that tidal dynamics did not change when the model was run for more cycles. The time step is set at 3 s.

3.2.2 Vegetation parameterisations

We test the effect of vegetation on currents under four parameterisations. Parameters have been selected such that similar drag is generated under each parameterisation.

Fixed bed roughness The drag by vegetation is implemented via a rougher bed in vegetated areas compared to non-vegetated areas. Our model describes bed roughness by a Chézy coefficient. We set $C_z = 7$ m$^{1/2}$/s such that the drag generated is in the same order as the depth-dependent roughness for the range of inundation depths on the salt marshes. The bed roughness is set at $C_b = 65$ m$^{1/2}$/s for non-vegetated areas (*Marciano et al.*, 2005).

Depth-dependent bed roughness *Baptist et al.* (2007) proposed a formulation in which the effective bottom drag is function of vegetation height h_v and water depth h. They distinguished between flow through emergent ($h < h_v$) and over submerged vegetation ($h > h_v$). When vegetation is emergent, the flow resistance is assumed constant over the water column and depends on the frontal area of the vegetation, which is estimated under the assumption of rigid cylindrical stems. When vegetation is submerged, the velocity profile is divided into two parts: (1) the vegetated zone, where the velocity is low and vertically uniform, and (2) the free flow zone, where a logarithmic velocity profile is applied. The equivalent Chézy coefficient is defined as

$$\begin{aligned} C_z(x,y,t) &= \sqrt{\frac{1}{1/C_b^2 + C_{Dc} n_v b_v h/(2g)}} && \text{if } h < h_v \\ C_z(x,y,t) &= \sqrt{\frac{1}{1/C_b^2 + C_{Dc} n_v b_v h_v/(2g)}} + \frac{\sqrt{g}}{\kappa} \ln\left(\frac{h}{h_v}\right) && \text{if } h > h_v \end{aligned} \tag{3.1}$$

Herein, $C_{Dc} = 1$ is the dimensionless drag coefficient (*Tanino and Nepf*, 2008), $g = 9.81$ m/s^2 is the gravitational acceleration and $\kappa = 0.41$ is the von Kármán constant. The Chézy coefficient is updated every time step in accordance with the local water depth.

Trachytope model The trachytope model considers vegetation a bottom roughness element, but partially implements its effect as a momentum sink term (*Al-Asadi and Duan*, 2017). The effect of vegetation on flow is partially modelled via Chézy roughness

$$C_z(x,y,t) = C_b + \frac{\sqrt{g}}{\kappa} \ln\left(\frac{h}{h_v}\right) \sqrt{\frac{1}{C_{Dc} n_v b_v h_v/(2g)}} \qquad \begin{array}{ll} C_z(x,y,t) = C_b & \text{if } h < h_v \\ & \text{if } h > h_v \end{array} \tag{3.2}$$

and partially via a sink term in the momentum equations $-\frac{\lambda}{2}u^2$ in which

$$\begin{array}{ll} \lambda(x,y,t) = C_{Dc} b_v n_v & \text{if } h < h_v \\ \lambda(x,y,t) = C_{Dc} b_v n_v + \dfrac{h}{h_v}\dfrac{c_b^2}{C_z^2} & \text{if } h > h_v \end{array} \tag{3.3}$$

and u is the current velocity. The combined roughness via bottom friction (Eq. 3.2) and momentum sink (Eq. 3.3) is equivalent to water depth-dependent bed roughness (Eq. 3.1) and have been defined such that the ratio u/C_z^2 remains constant when the water level rises or falls (*Deltares*, 2018). The available implementation in Delft3D includes the momentum sink term in the depth-averaged momentum equations in a depth-averaged model or in the top layer of a 3D model.

Momentum sink term Delft3D includes a vegetation module in which the drag by vegetation is included as a sink term in the momentum equations. Plant morphology is simplified to rigid cylindrical stems. As currents flow around vegetation, momentum is lost due to the canopy drag force

$$F_c(x,y,z,t) = \frac{1}{2}\rho C_{Dc} b_v n_v |u| u. \tag{3.4}$$

Herein, $\rho = 1025$ kg/m^3 is the density of seawater. The drag force is a function of the vertical position in the water column z such that drag is only exerted over the height of the vegetation. Drag coefficient $C_{Dc} = 1$ matches the depth-dependent bed roughness parameterisation. Finally, the work done by the drag force is implemented as a turbulence source term in the k-ϵ turbulence closure model in Delft3D (*Uittenbogaard and Klopman*, 2001).

In addition to the four vegetation formulations, we also run the model without vegetation cover. The no vegetation model has the same morphology as the parameterisations with vegetation. The bottom roughness equals the bed roughness $C_b = 65$ m$^{1/2}$/s over the full domain.

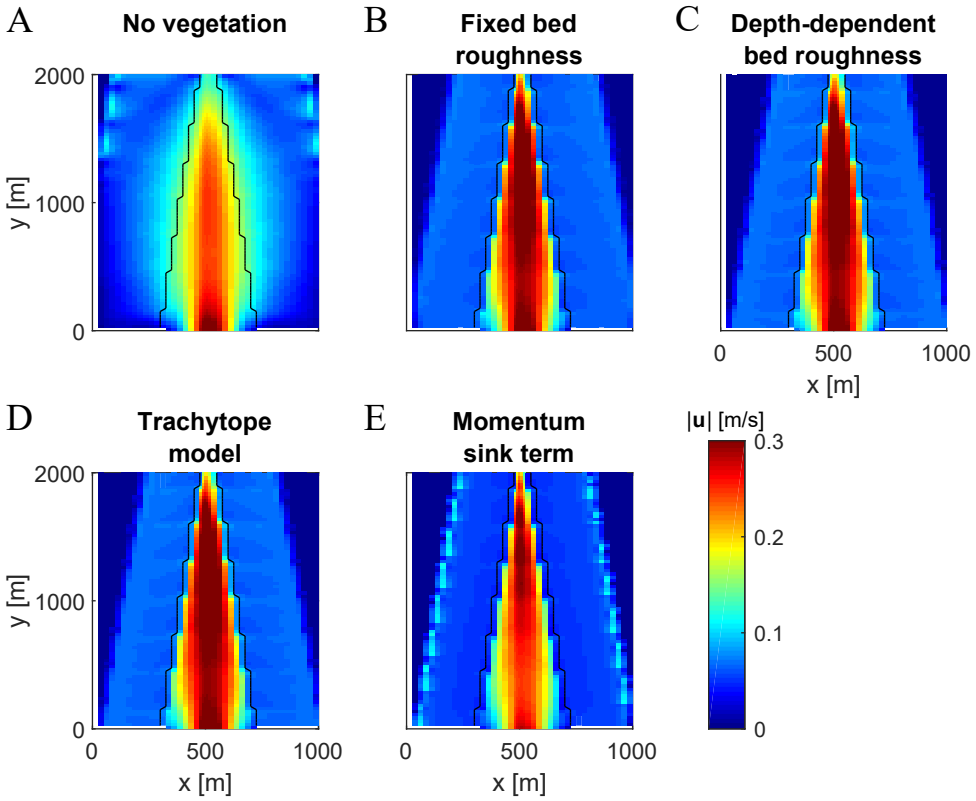

Figure 3.2: Depth-averaged current velocity magnitude at 40 minutes before high water under five model set ups: (a) no vegetation, (b) fixed bed roughness, (c) depth-dependent bed roughness, (d) trachytope model, and (e) momentum sink term. The black contour denotes the edge of the salt marsh.

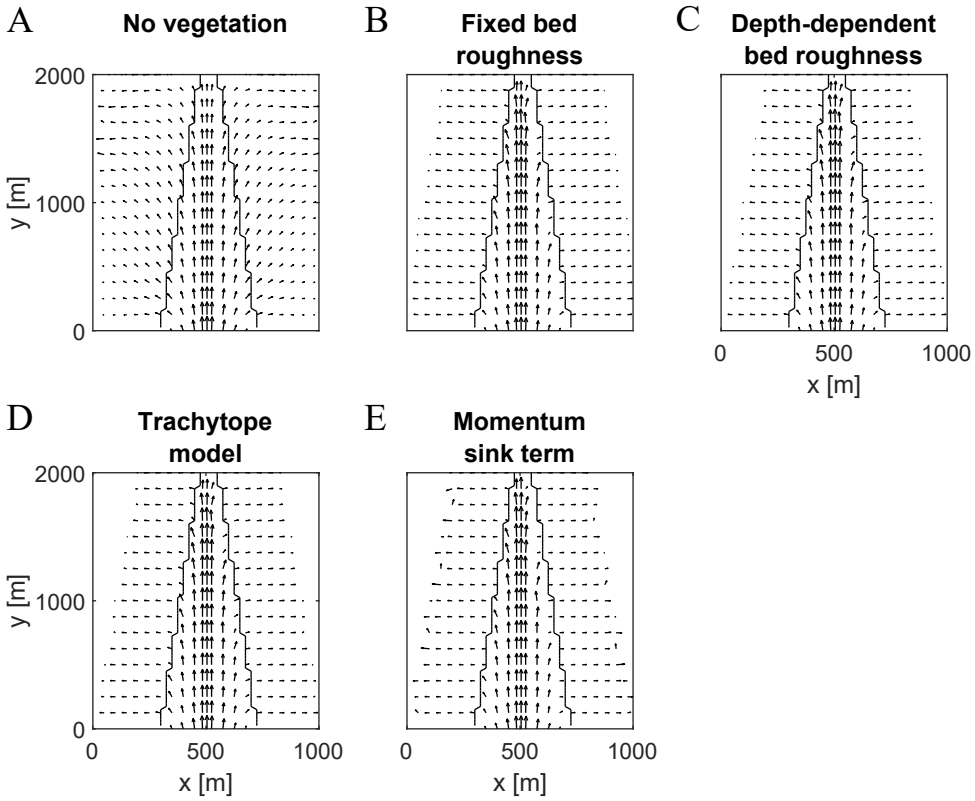

Figure 3.3: Direction of the depth-averaged currents at 40 minutes before high water under five model set ups: (a) no vegetation, (b) fixed bed roughness, (c) depth-dependent bed roughness, (d) trachytope model, and (e) momentum sink term. The black contour denotes the edge of the salt marsh.

3.3 Results

3.3.1 Depth-averaged modelling

Based on our depth-averaged model runs, we find that vegetation has a significant impact on the current magnitude and direction on the salt marshes and in the main estuary channel. The results are presented at 40 min before high water when most of the salt marsh area is inundated and current velocities are high. The results under ebb flow were similar to those under flood flow.

Salt marshes contribute to flow concentration through the main estuary channel (Fig. 3.2). When vegetation is absent, current velocities gradually decrease at increasing distance from the central axis of the estuary as the water depths become shallower and velocities from channel to salt marsh. When vegetation is present, there is a clear distinction between the high velocities in the main channel and the low velocities over the salt marsh. The velocities over the salt marsh are lower compared to the reference case without vegetation due to additional drag by the vegetation. Conversely, the velocities in the channel have increased as flow concentrates in the main channel. The effects of vegetation are qualitatively similar under all four vegetation parameterisations, but velocities are slightly lower under the momentum sink term on the salt marshes and in the channel.

The direction of flood currents supports the channelling effect of vegetation (Fig. 3.3). The flood currents are directed to the northwest and northeast in the reference case without vegetation (Fig. 3.3a), which shows that currents partly flow in the along-channel direction (vertical in Fig. 3.3). However, the current direction is strictly in cross-channel direction (horizontal in Fig. 3.3) when vegetation is present under all four vegetation parameterisations (Fig. 3.3b-e). These flow patterns resemble flooding of salt marsh platforms from a direction perpendicular to the nearest creek as was found in prior modelling studies (*Temmerman et al.*, 2005; *Ashall et al.*, 2016; *Wu et al.*, 2017). As vegetated salt marshes flood from a direction perpendicular to the main channel following the increased flow resistance over the marshes, the volume of water that passes through the main channel increases. The increase in discharge elevates flow velocities through the main channel when vegetation is present.

3.3.2 3D modelling

Our three-dimensional model runs show that the vertical structure of horizontal velocity, turbulence, water level and bed shear stress are sensitive to vegetation parameterisation. The model outputs are presented at a location central on the salt marsh where the vegetation is fully submerged (Fig. 3.1). The vertical profiles of velocity and turbulent energy are presented at 40 min before still high water and the time series of water level and bed shear stress are evaluated for the full period that the salt marsh is inundated.

The vertical profiles of horizontal velocity and turbulent energy differ significantly between the four vegetation parameterisations (Fig. 3.4). The two implementations via bed roughness (fixed roughness and depth-dependent roughness) result in near-zero current velocities at the bed and increase logarithmically over the water column. They generate strong turbulence directly above the bed. Alternatively, the trachytope model displays a parabolic velocity profile over the water column with a bed velocity that is similar to the reference model without vegetation. The parabolic shape of the velocity profile under the trachytope model follows from the implementation of the resistance terms. A bed friction term produces resistance at the bottom and a momentum sink is implemented in the top layer of the water column. Hence, the resistance to the flow is the largest at the bed and water surface. This leads to low velocities at the top and bottom of the water column and maximum velocity central in the water column. The turbulence generated over the water column is comparable to the reference model without vegetation over the full water column. Finally, the velocity and turbulence profiles under the momentum sink term relate to the height of the vegetation as it is only implemented for the part of the water column that is covered by plants. The velocity within the vegetation is constant over its height and increases in the free flow zone above the vegetation. Furthermore, the turbulent energy is maximal directly above the vegetation canopy.

Salt marsh vegetation may delay the drainage of flooded salt marshes, but results are sensitive to the parameterisation of vegetation (Fig. 3.5a). The two bed roughness and the momentum sink term parameterisations show that the drainage of salt marshes during ebb tide is delayed by approximately 60 minutes when vegetation is present. The longest delays are modelled by the momentum sink term parameterisation as the free flow layer over vegetation disappears late in the tidal cycle, and flow velocities are reduced over the full water column. Conversely, the water level modelled under the trachytope parameterisation is similar to the reference case without vegetation.

Modelled bed shear stresses show that they are sensitive to parameterisations of drag by vegetation via a bed roughness coefficient (Fig. 3.5b). As the bed shear stress is a function of bottom roughness, the bed shear stress modelled by the two

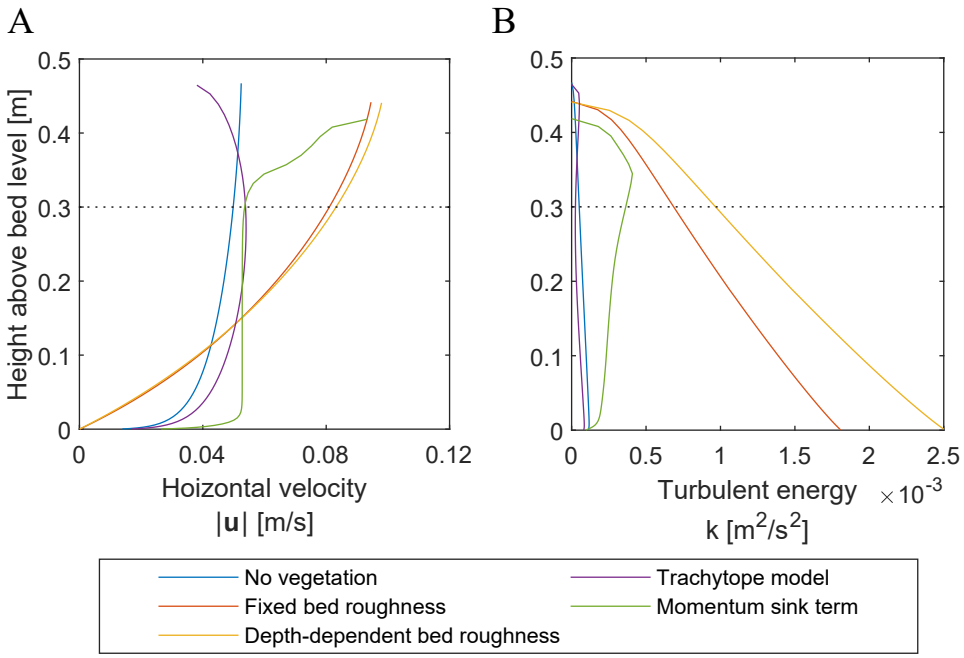

Figure 3.4: Vertical distribution of (a) the current velocity magnitude and (b) the turbulent energy on the salt marsh at peak flood currents (40 minutes before high water) under five model set ups. The dotted black line denotes the height of the vegetation.

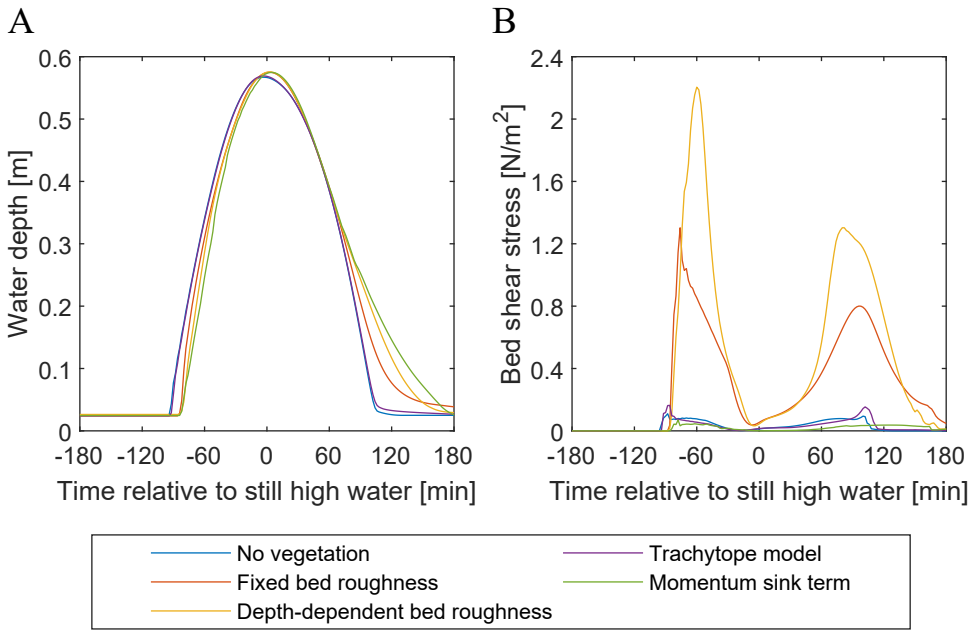

Figure 3.5: Time series of (a) water level and (b) bed shear stress on the salt marsh under five model set ups.

bed roughness parameterisations is up to ten times higher than those modelled by the trachytope model, the momentum sink term and the reference case without vegetation. Furthermore, the bed shear stress modelled by the momentum sink term is lower than the trachytope model during the ebb tide as the marsh is drained more gradually under the former model.

3.4 Comparison of vegetation parameterisations

The effect of the four vegetation parameterisations on the depth-averaged currents is qualitatively similar, but the velocity structure, turbulence, water level and bed shear stress are sensitive to the parameterisation. The fixed and depth-dependent bed roughness parameterisations result in comparable hydrodynamic parameters. However, they generate higher turbulence and shear stresses at the bed than the trachytope model and the momentum sink term (Fig. 3.4-3.5). The depth-dependent bed roughness includes a plant submergence term, but its impact on the investigated hydrodynamic parameters is small. Both parameterisations exhibit the steepest gradient in the vertical velocity profile, the highest shear stresses, and the maximum turbulent energy at the bed of the four param-

eterisations studied here.

The trachytope model reduces bed shear stress by partly implementing drag by vegetation via the momentum balance. However, as the drag by vegetation is split over the bed roughness coefficient and a sink term in the momentum balance to tune the bed shear stress precisely, the velocity profile attains a parabolic shape for which no evidence was found in experimental studies. The implementation of the momentum sink term in the top layer of the water column may be practical from a numerical perspective, but lacks physical grounds. Furthermore, it is the only parameterisation in which drainage time of the marsh is not modified by the presence of vegetation.

The momentum sink term is the only parameterisation where the vertical velocity profile is linked to the height of vegetation with a constant velocity inside the vegetation and a free flow zone above the vegetation. This profile closely resembles theoretical descriptions and experimental results (*Baptist et al.*, 2007; *Nepf*, 2012a). Furthermore, the peak in turbulent energy directly above the canopy of the vegetation has also been described in the literature (*Nepf*, 2012b).

Based on our model results, we find that the hydrodynamics are sensitive to the parameterisation of vegetation when considered in three dimensions. Although the idealised model results cannot be validated by observations, the velocity profile as produced by the momentum sink term finds most support in literature. The damping of the velocity inside the vegetation and a free flow zone above the canopy has been well established (see Section 2.3.3 for a description). This profile has only been reproduced by the momentum sink term parameterisation. Furthermore, modelling vegetation as objects that generate drag over a section of the water column matches the real-world situation better than a rough bottom.

Despite the lack of benchmark observations, our results show that the momentum sink term strongly resembles well-established physics much better than the other three parameterisations, which suggests that it is the preferred method of modelling current-vegetation interactions. The observed uncertainty in hydrodynamic parameters show that the increased physical representation of vegetation in the momentum sink term outweighs its downside as a more complex model. However, additional validation of the current velocities against field data is required when applying this parametrisation in computational models as no validation is given in this chapter and real coastal environments have complexer topographies than the idealised estuary that is presented here. Furthermore, this argument may not hold for depth-averaged modelling when the vertical variations in velocity and turbulence are not included.

3.5 Conclusions

Salt marsh vegetation modifies the hydrodynamics in estuaries, which is important for flood risk. Here, we have studied the uncertainty of hydrodynamics to parameterisations of vegetation in computational models. We have set up a model of an idealised estuary in which we have included four parameterisations: (i) a fixed bed roughness; (ii) a water depth-dependent bed roughness; (iii) the trachytope model; and (iv) a momentum sink term.

Our model results show that the magnitude of the depth-averaged flow velocity and direction are not sensitive to the parameterisations. However, the vertical structure of the velocity magnitude, turbulence, water level and bed shear stress are uncertain under different parameterisations of the current-vegetation interaction. The velocity structure as modelled via a momentum sink term best resembles literature and prior experimental studies. Conversely, parameterisations via bottom roughness predict high bed shear stresses and the trachytope model generated a parabolic velocity profile for which we found no basis in literature. As estuary hydrodynamics are sensitive to vegetation parameterisations, it is essential to model the flow-vegetation interaction adequately.

Our results are important for modelling flood risks as vegetation can modify current magnitudes, flow direction and drainage time of flooded areas. Model results of all parameterisations showed a reduction of current velocities over salt marshes and an increase in flow velocities through the main estuary channel. Furthermore, vegetation prevents along-channel flow over salt marshes. Finally, three out of four model setups showed that vegetation increased the drainage time of flooded areas.

Based on a comparison between the four parameterisations, the momentum sink term is proposed as the preferred current-vegetation parameterisation for computational models. The velocity profile best resembles established experimental observations and theoretical descriptions. Furthermore, it is physically most intuitive as it includes most vegetation properties. Although the momentum sink term requires more data on the vegetation, the variation of modelled hydrodynamic parameters across the parameterisations suggests that the investment in the vegetation data pays off in the form of more accurate model results. Therefore, the momentum sink term will be included in the coupled current-wave-vegetation model which will be further developed in Ch. 7. Although validation against measured flow velocities will be required to validate the performance of the momentum sink term in an estuary with more complex topography.

Chapter 4

Experimental study on vegetation flexibility as control parameter for wave damping and velocity structure

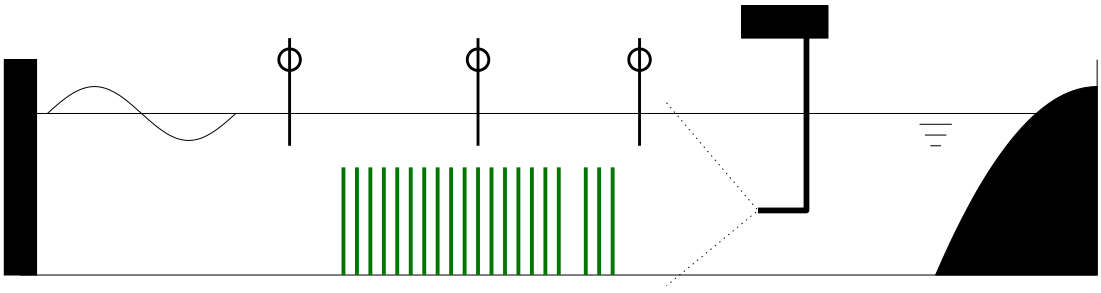

4.1 Introduction

Nature-based coastal defences in the form of vegetated foreshores are increasingly common in coastal protection schemes. The vegetation reduces wave impact on natural beaches and coastal defence structures (*Temmerman et al.*, 2013; *Möller et al.*, 2014; *Leonardi et al.*, 2018) and mitigates the impacts of storm surges (*Wamsley et al.*, 2009). At the same time, they enhance natural habitats (*Nordstrom*, 2014), provide recreational opportunities (*Foster et al.*, 2013), and can act as a grazing area for cattle (*Davidson et al.*, 2017).

Salt marshes are vegetated tidal wetlands that can be part of a nature-based coastal defence solution. The potential of their vegetation to damp waves has been shown in the field (*Jadhav et al.*, 2013) and in large-scale experiments (*Möller et al.*, 2014; *Losada et al.*, 2016). Furthermore, they capture and bind sediments (*Fagherazzi et al.*, 2012), which contributes to coastal stability (*Bouma et al.*, 2014) and provides adaptation to sea level rise (*French*, 1993).

In an attempt to quantify the impact of vegetation on wave attenuation, computational modellers have proposed different approaches. *Price et al.* (1968) used a high viscous layer to model the impact of submerged seaweed. This approach was later extended by *Mork* (1996), who also included form drag from the canopy and near the substrate. Alternatively, *Camfield* (1983) studied the impact of vegetation on wind-driven wave growth via an enhanced bottom drag coefficient. Recent modelling studies have used this simple approach to simulate vegetation impacts on waves (*Stark et al.*, 2016) and storm surges (*Wamsley et al.*, 2009). However, both approaches require additional formulations to relate plant properties to viscosity and bottom drag respectively.

Using an alternative approach, *Dalrymple et al.* (1984) developed a direct relationship for wave attenuation as a function of wave and vegetation parameters. By simplifying plant geometry to rigid cylinders and assuming the validity of linear wave theory (see e.g. *Dean and Dalrymple*, 1991, for details), a uniform bed and monochromatic wave trains, they quantified losses in wave energy due to work done by the drag force on the vegetation. Ultimately, they showed that this resulted in a reciprocal decay in wave height over a vegetation field.

Mendez and Losada (2004) expanded on *Dalrymple et al.* (1984) by introducing new relations for random sea states and bed slope effects. Furthermore, they validated their work with kelp experiments by *Dubi* (1997). They showed that the drag coefficient C_{Dw} is key in predicting wave attenuation by vegetation because it is the only parameter that cannot be readily measured in the field and it depends on the hydrodynamic conditions. It was shown that its value was inversely related to the Keulegan-Carpenter number (KC; *Mendez and Losada*, 2004). Yet, the results cannot be easily expanded to other studies, because the

drag coefficient also acts as a calibration parameter that compensates for the assumptions made, such as the simplification of the plant geometry.

The framework as set out by *Dalrymple et al.* (1984) and *Mendez and Losada* (2004) has been successfully applied in experiments with artificial and real salt marsh vegetation to obtain additional relations for the bulk drag coefficient. For example, *Jadhav et al.* (2013) confirmed an inverse relation between the KC number and the drag coefficient based on measurements on a *Spartina Alterniflora* marsh. Alternatively, drag coefficient has been related to vegetation Reynolds number Re in experimental studies. This includes experiments with vegetation mimics, using a variety of materials, plant shapes and plant dimensions (*Augustin et al.*, 2009; *Koftis et al.*, 2013; *Anderson and Smith*, 2014; *Hu et al.*, 2014; *Ozeren et al.*, 2014; *Chen et al.*, 2018; *Phan et al.*, 2019), as well as experiments with real vegetation such as *Puccinellia Maritima* and *Elymus Athericus* (*Möller et al.*, 2014) and *Puccinellia Maritima* and *Spartina Anglica* (*Lara et al.*, 2016; *Losada et al.*, 2016). Regardless of whether KC or Re is used, all studies found a reduction in drag coefficient for increased orbital wave particle velocities which are associated with higher waves.

However, a comparison by *Vuik et al.* (2016) revealed that for hydrodynamic conditions typical for a salt marsh, the drag coefficients ranged from 0.13 to 5.75, which differ by a factor of 44. This indicates that hydrodynamic conditions are not a sufficient predictor for the drag coefficient. Submergence ratio (*Mendez and Losada*, 2004; *Anderson and Smith*, 2014; *Garzon et al.*, 2019a) and biomass (*Maza et al.*, 2015) have been studied, but results are not consistent among experiments and both parameters are accounted for in the framework by *Dalrymple et al.* (1984) and *Mendez and Losada* (2004). This suggests that other untested parameters may be important.

Recently, *Paul et al.* (2016) have shown that plant flexibility may affect the potential of vegetation to attenuate waves, particularly when orbital velocities are low. Although their results have been obtained using a small quantity (max 8) of rectangular Lexaan strips instead of a full vegetation meadow, it has drawn attention to the potential importance of flexibility which varies greatly among plant species (*Chatagnier*, 2012). These observations are supported by the low drag coefficients reported in studies with flexible grasses (e.g. *Möller et al.*, 2014). Furthermore, numerical modelling exercises have shown that plant swaying reduces the drag forces on flexible vegetation (*Méndez et al.*, 1999; *Mullarney and Henderson*, 2010; *Luhar and Nepf*, 2016). However, *Augustin et al.* (2009) found no difference between rigid and flexible mimics. Therefore, additional research is needed on how the plant flexibility affects wave attenuation.

Experimental results have also challenged the assumption that the velocity structure follows linear wave theory in the presence of vegetation. For instance,

the orbital velocities were preferentially attenuated within meadows of wide rigid cylinders (*Lowe et al.*, 2005; *Pujol et al.*, 2013) and flexible vegetation (*Luhar et al.*, 2010; *Rupprecht et al.*, 2017). Furthermore, wave-averaged net currents were observed around artificial rigid (*Pujol et al.*, 2013; *Hu et al.*, 2014; *Abdolahpour et al.*, 2017) and flexible (*Luhar et al.*, 2010; *Abdolahpour et al.*, 2017) vegetation patches. These modifications in the velocity structure directly impact the magnitude of the drag force and the work done by it.

However, the magnitude of velocity attenuation and the direction and position of net currents differ between rigid and flexible vegetation. In an experiment with artificial rigid and flexible vegetation under equal wave conditions, *Pujol et al.* (2013) identified velocity attenuation by rigid vegetation only. Furthermore, rigid vegetation induces net currents in the direction of wave propagation through the top of the vegetation (*Pujol et al.*, 2013) and flexible vegetation near the bottom (*Luhar et al.*, 2010; *Rupprecht et al.*, 2017).

Thus, plant flexibility may also be a key predictor for changes in wave-driven velocities, but much remains unclear in the absence of high-quality comparative data. Rigid and flexible vegetation with identical shapes have not yet been tested. Cylinders were used to mimic rigid vegetation (*Lowe et al.*, 2005; *Pujol et al.*, 2013; *Hu et al.*, 2014; *Abdolahpour et al.*, 2017) as opposed to blades (*Luhar et al.*, 2010; *Pujol et al.*, 2013; *Abdolahpour et al.*, 2017) or real grasses (*Rupprecht et al.*, 2017) for flexible vegetation. Furthermore, measurements have been restricted to points (*Hu et al.*, 2014; *Abdolahpour et al.*, 2017) or cross-sections (*Lowe et al.*, 2005; *Luhar et al.*, 2010; *Pujol et al.*, 2013; *Abdolahpour et al.*, 2017). Full velocity fields have not been measured yet.

Therefore, we tested wave attenuation by and the velocity structure around rigid and flexible vegetation meadows that differ in flexibility only. Plant parameters and wave conditions were directly derived from salt marshes in South Wales, UK, to mimic realistic plant properties for this study. The salt marshes in South Wales exhibit diverse vegetation with large variation in plant stem flexibility, which is important to this study. As a further key element, Particle Image Velocimetry (PIV) is used to measure the velocity structure in the x-z plane around vegetation.

This chapter is organised as follows. Section 4.2 sets out the theoretical background that is relevant to our experiments. The setup of the experiments is described in Section 4.3. The results are presented in Section 4.4 and discussed in Section 4.5. Finally, the conclusions are drawn in Section 4.6.

4.2 Theoretical background

Let us define a coordinate system (Fig. 4.1), where the x-axis is in the direction of wave propagation with $x = 0$ at the front edge and $x = L_v$ at the back edge of the vegetation. Furthermore, the z-axis describes the vertical position with respect to the water column such that $z = 0$ depicts the still water surface and $z = -h$ the bed level. Herein, waves travel over a flat bottom with a vegetation field. Following *Dalrymple et al.* (1984), plant geometry is simplified to rigid upright cylinders with height h_v, diameter b_v and spacing S_v, such that $S_v = n_v^{-0.5}$ with n_v as the stem density in stems/m^2. Furthermore, sinusoidal waves with height $H(x)$ and period T are imposed on the domain.

When waves travel over vegetation fields, energy is dissipated due to the work done by the waves on the plants (*Dalrymple et al.*, 1984). A time-averaged wave dissipation constant per unit horizontal area is defined as

$$\epsilon_v = \int_{-h}^{-h+h_v} \overline{\boldsymbol{F}\boldsymbol{u}} dz. \tag{4.1}$$

$\epsilon_v = -c_g \partial E/\partial x$ is the wave energy dissipation per stem, where the wave group velocity is given by $c_g = \frac{\omega}{2k}\left(1 + \frac{2kh}{\sinh 2kh}\right)$ and the wave energy is given by $E = \rho g H^2/8$. Herein, ω is the wave angular frequency, k is the wave number, $\rho = 1000$ kg/m^3 is the density of water, and $g = 9.81$ m/s^2 is the gravitational acceleration. Furthermore, $\boldsymbol{F} = (F_x, F_z)$ is the force exerted by the waves on the vegetation per unit volume and $\boldsymbol{u} = (u, w)$ is the local flow velocity. The horizontal component of the wave force is typically considered dominant, i.e. $\boldsymbol{F}\boldsymbol{u} \approx F_x u$ (*Kobayashi et al.*, 1993; *Méndez et al.*, 1999). F_x is given by a Morison type equation (*Morison et al.*, 1950), according to

$$F_x = \frac{1}{2}\rho C_{Dw} b_v n_v |u_r| u_r + \frac{\pi}{4}\rho C_M b_v^2 n_v \frac{\partial u_r}{\partial t}, \tag{4.2}$$

where u_r is the relative velocity between water and vegetation, C_{Dw} is the drag coefficient, and C_M is the inertia coefficient. The effect of vegetation motion is considered through calibration of the drag coefficient (*Mendez and Losada*, 2004; *Möller et al.*, 2014). Additionally, the contribution of the drag term is expected to exceed the contribution of the inertia term with respect to wave attenuation because the inertia term acts out of phase with the velocity (*Dalrymple et al.*, 1984; *Kobayashi et al.*, 1993; *Mendez and Losada*, 2004). Under these conditions, the wave force reduces to

$$F_x = \frac{1}{2}\rho C_{Dw} b_v n_v |u| u. \tag{4.3}$$

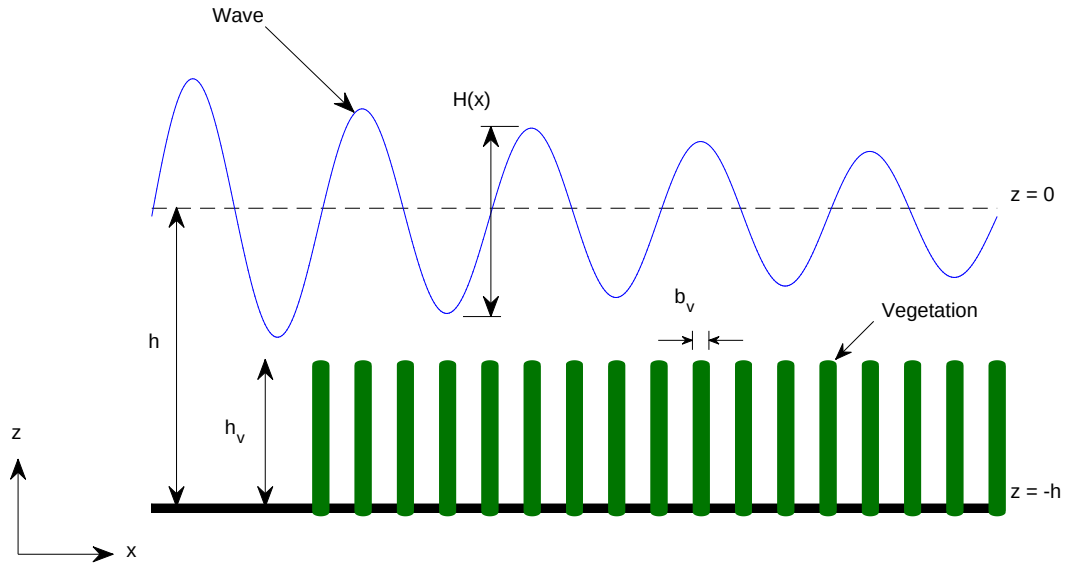

Figure 4.1: Schematisation of wave attenuation over vegetation.

Further assuming the validity of linear wave theory, *Dalrymple et al.* (1984) showed that waves decay reciprocally with distance across vegetation, according to

$$H(x) = \frac{H_0}{1 + \beta x} \tag{4.4}$$

with

$$\beta = \frac{4}{9\pi} C_{Dw} b_v n_v H_0 k \frac{\sinh^3 k\alpha h + 3 \sinh k\alpha h}{(\sinh 2kh + 2kh) \sinh kh} \tag{4.5}$$

Herein, H_0 is the wave height at the front edge of the vegetation field, β is the wave attenuation coefficient, and $\alpha = h_v/h$ is the submergence ratio. According to Eq. 4.5, the magnitude of wave dissipation is a function of vegetation properties, flow conditions and the drag coefficient. Importantly, the drag coefficient implicitly acts as a calibration parameter for the assumptions made. The default value of C_{Dw} for rigid cylinders is therefore not applicable.

4.3 Experimentation

4.3.1 Flume setup

Experiments with rigid and flexible plant mimics were conducted in the wave flume of the Coastal Laboratory of Swansea University, UK. The flume is 30.7 m in length, 0.8 m in width and 1.2 m in height. It has glass sidewalls and a metal bottom. The flume has a piston-type wavemaker with active wave absorption at one end and a parabolic wave damper of reticulated foam at the other end (Fig. 4.2a).

Rigid and flexible vegetation mimics were fixed on the flume floor. The rigid vegetation was created from bamboo dowels ($\rho_v = 350$ kg/m^3; Fig. 4.2b) and flexible vegetation from silicon sealants ($\rho_v = 998$ kg/m^3; Fig. 4.2c). The two plant mimics differed in flexural rigidity, $EI_v = 9.0 \pm 4 \times 10^{-2}$ Nm^2 for the dowels and $EI_v = 1.7 \pm 0.3 \times 10^{-5}$ Nm^2 for the sealants. Both vegetation types were cylinders with a diameter of 5 mm and a height of 300 mm. They were fitted into aluminium plates (500 mm long, 750 mm wide, 0.9 mm thick) with pre-drilled holes. The holes were aligned in a series of rows normal to the wave direction. The spacing between rows was 30 mm, and the spacing between stem centres on a row was 30 mm for a stem density of 1111 stems/m^2. However, subsequent rows had a lateral shift of 15 mm to obtain a staggered grid which resembles the scattering of real vegetation.

The vegetation plates were attached to the flume floor by suction cups at the plate centres, corners and edge centres. They attached well to the floor with minimum separation between plate and flume floor. Three rigid and flexible vegetation plates were constructed for a total vegetation length of 1.5 m. Following *Luhar et al.* (2010) and *Pujol et al.* (2013), two rows of vegetation were removed to create a 90 mm gap to allow PIV measurements within the plant meadow. It is assumed that the orbital water particle motion within this gap will not differ from its surroundings, which is validated by repeating each run without a gap in the vegetation. The measured wave damping and water particle velocities around the vegetation field (above and downstream) did not differ when the gap was removed, which provided confidence that the wave dynamics were unaffected by the gap.

Three wave gauges (WG1, WG2 & WG3) and a PIV system (Dantec Systems) were installed to measure the wave-induced variations in water surface elevation and particle velocity (Fig. 4.2a). WG1 was placed 1.05 m upstream of the vegetation patch, WG2 was placed central in the patch, and, finally, WG3 was placed 0.10 m downstream of the vegetation. Furthermore, a laser inside the flume and a camera on the side were the main components of the PIV system to measure the

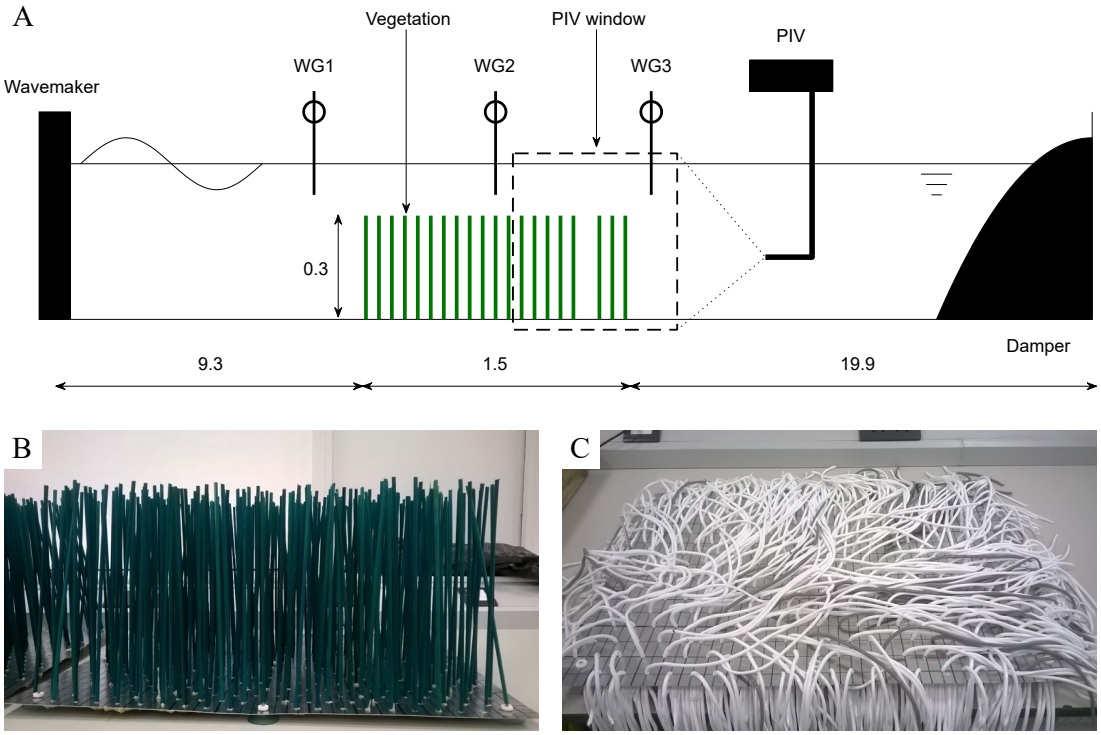

Figure 4.2: (a) Sketch of the experimental set-up. All dimensions are in metres. Figure is not to scale; (b) Artificial rigid vegetation; (c) Artificial flexible vegetation.

water particle velocities. The laser was placed 2-3 m upstream of the vegetation patch. Its exact location was optimised for each water depth. Details about wave attenuation and particle velocity measurements are provided in Sections 4.3.4 and 4.3.5 respectively.

Despite the presence of a wave damper at the end of the flume, the impact from wave reflection was significant. Therefore, only the time window unaffected by reflected waves was used in the data analysis. This was defined as the period between the full wave development and the return of the first reflected wave to WG3 (*Möller et al.*, 2014). Waves were considered fully developed when the water level reached 95% of the incident wave amplitude and at least five waves had passed. The return time was derived from shallow water wave theory. Four to eleven waves fell within the curtailed frame, depending on wave period and water depth. Therefore, each condition was run three times to obtain sufficient data: two times with a gap in the vegetation and one run without a gap.

4.3.2 Wave conditions

The rigid and flexible vegetation patches were subjected to 24 regular wave conditions (Table 4.1). Specifically, the wave height varied between 0.08 and 0.20 m, the wave period between 1.4 and 2.0 s, and the water depth between 0.60 and 0.30 m. The wave conditions have been selected to investigate the sensitivity in these critical hydrodynamic parameters. They also provide a realistic range for the Keulegan-Carpenter number KC and Reynolds number Re, which are commonly used to describe the hydrodynamic regime around vegetation. This is explored in detail in Section 4.3.3. A velocity scale, u_c, is defined as the maximum orbital velocity at stem centre ($z = -h + 1/2h_v$) in front of the vegetation ($x = 0$) based on linear wave theory. Each condition was run three times for both vegetation types. Finally, control runs without vegetation were conducted for cases R3, R13, R23 and R33. Unfortunately, instrument malfunctioning occurred during 14 out of 264 measurements (water surface and velocity measurements). The affected cases are listed in Table 4.1).

All conditions were wave only, i.e. without currents. Although waves and currents may occur simultaneously under field conditions (i.e. *Garzon et al.*, 2019a), understanding the impact of flexible vegetation under waves only is a prerequisite for understanding the more complex scenario of simultaneous occurrence of waves and currents. Furthermore, maximum wave height typically occurs during peak high water when current velocities are often small. Nonetheless, the study of wave-current interaction is suggested as an avenue for future research.

4.3.3 Experiment similarity

Past studies have shown that drag coefficient relationships for wave attenuation strongly rely on hydrodynamic and vegetation conditions (see Section 2.4.3 for a review). It is important that selected experimental conditions represent field conditions. Therefore, the experimental conditions in this study are supported by plant data from two field campaigns in South Wales estuaries and wave data from a concurrent numerical modelling study of wave penetration in a sheltered macrotidal estuary (*Bennett et al.*, 2020), which is typical for South Wales. Details are provided in Appendix A.

There is no scale difference between field and flume, but it remains key to verify that the wave-vegetation interactions are similar. Four components control this interface: (i) the plant dimensions, (ii) the incoming wave dynamics, (iii) the hydrodynamic impact on the waves by the vegetation, and (iv) the response of the plants to the orbital wave motion (plant swaying). A detailed list of parameters and ratios is provided in Table 4.2.

First, the dimensions h_v, b_v, and n_v of the vegetation mimics are within the

Table 4.1: List of tested wave conditions. Each condition was tested three times with rigid and flexible vegetation. (R) and (F) denote that a parameter is associated with (R)igid or (F)lexible vegetation.

Case	**Wave type**	H [m]	T [s]	h [m]	u_c [m/s]	KC	L	F_r	Re	Ca (R)	Ca (F)
R1*‡	Regular	0.15	1.4	0.60	0.19	53	7.1	0.08	945	0.05	279
R2‡	Regular	0.15	1.6	0.60	0.22	69	5.5	0.09	1077	0.07	362
R3‡	Regular	0.15	1.8	0.60	0.23	84	4.5	0.10	1169	0.08	427
R4‡	Regular	0.15	2.0	0.60	0.25	99	3.8	0.10	1235	0.09	476
R5‡	Regular	0.10	1.8	0.60	0.16	56	6.7	0.06	779	0.04	190
R6‡	Regular	0.20	1.8	0.60	0.31	112	3.4	0.13	1559	0.15	755
R11	Regular	0.15	1.4	0.50	0.23	65	5.8	0.10	1160	0.08	421
R12†‡	Regular	0.15	1.6	0.50	0.26	82	4.6	0.12	1277	0.10	510
R13	Regular	0.15	1.8	0.50	0.27	98	3.9	0.12	1358	0.11	576
R14	Regular	0.15	2.0	0.50	0.28	113	3.3	0.13	1416	0.12	623
R15	Regular	0.10	1.8	0.50	0.18	65	5.8	0.08	906	0.05	256
R16	Regular	0.20	1.8	0.50	0.36	130	2.9	0.16	1811	0.20	1018
R21	Regular	0.15	1.4	0.40	0.29	81	4.7	0.15	1447	0.13	653
R22	Regular	0.15	1.6	0.40	0.31	99	3.8	0.16	1544	0.14	744
R23‡	Regular	0.15	1.8	0.40	0.32	116	3.3	0.16	1610	0.16	810
R24	Regular	0.15	2.0	0.40	0.33	133	2.8	0.17	1658	0.17	863
R25†‡	Regular	0.10	1.8	0.40	0.21	77	4.9	0.11	1074	0.07	360
R26†‡	Regular	0.12	1.8	0.40	0.26	93	4.1	0.13	1288	0.10	519
R31	Regular	0.10	1.4	0.30	0.25	70	5.4	0.14	1242	0.09	482
R32	Regular	0.10	1.6	0.30	0.26	82	4.6	0.15	1287	0.10	517
R33	Regular	0.10	1.8	0.30	0.26	95	4.0	0.15	1317	0.10	541
R34	Regular	0.10	2.0	0.30	0.27	107	3.5	0.16	1339	0.11	558
R35	Regular	0.08	1.8	0.30	0.21	76	5.0	0.12	1054	0.07	347
R36	Regular	0.12	1.8	0.30	0.32	114	3.3	0.18	1580	0.15	783

* The velocity measurements around rigid vegetation is based on 1 instead of 2 runs. † The velocity measurements around flexible vegetation is based on 2 instead of 3 runs. ‡ The water surface measurements over flexible vegetation is based on 2 instead of 3 runs.

range typical for South Wales. Furthermore, the relative share of vegetation in the water column is expressed by the submergence ratio $\alpha = h_v/h$ (e.g. *Augustin et al.*, 2009; *Koftis et al.*, 2013) and relative stem frontal area $\lambda_f = h_v b_v n_v$. The conditions considered in this study, $\alpha = 0.50$ – 1.0 and $\lambda_f = 1.67$, are within the range of field conditions.

Second, the incoming wave conditions have been selected within the range of numerical modelling results central on the salt marshes (*Bennett et al.*, 2020). These served as direct input to the wavemaker. Therefore, key ratios such as the Froude number $F_r = u_c/\sqrt{gh}$ (e.g. *Bullock et al.*, 2001) and relative wave height $H_r = H/h$ are automatically satisfied among field and experiment conditions. However, waves with a height up to 0.80 m were observed at the edge of a salt marsh in *Bennett et al.* (2020). These could not be reproduced in the wave flume due to its limited height.

Third, the hydrodynamics around salt marsh plants are controlled by the wake structures induced by the vegetation, expressed by the vegetation Reynolds Number $Re = u_c b_v/\nu$ (e.g. *Nepf*, 1999), in which ν is the kinematic viscosity. Alternatively, the Keulegan-Carpenter number $KC = u_c T/b_v$, which is effectively a ratio between wave excursion and stem diameter, has been identified as a predictor the for drag coefficient on cylinders (*Keulegan and Carpenter*, 1958). Re and KC fall within the range of field conditions (Table 4.2). Specifically, Re varies from 779 to 1811 and KC varies between 53 and 133 depending on test conditions (Table 4.1).

Fourth, plant swaying is induced by wave forcing on flexible vegetation. *Luhar and Nepf* (2016) showed that plant swaying is controlled by the Cauchy Number $Ca = \rho b_v u_c^2 h_v^3/EI_v$ as the ratio of drag force over restoring forces due to stiffness, and the excursion ratio $L = h_v/A_w$ as the ratio of stem length over water particle excursion $A_w = u_c T/(2\pi)$. Buoyancy may delay the onset of plant bending but is not expected to affect wave dynamics when wave forcing is significant (large Ca) (*Luhar and Nepf*, 2011, 2016; *Luhar et al.*, 2017; *Henderson*, 2019). The Cauchy numbers of rigid ($Ca = 0.04$-0.20) and flexible ($Ca = 200$-1000) mimics cover the range of real vegetation in South Wales ($Ca = 1.5$-100) and those reported in the literature (e.g. *Rupprecht et al.*, 2017, reported $Ca = 1.5$-100 for *E. Athericus* and *P. Maritima*). Also, the excursion ratio matches well, with $L = 2.8$-7.1 in the experiments, compared to $L = 2.9$-7.4 in the field.

Table 4.2: List of parameter values for field and experiment conditions. It is divided in sections plant data (top), wave data (middle) and dimensionless ratios (bottom).

Parameter		**Field (S. Wales)**	**Rigid mimics**	**Flexible mimics**	**Unit**
Vegetation height	h_v	231–590	300	300	mm
Vegetation diameter	b_v	0.74–5.50	5	5	mm
Vegetation density	n_v	214–2275	1111	1111	m^{-2}
Young's modulus	E_v	139-2343	2917	0.56	MPa
Flexural rigidity	EI_v	1.9×10^{-5}–2.6×10^{-2}	9.0×10^{-2}	1.7×10^{-5}	Nm^2
Bulk density†	ρ_v	N/A	350	998	kg/m^3
Water depth	h	0-0.6	0.30-0.60	0.30-0.60	m
Wave height	H	0.1-0.2	0.08–0.20	0.08–0.20	m
Wave period	T	2.0	1.4-2.0	1.4–2.0	s
Velocity scale	u_c	0.17-0.33	0.16-0.36	0.16–0.36	m/s
Submergence ratio	α	0.39-1.0	0.5-1.0	0.5–1.0	-
Relative frontal area	λ_f	0.57-6.10	1.67	1.67	-
Froude number‡	F_r	0.10	0.10	0.10	-
Reynolds number‡	Re	185–1375	1250	1250	-
KC number‡	KC	91-676	100	100	-
Cauchy number‡	Ca	1.55-103	0.09	488	-
Excursion ratio‡	L	2.9–7.4	3.8	3.	-

† All field vegetation was observed to be buoyant, but the exact bulk densities could not be measured accurately with available equipment.

‡ Reference hydrodynamic conditions: $H = 0.15$ m, $T = 2$ s, $u_c = 0.25$ m/s.

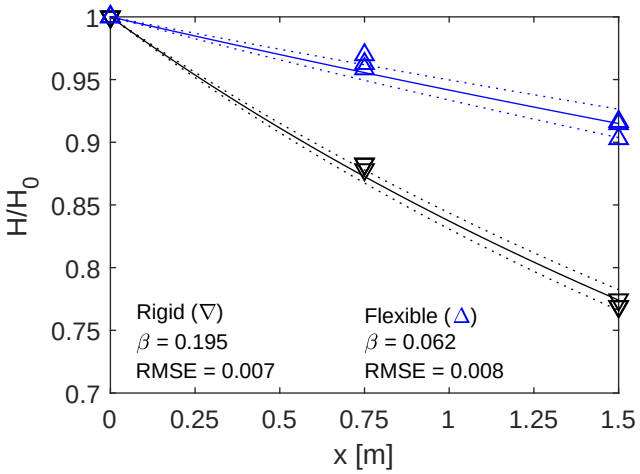

Figure 4.3: Wave attenuation parameter β fitted to the wave height measurements for case R34. The triangles indicate normalized wave heights H/H_0 at each wave gauge for the three test runs. The solid lines denote the fitted attenuation function (Eq. 4.4) and the dotted lines denote the 95% confidence interval. The root-mean-square error given is of H/H_0 in WG2 and WG3.

4.3.4 Wave attenuation measurements

The wave attenuation parameter β is obtained from the energy spectra that are derived from wave gauges in front of (WG1), halfway (WG2), and after (WG3) the artificial vegetation patch (Fig. 4.2a). Measured water surface elevation time series were curtailed to the maximum number of fully developed waves within the timeframe unaffected by reflection. We corrected for phase differences between each gauge in this process to obtain equivalent time series. These were used to calculate the wave energy spectra and, subsequently, zeroth spectral moment wave height $H_{m,0}$ at each gauge.

The zeroth spectral moment wave height was previously successfully applied for irregular waves by *Koftis et al.* (2013) and *Anderson and Smith* (2014) and was preferred over zero up-crossing because the nonlinear interactions in shallow water induced higher-order harmonics. Furthermore, this concept is consistent with the attenuation in wave energy as described in Section 4.2.

The three runs for each test condition were combined, and a single β was fitted to Eq. 4.4 using the least-squares method (Fig. 4.3). Then, the associated drag coefficient C_{Dw} can be obtained via Eq. 4.5. The control experimental runs without vegetation showed that the contribution of bottom friction to wave damping did not affect the results ($\beta < 0.005$).

4.3.5 Water particle velocity measurements

Water particle velocities over, after and within the vegetation were measured using Particle Image Velocimetry (PIV; Dantec Systems). Polyamid seeding particles that follow water particle motion are added to the flume. By shooting two frames of the particle positions, their velocity can be calculated from their movement in between the pair of frames. Crucially, the pairing frames are shot with minimal time difference, here 2 ms. Illumination in the x-z plane is provided by a laser and images are shot by a high-resolution camera through the glass walls of the flume.

The laser (Nano L 100–50 PIV, Litron Lasers) was placed inside the water column downstream of the vegetation patch to avoid interference with the wave motion. The camera (Speedsense 1040) placement and zoom were adjusted to maximize resolution whilst retaining view over the full water column. Image pairs were shot at a rate of 50 frames per second with a resolution of 2320 $\times$ 1726 pixels (width $\times$ height). Specifically, for water shallower than 0.45 m, the resolution was 0.30 mm per pixel, and for water deeper than 0.45 m, the resolution was 0.35 mm per pixel.

Post-processing was conducted using Dantec's DynamicStudio 2015a to obtain water particle velocities. Best results were obtained with the adaptive PIV algorithm, which calculates velocities based on cross-correlation between image pairs with interrogation areas adapted to seeding densities and flow gradients. As the observed wave motion predominantly behaved as a third-order stokes wave due to the limited water depth (*Le Méhauté*, 1976), the particle velocity time series at each point in the x-z plane are derived using the three primary harmonics: the natural frequency and the first- and second-order higher harmonics (following e.g. *Luhar and Nepf*, 2016). We found that higher-order harmonics did not significantly improve the results.

The amplitudes and phases of each harmonic are obtained using a Fast Fourier Transform analysis of the measured velocities. Importantly, the water surface elevation measurements are not used in this derivation, i.e. the resulting particle velocities are based on the PIV signal and periodicity only. The PIV-derived velocities were compared against linear wave theory for the control runs without vegetation at three points in the water column (Fig. 4.4). They showed excellent correlation ($r^2 \geq 0.97$) against estimates based on linear wave theory and measured wave height spectradespite the presence of small measurement noise in the wave troughs near the water surface ($z = -0.1$ m).

The orbital velocity magnitude and net currents were obtained from the PIV-derived horizontal $u(x, z, t)$ and vertical $w(x, z, t)$ velocity signals. We define the amplitude of the orbital velocity as $[u, w]_{amp}(x, z) = (\max[u, w] - \min[u, w])/2$. Hereinafter referred to as velocity amplitude, it serves as a phase-independent

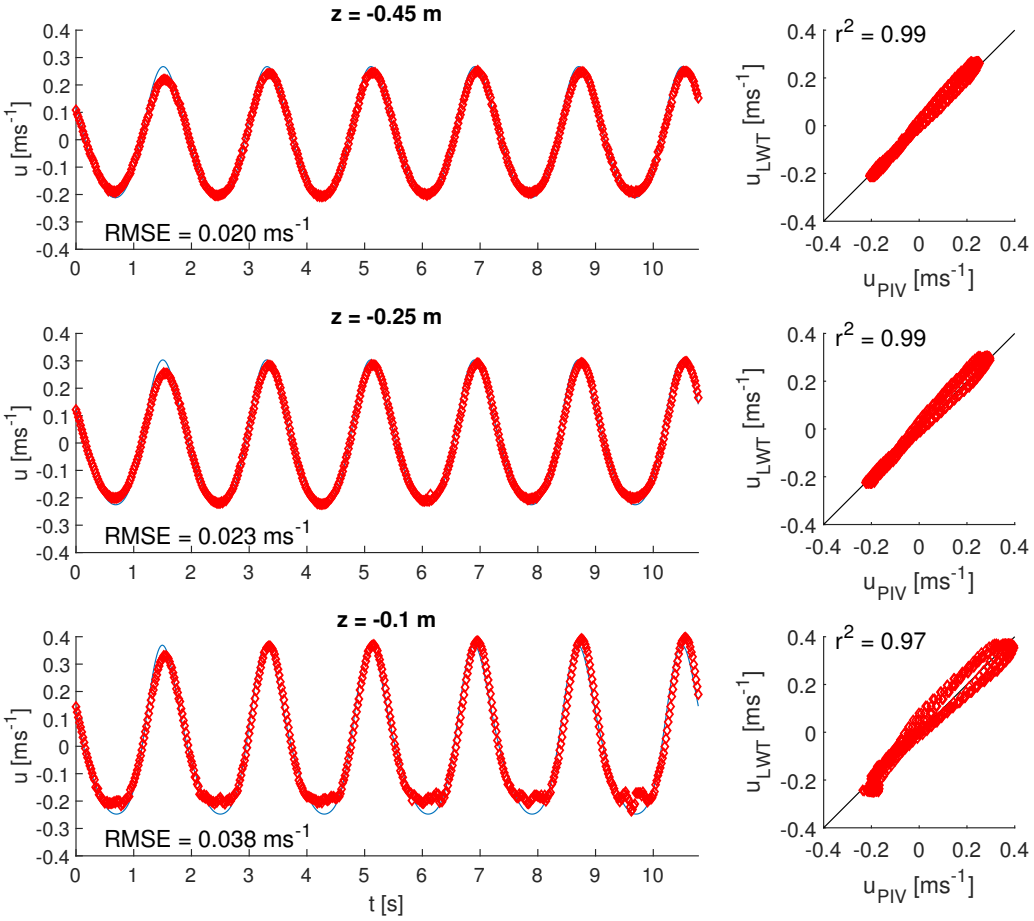

Figure 4.4: Comparison of the PIV-derived particle velocity measurements for case R13 without vegetation. The blue line depicts the predicted horizontal water particle velocities based on linear wave theory using measured wave harmonics. The red diamonds depict PIV-derived water particle velocities.

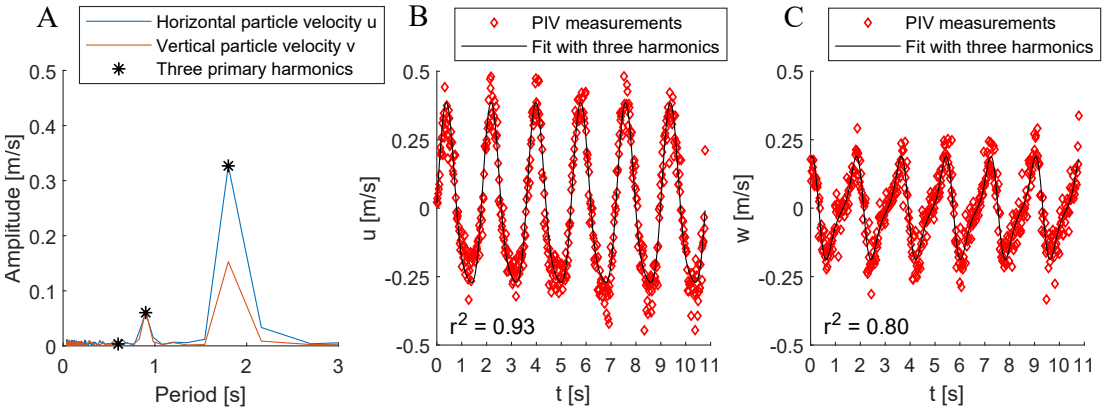

Figure 4.5: Transformation of a PIV output signal to a signal used in the analysis of water particle velocities for case R33 with rigid vegetation. (a) displays the Fast Fourier Transform of the horizontal (blue) and vertical (orange) particle velocities. (b) shows the quality of fit of the three harmonics (black line) against PIV-derived velocities (red diamonds) for horizontal particle velocities and (c) shows this for vertical particle velocities.

measure of the magnitude of the periodic orbital velocity signals. It enables comparison of the horizontal and vertical velocity components separately and is independent of wave phase. Although other definitions of a velocity magnitude, such as the root-mean-square velocity (*Lowe et al.*, 2005), would have been equally valid, our definition was selected for its simplicity. Furthermore, we obtain wave-averaged net velocities $U_{net}(x,z) = \frac{1}{T}\int_0^T u dt$ and $W_{net}(x,z) = \frac{1}{T}\int_0^T w dt$ in horizontal and vertical direction respectively.

The main advantage of this method for our study is that it is robust for noisy signals. This is shown for case R33 with rigid vegetation in Figure 4.5, which has been identified as a case with high noise. The conditions are near-emergent with maximum relative wave height. Therefore, strong wave-vegetation interaction can be expected. Yet the fit of the three primary harmonics is excellent for both horizontal ($r^2 = 0.93$) and vertical ($r^2 = 0.80$) water particle velocities.

4.4 Results

4.4.1 Drag coefficient for wave attenuation

The wave attenuation parameter β and drag coefficient C_{Dw} have been fitted for all 24 test cases on the basis of Eq. 4.4-4.5. The average root-mean-square error in H/H_0 was 0.011 for rigid vegetation and 0.010 for flexible vegetation. The best fit for the drag coefficient was found to be a function of KC. Following *Kobayashi et al.* (1993), we used the equation

$$C_{Dw} = \left(\frac{a}{KC}\right)^b + c \tag{4.6}$$

to obtain a relationship between C_{Dw} and KC with $c \geq 0$. For rigid vegetation, we found

$$C_{Dw} = \left(\frac{81}{KC}\right)^{0.36} + 0 \tag{4.7}$$

with $r^2 = 0.54$ (Fig. 4.6a). Alternatively, for flexible vegetation, we obtained

$$C_{Dw} = \left(\frac{43}{KC}\right)^{5.3} + 0.26 \tag{4.8}$$

with $r^2 = 0.54$ (Fig. 4.6b). The drag coefficient of rigid vegetation is up to 70% lower than the drag coefficient of flexible vegetation for $KC > 65$ (Fig. 4.7). The difference appears reduces in the range $53 < KC < 65$ but support is limited with only four conditions tested within this range.

The C_{Dw}-relations exhibit similar trends as found in earlier studies (Fig. 4.7). The fitted C_{Dw} of rigid vegetation is compared with fits obtained by birch dowels ($h_v = 480$ mm, $b_v = 9.4$ mm, $n_v = 350$ stems/m^2, EI_v not reported) in *Ozeren et al.* (2014) and *S. Alterniflora* ($h_v = 220$ mm, $b_v = 8$ mm, $n_v = 422$ stems/m^2, $EI_v = 1.5 \times 10^{-2}$ Nm^2) in *Jadhav et al.* (2013). Although *S. Alterniflora* is a natural plant, *Jadhav et al.* (2013) find that it can reasonably be approximated as a rigid cylinder based on their observations and its flexural rigidity value (Table 4.3). The C_{Dw} values found in this study are 15–50% lower than in *Ozeren et al.* (2014) and *Jadhav et al.* (2013). In case of *Ozeren et al.* (2014), only a small portion of their test runs was conducted within the range considered here, with most runs instead in the range $5 < KC < 30$. In case of *Jadhav et al.* (2013), a possible explanation is that we observed preferential attenuation of orbital velocities within the canopy (further discussed in Section 4.4.3) whereas they only found preferential attenuation for a narrow frequency band based on numerical analysis. Preferential attenuation is not accounted for in Eq. 4.5 and

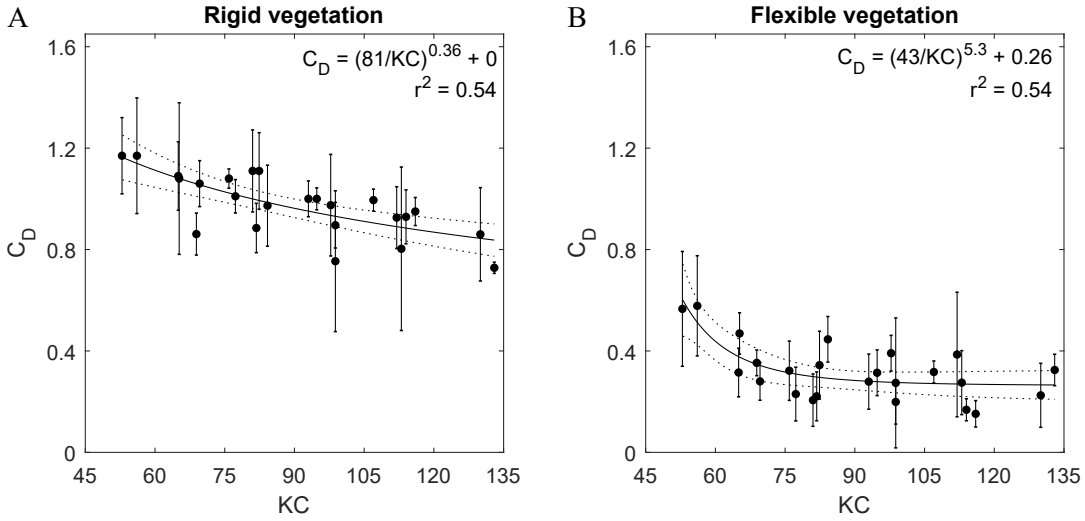

Figure 4.6: Empirical relations for drag coefficient C_{Dw} as function of the Keulegan-Carpenter number for (a) rigid and (b) flexible vegetation. The error bars denote the 90% confidence interval in derived C_{Dw} values and the dotted lines denotes the 95% confidence interval of the fit.

will therefore lead to a reduced C_{Dw} value. Furthermore, the wave conditions and canopy density differed between this study and *Jadhav et al.* (2013). With respect to flexible vegetation, the fit is compared with *Sánchez-González et al.* (2011) who studied wave damping over polyethylene blades ($h_v = 100$ mm, $b_v = 3$ mm, $n_v = 2.7 \times 10^5$ stems/m^2, $EI_v = 4.0 \times 10^{-7}$ Nm^2. Figure 4.7 shows that the visual agreement between the obtained fits for flexible vegetation is very good despite an increased curvature in our fit.

Table 4.3: List of fitted coefficients in Eq. 4.6 in literature.

Publication	**Vegetation**	$\boldsymbol{a}$	$\boldsymbol{b}$	$\boldsymbol{c}$	$\boldsymbol{KC}$	$\boldsymbol{EI_v}$ [Nm^2]
This study	Bamboo dowels	81	0.36	0	53-133	9.0×10^{-2}
Jadhav et al. (2013)	*S. Alterniflora*	139.8	0.86	0	25-135	1.5×10^{-2}
Ozeren et al. (2014)	Birch dowels	7.995	1.22	1.28	5-95	Stiff
This study	Silicon rods	43	5.3	0.26	53-133	1.7×10^{-5}
Sánchez-González et al. (2011)	Polyethylene blades	30.1	1.08	0	15-425	4.0×10^{-7}

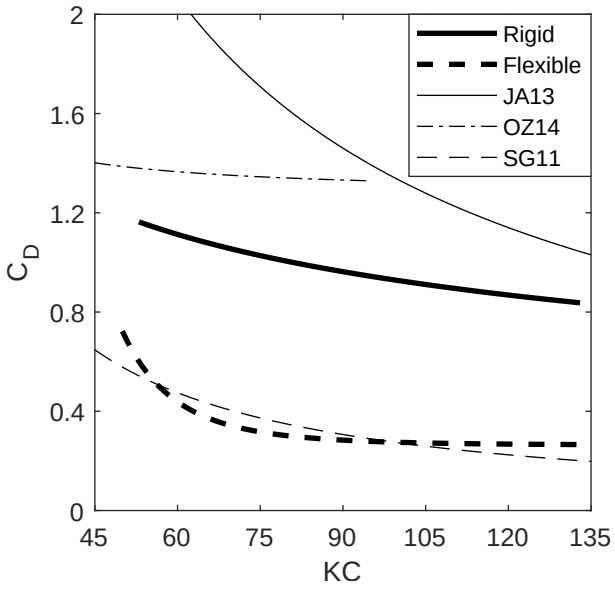

Figure 4.7: Comparison of the drag coefficient relations for rigid and flexible vegetation with relations in *Jadhav et al.* (2013) (JA13), *Ozeren et al.* (2014) (OZ14), and *Sánchez-González et al.* (2011) (SG11).

4.4.2 Sensitivity of the drag coefficient to hydrodynamic parameters

To further investigate the contribution of hydrodynamic conditions to the drag coefficient, we have plotted our results against five dimensionless hydrodynamic predictors (Fig. 4.8): the relative wave height H_r, the submergence ratio α, wave steepness λ, Froude number F_r and vegetation Reynolds number Re. First, the relative wave height and submergence ratio address the contribution of scaled wave height and water depth. Then, wave steepness $\lambda = H/L_{wave}$, with L_wave as the wavelength, highlights the impact of the wave shape. Furthermore, $F_r = u_c T/L_{wave}$ is the ratio between horizontal water particle velocity with respect to wave celerity at shallow water conditions. Finally, the Reynolds number is a frequently used predictor for the drag coefficient (*Augustin et al.*, 2009; *Koftis et al.*, 2013; *Anderson and Smith*, 2014; *Hu et al.*, 2014; *Möller et al.*, 2014). All conditions have been fitted using a function equivalent to Eq. 4.6 to allow comparison with the KC number.

The results for rigid vegetation show a good fit for a relationship between C_{Dw} and Re. The r^2-coefficient for this relationship is decent at 0.36, but lower than the goodness-of-fit between C_{Dw} and KC in our experiments. Conversely, $r^2 < 0.20$ for all four other predictors. Re and KC both define their hydrodynamic length scale in terms of vegetation diameter b_v, while relative wave height, submergence ratio, wave steepness and Froude number are functions of hydrodynamic parameters only. This indicates that the diameter of rigid vegetation is an important predictor for wave-vegetation interactions.

The fitted C_{Dw} for flexible vegetation correlates equally well with Re, H_r, and F_r as with the KC number. The common ground among these predictors is that higher H or u_c correlates with lower drag coefficients. Also, H_r and F_r are not a function of a vegetation property such as b_v or h_v. Yet, the drag coefficient correlates equally well to H_r and F_r as it does to KC and Re which are a function of b_v, and they perform better than α as an indicator for C_{Dw}. This indicates that an indicator for C_{Dw} of flexible vegetation does not require a vegetation parameter, unlike rigid vegetation for which the drag coefficient only correlates well to KC and Re. The suggests that the wave dynamics over flexible vegetation are predominantly controlled by the hydrodynamic conditions.

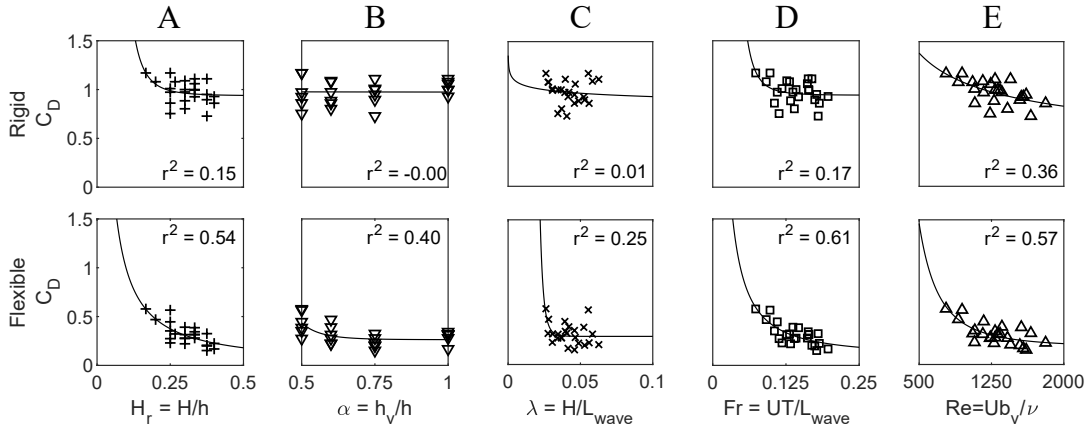

Figure 4.8: Sensitivity of the drag coefficient C_{Dw} to five predictors, from left to right: (a) Relative wave height H_r, (b) submergence ratio α, (c) wave steepness λ, (d) Froude number F_r, and (e) Reynolds number Re.

4.4.3 Water Particle Velocities

The velocity field is presented in the normalized coordinate system (x^*,z^*). The normalized horizontal axis $x^* = x/L_v$ is defined such that $x^* = 0$ represents the upstream edge and $x^* = 1$ the downstream edge of the meadow. Likewise, the normalized vertical axis $z^* = (z+h)/h_v$ is defined such that $z^* = 0$ corresponds to the flume bottom and $z^* = 1$ to the canopy of the vegetation. The PIV-window ranges from $x^* = 0.75$ to $x^* = 1.2$ for $h = 0.50$ and 0.60 m, and from $x^* = 0.8$ to $x^* = 1.15$ for $h = 0.30$ and 0.40 m.

Analysis on the velocity magnitudes focuses on the horizontal particle velocities, because they are key to the drag force (Eq. 4.3), exceed the magnitude of vertical particle velocities (Fig. 4.5), and control the magnitude of the orbital motion (e.g. *Pujol et al.*, 2013). Alternatively, both horizontal and vertical velocities are used for the analysis of the flow patterns. We define $U^*(x^*, z^*) = u_{amp}/u_0$ as the normalized amplitude of the horizontal velocity. $u_0(x^*, z^*)$ is the velocity profile based on linear wave theory using the three primary water surface harmonics at WG2, which is consistent with the derivation of u_{amp} (Section 4.3.5). It has been derived independently from the PIV-measurements and is corrected for wave attenuation. We refer to Appendix B for a detailed description. It should be noted that U^* closely resembles the attenuation parameter α_w in *Lowe et al.* (2005), but includes higher-order harmonics and the impact of wave attenuation.

Fig. 4.9 displays the full normalized velocity field U^* for case R13 with rigid, flexible and no vegetation. The blank areas correspond to vegetation. The horizontal particle velocities are amplified above the rigid vegetation canopy and reduced inside (Fig. 4.9a). The reduction is the strongest directly below the

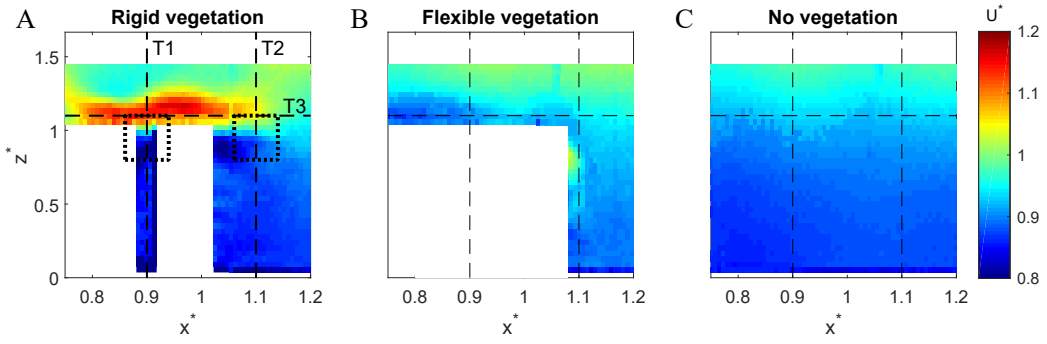

Figure 4.9: Normalized horizontal particle velocity fields around (a) rigid vegetation, (b) flexible vegetation, and (c) no vegetation. All runs are conducted under conditions R13. The blank areas correspond to vegetation including plant swaying. Transects T1 ($x^* = 0.9$), T2 ($x^* = 1.1$) and T3 ($z^* = 1.05$) are used in further figures. The dotted boxes denote the close-ups, which are associated with T1 and T2 respectively.

canopy. Alternatively, the velocity field around flexible vegetation does not differ from the velocity field without vegetation (Fig. 4.9b-c). The gradient in the velocity field without vegetation indicates that u_0 slightly overpredicts bottom velocities ($U^* \approx 0.9$ at the bottom). Therefore, the no vegetation cases were used as a complementary reference, in addition to U^*, to identify vegetation-induced alterations in the orbital velocities.

The velocity fields are averaged over tests with identical submergence ratios to generalize results. They are compared along transects T1 ($x^* = 0.9$), T2 ($x^* = 1.1$) and T3 ($z^* = 1.05$), which are strategically located inside, upstream of, and over the vegetation. As swaying of flexible vegetation prevented measurements inside the canopy, T1 is evaluated for rigid and no vegetation only. The averaging over runs with identical submergence ratios was done, because it was found that the wave dynamics were more sensitive to the submergence ratio than to the wave height and wave period. The grouping of data also allows for the definition of uncertainty in the form of observation intervals. The accuracy of these intervals increases when more runs are combined. As will be shown, the observation intervals are relatively narrow which justifies the averaging of runs with identical submergence ratio.

Transect T1 highlights the impact of submerged rigid vegetation ($\alpha < 1$) on the vertical velocity structure with amplification of orbital velocities above the canopy and attenuation within (Fig. 4.10a). A layer with increased velocity develops directly above the canopy with its peak where $z^* \in [1.0, 1.2]$ and diminishes further above the vegetation. Conversely, the velocity amplitude is

reduced inside the vegetation patch. This reduction is the strongest in the layer directly below the canopy where $z^* \in [0.8, 1.0]$ and decreases near the bottom. However, an exception is the deeply submerged case $\alpha = 0.50$ for which velocities are diminished strongly over the full vegetation column. The impact of emergent rigid vegetation is smaller than that of submerged vegetation. For the submerged case, the normalized velocity amplitude displays a gradient over the vegetation column, with higher velocities near the top of the canopy and lower velocities near the bottom. This may be related to wave crests that still elevate above the canopy for given conditions.

The plant submergence ratio α appears to be a key parameter in quantifying the velocity structure because it controls whether an amplified layer develops and the magnitude of the velocities therein. The velocity amplification increases with the submergence ratio. Maximum amplification is observed at $\alpha = 0.75$ with $U^* = 1.25$. Furthermore, the standard deviation of the normalised horizontal velocity structure is low (σ = 0.02-0.08) at any given water depth despite variations in wave period and height. This supports the notion of α as a key parameter.

Finally, normalized velocity vectors around the canopy show the velocity gradient between the amplified and the attenuated water layers (Fig. 4.10b). The velocities are amplified above the vegetation under a wave crest and attenuated below the canopy during the wave trough. The velocities above the canopy at wave trough are as expected from linear wave theory. The stronger amplification of case R23 under wave crests agrees with the positive correlation of submergence ratio on amplification.

Alternatively, the impact of vegetation at cross-section T2 is small for both rigid and flexible vegetation (Fig. 4.11). This location was selected as it is just outside the range of vegetation swaying such that flexible vegetation can be included in the analysis. It turns out that the normalized orbital velocity structure is constant over the water depth for all cases. At the same time, U^* for both rigid and flexible vegetation is close to the respective reference case without vegetation for all water depths. The only exception is the amplification by rigid vegetation at $\alpha = 0.75$, when $U^* = 1.12$ at $z^* = 1.05$, but this is much smaller than at transect T1 and coincides with the highest variability in the observations.

Rigid vegetation appears to be key for the development of a water layer with amplified orbital velocities directly above the canopy. Figure 4.12 shows U^* at $z^* = 1.05$ as a function of x^*. This elevation matches the peak net velocities in Fig. 4.10. The data gaps coincide with the position of WG3. The cases with flexible vegetation and without vegetation all display a constant normalized velocity amplitude of U^* = 0.90-0.93. Conversely, all three cases with submerged rigid vegetation feature an amplified layer with $U^* \approx 1.05$ for $\alpha = 0.50$, $U^* \approx 1.13$ for $\alpha = 0.60$ and $U^* \approx 1.23$ for $\alpha = 0.75$. Furthermore, the amplification is relatively

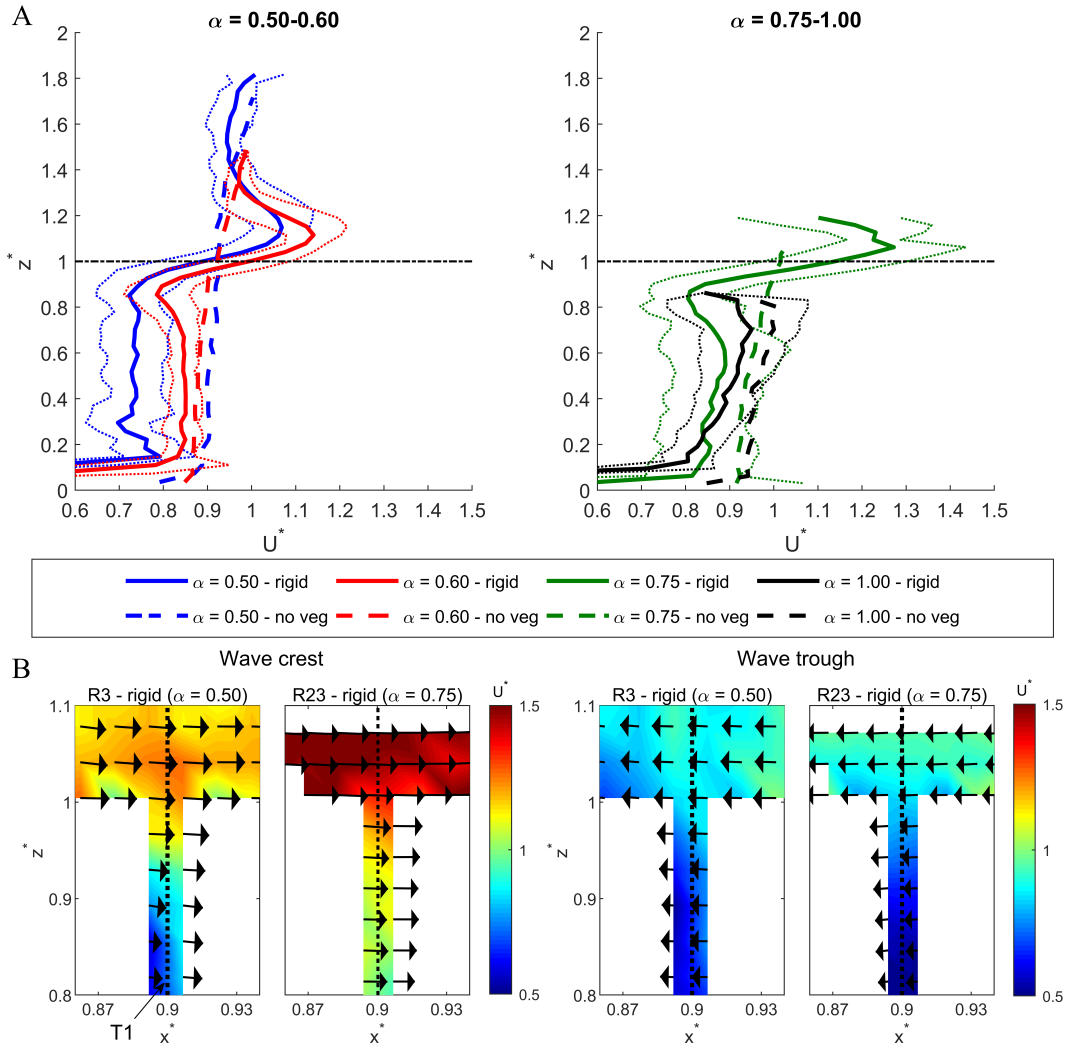

Figure 4.10: The normalized horizontal particle velocity structure at transect T1, showing (a) the vertical profile of the normalised horizontal velocity magnitude at low (left) and high (right) submergence ratio, where data points are averaged over all tests with identical submergence ratio. The dotted lines denote the mean ± two standard deviations of the observations (σ). The dash-dotted line is the canopy height. (b) A close-up of the normalised velocity field around the vegetation canopy. The black vectors denote the magnitude and direction of the particle velocities. The velocities are averaged over all wave crests/troughs in a single test run. The vector density is reduced in the horizontal direction by a factor of 2 for visibility. The blank areas coincide with vegetation. Finally, the dotted line represents the transect position.

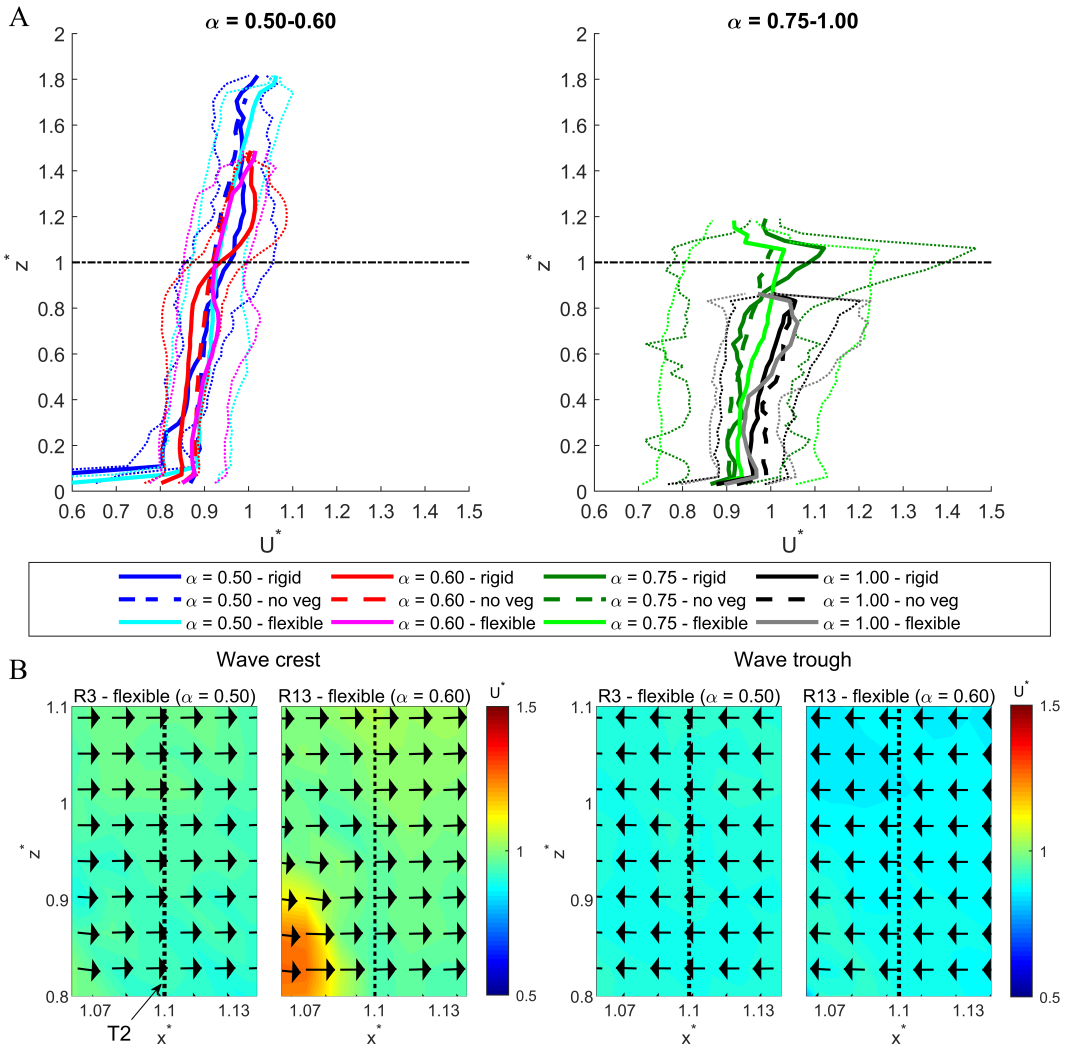

Figure 4.11: The normalized horizontal particle velocity structure at transect T2. See Fig. 4.10 for full description.

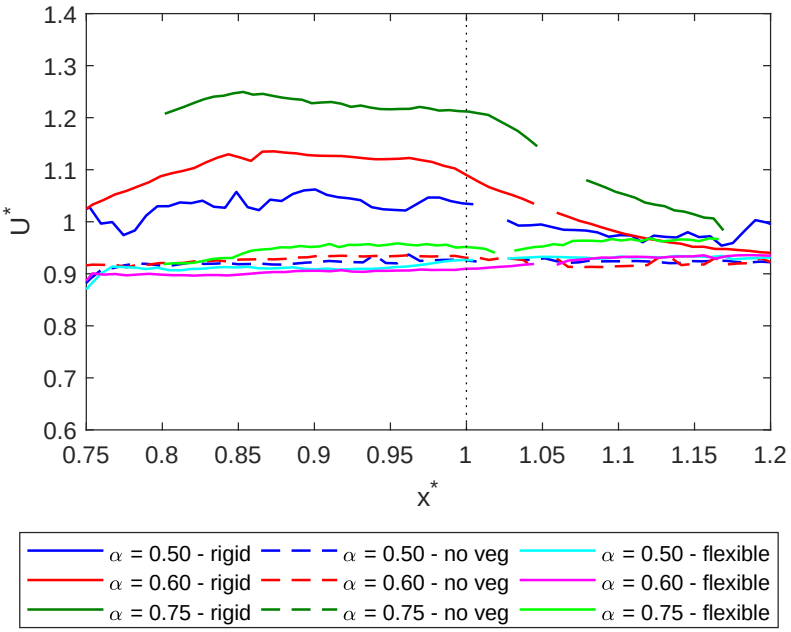

Figure 4.12: The normalized horizontal particle velocity U^* as function of along-patch coordinate $x^* = x/L_v$ at transect T3 ($z^* = 1.05$). Results are averaged over all runs with equal submergence ratio and vegetation type. The dotted line represents the downstream edge of the vegetation. The data gaps coincide with interference from WG3.

constant over the vegetation within the PIV-window, which suggests that the velocity field is unaffected by the gap at $x^* = 0.9$. The velocity amplification reduces linearly downstream of the vegetation and returns to its normal level at $x^* = 1.15$.

Furthermore, we find that rigid vegetation can induce two types of flow circulation depending on the submergence ratio. A net downstream current develops around $z^* = 1$ for both submerged and emergent vegetation at transect T1 (Fig. 4.13a). This is compensated by an upstream current high above the canopy for deeply submerged vegetation ($\alpha \leq 0.60$) or within the vegetation for emergent and near-emergent vegetation ($\alpha \geq 0.75$). The former results in a counter-clockwise circulation above the vegetation, and the latter results in a clockwise circulation through the vegetation.

The net currents at transect T2 support the presence of flow rotations over and through the vegetation. The circulations identified over and through rigid vegetation can still be identified, but with reduced net downstream velocities of

up to 0.015 m/s instead of 0.040 m/s (Fig. 4.13b). The decrease in net horizontal velocities at transect T2 for rigid vegetation comes with an increase of net vertical velocities consistent with the rotational motion (Fig. 4.13c). A net upward velocity develops for deeper submerged rigid vegetation cases, which is associated with a counter-clockwise motion. Alternatively, net downward currents develop below the canopy for the near-emergent case, which is consistent with clockwise rotation through the vegetation. The circulation for emergent rigid vegetation can no longer be identified, which may indicate that the rotation develops on a shorter scale.

Interestingly, a 0.01 m/s net downstream stream current is also identified for flexible vegetation at α=0.60, but not at other submergence ratios (Fig. 4.13d). The corresponding upstream currents are equally distributed over and through the vegetation. It is unclear whether this is a local circulation induced by the edge of the swaying motion or a larger circulation around the vegetation patch. The wave-averaged current is not identified for deeper submergence and the net vertical velocities (Fig. 4.13e) do not provide further support. Currents at other submergence ratios do not exceed 0.005 m/s.

4.5 Discussion

4.5.1 Impact of plant flexibility on wave attenuation

Stem flexural rigidity appears to be a key parameter for determining the drag coefficient for wave attenuation. Our results show that the drag coefficient of flexible vegetation is up to 70% lower than rigid vegetation under identical hydrodynamic conditions (Fig. 4.7). This decrease is of the same order as has been estimated previously. *Mullarney and Henderson* (2010) and *Maza et al.* (2013) studied the impact of plant swaying on drag force using numerical models. They found 70% and 50% reductions in drag coefficients respectively. Alternatively, *Riffe et al.* (2011) find a 50% reduction in drag force for flexible vegetation in a field study. The magnitudes of the reductions in wave damping by flexible vegetation are in the same order of magnitude despite differences in plant morphology (cylindrical versus blades), wave conditions, and flexural rigidity of the flexible vegetation.

The reduced wave damping capacity of flexible vegetation has been attributed to vegetation swaying. The physical explanation is two-fold. First, swaying of the vegetation reduces the frontal area of the vegetation. This reduces the total work that can be exercised by the drag force and, consequently, directly reduces the energy lost in a wave travelling over vegetation (*Dalrymple et al.*, 1984). Secondly, the relative velocity between water and vegetation reduces when vegetation sways

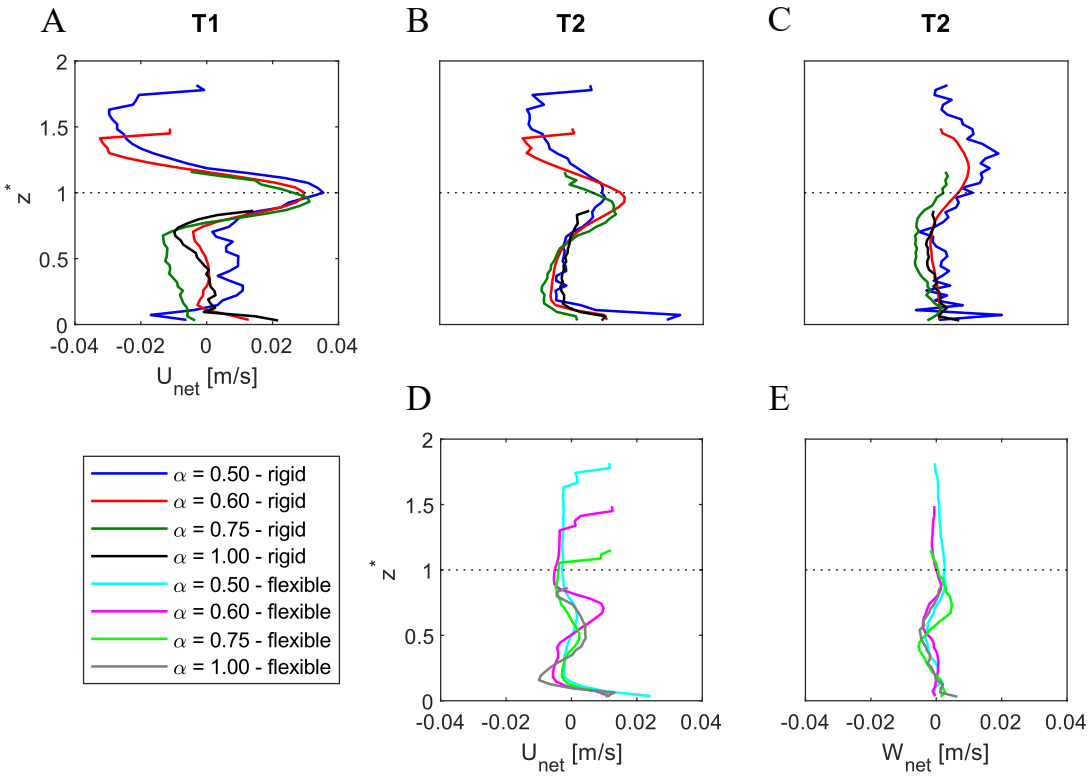

Figure 4.13: Vertical profile of wave-averaged net velocities: (a) net horizontal velocities at T1; (b) & (d) net horizontal velocities at T2; (c) & (e) net vertical velocities at T2. The top row features rigid vegetation and the bottom row flexible vegetation.

with the flow (*Méndez et al.*, 1999). These effects are not accounted for in Eq. 4.5 and will thus lead to a lower calibrated drag coefficient.

The negative impact of plant swaying on wave attenuation is supported by our experimental results and literature. First, we found that the drag coefficient for flexible vegetation correlated equally well to predictors that related to wave conditions only, whereas the drag coefficient for rigid vegetation only related well to predictors that did include stem diameter (Fig. 4.8). This indicates that flexible vegetation follows flow and rigid vegetation controls flow. Furthermore, *Möller et al.* (2014) found low drag coefficients for plants with low flexural rigidities, which were observed to sway significantly (*Rupprecht et al.*, 2017). In a separate study on a limited number of plant mimics, *Paul et al.* (2016) also identified the reduction in stem frontal area via stem bending as a key parameter in the prediction of the drag coefficient.

4.5.2 Wave-induced circulation

Wave-averaged velocity fields from our experiment show that the mean currents drive a circulation over or through rigid vegetation, depending on the submergence ratio (Fig. 4.14). Like prior studies (*Pujol et al.*, 2013; *Abdolahpour et al.*, 2017), we find a mean current in the direction of wave propagation directly above the canopy. This net downstream current has been associated with boundary layer streaming, which follows from the shear stresses at the top of the vegetation (*Luhar et al.*, 2010; *Pujol et al.*, 2013; *Van Rooijen et al.*, 2020). As the flume is a closed system, a mean current in the direction of wave propagation must be compensated for by a return flow. Under sufficiently submerged conditions ($\alpha \leq 0.60$), the return flow occurs in the region between the top of the vegetation canopy and free surface. However, as a vegetation-free region is not available under shallow conditions ($\alpha \geq 0.75$), the return flow passes through vegetation itself. This results in an anti-clockwise circulation, when current returns above the canopy (Fig. 4.14, top row) or a clockwise circulation through the vegetation, when the current returns inside the canopy (Fig. 4.14, middle row).

Our velocity fields extend the framework for velocity structures as proposed by *Pujol et al.* (2013). We compare results for submerged ($\alpha = 0.50$, Fig. 4.14: top row) and emergent ($\alpha = 1.0$, Fig. 4.14: middle row) rigid vegetation and submerged flexible vegetation ($\alpha = 0.50$, Fig. 4.14: bottom row). The circulations over and through rigid vegetation in our study fit their vertical velocity structure inside the meadow. Both studies show a mean current in the direction of wave propagation through the canopy and a return flow that depends on submergence ratio. Results also agree that flexible vegetation does not impact the flow field.

The circulation through a flexible meadow, as described by *Luhar et al.* (2010), could not be reproduced. The submergence ratio $\alpha = 0.50$, which was used in

Luhar et al. (2010), did not lead to the generation of mean currents (Fig. 4.14, bottom row). We find a weak mean current in the direction of wave propagation when $\alpha = 0.60$, but its magnitude and position do not agree with *Luhar et al.* (2010). Forcing with a smaller wave amplitude, they find net velocities up to 0.073 m/s, which even exceed net current velocities induced by rigid vegetation in our study by a factor of two. Furthermore, the position of the peak velocity is located at $z^* = 0.35$ in *Luhar et al.* (2010) compared to $z^* = 0.70$ in our study. Disagreements may be related to the difference in the geometry of vegetation used in the two studies. *Luhar et al.* (2010) used blades instead of stems where six blades were attached to a single point in the flume bottom. Therefore, the stem spacing can be lower near the bottom than in the canopy, which may promote the convergence of currents in this area. Also, the higher frontal area for blades (up to $\lambda = 4.2$) as opposed to cylinders ($\lambda = 1.7$) may have contributed to the different observations (*Abdolahpour et al.*, 2017).

Differences between rigid and flexible vegetation are consistent with *Abdolahpour et al.* (2017). They developed an empirical relation for the magnitude of wave-driven currents as a function of the vertical particle excursion, plant dimensions and drag coefficient. Specifically, the drag coefficient correlates positively to the magnitude of the wave-driven currents. Our results show that rigid vegetation has a higher drag coefficient than flexible vegetation and will, therefore, develop significant net currents at lower vegetation densities and wave heights.

The presence of flow circulations around vegetation implies that the wave-current field is not uniform and irrotational. The vegetation patch acts, from a hydrodynamic perspective, as a source of vorticity. This may affect wave shape and, thereby, Equations 4.1-4.5 which assume a sinusoidal wave shape (*Dalrymple et al.*, 1984). A detailed analysis of the wave shape and its implications is beyond the scope of this study, but it may have affected the drag coefficient, which acts as a calibration parameter.

4.5.3 Orbital velocity structure

The wave orbital velocity structure under rigid vegetation is characterized by a layer of amplified orbital velocity directly above the canopy and a layer of reduced orbital velocity directly below it (Fig. 4.10). Orbital velocities far above or far below the canopy appear to be unaffected. Conversely, flexible vegetation appears not to impact the velocity structure. Therefore, this section will focus on rigid vegetation only.

Our findings agree with *Koftis et al.* (2013), who found that for a set of point measurements, maximum orbital velocities were attained directly above the water column. However, others found that the velocities within the meadow were

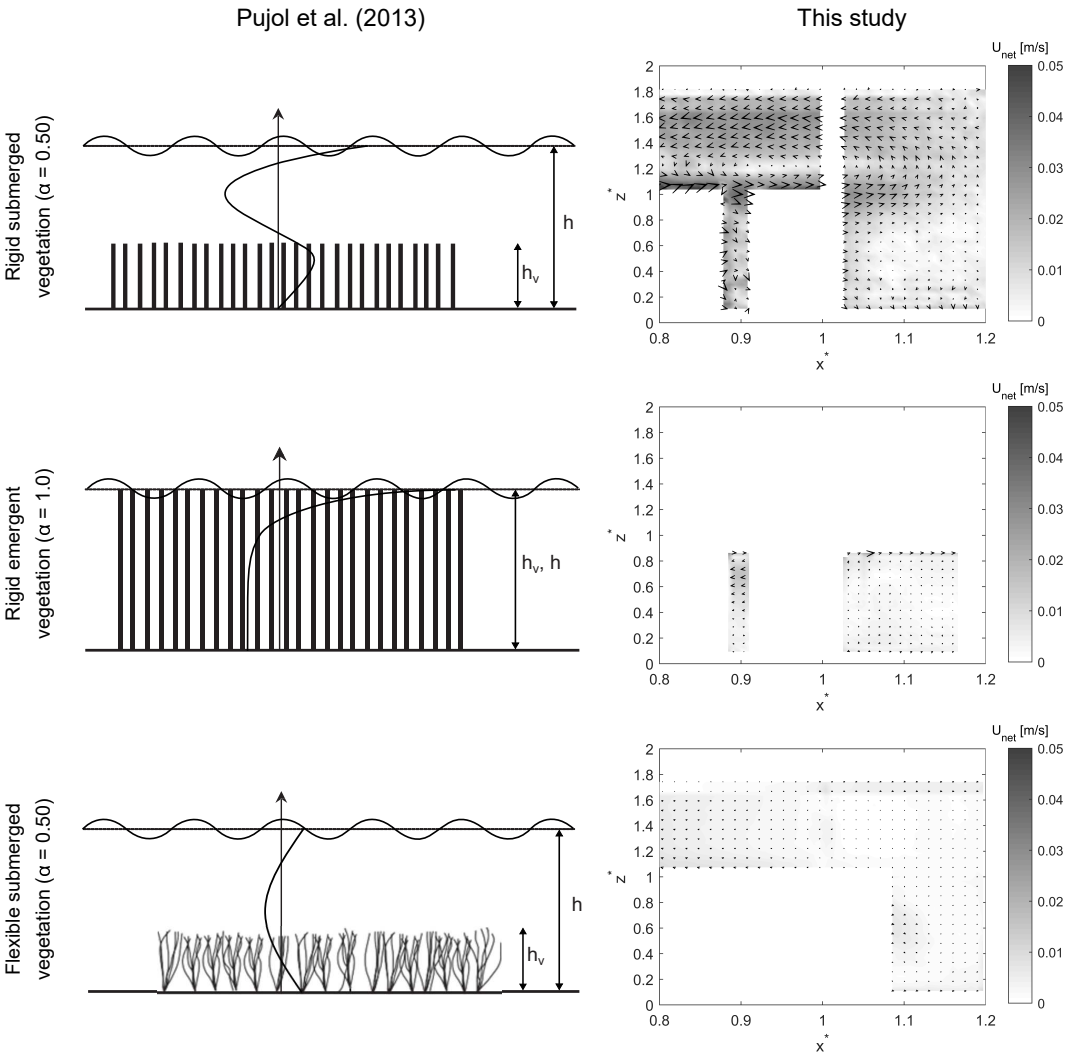

Figure 4.14: Comparison of the wave-averaged mean velocity fields as proposed in *Pujol et al.* (2013, left column) and found in this study (right column) under equal submergence ratios: submerged rigid vegetation ($\alpha = 0.50$, top row), emergent rigid vegetation ($\alpha = 1.0$, middle row) and submerged flexible vegetation ($\alpha = 0.50$, bottom row). The gap in the top row coincides with WG3. Further blank areas correspond to vegetation, including swaying for (c).

uniformly attenuated and did not observe an amplified layer above the vegetation (*Lowe et al.*, 2005; *Luhar et al.*, 2010; *Pujol et al.*, 2013).

The lack of strong attenuation of orbital velocity inside the vegetation patch appears to be related to the layout of the vegetation canopy. *Lowe et al.* (2005) showed that velocity attenuation is a function of the ratio of wave excursion to stem spacing ($u_c/\omega S_v$) and the ratio of stem spacing to stem diameter (S_v/b_v). In this study, $u_c/\omega S_v = O(10^{-2})$ and $S_v/b_v = 6$ relate to inertia dominated flow with large stem spacing. Both contribute to low velocity attenuation within the canopy. For example, *Lowe et al.* (2005) show that attenuation is absent for inertia dominated flow with $S_v/b_v = 7.8$.

We propose that water layers with the amplified/ diminished velocities above and below the canopy, which were observed in detail for the first time in this study, follow from an unsteady wave-induced net current (Section 4.5.2). This is shown by analysing horizontal particle velocity differences between run R13 with rigid vegetation and without vegetation for five wave cycles (Fig. 4.15). The net current that results from the wave-vegetation interaction can be clearly identified by the red colour around the canopy (black dashed line). This current flows above and below the canopy over a wave cycle. Specifically, the current acts above the canopy when a wave crest passes and below when a trough passes. Thus, it appears at a constant relative depth such that the mean depth is at the vegetation canopy.

As the mean current is in the direction of wave propagation, it is aligned with the horizontal orbital velocities at wave crests, leading to velocity amplification directly above the canopy. Equally, it opposes the horizontal orbital velocities during wave troughs, leading to attenuation directly below the canopy. Both effects are confirmed by temporal analysis of selected points in Fig. 4.15b-c. Other velocity differences can be attributed to slight differences in wave shape as a result of rigid vegetation.

4.5.4 Length of the vegetation field

The length of the vegetation field used in this study is 1.5 m. Although longer canopies may provide additional data to confirm observed trends, we believe that the length of the experimental canopy is sufficient for the wave dynamics to adjust to the presence of vegetation. The adjustment length is controlled by the canopy drag length (*Coceal and Belcher*, 2004; *Lowe et al.*, 2005), according to

$$L_D = \frac{2h_v\,(1-\lambda_p)}{C_{SD}\lambda_f} \tag{4.9}$$

where $\lambda_p = \pi b_v^2 h_v n_v/4$ is the vegetated area per unit ground area and C_{SD} is the sectional drag coefficient. C_{SD} differs from C_{Dw} as it relates to the in-canopy

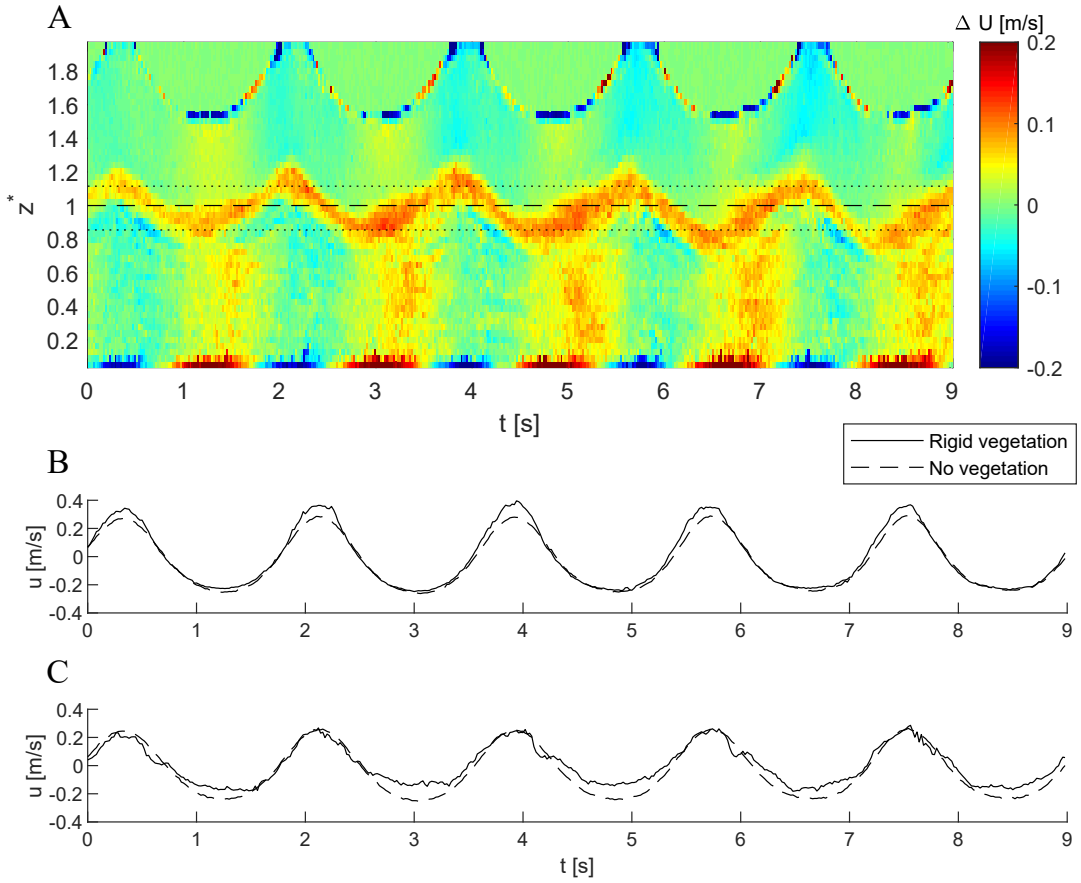

Figure 4.15: Difference in horizontal particle velocities between rigid vegetation and no vegetation under equal wave conditions (R13). Results are presented over five wave cycles ($T = 1.8$ s). Top plot (a) displays the temporal variation along transect T1. Herein, the dashed line depicts the canopy, the top dotted line corresponds to the location of plot (b) and the bottom dotted line to plot (c). Middle plot (b) shows observed horizontal particle velocities at $z^* = 1.1$ with rigid vegetation and without vegetation. Likewise, bottom plot (c) presents observed horizontal particle velocities at $z^* = 0.85$.

flow velocity rather than the ambient flow velocity and does not include plant swaying through calibration (*Lowe et al.*, 2005). An estimate of C_{SD} is made by correcting the fitted drag coefficient of rigid vegetation (Eq. 4.7) for in-canopy velocity attenuation. The observed attenuation is approximately 20% (Fig. 4.10a) and C_{Dw} is proportional to U^{-3} when derived through wave height measurements (Eq. 4.1, 4.3, 4.5). Therefore, we estimate

$$C_{SD} = \left(\frac{520}{KC}\right)^{0.36}. \tag{4.10}$$

At $KC = 133$ which is the conservative limit of our range, $C_{SD} = 1.63$. Furthermore, $\lambda_f = 1.67$ and $\lambda_p = 0.022$. We find that $L_D \approx 0.22$ m and $L_v/L_D = 6.9$ with the in-canopy velocity measurements at $6.2L_D$. *Lowe et al.* (2005) find that the adjustment length is $3L_D$-$5L_D$ which is satisfied by our experimental conditions. Our experimental results along horizontal transects T3 (Fig. 12) also suggest the velocity structure has adjusted to the presence of vegetation as the velocity amplitude remains constant over the back section of the vegetation which has been the focus of our measurements. Finally, we note that the observed wave damping over the vegetation field is significant as it ranges between 2% and 25% depending on vegetation and wave conditions.

4.5.5 Implications for nature-based coastal defences

Most natural salt marsh vegetation exhibits a mix of rigid shrubs and flexible grasses. These mixed marshes are not only beneficial for biodiversity but combined rigid and flexible vegetation is complementary to coastal protection. While both attenuate wave energy, the damping capacity of rigid vegetation exceeds that of flexible vegetation. Foreshores with rigid vegetation can be up to 70% thinner than foreshores with flexible vegetation to provide the same level of protection. It is expected that the level of protection that semi-flexible vegetation provides will be between the limits of rigid and flexible vegetation. Furthermore, the wave-induced currents in rigid vegetation patches can promote sediment transport to the higher marshes, potentially increasing marsh accretion. This may enable marshes to increase elevation to combat the potential impacts of sea level rise and can act as a buffer against extreme events. Alternatively, swaying of flexible plants can prevent stem breaking (*Rupprecht et al.*, 2017; *Vuik et al.*, 2018b). Therefore, flexible species can be expected to remain effective during higher wave energy conditions.

However, the differences in plant flexibility have to be considered when modelling the impact of mixed vegetation salt marshes on hydrodynamics and wave height. Much research effort has been invested in finding single relations to predict a drag coefficient for salt marshes (e.g. *Möller et al.*, 2014; *Losada et al.*,

2016). While these have led to useful relationships and have proven the capacity to model wave attenuation, the relations may only be applicable for a specific set of species, or rather a specific combination of plant flexibilities used in such experiment.

In contrast, this study has identified the different wave-vegetation interactions at the rigid and flexible limits and provides drag coefficients associated with these limits. Although the mimics have been based on the South Wales salt marshes, the results show wave attenuation to be a function of plant flexibility. The range of flexural rigidities in South Wales is wide and also covers, for instance, the species in US salt marshes (*Feagin et al.*, 2011; *Chatagnier*, 2012). Therefore, our results have a wider application.

4.6 Conclusions

A laboratory study under controlled conditions using artificial rigid and flexible vegetation has provided us with the opportunity to study the impact of plant flexibility on the drag coefficient and the velocity structure. For the first time, we test mimics that differ in flexural rigidity only under conditions that have been directly derived from the field. We have selected rigid and flexible vegetation mimics that represent a wide range of plant flexibilities found in typical South Wales salt marshes. Drag coefficients were derived from measured wave attenuation and, as a further novelty, we have measured the velocity field in and around the vegetation using PIV.

Our results show that both rigid and flexible vegetation damp waves, but rigid vegetation provides superior damping. This is expressed via a drag coefficient; i.e. a higher drag coefficient means stronger damping. We find that the drag coefficient for flexible vegetation is up to 70% lower than for rigid vegetation. Plant swaying of flexible vegetation reduces the plant frontal area and the relative velocity difference between plants and water. Both have a negative effect on the drag forces and associated energy losses. As a result, swaying flexible plants will damp waves less than rigid plants that do not sway.

Furthermore, we find that rigid vegetation alters the velocity structure, while flexible vegetation does not. Specifically, the interaction between waves and rigid vegetation induces a current in the direction of wave propagation through the top of the vegetation. This current propagates above and below the canopy in phase with the water surface. For submerged vegetation, this results in amplified horizontal particle velocities above the vegetation canopy and reduced velocities within the vegetation. The magnitude of the current and the amplification depends on the submergence ratio. A stronger current and amplification develop for higher submergence ratios. Finally, a return current develops high in the water

column when the vegetation is sufficiently submerged or, otherwise, through the meadow.

Based on these outcomes, it can be concluded that different salt marshes may provide different levels of protection against wave action, depending on the flexibility of established species. A single drag coefficient for salt marshes may not exist. Plant flexibility appears to be a key control parameter when defining a drag coefficient for a given salt marsh. This study has set out the limits and impacts of the latter, but additional research is required to further quantify the impact of plant flexibility and associated swaying to predict drag coefficients for a wide range of habitats.

Chapter 5

Modelling wave attenuation by flexible coastal vegetation

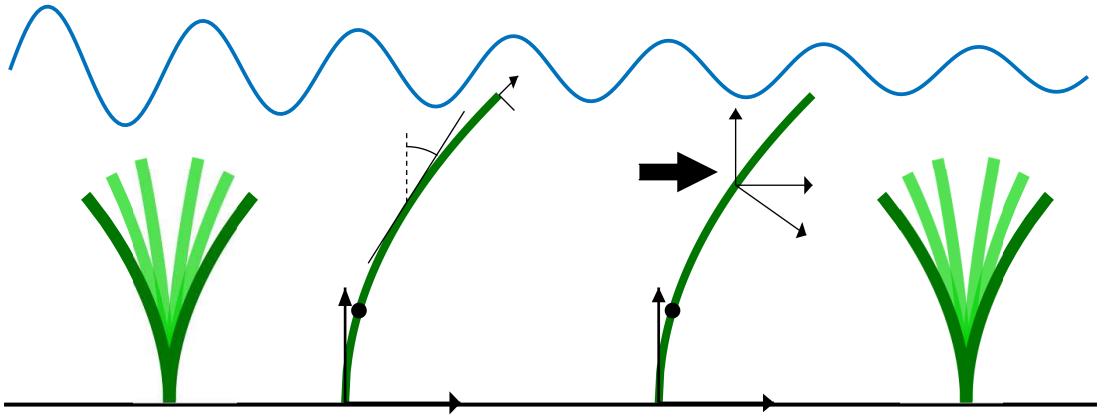

5.1 Introduction

Stem motion of flexible vegetation can impact wave damping significantly as has been demonstrated in experimental (Chapter 4 and *Riffe et al.*, 2011; *Paul et al.*, 2016; *Luhar et al.*, 2017) and computational studies (*Luhar and Nepf*, 2016; *Mullarney and Henderson*, 2010). Vegetation species are broadly classified as rigid or flexible. Rigid vegetation, like woody shrubs, does not move over a wave cycle, whereas flexible vegetation, like thin grass, sways as its rigidity is insufficient to resist stem bending. The excursion of flexible species increases when its flexural rigidity decreases or wave forces increase (*Luhar et al.*, 2017). As stem bending increases, the plant frontal area and the relative velocity between water and stem decrease (*Méndez et al.*, 1999; *Paul et al.*, 2016). Both limit the wave forces on the plant and may reduce wave damping by up to 50-70% based on our experimental results and literature (*Mullarney and Henderson*, 2010; *Riffe et al.*, 2011; *Luhar et al.*, 2017). However, as the interaction between plant motion and wave forces is reciprocal, quantifying wave damping for species with arbitrary flexibility poses a challenge. Computational models can be a valuable tool to quantify wave damping for variable vegetation properties. For rigid vegetation, *Dalrymple et al.* (1984) simplified vegetation fields to arrays of rigid cylinders on a flat bottom and assumed validity of linear wave theory to model damping of monochromatic waves. Under these assumptions, they demonstrated that wave damping is dominated by drag, and wave heights reduce proportionally to the distance travelled over vegetation. Using the same modelling framework, *Mendez and Losada* (2004) proposed to calibrate the drag coefficient to include the effect of stem motion. Their model was successfully applied in our laboratory investigations, other flume studies(*Augustin et al.*, 2009; *Koftis et al.*, 2013; *Anderson and Smith*, 2014; *Möller et al.*, 2014; *Losada et al.*, 2016) and field observations (*Bradley and Houser*, 2009; *Jadhav et al.*, 2013; *Garzon et al.*, 2019a), but the calibrated drag coefficients vary widely between plant species and test conditions (see Section 2.4.3 for an overview). Thus, site-specific calibration for each coastal habitat is required.

Alternatively, an effective stem length can be employed to include the effect of stem bending in a rigid vegetation model. The effective stem length is the height of a rigid stem that generates equal drag as that of the (longer) flexible stem (*Luhar and Nepf*, 2011). *Paul et al.* (2016) proposed using the observed frontal area as the effective vegetation length, based on experiments with lexaan strips. Instead, *Luhar et al.* (2017) fitted an analytical model for the effective length of flexible seagrass based on a scaling analysis of the equations of stem motion but suggested that different fits for different species are required. Their model was expanded to a predictive model for wave damping by *Lei and Nepf* (2019), who

further discriminated between rigid and flexible stem sections and introduced a new fit for the effective stem length.

Other models have included vegetation motion explicitly by modelling stems as flexible rods. *Méndez et al.* (1999) solved the excursion of the tip using stem-averaged velocities and a linearised drag force in an idealised model. Vertical variations in the velocity profile were included by *Mullarney and Henderson* (2010), and the buoyancy force was included in *Henderson* (2019). However, these models are limited to stems with small deflections. Alternatively, complex computational models included friction, inertia and buoyancy forces to solve stem motion under strong plant bending for individual stems (*Luhar and Nepf*, 2016; *Leclercq and de Langre*, 2018) and vegetation fields (*Maza et al.*, 2013; *Chen and Zou*, 2019). However, the computational cost for these models is high, which makes them unsuitable for large areas.

The various modelling approaches show a trade-off between complexity, accuracy, computational cost and applicability, but the optimal balance for practical cases remains unclear. Simple models can be easily applied, but require site and plant-specific calibration. Alternatively, complex models add processes which can reduce the variation in calibration, but at a computational cost and potentially increasing model errors. Therefore, the accuracy gains by including additional mechanisms must be carefully weighed against the extra computational costs. Furthermore, no complex model has been successfully validated across multiple species of real vegetation that differ in flexibility.

In this chapter, we aim to provide a novel versatile mathematical modelling framework for wave damping by plant species with arbitrary flexibility. A balance between complexity and applicability is obtained by including only the key mechanisms involved in the wave-vegetation interaction. These mechanisms are identified by combining experimental data of wave damping and wave velocity fields, obtained in Chapter 4, with plant motion. Based on the key physics, we develop a new modelling framework with applicability across cylindrical vegetation species and hydrodynamic conditions without the need for plant-specific calibration. The new wave-vegetation model will mark a significant contribution to the coupled current-wave-vegetation model, which will be developed in Chapter 7.

This chapter is structured as follows: Section 5.2 discusses the wave-vegetation interaction. Section 5.3 discusses the experimental data, including plant motion, with the aim of justifying model assumptions. The modelling framework is described in Section 5.4 and validated in Section 5.5. The implications for nature-based coastal defences are discussed in Section 5.6. Finally, conclusions are provided in Section 5.7.

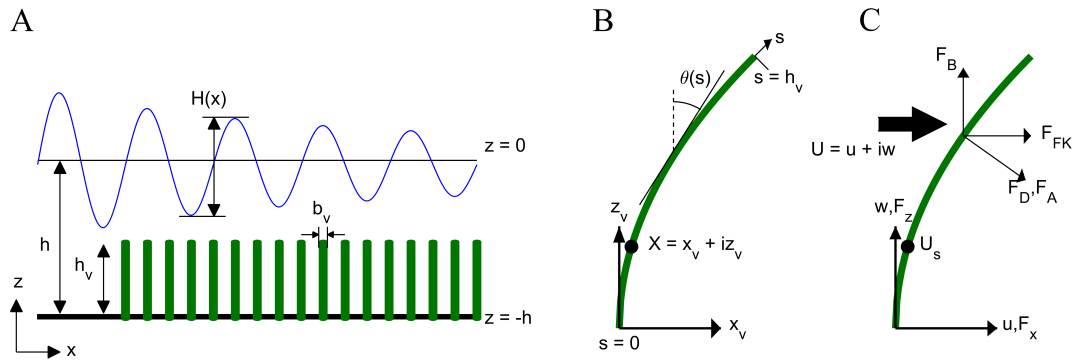

Figure 5.1: Definition sketches of the coordinate system of the wave-vegetation interface at (a) canopy- and (b) plant-scale. (c) shows the velocities and forces at plant-scale.

5.2 Theoretical background

5.2.1 Coordinate system

Let us define a coordinate system at canopy-scale (Fig. 5.1a), where waves travel over a vegetation field on a flat bed. The direction of wave propagation is normal to the canopy and parallel to the x-axis with $x = 0$ at the upstream edge of the vegetation. The z-axis describes vertical position with respect to the water column such that $z = 0$ depicts the still water surface and $z = -h$ the bed level. The waves are modelled by their height $H(x)$, period T and velocity field $U(x, z, t) = u + iw$, where the real and complex parts denote the horizontal and vertical directions respectively.

A single stem in the canopy is modelled as a cylinder with height h_v, diameter b_v, and flexural rigidity EI_v. Plant density n_v defines the number of stems per unit area. We introduce a coordinate system at plant-scale to define stem motion (Fig. 5.1b). Along-stem coordinate s is defined such that $s = 0$ is the root and $s = h_v$ is the tip of the stem. Stem posture $X = x_v + iz_v$ follows the complex coordinate system. The stem moves at velocity $U_{veg} = \partial X/\partial t$ and its bending with respect to an upright stem is defined by bending angle $\theta(s, t)$. Finally, we define wave velocities $U_s(s, t) = u_s + iw_s$ and forces $F(s, t) = F_x + iF_z$ at the stem (Fig. 5.1c).

Dimensionless parameters will be employed for all variables throughout this chapter (denoted by asterisks). We introduce scaled coordinates

$$x_* = \frac{x}{A_w}, \quad z_* = \frac{z}{h_v}, \quad s_* = \frac{s}{h_v}, \quad t_* = t\omega \tag{5.1}$$

and quantities

$$X_* = \frac{X}{h_v}, \quad H_* = \frac{H}{h}, \quad U_* = \frac{U}{u_c}, \quad U_{veg*} = \frac{U_{veg}}{u_c}, \quad F_* = \frac{F}{\rho b_v u_c^2}. \tag{5.2}$$

Herein, $\omega = 2\pi/T$ is the wave angular frequency, u_c is the velocity scale, $A_w = u_c/\omega$ is the typical wave excursion length and $\rho = 1000$ kg/m^3 is the water density. The velocity scale, u_c, is defined as the amplitude of the horizontal wave orbital motion (*Hu et al.*, 2014) according to

$$u_c = \frac{1}{2}(u_f + u_b) \tag{5.3}$$

where u_f is the peak forward velocity, u_b is the peak backward velocity. u_f and u_b may be measured or based on linear wave theory. *Hu et al.* (2014) recommend that the velocity scale is representative of the spatially averaged velocity. Therefore, we consider the velocities halfway the vegetation height.

Furthermore, we introduce two dimensionless quantities that control wave-vegetation interaction for flexible vegetation (*Luhar et al.*, 2017): the Cauchy number

$$Ca = \frac{\rho b_v u_c^2 h_v^3}{EI_v} \tag{5.4}$$

being the ratio between wave forces and stem stiffness, and the excursion ratio

$$L = \frac{h_v}{A_w} \tag{5.5}$$

being the ratio between stem length and wave excursion. The Cauchy number is relevant as a dimensionless scale of the bending stiffness of vegetation. The excursion ratio is important for the bending behaviour of vegetation (*Luhar and Nepf*, 2016). When the vegetation is longer than the wave excursion ($L > 1$), the vegetation will not fully extend over a wave cycle. The vegetation dynamics are not limited by its length. Alternatively, when the wave excursion is longer than the vegetation ($L < 1$), flexible vegetation may fully extent over a wave cycle such that it is limited by its length. During a part of the wave cycle, the vegetation will be stretched and unable to continue moving. The plants act as immobile bed rods, which is comparable to their behaviour under unidirectional currents (Section 2.3.2). Thus, L is important for the regime of vegetation swaying.

5.2.2 Wave-vegetation interaction

Vegetation interacts with dynamic forces induced by waves and the static buoyancy force (Fig. 5.1c). The interaction is one-way for rigid vegetation and two-way for flexible vegetation. We consider three wave-induced forces that act on vegetation. These are given per unit stem length, and are scaled (according to Eq. 5.1-5.2) equivalents of Eq. 2.14, 2.16-2.17: the drag force;

$$F_{D*} = \frac{1}{2} C_{Dw} |u_{rn*}| u_{rn*} e^{-i\theta}, \tag{5.6}$$

the added mass force;

$$F_{A*} = \frac{1}{2} C_A \frac{\pi^2}{KC} \frac{\partial u_{rn*}}{\partial t_*} e^{-i\theta}, \tag{5.7}$$

and the Froude-Krylov force;

$$F_{FK*} = \frac{1}{2} \frac{\pi^2}{KC} \frac{\partial U_{s*}}{\partial t_*}. \tag{5.8}$$

Herein, $u_{rn*} = \Re\left(U_{r*} e^{i\theta}\right)$ and $u_{rp*} = \Im\left(U_{r*} e^{i\theta}\right)$ are the stem-normal and stem-parallel components of the relative velocity between water and stem $U_{r*} = U_{s*} - U_{veg*}$. C_{Dw} and C_A are coefficients for drag and added mass respectively and $KC = u_c T / b_v$ is the Keulegan-Carpenter number. The drag coefficient

$$C_{Dw} = \left(\frac{730}{Re}\right)^{1.37} + 1.04 \tag{5.9}$$

was derived via direct force measurements on field of rigid cylinders in the range $300 < Re < 4700$ by *Hu et al.* (2014), where $Re = u_c b_v / \nu$ is the Reynolds number with $\nu = 10^{-6}$ m^2/s as the kinematic viscosity. The drag coefficient is commonly calibrated to include the effect of vegetation swaying (e.g. *Mendez and Losada*, 2004) but in this chapter we include plant motion explicitly such that Eq. 5.9 is applied to all vegetation types. Eq. 5.9 was preferred over Eq. 4.7, which was derived for rigid vegetation in Chapter 4, because Eq. 5.9 is derived over a wider range of hydrodynamic conditions and was obtained using direct force measurements instead of calibration . $C_A = 12.63 KC^{0.0583} - 15.09$ satisfies empirical data by *Keulegan and Carpenter* (1958) for $KC \geq 20$. We note that their C_M equals $C_A + 1$ in this study as we define the added mass and Froude-Krylov forces separately (*Dean and Dalrymple*, 1991). The friction force, based on *Zeller et al.* (2014), is of negligible magnitude for the condition considered here (Re = 570-1500) and therefore omitted.

The magnitude of F_{A*} and F_{FK*} relative to F_{D*} is controlled by the ratio $\pi^2 / (KC|u_{rn*}|)$. KC is of the order $O(10^2)$ for conditions considered in this study

as is a realistic value for field conditions (*Jadhav et al.*, 2013). In case of rigid vegetation, $|u_{rn*}| = |u_{s*}| = O(10^0)$ and the relative magnitude of F_{A*} and F_{FK*} is of order $O(10^{-1})$. The same scaling argument has also been employed for flexible vegetation (e.g. *Mullarney and Henderson*, 2010), but when the relative velocity reduces due to vegetation swaying, F_{A*} and F_{FK*} may be of similar magnitude as F_{D*}. Therefore, we do consider F_{A*} and F_{FK*} at this stage of our analysis. Finally, the net buoyant force

$$F_{B*} = \frac{1}{4}\pi(\rho' - 1)\frac{gb_v}{u_c^2}i \tag{5.10}$$

is not exerted by waves but can modify plant posture (*Zeller et al.*, 2014). It features $g = 9.81$ m/s^2 as the gravitational acceleration and $\rho' = \rho_v/\rho$ as the ratio between the vegetation bulk density (ρ_v) and the water density.

Swaying by flexible vegetation affects the magnitude and direction of the wave forces (Eq. 5.6-5.8). We consider inextensible stems, homogeneous cylindrical cross-sections, homogeneous flexural rigidity, and no interaction between stems. Instead, the sheltering of downstream vegetation can be included through the velocity scale (Eq. 5.3). Under these conditions, plant motion is controlled by the force balance (*Mullarney and Henderson*, 2010; *Luhar and Nepf*, 2016), according to

$$\frac{1}{2}\frac{\pi^2}{KC}\rho' Ca\frac{\partial U_{veg*}}{\partial t_*} + \left(\frac{\partial^3\theta}{\partial s_*^3} - i\frac{\partial\theta}{\partial s_*}\frac{\partial^2\theta}{\partial s_*^2}\right)e^{-i\theta} = Ca\left(F_{D*} + F_{A*} + F_{FK*} + F_{B*}\right). \tag{5.11}$$

The first term on the left-hand side is the stem inertia and the second term expresses bending resistance. The wave and buoyancy forces control plant motion via the forcing term on the right-hand side. Conversely, plant motion controls the direction and the magnitude of the wave forces. This two-way interaction between wave forces and stem motion poses the main challenge in solving wave forces on flexible vegetation. Therefore, our experiments, described in Section 5.3, aim to identify the key physical interactions relevant to wave damping to justify simplifications of Eq. 5.11. Specifically, we will investigate the relative magnitude of F_{A*} and F_{FK*}, the predominant stem section that contributes to stem bending, and whether the effect of plant bending on force direction (stem reconfiguration) or relative velocity (stem velocity) is most important.

5.2.3 Wave damping

Wave damping over a flat bottom is controlled by the conservation of wave power (*Dalrymple et al.*, 1984), according to

$$c_{g*}\frac{\partial E_*}{\partial x_*} = -8\lambda_f F_r^2 D^{-1}\epsilon_{v*} \tag{5.12}$$

where $E_* = H_*^2$ is the wave energy and $c_{g*} = \frac{1}{2k_*} + \frac{D}{\sinh 2k_* D}$ is the wave group velocity. We have introduced $\lambda_f = n_v b_v h_v$ as the relative frontal area, $F_r = u_c/\sqrt{gh}$ as the Froude number, $D = h/A_w$ as the ratio between water depth and wave excursion, and $k_* = kA_w$ as the dimensionless wave number. Furthermore, ϵ_{v*} is the energy dissipation per stem due to the work done by wave forces (*Dalrymple et al.*, 1984) given by

$$\epsilon_{v*} = \int_{s_*=0}^{1} \overline{F_w \cdot U_{s*}} ds_*. \tag{5.13}$$

Here the overbar denotes phase-averaging over a wave cycle. Although F_{A*} and F_{FK*} can be of sufficient magnitude to control plant motion, they act out of phase with the water motion such that their phase-averaged work done by them is considered to be negligible. This argument strictly requires that the phase difference between U_{s*} and u_{rn*} is small, which is reasonable given that the phase difference between water and stem motion reduces when vegetation velocities increase (*Mullarney and Henderson*, 2010). Finally, we will employ

$$W_* = F_* \cdot U_{s*} \tag{5.14}$$

as a short-hand notation for the time-dependent work done (W_*) by waves per unit stem length.

The solution of Eq. 5.12 in terms of wave height expresses a decay in the direction of wave propagation. In case of rigid vegetation, *Dalrymple et al.* (1984) showed that the solution in terms of wave damping is given by

$$H_* = \frac{H_{0*}}{1 + \beta_* x_*}, \tag{5.15}$$

where H_{0*} is the incident wave height, and β_* is the damping coefficient, scaled as $\beta_* = \beta A_w$. In case of flexible vegetation, Eq. 5.15 holds when the vegetation dynamics remain constant, i.e. u_{rn*} damps proportionally to H_*. This is assumed to be the case in this study given that the vegetation fields in our experiments and validation cases are short with a length of 1.5 m and up to 40 m respectively.

5.3 Wave attenuation analysis under observed plant motion

5.3.1 Laboratory experiments

We combine measurements of wave damping and water particle velocities, as described in Chapter 4, with observations of plant motion to derive the wave forces on vegetation. Experiments of wave damping over rigid and flexible vegetation canopies were conducted in the wave flume of the Coastal Laboratory of Swansea University, UK, to identify key mechanisms in the wave-vegetation interaction (Fig. 4.2). The canopies were subjected to 24 regular wave conditions for which the observed wave damping coefficients and velocity scales, based on Eq. 5.3 are presented in Table 5.1. Wave damping was measured using three resistance type wave gauges, and water particle velocity fields were derived using Particle Image Velocimetry (PIV). Detailed descriptions of the experimental setup, wave damping measurements and water particle velocity measurements are provided in Section 4.3.

The velocity at the vegetation stems (U_s) was obtained from the PIV-derived velocity fields (U). The velocity at rigid stems was taken from the water particle velocities inside the canopy. The velocity structure was considered fully developed as the gap was more than five drag length scales (*Lowe et al.*, 2005) downstream of the canopy edge. The control runs with reversed vegetation prevented velocity measurements for one run per condition. Alternatively, the velocity at flexible stems was derived from the vertical velocity structure at the downstream edge for which stem motion can be identified simultaneously. Based on comparisons with control runs without vegetation, we found that flexible vegetation did not disturb the flow velocity structure apart from damping proportional to the wave height. Hence, the wave-vegetation interaction at the downstream edge is assumed to be representative for the whole canopy when velocity damping is accounted for.

Plant motion of flexible vegetation was derived from the frames captured by the PIV-camera through fitting a circular arc between the tip and the root for each frame (Fig. 5.3). We assume stem inextensibility such that the arc length equals vegetation height, and downstream bending as this is the dominant direction under extreme motion (*Rupprecht et al.*, 2017). Under these assumptions, the stem position has a unique solution when the chord length d between the tip and the root satisfies $1 > d/h_v \geq 2/\pi$ (Fig. 5.3a). If $d = h_v$, a straight stem between root and tip is fitted (Fig. 5.3b). Finally, a circular arc cannot be fitted when $d/h_v < 2/\pi$, which may occur under extreme bending. The smallest semi-circle with diameter $d = 2h_v/\pi$ is fitted instead (Fig. 5.3c). Tip positions of a stem at the downstream edge of the patch have been identified manually for each frame

by two independent controllers (Fig. 5.3d). This was found to be more accurate than automatic identification due to the variation in illumination and the low contrast between stems in the canopy. It is noted that a circular arc may not accurately represent all stem configurations, but it does accurately represent the motion of the tip which sways the most and is identified directly. Additionally, the errors in plant posture may have a limited impact on wave damping as we will show in the following sections. An example of the computed plant motion is included in Figure 5.2b. Further details on the stem posture algorithm and test cases can be found in Appendix C.

The observed plant motion ranged from straight stems to fully flattened canopies. Plant motion was developing during the measurement period with 25% of the runs exhibiting a change in the maximum bending angle of more than 10°. It is expected that this affected the measured wave damping and the wave forces equally. The vegetation velocity is derived numerically through a central difference scheme on the plant configuration. Following the derivation of water particle velocities, we have applied a Fourier filter to retain only the natural and first-order harmonics of the vegetation velocity.

The wave-induced forces are computed based on the velocity signal and plant motion, according to Eq. 5.6-5.8 (Fig. 5.2b). Then, the force-derived damping coefficients β_{for} was solved numerically through substitution of Eq. 5.15 in Eq. 5.12 (Fig. 5.2c). This produces a third-order polynomial function which may provide three instead of one solution for β_{for}. In these instances, the β_{for} which is closest to β_{exp} is selected, where β_{exp} is the experimentally derived damping coefficient (Fig. 5.2a). β_{for} reproduces β_{exp} over rigid vegetation very well ($r^2 = 0.76$) and β_{exp} over flexible vegetation acceptably ($r^2 = 0.26$; Fig. 5.4). Importantly, wave damping over flexible vegetation is predicted in the right order of magnitude using a drag coefficient that was derived on rigid vegetation. Thus, unlike prior studies, a calibration of the drag coefficient for flexible vegetation was not required to successfully predict wave damping over rigid vegetation. Instead, a wave damping in the right order of magnitude was achieved by explicitly including the plant motion effect in the drag force (Eq. 5.6).

5.3.2 Key mechanisms in the wave-vegetation interaction

Force magnitudes We find that the drag force is the dominant wave force on flexible vegetation, but the added mass and Froude-Krylov forces increase in relative magnitude when plant motion increases at higher Ca and towards the tip of the stem (Fig. 5.5). The plant motion is limited at low Ca and at the bottom of the stem, where the motion is constrained by its root. When plant motion increases, the ratio $\pi^2/(KC|u_{rn*}|)$ increases such that the magnitudes of F_{A*} and F_{FK*} increase relative to F_{D*}. Our experimental results show that the

Table 5.1: List of tested wave conditions and damping coefficients for rigid and flexible vegetation. u_c is derived from measured velocities according to Eq. 5.3. * Based on 2 instead of 3 runs; † Based on 1 run; Data quantity was reduced by control runs (u_c, rigid), or instrument malfunctioning. ‡ Plant motion not captured due to a moving floor plate.

				Rigid vegetation				**Flexible vegetation**			
	$\boldsymbol{H}$	$\boldsymbol{T}$	$\boldsymbol{h}$	$\boldsymbol{u_c}$	$\boldsymbol{Ca}$	$\boldsymbol{L}$	$\boldsymbol{\beta_{exp}}$	$\boldsymbol{u_c}$	$\boldsymbol{Ca}$	$\boldsymbol{L}$	$\boldsymbol{\beta_{exp}}$
Case	**[m]**	**[s]**	**[m]**	**[m/s]**	**[-]**	**[-]**	**[10^3/m]**	**[m/s]**	**[-]**	**[-]**	**[10^3/m]**
R1	0.15	1.4	0.60	0.13†	0.02	11	42 (6)	0.15	178	8.9	20 (9)*
R2	0.15	1.6	0.60	0.15*	0.04	7.6	38 (4)	0.19	278	6.2	16 (3)*
R3	0.15	1.8	0.60	0.17*	0.04	6.3	49 (9)	0.20	326	5.1	23 (5)*
R4	0.15	2.0	0.60	0.18*	0.05	5.3	42 (16)	0.22*	390	4.2	15 (16)*
R5	0.10	1.8	0.60	0.11*	0.02	9.2	39 (8)	0.14	146	7.6	20 (8)*
R6	0.20	1.8	0.60	0.21*	0.07	4.9	63 (9)	0.25	498	4.1	26 (19)*
R11	0.15	1.4	0.50	0.17*	0.04	7.9	72 (10)	0.19	271	7.2	21 (7)
R12	0.15	1.6	0.50	0.20*	0.06	6.0	67 (8)	0.21	352	5.5	17 (8)*
R13	0.15	1.8	0.50	0.20*	0.06	5.2	80 (18)	0.23	411	4.6	32 (6)
R14	0.15	2.0	0.50	0.22*	0.08	4.2	70 (30)	0.25	472	3.8	24 (12)
R15	0.10	1.8	0.50	0.14*	0.03	7.4	59 (18)	0.16	191	6.7	26 (5)
R16	0.20	1.8	0.50	0.26*	0.10	4.1	94 (22)	0.30	692	3.5	25 (15)
R21	0.15	1.4	0.40	0.20*	0.06	6.9	145 (23)	0.23	397	6.0	27 (15)
R22	0.15	1.6	0.40	0.21*	0.07	5.5	125 (13)	0.25	507	4.6	28 (13)
R23	0.15	1.8	0.40	0.22*	0.07	4.8	138 (9)	0.27	556	3.9	22 (9)*
R24‡	0.15	2.0	0.40	0.23*	0.08	4.1	108 (4)	0.25	498	3.7	48 (10)
R25	0.10	1.8	0.40	0.16*	0.04	6.7	97 (7)	0.18*	240	6.0	22 (12)*
R26	0.12	1.8	0.40	0.18*	0.05	5.8	116 (9)	0.21*	355	4.9	32 (14)*
R31	0.10	1.4	0.30	0.16*	0.04	8.6	210 (19)	0.18	266	7.3	56 (16)
R32	0.10	1.6	0.30	0.16*	0.04	7.3	219 (32)	0.20	309	5.9	68 (28)
R33	0.10	1.8	0.30	0.18*	0.05	5.9	197 (9)	0.21	333	5.1	62 (19)
R34	0.10	2.0	0.30	0.17*	0.04	5.6	195 (9)	0.20	325	4.6	62 (9)
R35	0.08	1.8	0.30	0.14*	0.03	7.5	169 (6)	0.17	238	6.0	51 (20)
R36	0.12	1.8	0.30	0.20*	0.06	5.3	219 (27)	0.24	444	4.4	40 (11)

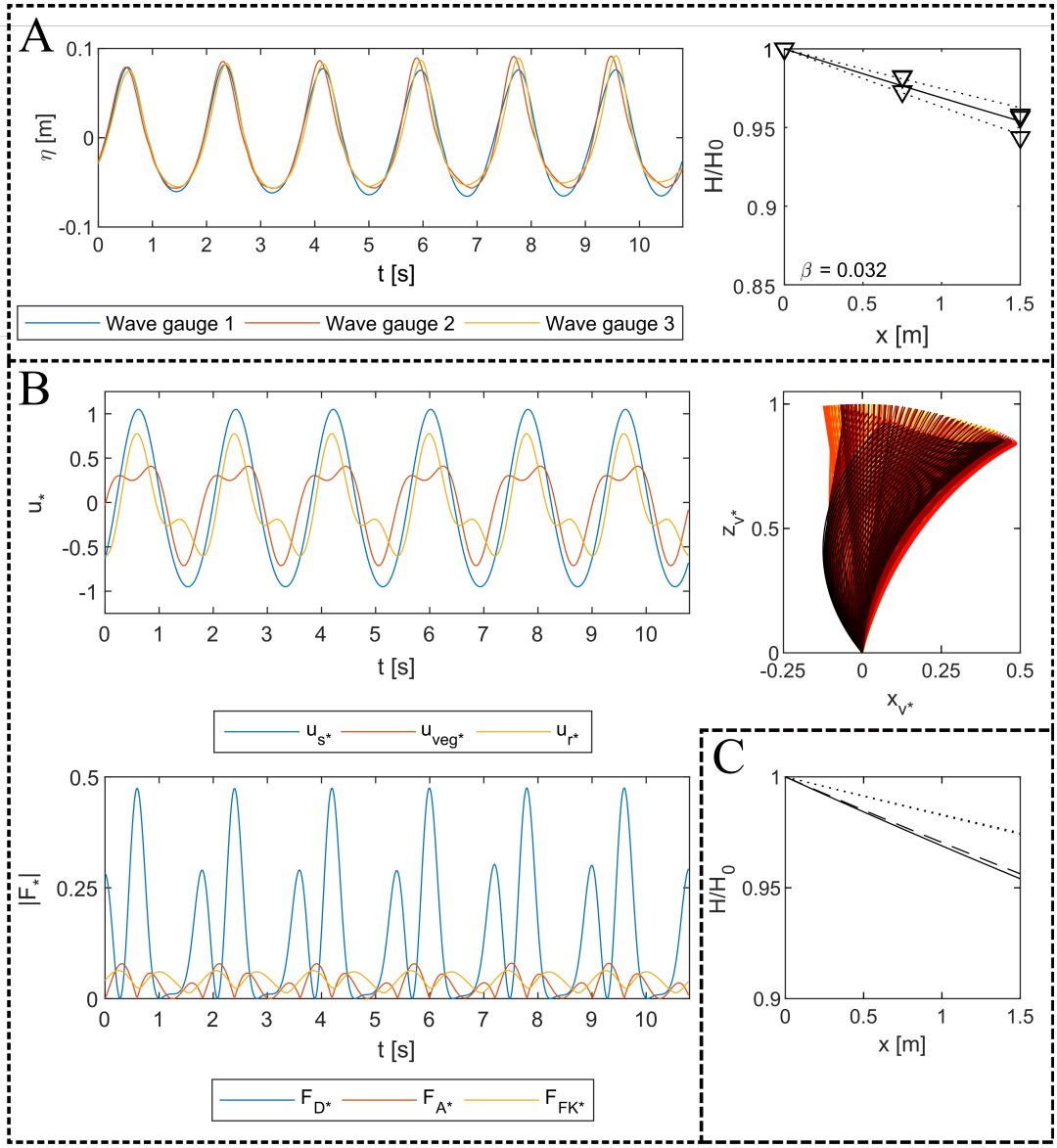

Figure 5.2: Schematisation of the data collection from (a) wave gauges and (b) PIV, and (c) comparison of derived β under conditions R13 with flexible vegetation. Top left: time series of the water surface elevation as measured by the three wave gauges and corrected for phase differences. Top right: the data of the three repeats (triangles, some data points are overlapping) is combined to fit β_{exp} (solid line) with 95% confidence interval (dotted lines). Middle left: PIV derived horizontal particle velocities, vegetation velocity and relative velocity at $s_* = 0.5$. Middle right: PIV-derived plant motion. The colouring denotes the time and ranges from yellow (start of run) to black (end of run). Bottom left: Magnitudes of the wave forces at $s_* = 0.5$. Bottom right: Comparison of the force-derived β_{for} (dashed line) with β_{exp} (solid line). The dotted lines (only one is visible due to overlapping) denote β_{for} of the other repeats of R13.

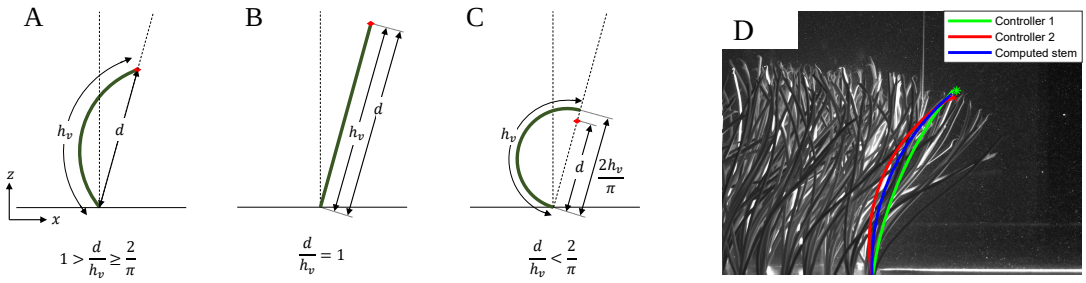

Figure 5.3: Schematisation of the derivation of the plant position from a fixed root and identified tip position (red diamond) under three conditions: (a) a bent stem, (b) a straight stem and (c) extreme stem bending; and (d) application for a sample image.

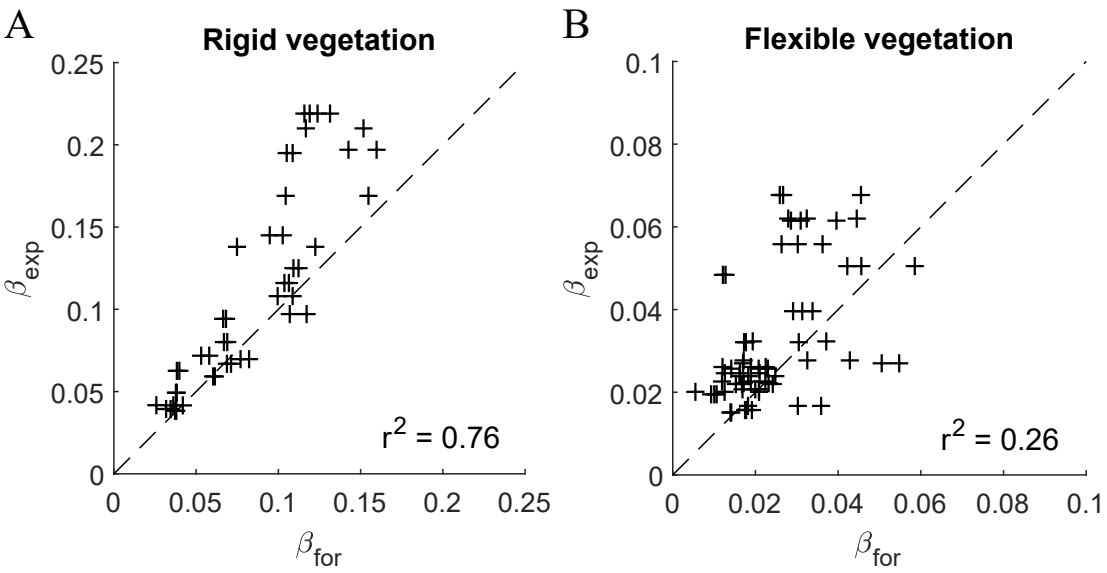

Figure 5.4: The correlation between the force-derived damping coefficient β_{for} and the measured damping coefficient β_{exp} for (a) rigid and (b) flexible vegetation. The dashed line denotes a perfect fit.

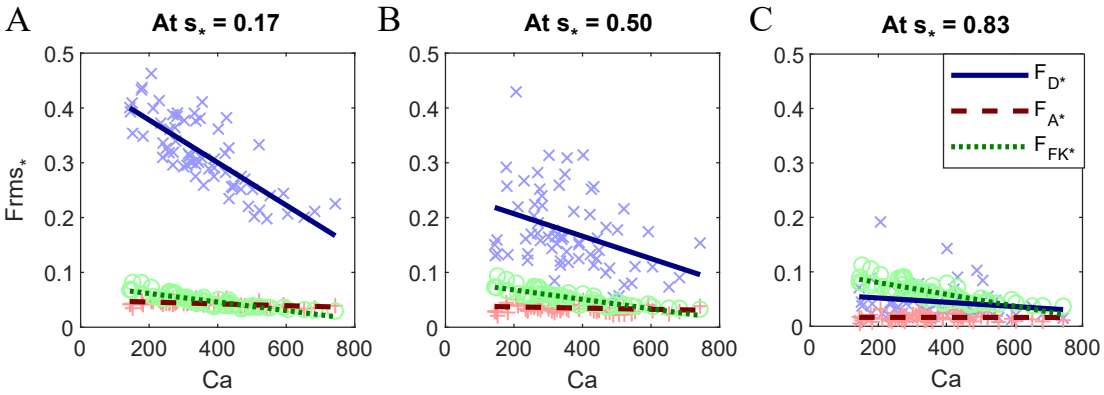

Figure 5.5: Root-mean-square magnitude of the drag force F_{D*}, the added mass force F_{A*}, and the Froude-Krylov force F_{FK*} on flexible vegetation as function of the Cauchy number at (a) $s_* = 0.17$, (b) $s_* = 0.5$, and (c) $s_* = 0.83$.

root-mean-square magnitudes of F_{A*} and F_{FK*} are in the range of 15-20% of F_{D*} at $s_* = 0.17$, 25-35% at $s_* = 0.5$, and 100% at $s_* = 0.83$. Although the relative magnitude of F_{A*} and F_{FK*} increases towards the tip, their magnitude remains low compared to the drag force exerted on the bottom section of the stem.

Distribution of wave energy dissipation The distribution of energy dissipation versus stem length shows that most energy is dissipated where the stem is upright and its motion is minimal (Fig. 5.6). The dissipation over an upright rigid stem is approximately constant along its length with a peak in dissipation at the tip where amplified velocities were observed due to wave-driven currents through the top of the canopy (see e.g. *Pujol et al.*, 2013; *Abdolahpour et al.*, 2017). Alternatively, the wave dissipation is concentrated at the bottom part of the stem for flexible vegetation with near-zero to negative contributions at the top section ($s_* > 0.7$). The decreasing contribution to energy dissipation over the stem length is inversely proportional to stem motion, which is absent at the fixed root and maximum at the tip. The negative energy dissipation at the top of a flexible stem follows from stem velocities locally exceeding water velocities, which agrees with modelling results in *Mullarney and Henderson* (2010).

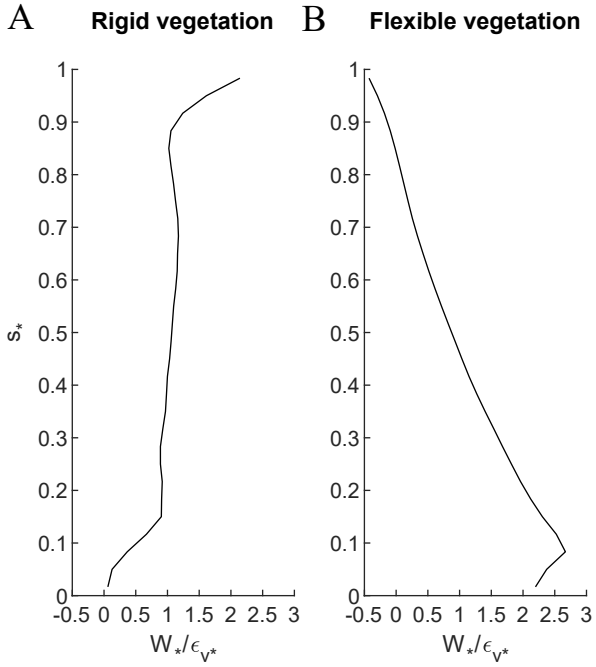

Figure 5.6: Average rate of energy dissipation versus the along-stem coordinate for (a) rigid and (b) flexible vegetation.

Stem reconfiguration versus stem velocity The swaying of flexible vegetation reduces wave damping in two ways. First, reconfiguration of the stem posture reduces the stem frontal area (*Paul et al.*, 2016) and modifies the direction of wave forces (*Zeller et al.*, 2014; *Luhar and Nepf*, 2016). Second, stem velocity reduces the relative velocity between stem and water (e.g. *Mendez and Losada*, 2004). Both mechanisms reduce the work done by the drag force but have not been quantified individually. To identify the dominant mechanism, we quantify β by modifying Eq. 5.6 such that it solely includes stem reconfiguration or stem velocity. Wave damping by stem reconfiguration includes the directionality of the drag force relative to the stem, but the vegetation velocity is set at zero such that

$$F_{D*} = \frac{1}{2} C_{Dw} |u_{n*}| u_{n*} e^{-i\theta} \tag{5.16}$$

with u_{n*} as the stem-normal component of the water velocity. Alternatively, stem velocity includes the relative velocity in the force equations, but the stem is considered upright for the directionality of the forces, i.e.

$$F_{D*} = \frac{1}{2} C_{Dw} |u_{r*}| u_{r*}. \tag{5.17}$$

Finally, we consider the rigid stem drag force which excludes both stem reconfiguration and stem velocity as a reference for the relative contribution of each mechanism. The rigid stem drag force is given by

$$F_{D*} = \frac{1}{2} C_{Dw} |u_{s*}| u_{s*}. \tag{5.18}$$

The respective wave damping coefficients are obtained, as described in Section 5.3.1. The contributions of the bending (Eq. 5.16) and relative velocity (Eq. 5.17) to wave damping are scaled against the damping that is simulated by the full drag force equations (Eq. 5.6) and the damping simulated by the rigid stem drag force (Eq. 5.18).

Our results show that stem velocity is more important than stem reconfiguration. The inclusion of stem velocity explains 92.3% of the observed reduction in ϵ_{v*} due to plant motion, whereas the individual contribution of the stem reconfiguration is 34.6% (Fig. 5.7). Thus, the stem velocity effect can explain almost all reduction in wave energy dissipation. Conversely, whilst stem bending can explain 34.6% of the reduction in wave energy dissipation individually, its added effect when the relative velocity is included is only 7.7%. These results fit with the concentration of energy dissipation at the lower section of the stem (Fig. 5.6), which is straighter than the top section. Stem bending is significant at the tip, but the contribution of the top section to wave energy dissipation is small.

5.4 Model for wave damping over flexible vegetation

5.4.1 Model assumptions

The key mechanisms in the wave-vegetation interaction justify our assumptions for modelling wave damping of regular waves over flexible vegetation. We assume that

1. Wave energy is dissipated where plant deflections are small, and the plant posture is near-vertical;

2. The drag force controls the wave-vegetation interaction.

Assumption 1 is supported by the concentration of energy dissipation in the upright lower part of a flexible stem and the dominant contribution of the relative velocity mechanism relative to stem bending. Assumption 2 follows from the observation that F_{A*} and F_{FK*} are an order of magnitude smaller than F_{D*} at the bottom section of the stem, which is key for wave damping. F_{A*} and F_{FK*}

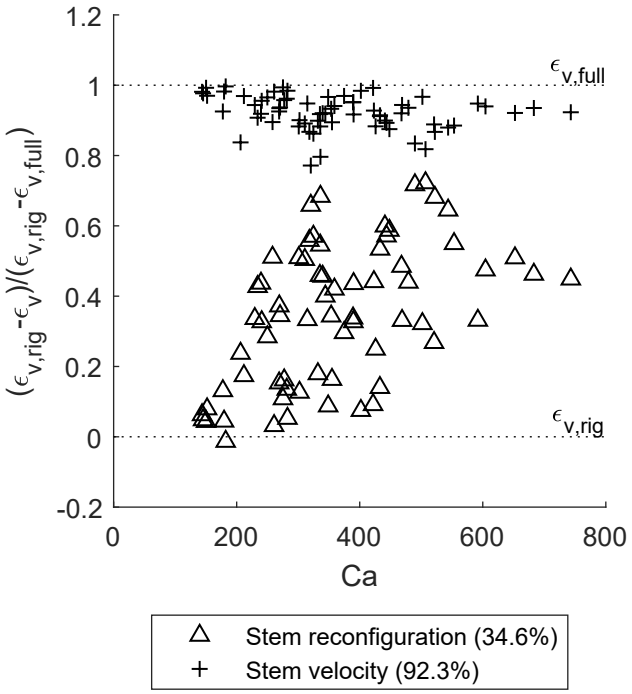

Figure 5.7: Individual contributions of stem reconfiguration (based on Eq. 5.16) and stem velocity (based on Eq. 5.17) effects to the reduction in the wave energy dissipation. The average contribution of each effect is given between brackets. The contributions are scaled relative to the energy dissipations based on the full drag force (Eq. 5.6, upper dotted line) and the drag force based on a rigid stem (Eq. 5.18, lower dotted line).

may be important at the top sections of a flexible stem, but their magnitude remains an order of magnitude smaller than F_{D*} at the bottom section. We retain the assumptions of stem inextensibility, homogeneous cylindrical cross-sections, negligible stem inertia, homogeneous flexural rigidity and no interaction between stems.

Our model assumptions reflect those in small excursion models as in *Méndez et al.* (1999) and *Mullarney and Henderson* (2010), who used Euler-Bernoulli beam theory to solve vegetation motion. Here we have provided new experimental support for this type of model, and our model differs in the extension of plant motion to wave damping (Sections 5.4.3-5.4.5).

Scaling analysis shows that small excursion models are valid for $L \gg 1$ (*Luhar and Nepf*, 2016). Our experimental results ($L = 3-8$) show that the wave energy dissipation is concentrated at the bottom section of a stem where its velocity and excursion are low compared to the water velocity. This suggests that the model assumptions are valid for excursion ratios in the order $O(10^0)$. The model validation (Section 5.5) includes wave and vegetation conditions with L as low as 1 which covers most salt marsh (L = 0.3-10, see Appendix A and *Rupprecht et al.*, 2017)) and seagrass ($L = 0.5 - 6$, *Lei and Nepf*, 2019) conditions. In the case of $L < 1$, flexible vegetation may be fully extended, and the vegetation velocity may reduce to 0. Under these conditions, our model will provide a conservative estimate of the energy dissipation. Finally, the model is derived for cylindrical vegetation, but it can easily be extended to other plant geometries given appropriate relations for C_{Dw} and Ca.

5.4.2 Solution of plant motion

Under the model assumptions, vegetation motion is governed by horizontal stem excursion (x_*) which must satisfy the force balance (Eq. 5.11) in the horizontal direction. For a near-vertical stem, it is appropriate to scale x_v by the horizontal water particle excursion length A_w rather than by plant length h_v as was done up to this point, i.e. $x_{v*} = x_v/A_w$ and $u_{veg*} = \partial x_{v*}/\partial t_*$. Furthermore, the bending angle is approximated as $\theta \approx \partial x_{v*}/\partial z_{v*}$ and $s_* \approx z_{v*}$ at this small-deflection limit (*Luhar and Nepf*, 2016; *Mullarney and Henderson*, 2010). We consider thin stems for which stem inertia is negligible ($\pi^2\rho'/(2KC) \ll 1$). Finally, the drag force, now given by Eq. 5.17, is linearised for the purpose of solving the force balance only. Under these conditions, Eq. 5.11 simplifies as

$$\frac{\partial^4 x_{v*}}{\partial z_{v*}^4} = Q\left(u_{s*} - \frac{\partial x_{v*}}{\partial t_*}\right) \tag{5.19}$$

where scaled flexibility

$$Q = \frac{4}{3\pi} C_{Dw} CaL \int_0^1 (a_u - a_v) dz_{v*} \tag{5.20}$$

is a linearised parameterisation of the magnitude of drag force, and a_u and a_v are the amplitudes of the water and vegetation velocity respectively. Equivalent work is done over a wave cycle by the linearised drag as would be by quadratic drag (e.g. *Zimmerman*, 1982; *Méndez et al.*, 1999). The boundary conditions of Eq. 5.19 are defined as clamped at the root, $x_{v*} = \partial x_{v*}/\partial z_{v*} = 0$ at $z_{v*} = 0$, and free at the tip, $\partial^2 x_{v*}/\partial z_{v*}^2 = \partial^3 x_{v*}/\partial z_{v*}^3 = 0$ at $z_{v*} = 1$.

Wave and plant motion are periodic over a wave cycle and must satisfy the eigenvalue problem posed by Eq. 5.19. Therefore, we separate the motion quantities in a temporal mode following the monochromatic wave frequency and orthogonal spatial modes following the given eigenvalue problem (*Mullarney and Henderson*, 2010), according to

$$\begin{aligned} u_{s*} &= \Re\left(e^{it_*} \sum_{n=1}^{\infty} U_n \psi_n\right), \\ u_{veg*} &= \Re\left(e^{it_*} \sum_{n=1}^{\infty} V_n \psi_n\right), \\ x_{v*} &= \Re\left(e^{it_*} \sum_{n=1}^{\infty} X_n \psi_n\right). \end{aligned} \tag{5.21}$$

The spatiotemporal complex coefficients U_n, V_n and X_n denote the weights of each mode in spectral space. The spatial modes ψ_n satisfy $\partial\psi_n/\partial z_{v*} = \alpha_n \psi_n$ where α_n are the eigenvalues of each spatial mode. Further details regarding the structure of ψ_n are provided in Appendix D.

By substitution of Eq. 5.21 in Eq. 5.19 and summation over all spatial modes, we construct transfer function $G = a_G e^{i\phi_G}$ between the water and stem motion in physical space according to

$$V_f = G U_f \tag{5.22}$$

where $U_f(z_{v*}) = \sum U_n \psi_n = a_u e^{i\phi_u}$ and $V_f(z_{v*}) = \sum V_n \psi_n = a_v e^{i\phi_v}$ are complex temporal coefficients in physical space, and

$$G = \frac{\sum \left(\frac{1}{1 - \frac{i\alpha_n}{Q}}\right) U_n \psi_n}{\sum U_n \psi_n}. \tag{5.23}$$

Here, a_G denotes amplitude transfer from water to stem motion and ϕ_G denotes the phase lag between water and stem motion. Eq. 5.23 relates velocity

transfer to Q. When Q is small, typically for stiff vegetation, amplitude transfer from water to stem motion will be small, and their motion will be out of phase by 90°. Conversely, when Q is large, typically for flexible vegetation, stem motion will follow water motion closely in amplitude and phase. Due to the fixed root and the nature of the spatial eigenmodes, the velocity transfer is expected to increase from root to tip. As Q is a function of a_v, Eq. 5.23 is solved iteratively. There is a unique solution, as shown in E. The numerical implementation expands velocity structures to 10 spatial modes as additional modes did not change the resulting vegetation velocity and transfer function.

Additionally, we define the transfer function $R = a_R e^{i\phi_R}$ between water velocity and relative velocity, i.e. $U_f - V_f = RU_f$. By substitution of this definition in Eq. 5.22, it follows

$$R = 1 - G. \tag{5.24}$$

The velocity transfer is a linear transformation that can be applied to calculate (the amplitudes of the Fourier modes of) the relative velocity directly from (the amplitudes of the Fourier modes of) the wave velocities. It arises as the solution of Eq. 5.19. As a linear transformation, it is computationally very efficient, in particular in comparison to the alternative of recomputing the full velocity signals.

5.4.3 Work factor (χ)

To include the effects of plant motion on energy dissipation, we define z_{v*}-dependent work factor

$$\chi(z_{v*}) = \frac{\overline{W}_*}{\overline{W}_{rig*}}, \tag{5.25}$$

such that

$$\epsilon_{v*} = \int_{z_{v*}=0}^{1} \chi \overline{W}_{rig*} dz_{v*}, \tag{5.26}$$

where $\overline{W}_*$ is the phase-averaged work done over a stem with arbitrary stiffness and $\overline{W}_{rig*}$ is the work done over a rigid stem with equal dimensions. By substitution of Eq. 5.17, 5.24 in Eq. 5.14, the phase-averaged work done by the drag force on a stem is given by

$$\overline{W}_* = \frac{1}{4\pi} C_{Dw} \int_{t_*=0}^{2\pi} |\Re\left(RU_f e^{it_*}\right)| \Re\left(RU_f e^{it_*}\right) \Re\left(U_f e^{it_*}\right) dt_*. \tag{5.27}$$

We note that $\Re\left(e^{it_*}\right) = \cos t_*$ and set $\phi_u = -\phi_R$ without loss of generality as W_* is averaged over a wave cycle. Then, Eq. 5.27 reduces to

$$\overline{W}_* = \frac{2}{3\pi} C_{Dw} a_R^2 a_u^3 \cos\phi_R. \tag{5.28}$$

In case of rigid vegetation, $a_R = 1$ and $\phi_R = 0$ as velocity transfer is absent, such that

$$\overline{W}_{rig*} = \frac{2}{3\pi} C_{Dw} a_u^3 \tag{5.29}$$

and, by substitution of Eq. 5.28, 5.29 in Eq. 5.25,

$$\chi = a_R^2 \cos \phi_R. \tag{5.30}$$

Eq. 5.30 shows how the velocity transfer controls wave damping. Changes in amplitude and phase of the relative velocity directly affect the work done by waves on vegetation and, thereby, the wave damping. Defining χ is computationally more efficient than computing the vegetation and relative velocity time series.

5.4.4 Wave damping

A formulation for the wave damping coefficient β_* is obtained by substitution of Eq. 5.15, 5.26 in Eq. 5.12, which leads to

$$\frac{\beta_*}{(1 + \beta_* x_*)^3} = \frac{4 \lambda_f F_r^2}{D c_{g*} H_{0*}^2} \int_{z_{v*}=0}^{1} \chi \overline{W}_{rig*} dz_{v*}. \tag{5.31}$$

Eq. 5.31 represents a third-order polynomial which is solved numerically. There may be up to three roots that satisfy Eq. 5.31, of which the root closest to the estimate by linear wave theory (Eq. 5.33, Section 5.4.5) is selected.

5.4.5 Wave damping under linear wave theory

When the validity of linear wave theory inside the canopy is assumed, the velocity structure is controlled by the ambient velocity field. The amplitude of the water particle velocities is given by

$$a_u = \frac{H_* k_*}{2 F_r^2} \frac{\cosh L k_* z_{v*}}{\cosh D k_*} \tag{5.32}$$

Substitution of Eq. 5.15, 5.29, 5.32 in Eq. 5.31 and the application of the dimensionless dispersion relation $D F_r^2 = k_* \tanh D k_*$ reduce the conservation of energy to a single expression for β_*, according to

$$\beta = \frac{4}{3\pi} C_{Dw} \lambda_f D k_*^2 H_{0*} \frac{\int_{z_{v*}=0}^{1} \chi \cosh^3 (L k_* z_{v*}) \, dz_{v*}}{(\sinh 2 D k_* + 2 D k_*) \sinh D k_*} \tag{5.33}$$

We note that for rigid vegetation, $\chi = 1$ and Eq. 5.33 reduces to the rigid vegetation solution provided in *Dalrymple et al.* (1984).

5.5 Model validation

5.5.1 Validation of the velocity transfer function (G)

The modelled velocity transfer function G is validated against a measured transfer function based on the observed water and plant motion. The measured transfer function is derived from the amplitude and phase differences in the natural harmonic of the observed water particle and stem velocities (Section 5.3.1). The validation includes flexible vegetation only, as the transfer function for rigid vegetation is trivial.

The amplitude a_G of the transfer function is excellently reproduced by the model (Fig. 5.8, top row). The amplitude transfer is $a_G \approx 0$ at the root where the stem is clamped and increases towards the tip to $a_G \approx 1$ for both measured and modelled transfer functions. This indicates that the tip closely follows the water motion, and the relative velocity is small, which fits with observations that the energy dissipation is small at the tip. The coefficient of determination is excellent at $r^2 = 0.84$. The velocity transfer is slightly over1predicted at the tip where the assumption of a near-vertical stem affected only by the drag force may not hold. Additionally, the modelled transfer function is steady state, but the measured transfer function was still developing in 25% of the runs. In these cases, the measured transfer function is lower than the steady-state function, which may further contribute to the over-prediction of the modelled transfer function at the tip. The transfer function at the bottom section of the stem, which is important for wave damping is modelled correctly.

The phase ϕ_G is reproduced well for most experimental runs (Fig. 5.8, middle row). Both measured and modelled phases show that the stem velocities lead water motion by 45° at the root, which decreases towards the tip where the water motion leads stem motion by 10°. The scattering of experimental data is larger than predicted by the model due to natural variation in the wave-vegetation interaction not captured by the model and measurement errors in water and vegetation motion. The scattering is maximum at the root where stem motion is minimal and, therefore, phase calculations are most sensitive to measurement errors. A limited number of outliers (10 out of 68 successful runs) impact the coefficient of determination negatively ($r^2 = 0.37$). Yet, a visual comparison shows that most data points are centred around the line of perfect fit.

Work factor χ is excellently reproduced by the model (Fig. 5.8, bottom row). The measured work factor is derived from the measured transfer function via Eq. 5.30. The work done by waves on a flexible stem at the root is equal to the work done on a rigid stem as denoted by $\chi = 1$ at $s_* = 0$. The work factor decreases as the amplitude transfer from water to stem motion increases from

root to tip. Here, a negativeχ indicates that the stem velocities locally exceed the water velocities, and the relative velocity is fully out of phase with the water velocities. This behaviour agrees with *Mullarney and Henderson* (2010), who showed that the tip motion of flexible stems could exceed the water motion that forces it. The agreement between measured and modelled work factors is excellent at $r^2 = 0.87$.

5.5.2 Validation of the damping coefficient

The damping coefficient β is validated across five vegetation species with distinct biomechanical properties under medium and high energy wave conditions. These include wave damping by the rigid and flexible artificial vegetation (Section 5.3.1) and against three species of real salt marsh vegetation: *Spartina Anglica*, *Puccinellia Maritima* and *Elymus Athericus* (Fig. 5.9). These species differ in dimensions and flexural rigidity (Table 5.2) and have been tested under regular waves in large-scale flumes. The test conditions varied in water depth, wave height, wave period and stem density such that the model is validated across a wide range of wave and vegetation conditions.

S. Anglica and *P. Maritima* were tested in the Cantabria Coastal and Ocean Basin (CCOB) of the University of Cantabria, Spain (*Maza et al.*, 2015; *Lara et al.*, 2016; *Losada et al.*, 2016). *S. Anglica* is a stiff plant with the largest diameter of the species tested. Alternatively, *P. Maritima* is a thin and flexible salt marsh grass. The experimental conditions featured medium water depths ($h = 0.4$-0.6 m) and wave heights ($H = 0.15$-0.20 m) at a range of wave periods ($T = 1.2$-2.2 s) and vegetation densities ($n_v = 430$-2436 stems/m^2).

E. Athericus was tested in the Grosser Wellenkanal (GWK) of Forschungszentrum Küste in Hannover, Germany (*Möller et al.*, 2014; *Rupprecht et al.*, 2017). *E. Athericus* is a thin and tall semi-flexible salt marsh grass. A 40 m-long vegetation field was submerged in deep water ($h = 2$ m) and subjected to medium and high energy wave conditions ($H = 0.11$–0.89 m, $T = 1.5$-5.1 s). The vegetation density decreased as the experiments progressed due to stem breaking. Therefore, the model was run following stem density data provided in *Rupprecht et al.* (2017).

The model is run with plant and wave conditions of individual runs as input. It is assumed that wave damping by real vegetation is dominated by the cylindrical stems. Fig. 5.9 shows that the geometry of the tested *S. Anglica* and *P. Maritima* species is dominated by their stems, and the tested *E. Athericus* was considered cylindrical in *Rupprecht et al.* (2017). The velocity fields around real vegetation are based on linear wave theory (Section 5.4.5), which was also successfully applied in the wave damping analysis in *Losada et al.* (2016) and *Möller et al.* (2014). The drag coefficient for all species is given by Eq. 5.9. The

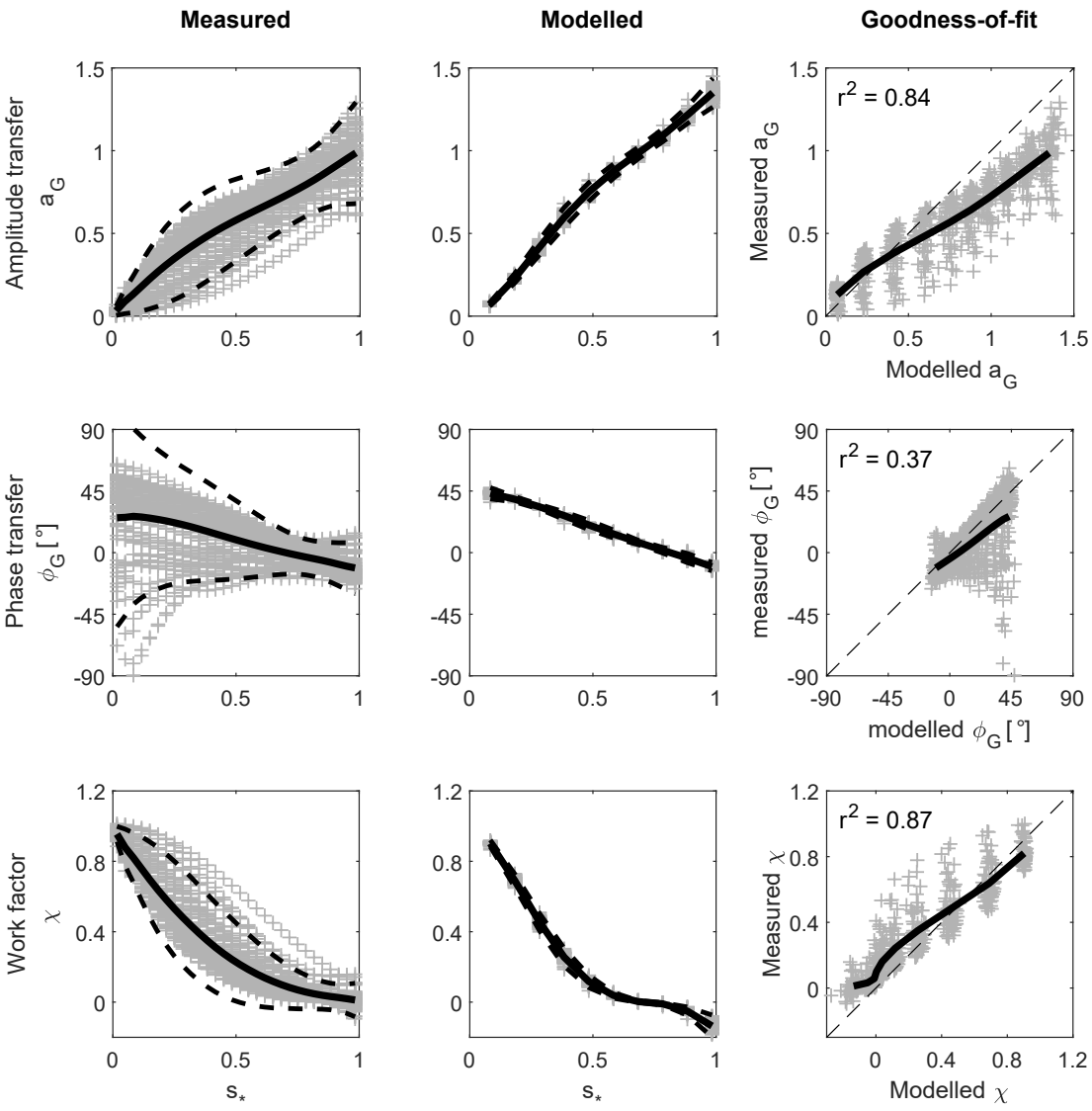

Figure 5.8: Validation of the velocity transfer function G between water and stem motion. Top row: amplitude transfer a_G; middle row: phase transfer ϕ_G; bottom row: work factor χ. The thick line denotes the mean of the measured (left column) or modelled (middle column) transfer functions, or the goodness-of-fit of the mean (left column). The dashed lines denote the 95% observation interval (mean $\pm$ 2 standard deviations), or the line of perfect fit (left column). The grey + signs represent individual observations.

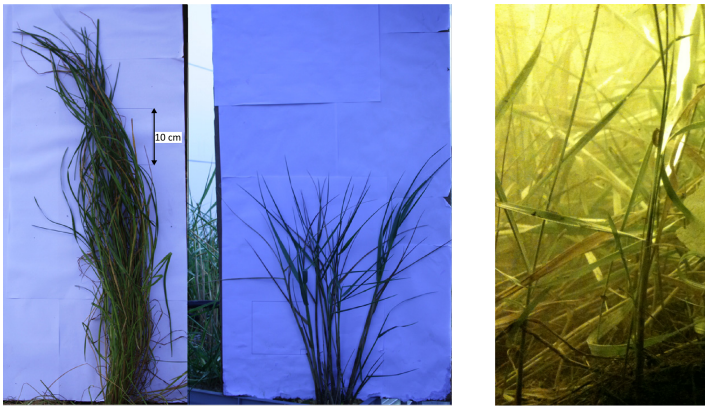

Figure 5.9: The three real vegetation species used in model validation. Photo of *P. Maritima* and S. Anglica is adapted from *Lara et al.* (2016). Photo of *E. Athericus* is provided through the courtesy of Iris Möller (no scale available).

velocity scale is based on linear wave theory halfway based on measured wave height halfway the vegetation field as an estimate of the spatially averaged velocity. This non-predictive definition of the velocity scale can be avoided if the vegetation field is divided into sufficiently short sections, as is typically done in large-scale computational wave models that use a gridded computational domain (e.g. SWAN, *Booij et al.*, 1999).

The agreement between modelled and measured wave damping is good with $r^2 = 0.66$ (Fig. 5.10), which shows that our model is applicable across a range of plant and wave conditions without plant-specific calibration. Excellent agreement is obtained for rigid and flexible artificial vegetation and for *E. Athericus*. The absence of vegetation motion is correctly modelled for rigid vegetation, as is the reduction in wave damping by flexible vegetation and *E. Athericus* due to plant swaying. Wave damping by *S. Anglica* and *P. Maritima* is predicted in the right order of magnitude but with a significant scattering of the data , as demonstrated by their normalised root-mean-square error (NRMSE) of 0.56 and 0.62 respectively. This is partly attributed to the difference in the experiment setup of CCOB. Unlike rectangular flumes where vegetation spans the entire flume width, the CCOB features a circular platform on which vegetation is positioned, which may contribute to wave diffraction and other three-dimensional hydrodynamic effects. These mechanisms are not included in our model, which assumes waves propagating normal to the vegetation. Furthermore, our omission of leaves and stem-stem interactions may have contributed to an underestimation of the measured wave damping, as is observed for *P. Maritima*. Finally, buoyancy, added mass, and Froude-Krylov forces may have initiated a non-passive plant motion,

Table 5.2: List of vegetation species used for model validation: rigid mimics (RM); flexible mimics (FM); *S. Anglica* (SA); *P. Maritima* (PM); *E. Athericus* (EA). n denotes the number of unique wave conditions.

	RM	**FM**	**SA**†	**PM**†	**EA**‡	**Unit**
Type	Artificial	Artificial	Real	Real	Real	-
h_v	300	300	284	473	700	mm
b_v	5.0	5.0	6.0	3.0	1.3	mm
EI_v	9.0×10^{-2}	1.7×10^{-5}	1.8×10^{-2}	8.7×10^{-5}	5.0×10^{-4}	Nm^2
n_v	1111	1111	430-729	877-2436	666-1225	m^{-2}
u_c	0.13-0.26	0.14-0.30	0.16-0.33	0.16-0.38	0.09-0.75	ms^{-1}
Ca	0.02-0.10	150-690	0.20-0.84	96-530	11-820	-
L	4.1-11	3.5-8.9	2.5-8.6	4.0-13	1.4-24	-
Q^*	0.19-0.29	1000-1600	0.82-2.0	1000-2300	650-1700	-
n	24	24	14	18	10	-

* At first iteration, i.e. $a_v = 0$.
† Reference: *Maza et al.* (2015); *Lara et al.* (2016); *Losada et al.* (2016)
‡ Reference: *Möller et al.* (2014); *Rupprecht et al.* (2017)

which is not captured by our model and thus contributes to uncertainty in β_{model}. Non-passive plant motion may also be initiated by wave-induced currents. Although not observed within flexible canopies in our experiments, they have been observed in *Luhar et al.* (2010) and *Abdolahpour et al.* (2017) (See Section 4.5.2 for a comparison of the observed wave-driven currents). A full list of the wave conditions, observed damping, and modelled damping is included in Appendix F.

5.6 Implications for nature-based coastal defences

5.6.1 Plant and wave parameters that control wave damping

Our results show that the capacity of coastal vegetation to damp waves can vary by multiple orders of magnitude depending on the wave and vegetation conditions. We find that the velocity transfer from water to stem motion is key to the magnitude of the drag force and the energy that can be dissipated. When a stem follows the water motion increasingly closely, its capacity to damp waves reduces. The scaled flexibility Q (Eq. 5.20) and the vertical velocity structure control the velocity transfer (Eq. 5.23). Considering $(a_u - a_v)$ is a solution term, and the velocity structure and C_{Dw} are broadly similar across vegetated areas,

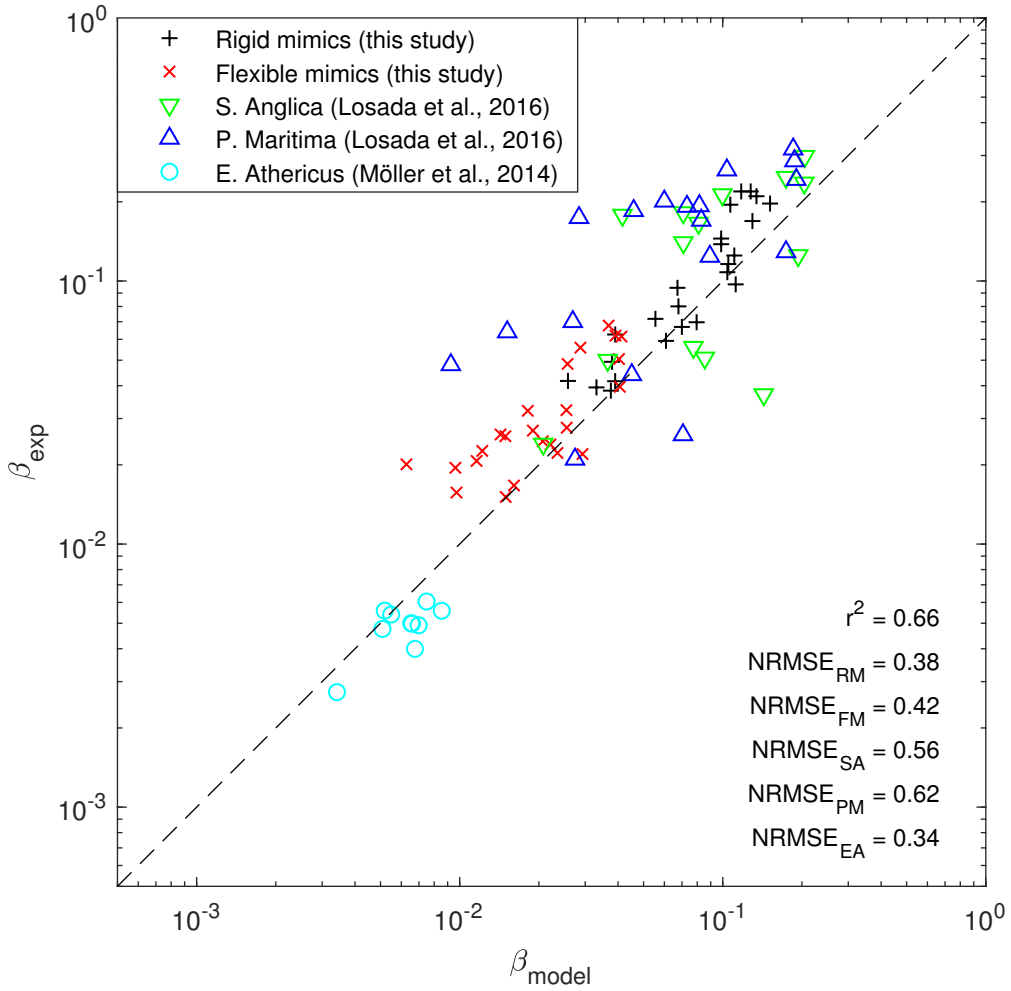

Figure 5.10: Validation of the modelled wave damping coefficients β_{model} against the measured wave damping coefficients β_{exp} across two types of artificial vegetation and three species of real vegetation. The dashed line denotes the line of perfect fit. The r^2 goodness-of-fit is given, as well as the normalised root-mean-square error (NRMSE) of each specie. RM: Rigid mimics; FM: Flexible mimics; SA: *S. Anglica*; PM: *P. Maritima*; EA: *E. Athericus*.

the term

$$CaL = \frac{\rho b_v \omega u_c h_v^4}{EI_v} \tag{5.34}$$

controls the velocity transfer. The term CaL highlights that velocity transfer is not only a function of stem flexural rigidity but also of stem dimensions and wave parameters. Our results agree with prior analytical studies by *Mullarney and Henderson* (2010) and *Luhar et al.* (2017) who also identified CaL as a key parameter for plant motion. It is noted that most parameters affect wave damping in multiple ways. For example, the plant dimensions control the velocity transfer and the plant area on which waves do work. Similarly, the wave velocity controls the velocity transfer function and the magnitude of the work done. Therefore, it is important that the wave-vegetation interaction is included explicitly when modelling nature-based solutions for wave damping.

5.6.2 Model application for nature-based coastal defences

Our model is a valuable tool to quantify wave damping by vegetation with arbitrary stiffness under variable wave conditions. It can be applied to any plant species whose morphology can be represented as a cylinder, including seagrasses, kelp forests, salt marshes and mangroves. The model can be adapted to vegetation with non-cylindrical stems given appropriate relations for C_{Dw} and Ca. As it does not require site-specific calibration, it can readily be applied to new nature-based coastal defences (e.g. created by managed realignment), to sites that are subject to changing conditions (e.g. seasonal variation in plant cover and wave climate, coastal squeeze, plant competition and migration) or to study interventions (e.g. grazing, mowing or planting). The model is also suitable to coastal habitats with mixed vegetation cover as the energy dissipation is effectively solved per individual stem.

5.6.3 Model limitations

Random waves The model has been developed for regular waves whereas most field sites are subjected to random waves. A model expansion for random waves under a Rayleigh distribution will be provided in Chapter 6.

Combined wave-current conditions Waves have been considered independently from currents, but surge- and tide-driven currents can occur with waves during storm events which affect the wave damping capacity of vegetation. *Losada et al.* (2016) showed that wave damping reduces in case of currents in the direction of wave propagation and increases in case of opposing currents. Therefore, our model may overpredict the wave damping during flood tide and with incoming surge flow and underpredict the wave damping during ebb tide and outgoing surge flow. Although the most extreme wave conditions are expected to occur at peak high water when the currents diminish, and our model results are applicable. This limitation can be overcome when currents are included in the force balance (Eq. 5.11), which is recommended for future research. Albeit typically smaller in magnitude, wave-induced currents may be included in a similar manner.

Stem breaking Rigid and semi-flexible vegetation species may break under extreme wave loading, which will significantly reduce their contribution to energy dissipation (*Vuik et al.*, 2018a). Stem breaking is not included in the model, but it could be important during storms of longer durations. However, *Rupprecht et al.* (2017) noted that the flexible *P. Maritima* did not break under extreme wave forcing. This favours the application of flexible species on vegetated foreshores and also highlights the need for models that include plant flexibility.

5.7 Conclusions

We have developed a new mathematical model for the damping of regular waves over flexible coastal vegetation, based on the key physical processes involved in the wave-vegetation interaction. Three mechanisms were identified during the experimental investigations as important for wave damping over rigid and flexible vegetation: (i) the drag force is the dominant force in the bottom section of a flexible stem; (ii) wave energy is dissipated in the bottom section of a flexible stem; (iii) wave energy dissipation is controlled by the velocity difference between water and stem rather than the reconfiguration of stem posture. We found that the energy dissipation by rigid stems was maximum at the stem tip where the wave velocities were the largest, while the dissipation by flexible stems was maximum at the upright bottom section where stem motion was the smallest.

Supported by our experimental investigations, we model vegetation as near-vertical flexible rods in which wave damping is controlled by the velocity transfer from water to stem motion. The velocity transfer is linked to a new work factor, which describes the reduction in wave dissipation relative to rigid vegetation due to plant motion. Wave damping in the model is a function of vegetation and wave parameters and does not require the calibration of the drag coefficient for different plant species.

We have successfully reproduced wave damping over vegetation for five coastal vegetation species, which differ in geometry and flexural rigidity, and under different wave climates. The model validation included three real vegetation species tested in large-scale experiments. Our model reproduced wave damping in the right order of magnitude for each species and for both medium and high energy wave conditions, which shows its validity across a wide range of representative field conditions.

As our model does not require site-specific calibration, it is particularly suited to areas with spatiotemporal variations in vegetation and hydrodynamic conditions. It benefits large areas or areas where interventions such as managed realignment, grazing, and the introduction of new species are considered. Furthermore, the model can be applied to vegetation of different types, sizes and flexibilities when the plant geometry can be represented as a cylinder.

Chapter 6

Modelling wave attenuation by vegetation under random wave conditions

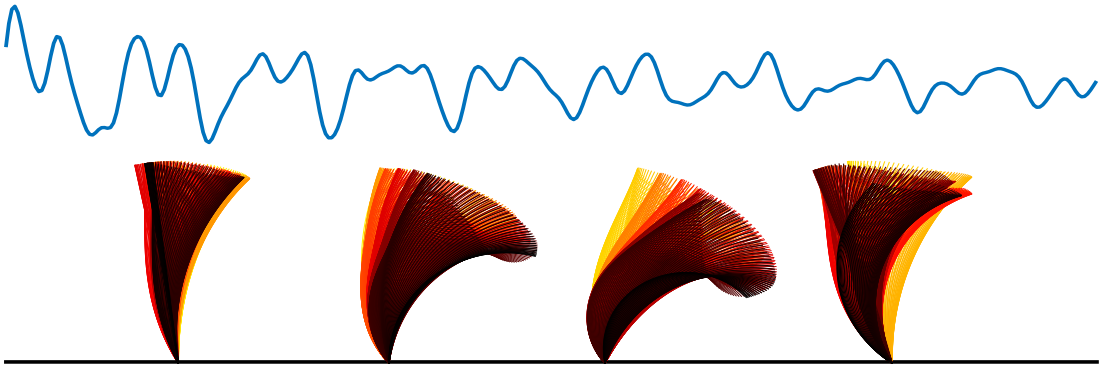

6.1 Introduction

The wave climate in coastal waters is driven by near-surface winds, which produces a spectrum of random waves that vary in height, phase and frequency (*Reeve et al.*, 2012). The observed wave time series at a fixed location is the superposition of many waves with different properties. The random wave spectrum is described by the significant wave height H_s or the root-mean-square wave height H_{rms}, and the peak wave period T_p, which replace the monochromatic wave parameters H and T. The combined presence of many wave components complicates their interaction with vegetation. An individual plant no longer interacts with a single wave but with multiple wave components simultaneously. Therefore, the wave damping capacity of a vegetation field subjected to a random wave climate will differ from the wave damping potential of the same vegetation field under a regular wave climate. As real-world coastal vegetation is almost always subjected to a random wave climate, it is essential for practical applications that a solution for this more complicated scenario is found.

Current random wave attenuation models rely on the calibration of a drag coefficient or require detailed information on the wave spectrum which is often unavailable. Wave damping of random waves over vegetation was first modelled by *Mendez and Losada* (2004) who expanded the monochromatic wave damping model by *Dalrymple et al.* (1984) under the assumption of a Rayleigh wave distribution. Their model excludes stem motion, but it was suggested that wave damping by flexible vegetation could be simulated when the drag coefficient was calibrated accordingly. The model has been successfully applied to a range of field (*Bradley and Houser*, 2009; *Jadhav et al.*, 2013; *Foster-Martinez et al.*, 2018) and flume (*Augustin et al.*, 2009; *Anderson and Smith*, 2014; *Möller et al.*, 2014; *Losada et al.*, 2016) studies but the drag coefficients differed by more than an order of magnitude for field conditions which limits its predictive value. *Chen and Zhao* (2012) developed a model for wave climates with a wider frequency spectrum based on the joint distribution of wave heights and periods by *Longuet-Higgins* (1983), but maintained the rigid vegetation assumption such that calibration of the drag coefficient is required. Alternatively, *Mullarney and Henderson* (2010) developed a model that solves plant motion through the Euler-Bernoulli beam equations for each wave frequency in a spectrum. Although originally only developed for small plant deflections, this type of model was found to be valid for flexible artificial and real vegetation (Chapter 5). Their solution relies on an accurate wave spectrum from a phase-resolving model, but these are computationally more expensive (*Suzuki et al.*, 2019) and less frequently used (see Section 2.5 for an overview) than phase-averaging models. Thus, there is a need for a model that is both applicable across plant species and can be coupled with a phase-averaged

wave model.

In this chapter, we expand the regular wave damping model, described in Chapter 5, to the scenario of a random wave climate under the assumption of a Rayleigh wave distribution. The model considers plant motion explicitly through work factor χ and the assumption of a Rayleigh distribution ensures that the model can be coupled with phase-averaged wave models. Like the regular wave damping model, wave attenuation is predicted based on wave and vegetation parameters only and does not require a plant-specific calibration of a drag coefficient. The new random wave model is validated against a set of experiments with artificial rigid and flexible vegetation conducted in the Swansea University Coastal Engineering Laboratory and observed wave damping over three real vegetation species in large wave flumes.

This chapter is organised as follows. Section 6.2 presents the model expansion for random waves. The random wave experiments are described in Section 6.3. the new model is validated against the observed wave damping in our experiments and those in literature in Section 6.4. Finally, conclusions are drawn in Section 6.5.

6.2 Random wave model

We assume that the nearshore wave climate can be approximated by a Rayleigh wave distribution. The Rayleigh distribution is commonly assumed to apply to wind waves and swell mixtures and provides a good approximation for most sea states (*Reeve et al.*, 2012). It assumes that the band of wave periods is narrow around peak period T_p and the observed wave signal is the summation of individual linear wave components. Under these assumptions, the wave heights are distributed according to

$$p(H_*) = \frac{2H_*}{H_{rms*}^2} e^{-\left(\frac{H_*}{H_{rms*}}\right)^2}, \tag{6.1}$$

where $p(H_*)$ is the probability of a wave of height H_* arriving and

$$H_{rms*} = \sqrt{\int_0^\infty H_*^2 p(H_*) dH_*} \tag{6.2}$$

is the root-mean-square wave height.

Each parameter that scaled with wave frequency ω in the regular wave model, now scales with peak wave frequency $\omega_p = 2\pi/T_p$. Work factor χ (Eq. 5.30) is computed at each wave height but only in frequency ω_p due to the narrow-banded distribution of wave periods. Furthermore, we assume that the velocity

field inside the vegetation canopy satisfies linear wave theory (following *Mendez and Losada*, 2004), according to

$$a_u(x_*, z_{v*}) = \frac{H_* k_{p*}}{2F_r^2} \frac{\cosh Lk_{p*} z_{v*}}{\cosh Dk_{p*}} \tag{6.3}$$

where parameters with subscript p are related to the peak wave period.

By substitution of Eq. 5.29 and 6.3 in Eq. 5.26, the energy dissipation per stem is given by

$$\hat{\epsilon}_{v*}(x_*) = \frac{C_{Dw} D^3}{12\pi \sinh^3 Dk_{p*}} \int_0^\infty \int_0^1 \chi p(H_*) H_*^3 \cosh^3(Lk_{p*} z_{v*}) dz_{v*} dH_*. \tag{6.4}$$

Parameters with accent $\hat{}$ are associated with random waves. It is noted that the drag coefficient of vegetation under random waves has been found to differ from regular waves (e.g. *Möller et al.*, 2014) but we have not found a suitable relation for the drag coefficient that has been derived for rigid cylinders with dimensions based on real vegetation and tested under random waves. Therefore, we will apply the C_{Dw}-relation (Eq. 5.9) by *Hu et al.* (2014) also for random waves. The velocity scale u_c (Eq. 5.3), used in the scaling procedure and to estimate C_{Dw}, is the root-mean-square velocity. It is derived via linear wave theory based on H_{rms}. Eq. 5.9 is valid within the range $300 < Re < 4700$.

The damping coefficient for random waves $\hat{\beta}$ describes the damping of H_{rms*} according to

$$H_{rms*} = \frac{H_{rms,0*}}{1 + \hat{\beta}_* x_*}, \tag{6.5}$$

where

$$\hat{\beta}_* = \frac{4}{3\pi} C_{Dw} \lambda_f D k_*^2 \frac{\int_0^\infty \int_{z_{v*}=0}^1 \chi p(H_{0*}) H_{0*}^3 \cosh^3(Lk_* z_{v*})\, dz_{v*} dH_{0*}}{H_{rms,0*}^2 (\sinh 2Dk_* + 2Dk_*) \sinh Dk_*} \tag{6.6}$$

is obtained by substitution of Eq. 6.4-6.5 in Eq. 5.12 with $E_* = H_{rms*}^2$ (*Mendez and Losada*, 2004). The double integral in Eq. 6.6 is solved numerically. The spatial integral is solved by dividing the stem in 10 sections with length $dz_{v*} = 0.1$. The integral over H_* is solved in parts of $dH_* = 0.1 H_{rms*}$ up to $H_* = 3.5 H_{rms*}$. This range includes 99.8% of the wave height distribution. Eq. 6.6 reduces to the rigid vegetation model (Eq. 2.28) by *Mendez and Losada* (2004) when $\chi = 1$, or to the regular wave model (Eq. 5.33) when Eq. 6.1 is replaced by a Dirac delta function.

6.3 Experiments

Artificial rigid and flexible vegetation have been tested under random wave conditions to validate the extended wave model. The experiments were conducted alongside the regular wave tests in the Swansea University Coastal Laboratory, described in Chapter 4. The experiment set up was identical, but the random wave conditions ran significantly longer than the regular wave conditions, as wave reflection did not induce standing waves. The reflection coefficient K_r during each test run was measured, and the reflected wave signal was subtracted from the incoming wave signal before post-processing. The duration of a random wave test run was set at 420 s during which around 250 waves were generated after the spin-up period. Motivated by the large number of waves per run, each condition was only run once.

Four random wave conditions that differed in water depth were tested (Table 6.1). The water depth ranged from 0.30 to 0.60 m. The input wave spectrum at the wavemaker was a JONSWAP spectrum (*Hasselmann et al.*, 1973) with peak enhancement parameter $\gamma_j = 3.3$. The significant wave height H_s was set at 0.15 m for $h = 0.4$–0.6 m and at $H_s = 0.10$ m at $h = 0.30$m. This corresponded to a root-mean-square wave height H_{rms} of approximately 0.10 m and 0.065 m respectively. H_{rms} was obtained from zero up-crossing of the time series measured at WG1, using MODIFIEDMZEROCROSS by *Eusebius* (2015). The peak period of each wave condition was set at $T_p = 1.8$ s. The reflection coefficient under these conditions ranged from 0.18 to 0.36. Thus, the energy of the reflected spectrum was 3-13% of the incident wave spectrum.

The measured distribution of wave heights and periods at WG1 in front of the vegetation field matches the Rayleigh distribution well. Fig. 6.1 shows the distributions of H and ω over flexible vegetation at each water depth. These results are also representative for rigid vegetation. The wave heights correlate very well with Eq. 6.1 with an average $r^2 = 0.89$ over the rigid and flexible vegetation runs combined. The wave frequencies are concentrated around the peak frequency, but high-frequency waves are observed at each water depth. The period of approximately 10% of the waves exceeds ω_p by more than a factor two. No waves were found to have a frequency smaller than $0.5\omega_p$. Given that the observed wave heights correlate very well with the Rayleigh distribution and 90% of the wave frequencies is within the range $0.5\omega_p \leq \omega \leq 2\omega_p$, the Rayleigh distribution is considered a good approximation of the simulated wave spectra.

Like regular waves, rigid vegetation damps random waves more than flexible vegetation. The random wave damping coefficient $\hat{\beta}$ is fitted to the reduction of the total energy contained in the wave spectrum (*Anderson and Smith*, 2014) in a manner similar to the regular wave tests (Section 4.3.4). The results are presented

Table 6.1: List of observed wave dynamics of random waves travelling over rigid and flexible vegetation. $H_{rms,0}$ is obtained from WG1 and u_c is estimated from linear wave theory at the upstream edge of the vegetation halfway the stem height.

				Rigid			Flexible		
	$\boldsymbol{H_s}$	$\boldsymbol{T_p}$	$\boldsymbol{h}$	$\boldsymbol{H_{rms,0}}$	$\boldsymbol{K_r}$	$\hat{\boldsymbol{\beta}}$	$\boldsymbol{H_{rms,0}}$	$\boldsymbol{K_r}$	$\hat{\boldsymbol{\beta}}$
Case	**[m]**	**[s]**	**[m]**	**[m]**	**[-]**	**[1/m]**	**[m]**	**[-]**	**[1/m]**
IR7	0.15	1.8	0.6	0.101	0.18	0.045	0.099	0.19	0.025
IR17	0.15	1.8	0.5	0.097	0.23	0.056	0.096	0.23	0.012
IR27	0.15	1.8	0.4	0.093	0.29	0.078	0.093	0.29	0.004
IR37	0.10	1.8	0.3	0.065	0.35	0.141	0.065	0.36	0.042

in Table 6.1. $\hat{\beta}$ ranged from 0.045 m^{-1} to 0.141 m^{-1} for rigid vegetation. $\hat{\beta}$ was lower over flexible vegetation for every wave condition. Wave damping reduced by 44-80% for cases IR7, IR17 and IR37, which is consistent with our results of the regular wave cases. However, the wave damping over flexible vegetation under conditions IR27 is very low at $\hat{\beta} = 0.004$. $\hat{\beta}$ is significantly lower than that of IR7 and IR37, whereas it is expected to lie in between that of IR7 and IR37 following the experimental results based on rigid vegetation. $\hat{\beta}$ is also lower than the damping results under any of the regular wave height conditions. Thus, the measured wave damping under condition IR27 appears to be inconsistent with other experimental results, but it is unclear what causes the very low $\hat{\beta}$ given the limited test runs with random waves. A similar argument may also be made for the damping observed under case R17 with flexible vegetation, but with less certainty as the damping of case IR17 is much closer to that of case IR7. Therefore, the low damping of case IR17 may also be related to experimental variability.

6.4 Validation

We validate the random wave damping model (Eq. 6.6) against the measured wave damping over five vegetation species, which were also used to validate the regular wave damping model. These include wave damping by the rigid and flexible artificial vegetation (Section 6.3) and against three species of real salt marsh vegetation: *S. Anglica*, *P. Maritima* (*Lara et al.*, 2016; *Maza et al.*, 2015; *Losada et al.*, 2016) and *E. Athericus* (*Möller et al.*, 2014; *Rupprecht et al.*, 2017). These species have cylindrical stems and have been tested under random waves in large-scale flumes but differ in dimensions and flexibility. The vegetation dimensions and the test facilities are described in detail in Section 5.5.2. The test conditions

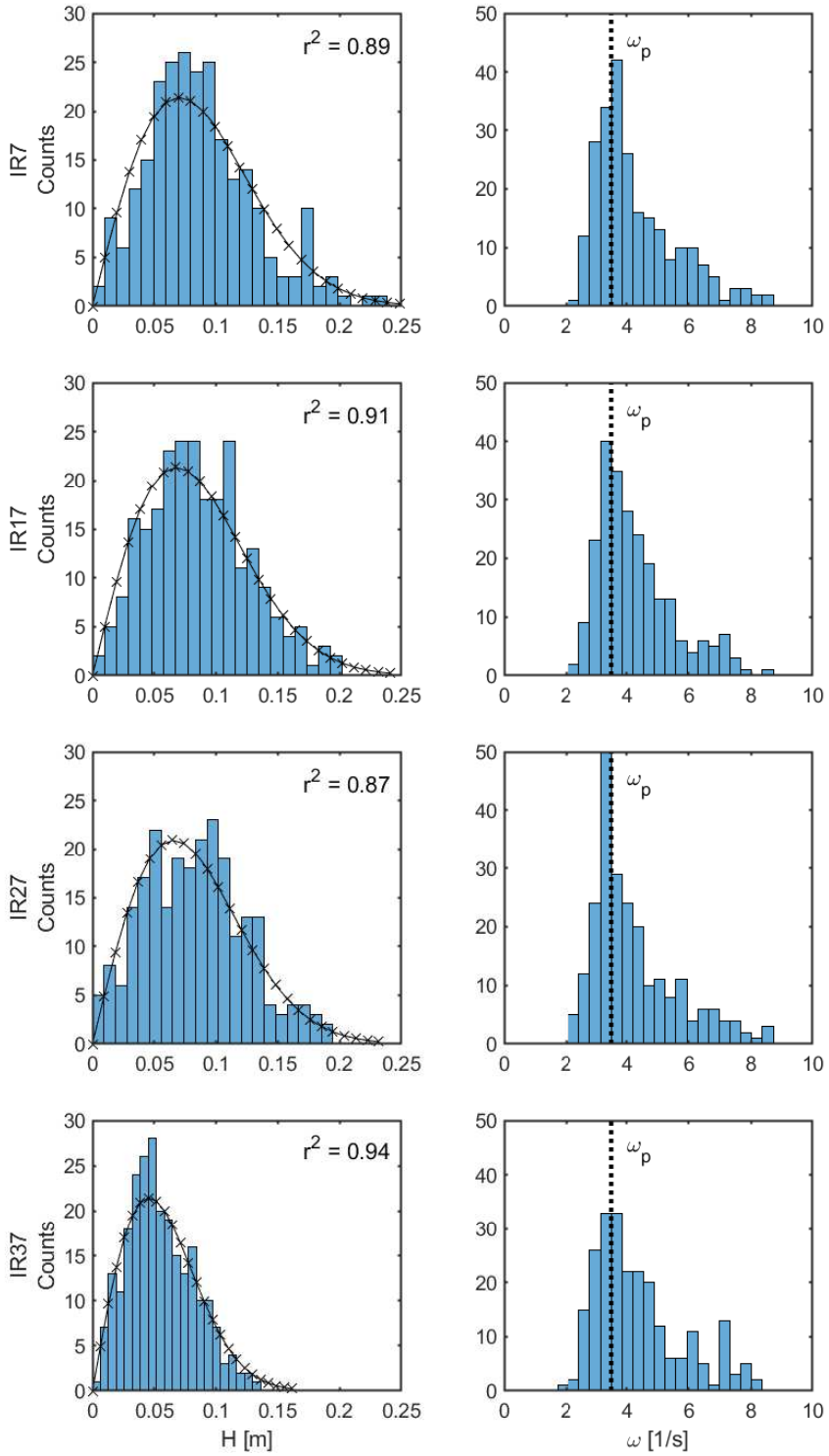

Figure 6.1: Distributions of the measured wave heights (left) and frequencies (right) at WG1. The results shown are from the flexible vegetation runs. The solid line with crosses denotes the Reyleigh distribution (Eq. 6.1, left) and the dotted line denotes the peak wave frequency ω_p (right).

varied in water depth, wave height, wave period and vegetation density such that the model is validated across a wide range of wave and vegetation conditions (Table 6.2).

The three real vegetation species were subjected to medium and high energy wave conditions. *S. Anglica* and *P. Maritima* were subjected to random wave spectra with $H_s = 0.12$ m and $T_p = 1.7$ s at water depths $h = 0.40$ and $h = 0.60$ m. The density of the vegetation ranged between n_v = 430-730 stems/m^2 for *S. Anglica* and between n_v = 877-2436 stems/m^2 for *P. Maritima*. Here, H_{rms} was estimated from H_s using $H_{rms} = H_s/\sqrt{2} \approx 0.085$m (*Reeve et al.*, 2012). *E. Athericus* was tested at water depth $h = 2$ m and under varying JONSWAP wave spectra. H_{rms} ranged from 0.12m to 0.87m and T_p ranged from 1.5 to 6.2 s. The vegetation density reduced from $n_v = 1225$ to $n_v = 666$ stems/m^2 as the experiments progressed due to stem breaking. The stem densities are based on stem breaking data reported in *Rupprecht et al.* (2017).

$\hat{\beta}$ is computed based on the plant and wave conditions of individual runs through Eq. 6.6. The drag coefficient C_{Dw} for all species is given by Eq. 5.9. The root-mean-square wave height used to estimate the velocity scale is obtained at halfway the stem length and at the centre of the vegetation field, as an estimate of the spatially averaged velocity.

The random wave model reproduces observed wave damping very well, but the estimated wave damping for individual species can be further improved (Fig. 6.2, Table 6.2). The goodness-of-fit is very good at $r^2 = 0.68$ and $\hat{\beta}$ is predicted in the right order of magnitude for all vegetation species. The best results are obtained for *S. Anglica* and *P. Maritima* for which all data is centred around the line of perfect fit, which is reflected in a low NRMSE for both *S. Anglica* (0.29) and *P. Maritima* (0.23). The wave damping is overpredicted by a factor 2.4 in case of rigid artificial vegetation for all test conditions, leading to a high NRMSE of 1.57. As a difference to regular wave damping, the velocities are based on linear wave theory instead of direct measurements. The regular wave tests revealed that orbital velocities are preferentially damped within a rigid vegetation canopy. The measured velocity was 20% lower than estimated from the linear wave theory. As $\hat{\epsilon}_{v*}$ is proportional to u_*^3, an overestimation of the velocity by 20% results in an overestimation of the wave damping by a factor 1.95. This explains most of the overprediction in the modelled $\hat{\beta}$ of rigid vegetation. However, the orbital velocities were not measured during the random wave tests. Therefore, the presence of preferential velocity damping could not be verified.

The wave damping over flexible artificial vegetation is reproduced well under cases FM1 and FM4, and reasonably under case FM2 but the model overpredicts wave damping under case FM3 by a factor 11. Case FM3 corresponds to wave condition IR27 in Section 6.3, which was found to be inconsistent with other

experimental results. This outlier results in a high NRMSE of 1.31. Finally, the wave damping over *E. Athericus* is correctly predicted a magnitude lower than the other vegetation species with the exception of case EA1, where wave damping is underpredicted by a factor 5. Conversely, $\hat{\beta}$ is overpredicted by a factor 1.7 on average for all other cases. The NRMSE is 0.81. Several factors may contribute to the observed overprediction. First, the orbital velocities may be damped preferentially in the vegetation canopy, but this cannot be verified as no velocity data exists. Second, six of the fourteen conditions have a Re lower than 300, which is outside the range for which C_{Dw} has been derived. The extrapolation to lower Re (as low as $Re = 20$ for case EA1) comes with additional uncertainty. Finally, *Möller et al.* (2014) find that the calibrated C_{Dw} of *E. Athericus* under random waves responds more strongly to variations of Re ($C_{Dw} \propto Re^{1.6}$) than under regular waves ($C_{Dw} \propto Re$). Here, we have applied the same C_{Dw}-relation for both regular and random waves which does not reflect this variability.

The model may be further improved by including preferential wave damping within the vegetation canopy and a C_{Dw}-relation that is developed based on irregular waves and a wider range of Re. *Lowe et al.* (2005) developed a model for wave damping inside the canopy based on the wave excursion length, stem diameter and stem spacing. These parameters are already included in our model, and both models could potentially be coupled to include preferential velocity damping. As *Lowe et al.* (2005) developed their model based on coral reefs with a diameter of 100 mm, their model would require validation before it is applied to salt marsh species that typically have a diameter smaller than 10 mm (*Mullarney and Henderson*, 2018). Furthermore, a new C_{Dw}-relation that is derived specifically for random waves and for a wider range of Re can improve the model predictions, as the C_{Dw}-relation used in this studied was developed specifically for regular waves and for $300 < Re < 4700$. Despite these limitations, the goodness-of-fit observed of the random wave damping model ($r^2 = 0.68$) is equally strong as that of the regular wave model ($r^2 = 0.66$).

6.5 Conclusions

We have successfully extended our model of regular waves over coastal vegetation, described in Chapter 5, to random wave climates. Assuming a Rayleigh wave spectrum and the validity of linear wave theory, we compute a work factor for every wave height in the wave spectrum. The random wave damping coefficient $\hat{\beta}$ is obtained by integration over the full wave spectrum and the stem length. Like the regular wave model, the wave damping is a function of plant and wave parameters only and does not require plant-specific calibration of a drag

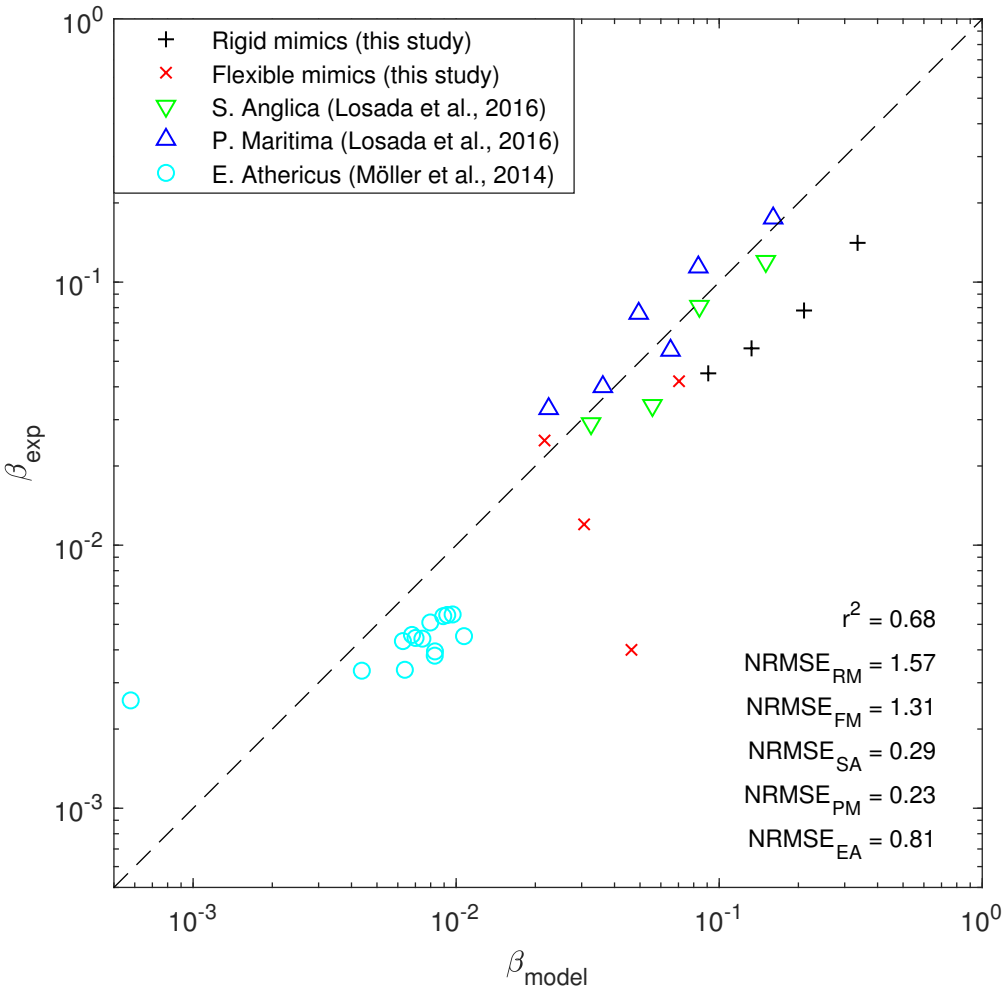

Figure 6.2: Validation of the modelled random wave damping coefficients $\hat{\beta}_{model}$ against measured wave damping coefficients $\hat{\beta}_{exp}$ for five vegetation species. The dashed line denotes the line of perfect fit. The r^2 goodness-of-fit is given, as well as the normalised root-mean-square error (NRMSE) of each specie. RM: Rigid mimics; FM: Flexible mimics; SA: *S. Anglica*; PM: *P. Maritima*; EA: *E. Athericus*.

Table 6.2: List of model validation data.

Case	Specie	n_v [m^{-2}]	h [m]	$H_{rms,0}$ [10^{-2}m]	T_p [s]	u_c [m/s]	β_{exp} [10^{-3}/m]	β_{model} [10^{-3}/m]
RM1	Rigid mimics	1111	0.6	10	1.8	0.15	45	91
RM2	Rigid mimics	1111	0.5	10	1.8	0.17	56	133
RM3	Rigid mimics	1111	0.4	9.3	1.8	0.19	78	210
RM4	Rigid mimics	1111	0.3	6.5	1.8	0.15	141	336
FM1	Flexible mimics	1111	0.6	10	1.8	0.15	25	22
FM2	Flexible mimics	1111	0.5	10	1.8	0.17	12	31
FM3	Flexible mimics	1111	0.4	9.3	1.8	0.20	4	46
FM4	Flexible mimics	1111	0.3	6.5	1.8	0.17	42	70
PM1	*P. Maritima*	2436	0.4	8.5	1.7	0.13	175	160
PM2	*P. Maritima*	2436	0.6	8.5	1.7	0.12	55	65
PM3	*P. Maritima*	1389	0.4	8.5	1.7	0.14	114	83
PM4	*P. Maritima*	1389	0.6	8.5	1.7	0.12	40	36
PM5	*P. Maritima*	877	0.4	8.5	1.7	0.16	76	49
PM6	*P. Maritima*	877	0.6	8.5	1.7	0.12	33	22
SA1	*S. Anglica*	729	0.4	8.5	1.7	0.13	120	150
SA2	*S. Anglica*	729	0.6	8.5	1.7	0.12	34	56
SA3	*S. Anglica*	430	0.4	8.5	1.7	0.14	81	84
SA4	*S. Anglica*	430	0.6	8.5	1.7	0.12	29	33
EA1	*E. Athericus*	1225	2	12	1.5	0.02	2.6	0.6
EA2	*E. Athericus*	1225	2	20	2.1	0.09	3.3	4.4
EA3	*E. Athericus*	1225	2	20	2.9	0.14	3.9	8.3
EA4	*E. Athericus*	1225	2	20	2.9	0.14	3.8	8.3
EA5	*E. Athericus*	1225	2	29	2.5	0.17	3.4	6.4
EA6	*E. Athericus*	1225	2	30	3.6	0.24	5.5	9.7
EA7	*E. Athericus*	1086	2	38	2.9	0.27	4.4	7.0
EA8	*E. Athericus*	1086	2	40	4.1	0.34	5.4	9.2
EA9	*E. Athericus*	1086	2	57	3.6	0.46	5.4	8.9
EA10	*E. Athericus*	1086	2	60	5.1	0.55	4.5	10.7
EA11	*E. Athericus*	666	2	74	4.1	0.64	4.3	6.3
EA12	*E. Athericus*	666	2	78	5.8	0.73	4.4	7.4
EA13	*E. Athericus*	666	2	83	4.4	0.73	4.6	6.8
EA14	*E. Athericus*	666	2	87	6.2	0.82	5.1	8.0

coefficient as long as the wave and vegetation conditions satisfy the range for which a preselected C_{Dw}-relation is valid. The validity of the C_{Dw}-relation used in this thesis is $300 < Re < 4700$.

The wave damping model is validated against observed wave damping over artificial rigid and flexible vegetation and three real vegetation species. Wave damping over artificial rigid and flexible vegetation was measured in the Swansea University Coastal Laboratory wave flume. The experiments revealed that waves generated under a JONSWAP sea state agreed well with the Rayleigh wave spectrum assumed in the model (waves heights: $r^2 = 0.89$; wave frequencies: 90% in the range $0.5\omega_p \leq \omega \leq 2\omega_p$). The wave damping over flexible vegetation was 44-80% lower than over rigid vegetation, which agrees with the regular wave damping experiments (Chapter 4). Wave damping measurements over the three real coastal vegetation species *S. Anglica*, *P. Maritima*, and *E. Athericus* were obtained from the literature.

The random wave damping over all vegetation species was reproduced in the right order of magnitude by the model with a goodness-of-fit of $r^2 = 0.68$. The damping over species *S. Anglica* and *P. Maritima* was reproduced best with all data points centred around the line of perfect fit. The wave damping over artificial flexible vegetation is reproduced well for three out of four wave conditions. Although in the right order of magnitude, the wave damping by the rigid artificial vegetation and *E. Athericus* is overpredicted by a factor 2, which may be attributed to preferential damping within the canopy and the limitations of the employed C_{Dw}-relation. The model is expected to improve the predictions for these species when coupled with a model for preferential damping, and when a C_{Dw}-relation specific to random waves is used.

Chapter 7

Computational modelling of the coastal protection function by salt marshes in the Taf Estuary

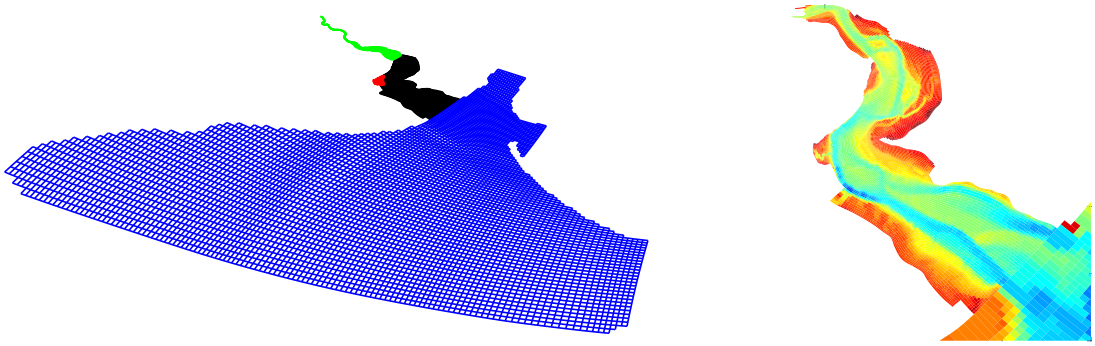

7.1 Introduction

The small-scale interaction of salt marsh vegetation with currents and waves ultimately provides protection to coastal communities by manipulating the wave-current field over large spatial scales. Our investigations into the current-vegetation and wave-vegetation interactions have provided evidence that salt marshes reduce nearshore current velocities and dampen wave heights, which reduces the load on coastal defence structures (*Vuik et al.*, 2016) and can enhance the resilience of coastal communities to flooding (*Sutton-Grier et al.*, 2015). So far, the impact of vegetation on wave and currents has been treated separately and in idealised environments. This is an obvious simplification of the real world where currents and waves simultaneously interact with vegetation. They are also affected by the local bathymetry with spatial variations in water depth and vegetation cover. Furthermore, the offshore wave, wind, and water level variations control the hydrodynamics in estuaries, which have not been considered up to this point. Although our current-vegetation and wave-vegetation models are key elements to quantify the wave-current field around salt marshes, they cannot do so on their own.

Large-scale numerical models are a potentially powerful tool to simulate the coastal defence function of salt marshes (*Hu et al.*, 2018). These models simulate coastal processes, including the hydrodynamic-vegetation interaction, over a spatially varying bed and under the simultaneous forcing of tides, currents and waves. They can provide detailed information on water levels, current velocities and wave climates over large spatial scales. Recently a growing body of studies has used numerical models to simulate storm surge (*Wamsley et al.*, 2009; *Hu et al.*, 2015; *Smolders et al.*, 2015; *Marsooli et al.*, 2016; *Stark et al.*, 2016; *Siverd et al.*, 2019) and wave attenuation (*Wamsley et al.*, 2009; *Vuik et al.*, 2016; *Garzon et al.*, 2019b) over salt marshes.

Although numerical models are supported by experimental and field observations (*Leonardi et al.*, 2018), they may currently provide limited insight into the coastal protection function of salt marshes due to their simplified parameterisation of vegetation. Most models are limited in three ways. First, conditions where the current-vegetation and wave-vegetation interactions are both important are rarely considered (an exception is *Wamsley et al.*, 2009). Second, flexible vegetation can only be considered through the calibration of a drag coefficient in large-scale numerical models (*Tempest et al.*, 2015). Third, models are often restricted to a single vegetation type. A notable example of the latter is the widely used open-source model SWAN (*Suzuki et al.*, 2012). These three simplifications induce uncertainties in the model outputs, which limit the insight they give in the coastal protection provided by salt marshes.

In this chapter, we aim to improve our understanding of the contribution of salt marshes to coastal protection by implementing our current-vegetation and wave-vegetation modelling techniques in the large-scale coastal modelling suite Delft3D. The current-vegetation interaction will be modelled via a momentum sink term, which was found to best resemble expected physical behaviour in a comparison of four different current-vegetation parameterisations (Chapter 3). The wave-vegetation interaction will be modelled through the physics-based random wave-vegetation interaction model, which was developed in Chapter 6, hereinafter referred to as the full flexible model. This model includes the effect of plant motion explicitly based on wave and vegetation conditions without the calibration of a drag coefficient. As the wave energy dissipation is solved per individual stem, the wave damping over multiple species can be included in our model. Furthermore, the interaction of currents and waves with vegetation will be modelled simultaneously for a selected case study site (Taf Estuary). The new current-wave-vegetation interaction model to simulate coastal protection by salt marshes will overcome the three limitations that were identified in current modelling techniques.

The Taf Estuary is selected as the case study site. It features the historic village of Laugharne, which solely relies on salt marshes for its protection against coastal flooding. Salt marshes cover an extensive area within the estuary and exhibit a wide variety of species, ranging from woody shrubs to flexible grasses. The flood risk in the estuary is simultaneously driven by storm surges and waves. The combination of storm surges, waves, and flexible salt marsh species makes the Taf Estuary a suitable case study to simulate the contribution of salt marshes to coastal protection. The new current-wave-vegetation model will be referred to as the Taf model.

This chapter is organised as follows: Section 7.2 describes the Taf Estuary in detail. Then, Section 7.3 discusses the set-up of the Taf model. Six vegetation scenarios are selected in Section 7.4 to investigate the impact of different vegetation conditions. The modelled water depth, current and wave fields are presented in Section 7.5. Section 7.6 compares the modelled wave field against predictions by the full flexible model. Finally, conclusions regarding the contributions of salt marshes to coastal protection are drawn in Section 7.7.

7.2 Study area: Taf Estuary

The Taf Estuary is situated in Carmarthen Bay in South Wales, United Kingdom (Fig. 7.1). The estuary is formed by a sinuous valley through which the river Afon Taf discharges into Camarthen Bay. The valley was cut out of red sandstone by glaciers during the last ice age (*Pye and Blott*, 2009). The boundaries of the current estuary are formed by its mouth between Ginst and Wharley point, and the tidal limit at St Clears (*Ishak*, 1997; *Pye and Blott*, 2009). The estuary measures 15 km in length and is 1.5 km wide at the mouth. Its width gradually narrows to 40 m at St Clears. The Taf Estuary confluences at its mouth with the Towy and Gwendraeth Estuaries (Fig. 7.1b). They share a common entrance into Carmarthen Bay, which is known as the Three Rivers Estuary.

The estuary can be classified as a macro-tidal spit-enclosed estuary (*Pye and Blott*, 2014). It has a spring tidal range of 7.5 m (*Jago*, 1980). The estuary measures a total wet area of approximately 7.5 km^2 between its mouth and St Clears at high tide (*Ishak*, 1997). During low water, the estuary empties almost completely, and the extensive tidal flats are exposed (Fig. 7.1c). The estuary is flood-dominant with a tidal prism that ranges from 0.67×10^7 m^3 to 1.86×10^7 m^3 over the spring-neap cycle. The spit at Ginst point has developed following a gradual extension of the sand dunes from Pendine in the past 10,000 years in combination with land reclamation (*Walley*, 1996).

The Afon Taf is a small river with an average freshwater discharge of 7.0 m^3/s (*Ishak*, 1997). Extreme discharges range between 0.6 and 60 m^3/s in summer and winter respectively. Additionally, the rivers Cywyn and Coran discharge into the Taf Estuary. The river Cywyn discharges upstream of Laugharne, and the river Coran discharges through Laugharne. Both rivers are small streams with significantly smaller catchment areas than the Taf.

Laugharne is situated on the outer bend of the downstream-most turn in the estuary. The village is only separated from the estuary by a salt marsh. It has experienced major flooding events in the past centuries (Read, pers. comm) and a risk of coastal flooding was also identified in the most recent Shoreline Management Plan (SMP2; *Halcrow Group Ltd.*, 2012). A surge barrier has been proposed to mitigate flood risk, but this was rejected by the local community. Therefore, Laugharne remains at risk of coastal flooding.

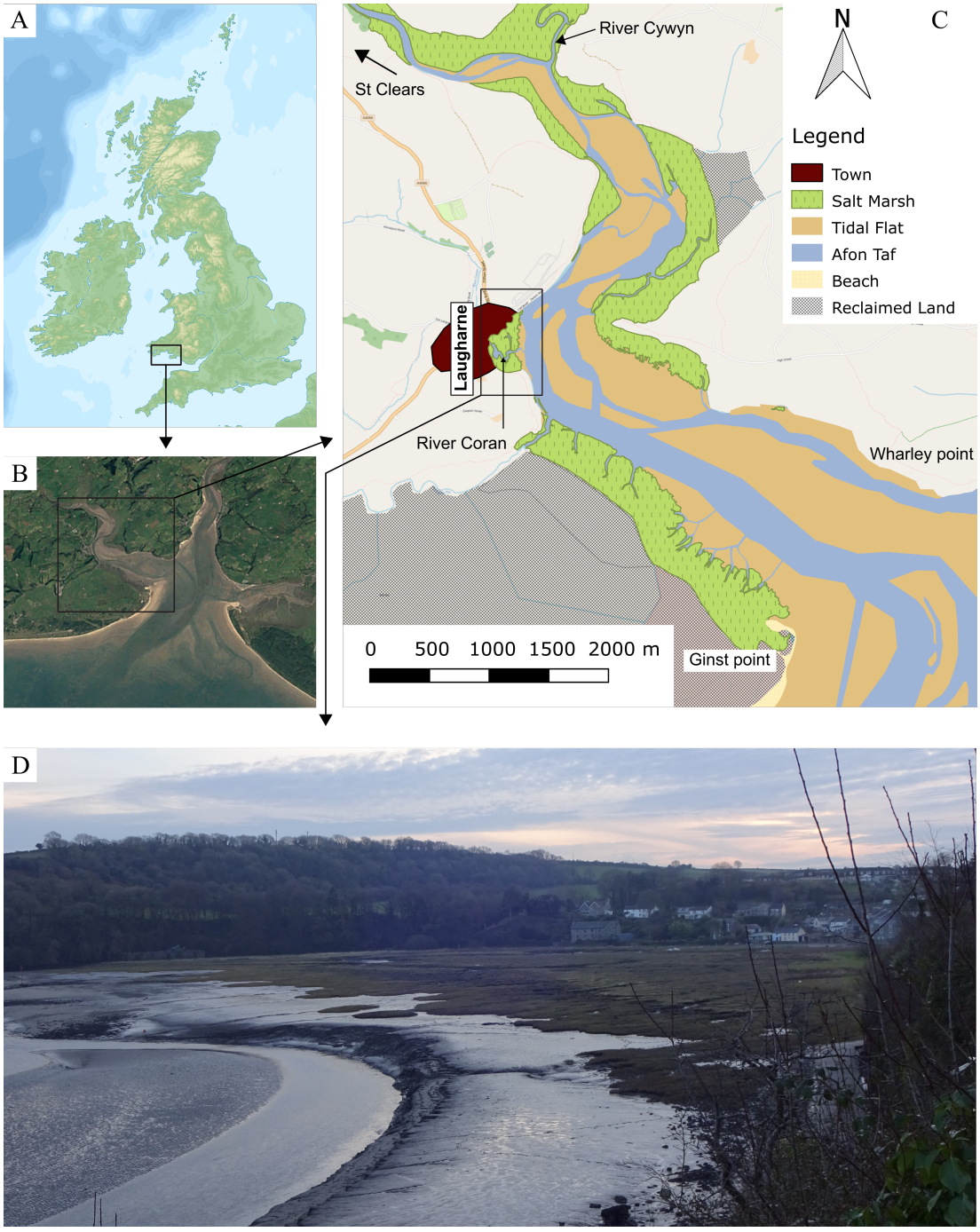

Figure 7.1: Topography of the Taf Estuary. (a) The British Isles; (b) the Three Rivers Estuary; (c) the Taf Estuary; (d) view on Laugharne and Laugharne Castle Marsh from the northern shore. Source (a): *Hellerick* (2013). Source (b): *Google Earth* (2018). Data courtesy of the salt marsh extents in (c): Contains Natural Resources Wales information © Natural Resources Wales and Database Right. All rights Reserved.

7.2.1 Salt marshes

The Taf Estuary features extensive salt marsh areas along its shorelines. The salt marshes have been rapidly expanding in the past century and currently occupy 279 ha in total in the estuary (*Bristow and Pile*, 2003). The lower estuary contains four salt marshes (Fig. 7.2). First, Laugharne Castle Marsh is located between Laugharne and the main estuary channel. The river Coran discharges through the marsh and acts as a salt marsh creek. Second, Laugharne South Marsh is located downstream of Laugharne and stretches from St. John's hill to Ginst point. Third, Laugharne North Marsh is located one kilometre upstream of Laugharne on the inner side of a bend in the estuary. Finally, Blackscar Marsh is located on the opposite of Laugharne, where it stretches through both valley bends. Laugharne Castle Marsh and Laugharne North Marsh are significantly smaller than Laugharne South Marsh and Blackscar Marsh.

The vegetation on the four salt marshes in the lower estuary has been classified according to the National Vegetation Classification (NVC; *Pigott et al.*, 2000). An NVC-type can be dominated by a single species or feature a mix of species. The classification was conducted in-situ in summer and autumn 2017. Eleven NVC-types were identified in the Taf Estuary (Fig. 7.2). The dominant NVC-type was SM14 which comprises almost half (48.6%) of the total salt marsh area (Table 7.1), mostly on the middle marshes. The NVC-types SM16 and SM6 are second and third most widespread with 13.1% and 12.7% relative area respectively. They are predominantly located on the higher and lower marshes respectively.

Species within an NVC-type were identified by field sampling. A 250×250 mm metal quadrat was haphazardly placed to obtain an unbiased selection of species present. The species and their relative cover of the ground area were identified visually. A cover of 100% denotes that the substrate is fully covered. A cover of less than 100% means that bare substrate is visible and a cover of more than 100% is obtained when the substrate is covered by multiple species simultaneously. 125 quadrats were sampled this way. The relative cover per species within an NVC-type was found through averaging. The cover per species over the full estuary was found trough weighted averaging with respect to the area across all NVC-types. NVC-types MG13 and SM18 were not sampled. MG13 is a terrestrial NVC-type, which does not exhibit typical salt marsh species, and SM18 was omitted given its small area.

The average vegetation cover in the Taf Estuary is 102%, of which 89% is covered by the five dominant species (Table 7.1). The most dominant species is the woody semi-flexible shrub *Atriplex Portulacoides* (Fig. 2.4a), most commonly found on the middle marshes, with a 49% cover. The second most dominant species is the semi-flexible tall grass *Spartina Anglica* (Fig. 2.4b), most commonly found on the lower marshes, with a 17% cover. Third and fourth are the flexible

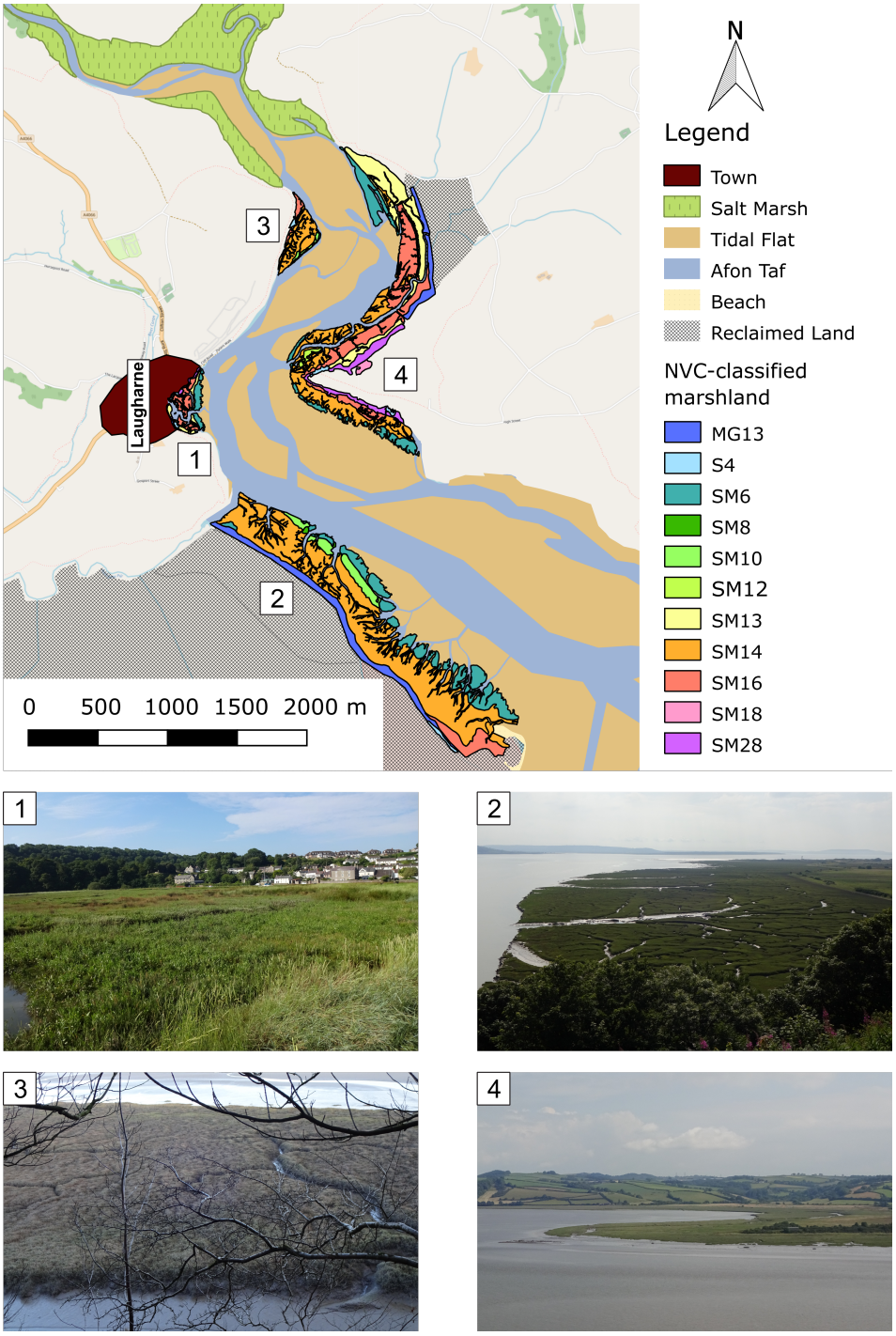

Figure 7.2: The four salt marshes in the lower Taf Estuary have been classified according to NVC-type. These salt marshes are (1) Laugharne Castle Marsh; (2) Laugharne South Marsh; (3) Laugharne North Marsh; (4) Blackscar Marsh. Data courtesy of the NVC-type classification: Tom Fairchild. Data courtesy of the upper estuary salt marsh extents: Contains Natural Resources Wales information © Natural Resources Wales and Database Right. All rights Reserved.

Table 7.1: List of vegetation species per NVC-type. Vegetation data provided by Tom Fairchild. AP: *A. Portulacoides*; SA: *S. Anglica*; FR: *F. Rubra*; PM: *P. Maritima*; AT: *A. Tripolium*. n is the number samples taken.

NVC Type	**AP**	**SA**	**FR**	**PM**	**AT**	**Other**	**Cover [%]**	**Area [%]**	***n***
MG13	-	-	-	-	-	-	-	9	0
S4	0	0	0	0	0	100	100	1	4
SM6	2	94	0	0	0	4	100	13	48
SM8	0	0	0	0	0	100	100	0	1
SM10	32	15	4	12	16	28	107	3	10
SM12	8	0	15	15	55	8	101	0	2
SM13	11	6	16	41	12	16	102	9	5
SM14	87	5	1	2	2	4	102	49	37
SM16	1	0	52	14	14	24	105	13	16
SM18	-	-	-	-	-	-	-	< 0.1	0
SM28	3	0	23	0	8	63	95	4	2
Weighted average	49	17	10	8	5	12	102		

grasses *Festuca Rubra* (Fig. 2.4c) and *Puccinellia Maritima* (Fig. 2.4d), both found on the higher marshes, with 10% and 8% cover respectively. Fifth is the rigid flower *Aster Tripolium* (Fig. 2.4e), which is found on the lower marshes, with 5% cover. 12% of the cover is provided by other vegetation species such as *Plantago Maritima* and *Elymus Repens*.

Samples of each of the five most common vegetation types were brought to the lab to measure the dimensions and the flexural rigidity of each specie. Details on the procedure are provided in Appendix A. The vegetation parameters that were obtained in the lab are listed in Table 7.2. The flexibility of each vegetation species is defined by its flexural rigidity EI_v and its scaled flexibility Q (Eq. 5.20, Section 5.4.2) based on wave conditions that are representative for the selected storm conditions (Section 7.3).

Table 7.2: Cover and plant parameters of the five dominant species in the Taf Estuary. The number of samples n is given separately for geometrical and mechanical tests. The scaled flexibility Q is computed using Eq. 5.20 with $h = 2$ m, $H_{rms} = 0.53$ m, $T_p = 3$ s and at first iteration, i.e. $a_v = 0$.

Specie	h_v [mm]	b_v [mm]	n_v [m^{-2}]	λ_f	n	EI_v [Nm^2]	Q	n
A. Portulacoides	334	2.58	2275	1.96	72	1.6×10^{-3}	12	10
S. Anglica	590	3.33	720	1.42	72	8.4×10^{-4}	264	4
F. Rubra	231	0.74	36000	6.08	9	3.4×10^{-5}	99	11
P. Maritima	335	0.85	3444	0.98	27	1.9×10^{-5}	785	15
A. Tripolium	487	5.50	214	0.57	24	2.6×10^{-2}	6	4

7.3 Model setup

We develop a current-wave-vegetation model of the Taf Estuary using Delft3D to investigate the contribution of salt marshes to coastal protection for this case study site. The coastal modelling suite Delft3D (*Lesser et al.*, 2004) has been successfully applied to study hydrodynamics in estuaries (*Ashall et al.*, 2016) and over salt marsh vegetation (*Temmerman et al.*, 2005). Delft3D consists of two main components: D-FLOW and D-WAVE. D-FLOW simulates the hydrodynamics excluding waves, such as currents, storm surges and stratification. D-WAVE simulates wave dynamics including wind-driven wave growth, depth-induced breaking and diffraction, using SWAN (*Booij et al.*, 1999). Rigid vegetation can be included in D-FLOW and D-WAVE. A two-way coupling between D-FLOW and D-WAVE is used, such that relevant hydrodynamical parameters are actively exchanged between the two modules.

The proven capability of Delft3D to model water levels, currents and wave fields around rigid vegetation, makes it a suitable modelling suite for this study. Wave damping over flexible vegetation is introduced by modifying vegetation input in D-WAVE based on our full flexible vegetation model. The combined current-wave-vegetation model of the Taf Estuary will be applied to simulate the hydrodynamics during a 1 in 100 year storm event.

7.3.1 Model domain

The model domain (Fig. 7.3) encompasses the Taf Estuary, the Three Rivers Confluence and the northern part of Carmarthen Bay. The offshore limit of the domain is located between Monkstone headland in the west and Burry Holms headland in the east. Extending the offshore limit in seaward direction did not affect the hydrodynamics within the Taf Estuary. The landward boundary is located at the tidal limit near St Clears. The Towy, Gwendraeth, and Loughor Estuaries are not modelled beyond their mouth, because it is expected that the dynamics within these estuaries do not affect the dynamics within the Taf Estuary.

The model domain is divided into four subdomains which differ in resolution. The four subdomains are: the bay, the lower estuary, Laugharne Castle Marsh, and the upper estuary. The bay subdomain covers Carmarthen Bay and the Three Rivers Confluence. It connects to the lower estuary between Ginst Point and Wharley Point. The resolution of the grid cells is approximately 200×400 m (cross × along dominant flow direction) at the offshore boundary and converges to cells of 100×100 m at the mouth of the Taf. The lower estuary ranges from the mouth of the Taf up to the upstream limits of the Laugharne North and Blackscar marshes. It connects to the upper estuary grid at its upstream boundary and to Laugharne Castle Marsh near Laugharne. This subdomain covers the Laugharne South, Laugharne North and Blackscar salt marshes but not Laugharne Castle Marsh. The grid cells range from 50×30 m at the mouth of the Taf to 25×20 m at the boundary of Laugharne Castle Marsh and 10×15 m at the upstream boundary. The Laugharne Castle Marsh subdomain encompasses the salt marsh in front of Laugharne. This subdomain is key to evaluate the flood risk for Laugharne. Therefore, the hydrodynamics in this domain are computed at the high resolution of 10×10 m and using ten vertical layers. Finally, the upper estuary domain ranges from the upstream boundary of the lower estuary to the tidal limit at St Clears. The grid cells measure approximately 20×30 m at the downstream boundary and reduce to 5×5 m at the upstream tidal limit. The selected grid resolution is based on the desired output resolution and a sensitivity analysis. The grid is the finest at the main area of interest at Laugharne Castle Marsh and the coarsest offshore in Carmarthen Bay. Furthermore, a sensitivity analysis showed that the hydrodynamics did not change on a finer grid.

The four subdomains were connected through domain decomposition boundaries between the domains in D-FLOW (*Deltares*, 2018). These provide a mutual exchange of hydrodynamic parameters between adjacent subdomains. Alternatively, the domains were nested within D-WAVE. Unlike domain decomposition, wave parameters are only transferred from the outer domains into the inner domains but not in reverse. This is acceptable as waves travel strictly from the

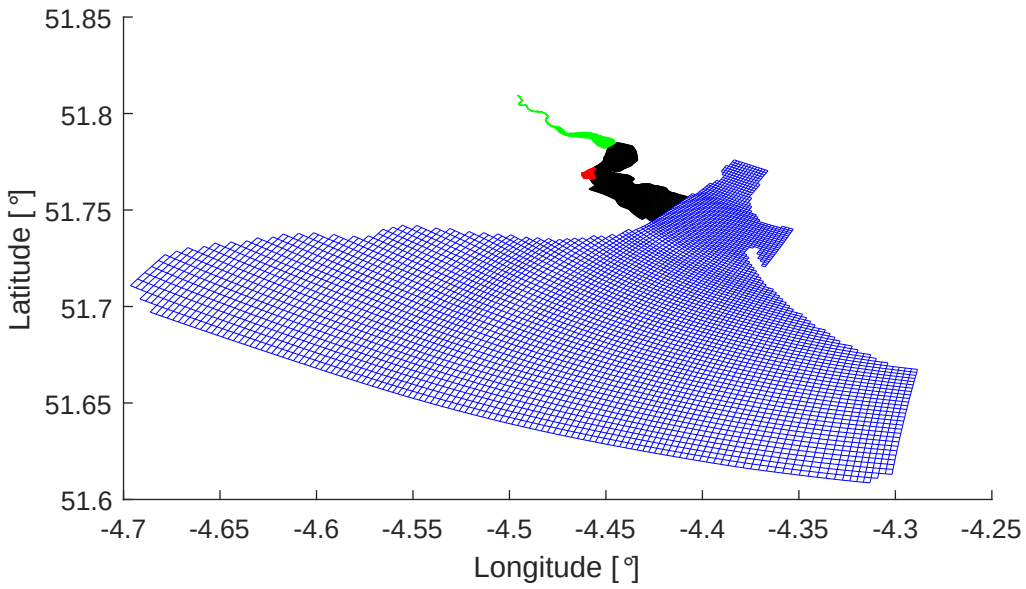

Figure 7.3: The computational model domain of the Taf model with four subdomains: the bay (blue), the lower estuary (black), the Laugharne Castle Marsh (red), the upper estuary (green).

offshore to the coastline. The order of nesting is (from the outer to the inner domain): bay, lower estuary, upper estuary, and Laugharne Castle Marsh.

The bathymetric data of the Taf Estuary has been obtained from various sources. The bathymetry within the lower Taf Estuary was measured during a new field campaign between 21 and 25 August 2017. The bottom elevation was measured using a small rigid-hull inflatable boat equipped with a single-beam sidescan sonar system (Simrad NSS Evo3 with Lowrance Structurescan 3D +Hi/Lo CHiRP Transducer). The bathymetry of the salt marshes and the shallower upper estuary was obtained from LiDAR data, surveyed by National Resources Wales (NRW) in 2013. The offshore bathymetry in Carmarthen Bay was obtained from multi-beam echo-sounder measurements by the UK Hydrographic Office (UKHO), who surveyed Carmarthen Bay at a 2 m resolution in 2013 up to the 5 m depth contour. No recent dataset was available for the Three Rivers Confluence. This bathymetry has been obtained from admiralty charts from 1977, which was the most recent data source available. The range of bathymetric data sets, which have been sampled by various methods and at different times, may inevitably induce errors. Therefore, the boundaries between different bathymetries have been smoothed to ensure a continuous seabed. Furthermore, the bathymetry has been compared with recent satellite imagery (*Google Earth*,

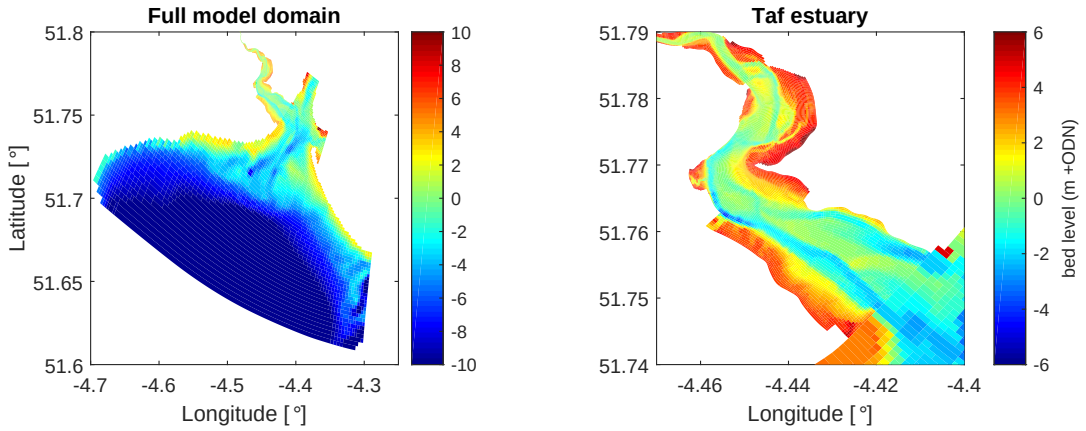

Figure 7.4: Bathymetry of the Taf model over the full model domain (left) and a close-up of the Taf Estuary (right).

2018) and visual observations at low tide during field trips to verify the model bathymetry as good as possible. The resulting bathymetry is shown in Fig. 7.4.

The model time step is set differently in D-WAVE and D-FLOW. The time step in D-FLOW is set at 3 s and the time step in D-WAVE is set at 900 s. This means that the wave wave field is computed after every 300 time steps in D-FLOW. The wave dynamics (and the wave input from D-WAVE into D-FLOW) are assumed constant over this period. This methodology is justified by the slower time scale over which the wave field changes compared to currents and water levels, and significantly reduces the computational cost.

7.3.2 Storm conditions

The storm conditions are defined by the wind, wave, water level and river discharge conditions. The storm event lasts for 75 h with increasing and receding wind, waves and water level over this period (*Bennett et al.*, 2020). The Taf Estuary and Laugharne may be vulnerable to two contrasting storm types that differ in wind direction (*Pye and Blott*, 2009). A preliminary study is conducted to identify the critical storm type. Subsequently, the associated wind, wave, water level and river discharge conditions are derived based on the selected storm conditions. These are used to force the hydrodynamics in the Taf model.

Storm type

Two contrasting storm types can produce flood risk in the Taf Estuary (*Pye and Blott*, 2009). First, the south-westerly storm is characterised by wind and swell waves from the Atlantic Ocean. The fetch length in this direction can be as large as 6000 km, which generates fast winds and high waves. However, it is unclear to what extent these can enter the estuary. The orientation of the estuary is perpendicular to this storm direction, and the entrance is sheltered behind Ginst point. Therefore, waves can only enter the estuary through diffraction which lowers their height. Alternatively, the easterly storm condition is characterised by moderate wind speeds and locally generated wind waves. The wind speed and wave height are limited by the reduced fetch of an easterly storm, but the direction of wave propagation is parallel to the main axis of the lower estuary. The wave field is expected to enter the estuary undisturbed, which may lead to higher waves at Laugharne despite the lower wind speed and offshore wave height.

A preliminary study has been conducted to determine the critical storm direction. The south-westerly wind direction is set at 255° with respect to the north (0° represents wind coming from the north), which is from the direction of the longest fetch. Alternatively, the easterly wind direction of 115° is parallel to the primary axis of the estuary. This section uses preliminary estimates of the extreme wind speed, offshore wave height and water level. The wind speed and wave height are estimates of their 1 in 100 year conditions. The water level is based on a 1 in 10 year condition. The offshore wave and water level conditions are set identical, as they arrive from the Atlantic Ocean and are considered independent from the local wind field. The discharge of the Taf is set at its average of 7.0 m^3/s (*Ishak*, 1997) and vegetation is not included. The full set of preliminary storm parameters is listed in Table 7.3. Each storm parameter will be re-evaluated in detail in Section 7.3.2 for the selected storm direction.

A comparison between the two storm directions shows that the easterly storm is critical for the wave height inside the Taf Estuary (Fig. 7.5). Although the south-westerly storm produces higher waves at the mouth of the Taf, the waves under the easterly storm maintain their height over a longer distance inside the estuary. The significant wave height at the seaward edge of Laugharne Castle Marsh is 0.3 m under the south-westerly storm compared to 0.8 m under the easterly storm direction. Therefore, the easterly storm is selected as the critical condition in the Taf Estuary.

Table 7.3: List of parameters of south-westerly and easterly storm conditions in a preliminary study. The wind and wave direction are with respect to north, i.e. $\theta_{wind} = 0$ denotes wind coming from the north.

Parameter	**Symbol**	**South-westerly storm**	**Easterly storm**	**Unit**
Peak wind speed	u_{wind}	27.73	16.28	m/s
Wind direction	θ_{wind}	255	115	°
Peak wave height	H_{max}	8.66	8.86	m
Maximum wave period	T_{max}	6.82	6.82	s
Wave direction	θ_{wave}	225	225	°
Peak water level	h_{max}	5.26	5.26	m
River discharge	Q_r	7.0	7.0	m^3/s
Storm duration	T_{storm}	75	75	h
Vegetation	-	no	no	-

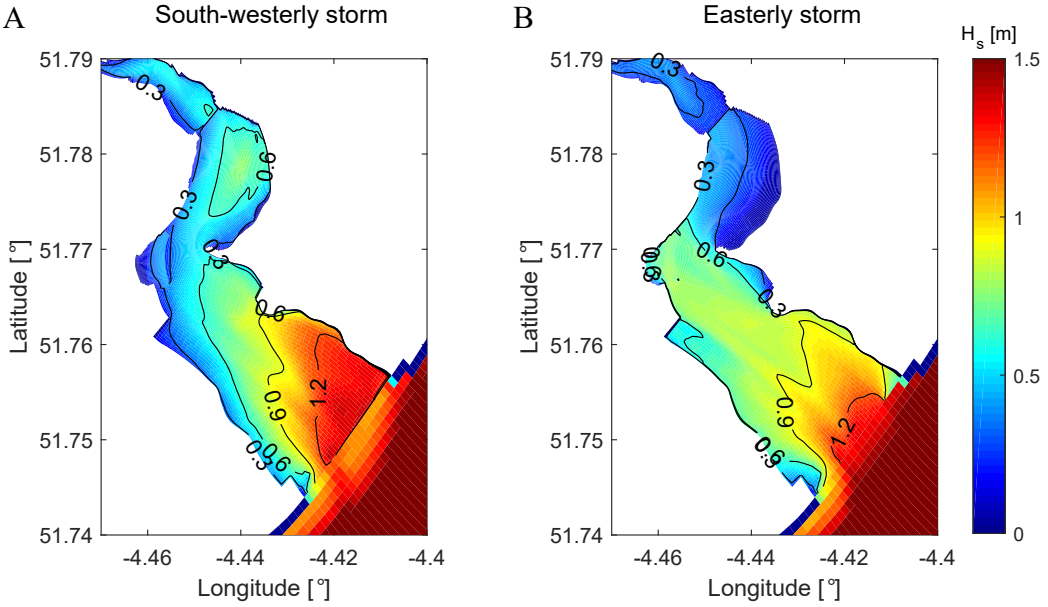

Figure 7.5: Modelled wave heights under (a) a south-westerly storm direction and (b) an easterly storm direction.

Boundary conditions

The wave, wind and water level conditions under extreme events in the Taf Estuary were statistically derived in *Bennett et al.* (2020). We select conditions with a 1 in 100 year probability for this study. The offshore significant wave height for a 1 in 100 year storm event was found to be 8.66 m. The corresponding wave direction is 255°, which is associated with swell waves coming from the Atlantic Ocean. It is assumed that the swell waves are generated on the ocean and are independent of the local wind field. The maximum wave period is 6.82 s. The wind conditions were based on measured wind speeds at the nearby Pembrey weather station. The wind speeds were filtered for winds arriving from easterly direction (between 45 and 135°) to obtain an estimated easterly wind speed of 16.28 m/s under a 1 in 100 year storm event (*Bennett et al.*, 2020). The offshore wave conditions are applied as a boundary condition on the southern boundary of the bay subdomain. The wind conditions are applied uniformly to each grid cell in the domain.

The offshore water level is the superposition of the base astronomical tide and a scaled storm surge (Fig. 7.6). The amplitude of the base astronomical tidal curve is taken between the mean high water spring tide and the highest astronomical tide (*McMillan et al.*, 2011), which is 4.35 m above Ordnance Datum Newlyn (ODN) (*Bennett et al.*, 2020). A scaled surge shape reflects the increase and decline of the water level during an extreme event. The event lasts for 75 hours, during which the maximum surge height reaches 1.16 m. The water level curve follows from the combined effect of the base astronomical tide and the surge shape. The peak water level is found to be 5.51 m ODN (*Bennett et al.*, 2020) when the maximum surge height coincides with a high tide. The water level curve is applied as a boundary condition to the offshore boundary of the bay subdomain.

Finally, the river discharge is set at 60 m^3/s, which is the extreme discharge measured in the period 1991-1995 (*Ishak*, 1997). This is a short time period, and no statistical extreme value analysis is carried out, but the river discharge is small compared to the tidal prism. The total water volume discharged during a 12.5 h tidal cycle under extreme conditions is 2.7×10^6 m^3 which is a magnitude smaller than the spring tidal prism of 1.9×10^7 m^3. It is expected that this difference is even larger during an extreme event. Furthermore, the water flow driven by the storm surge is concentrated within the two hours that precede high water, whereas the river discharge is steady. Therefore, the surge-driven dynamics are expected to dominate the coastal flood risk such that the uncertainty in the extreme river discharge will not significantly affect the model results. The river discharge is applied at upstream boundary of the upper estuary subdomain.

The full list of conditions associated with a 1 in 100 year easterly storm is

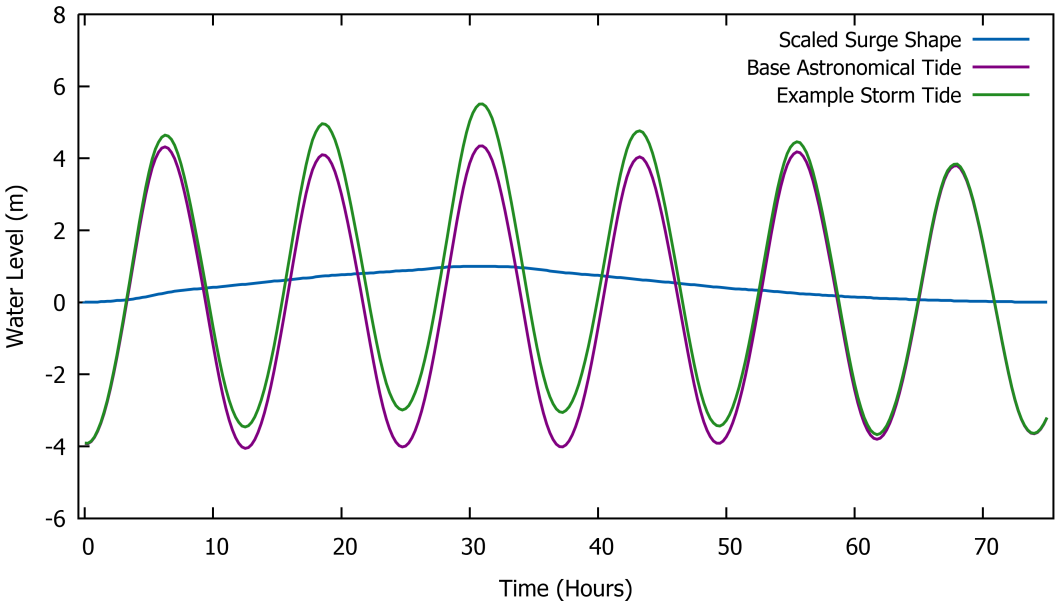

Figure 7.6: A sample water level curve as the superposition of the base astronomical tide and the scaled storm surge. Source: *Bennett et al.* (2020)

provided in Table 7.4.

7.3.3 Vegetation parameterisation

Salt marsh vegetation is modelled by cylinders that are described by their height h_v, diameter b_v, stem density per unit ground area n_v and flexural rigidity EI_v. The vegetation on the Laugharne South, Laugharne Castle, Laugharne North, and Blackscar salt marshes is included in the Taf model. The vegetation on the salt marshes further upstream in the estuary is not included, because these marshes are far upstream of Laugharne. The vegetation parameter will be set in accordance with selected vegetation scenarios (Section 7.4).

The vegetation interacts with currents and waves. Vegetation is considered rigid in its interaction with currents. Flexible species are not expected to bend significantly, because the current velocities within the vegetated region are significantly reduced (*Baptist et al.*, 2007). A bending angle of more than 25° is required to reduce the frontal area of the vegetation by more than 10%. Furthermore, the relative velocity effect is not applicable to currents that vary over the long time scale of a tidal cycle. Plants may move under the drag force exerted by currents, but a balance between drag force and restoring forces will be reached (*Luhar and Nepf*, 2011) after which the plant motion and its impact on the relative velocity are negligible. The large bending angle required to significantly reduce the plant

frontal area and the negligible effect of plant motion justify the assumption of rigid vegetation in its interaction with currents. The current-vegetation interaction is implemented through the momentum sink term parameterisation. It was found to produce the most realistic current and water level dynamics in a comparison between four different parameterisations in Delft3D (Chapter 3). Multiple vegetation species that differ in height, diameter, and density can be simulated simultaneously in Delft3D. The drag coefficient for current-vegetation interaction is set at $C_{Dc} = 1.0$ based on experiments with rigid cylinders by *Tanino and Nepf* (2008).

The wave-vegetation interaction is solved based on our novel wave damping model (Chapter 6) and includes the effect of flexible vegetation and a spatially varying drag coefficient. The vegetation module in SWAN (*Suzuki et al.*, 2012) is restricted to rigid vegetation with spatially uniform dimensions and drag coefficient but allows for spatial variations in vegetation density. This feature can be used to artificially include vegetation flexibility and spatially varying drag via a three-step methodology (Fig. 7.7). First, SWAN is run through D-WAVES without any vegetation present to simulate the base wave height, wave period and water depth over the domain. The base conditions are extracted at the peak of the storm surge when water depth and wave height are maximum. The wave conditions are combined with the spatially varying vegetation parameters.

Second, the wave energy dissipation per stem is calculated via the rigid vegetation model by *Mendez and Losada* (2004) on which SWAN is based, according to

$$\hat{\epsilon}_{swan} = \frac{1}{2\sqrt{\pi}}\rho C_{Dswan} b_v \left(\frac{k_p g}{2\omega_p}\right)^3 \frac{\sinh^3 k_p h_v + 3\sinh k_p h_v}{3k_p \cosh^3 k_p h} H_{rms}^3, \tag{7.1}$$

and via our full flexible model (Chapter 6), according to

$$\hat{\epsilon}_{ffm} = \frac{2}{3\pi}\rho C_{Dw} b_v \left(\frac{k_p g}{2\omega_p}\right)^3 \frac{\int_0^\infty \int_0^{h_v} \chi p(H) H^3 \cosh^3 k z_v \; dz_v dH}{\cosh^3 k_p h}, \tag{7.2}$$

where

$$p(H) = \frac{2H}{H_{rms}^2} e^{-\left(\frac{H}{H_{rms}}\right)^2} \tag{7.3}$$

is the Rayleigh wave distribution. $C_{Dswan} = 1$ is the fixed drag coefficient selected for SWAN, whereas the model wave drag coefficient

$$C_{Dw} = \left(\frac{730}{Re}\right)^{1.37} + 1.04 \tag{7.4}$$

is a function of the local Reynolds number $Re = u_c b_v/\nu$. Herein, the velocity scale u_c is estimated at a depth halfway the height of the canopy based on linear

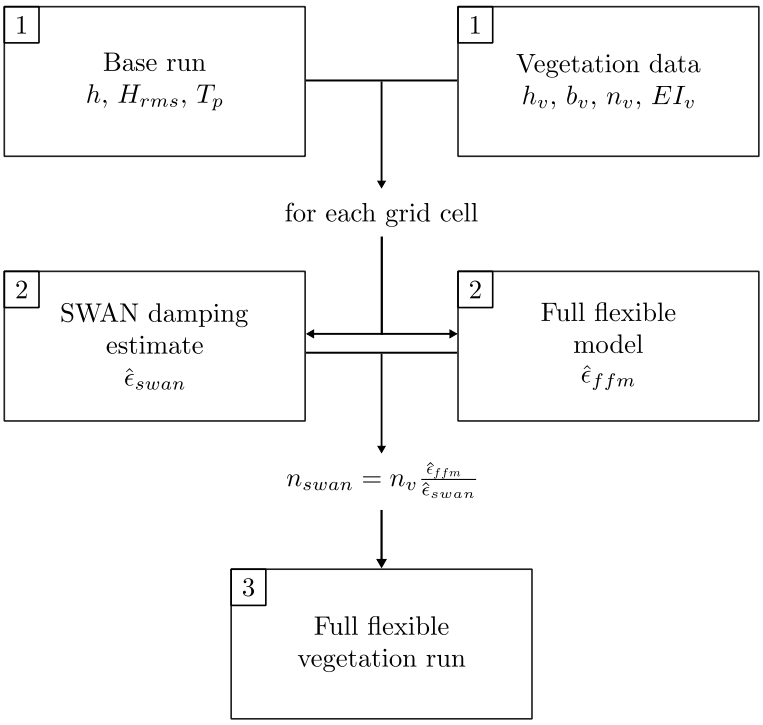

Figure 7.7: Flowchart of the three-step methodology to simulate flexible vegetation in SWAN through a corrected stem density n_{swan}.

wave theory. C_{Dw} is capped at 10 due to the lack of experimental observations with $C_{Dw} > 10$. When vegetation is rigid ($\chi = 1$) and $C_{Dswan} = C_{Dw}$, it follows that $\hat{\epsilon}_{swan} = \hat{\epsilon}_{mod}$.

Third, the artificial vegetation density

$$n_{swan} = n_v \frac{\hat{\epsilon}_{ffm}}{\hat{\epsilon}_{swan}} \tag{7.5}$$

is created to provide equal dissipation per unit ground area in SWAN ($n_{swan}\hat{\epsilon}_{swan}$) as by our full flexible model ($n_v\hat{\epsilon}_{mod}$) which includes vegetation flexibility and a spatially varying drag coefficient. n_{swan} serves as input for the full flexible vegetation model run in SWAN. An example of our three-step methodology is provided in Fig. 7.8.

The wave-vegetation interaction is solved outside Delft3D. Delft3D is run twice: an initial run to compute the base hydrodynamic conditions, and a second run to compute the wave field with salt marsh vegetation present. This methodology with two Delft3D runs is required, because the flexible vegetation model is applied outside Delft3D between the base run and the final run. Our model will be faster and more accurate when the full flexible model is implemented directly

in SWAN. The model would only need to be run once and two other model limitations would also be overcome. First, Eq. 7.1-7.5 are only evaluated under critical wave conditions, because the n_{swan} can only be entered as a fixed input value. A direct implementation of our model in SWAN could apply Eq. 7.1-7.5 each time step. Furthermore, the current methodology inherits a need for convergence. The base wave field which is used in Eq. 7.1-7.5 differs from the final wave field. When our model is directly implemented in SWAN, the wave field from the previous time step can be used to compute the wave damping such that it converges on a much shorter time scale. This chapter is a first investigation into the impact of vegetation flexibility on case study sites. Future research can further improve our understanding by implementing the full vegetation model directly in SWAN.

It is noted that the implementation of wave energy dissipation in SWAN differs from Eq. 7.1 in two ways (*Suzuki et al.*, 2012). The formulation in SWAN is expanded to include spectra of frequencies and directions. Furthermore, SWAN uses wave parameters associated with the mean wave period instead of the peak wave period. It is assumed that these modifications do not affect the magnitude of the correction as defined by Eq. 7.5.

7.3.4 Model validation

The Taf model, with its full list of parameters provided in Table 7.4, is validated against measured hydrodynamics under tide-dominated conditions. The validation provides confidence that the hydrodynamic processes are simulated satisfactory, which support the application of the Taf model across a wider range of hydrodynamic conditions. The model is validated against water depth and flow velocity measurements inside the Taf Estuary. The Taf model is run with only the tidal signal as the boundary condition. The vegetation condition is a uniform *A. Portulacoides* cover as the dominant species in the estuary.

Validation of water depth

Water depth data obtained from an ADCP deployed in the Taf was used to validate the numerical model. The ADCP was deployed during ten tidal cycles between 10 and 16 June 2018 in the main channel between the Laugharne South Marsh and Castle Marsh (see Fig. 7.10, D1). Water depths were measured in bins of 0.5 m, starting from a minimum of 1.0 m water depth. Comparison between the model results and measured water depths (Fig. 7.9a) at this location shows excellent agreement in phase and good agreement in amplitude. The visual difference in the peak high water levels between measurements and model relates to the bin classifications in the measured dataset. The values plotted are the minimum value of each bin, and the actual value may be up to 50 cm higher.

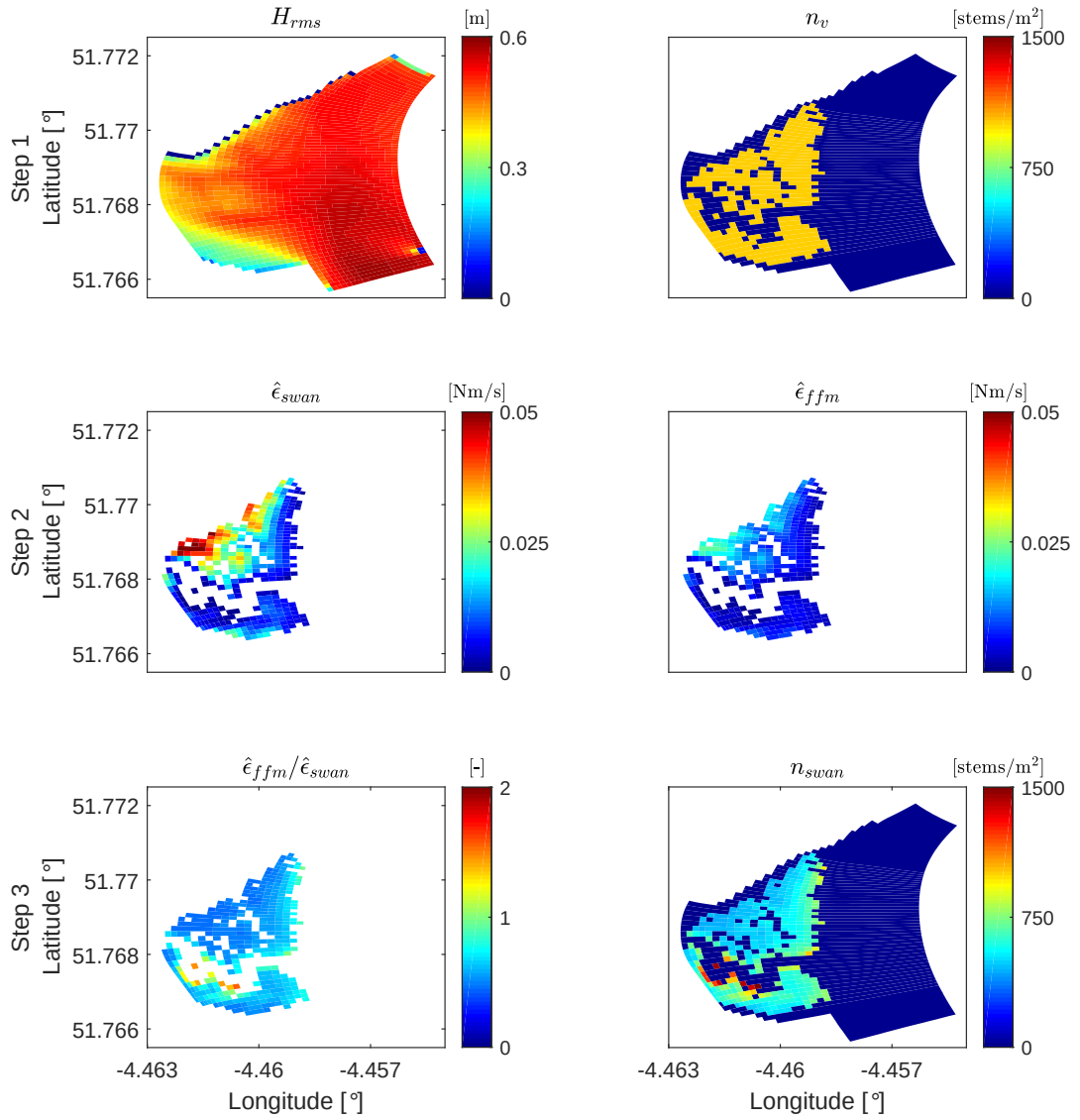

Figure 7.8: Example application of our three-step methodology to obtain corrected vegetation density maps for a full flexible vegetation run in the Taf model. Step 1 (top row): the wave conditions such as the wave height H_{rms} are estimated from a model run without vegetation. These are combined with vegetation parameters such as the vegetation density n_v. Step 2 (middle row): The wave energy dissipation per stem is calculated via a rigid vegetation model ($\hat{\epsilon}_{swan}$) and via our full flexible model ($\hat{\epsilon}_{ffm}$). Step 3 (bottom row): a corrected vegetation density n_{swan} is derived from the ratio $\hat{\epsilon}_{ffm}/\hat{\epsilon}_{swan}$. The example vegetation represents a uniform *P. Maritima* cover with density $n_v = 999$ stems/m^2 on Laugharne Castle Marsh.

Table 7.4: List of model parameters. The list is divided in storm conditions, vegetation parameters, physical parameters, and numerical parameters from top to bottom.

Parameter	**Symbol**	**Value**	**Unit**	**Motivation**
Peak wind speed	u_{wind}	16.28	m/s	*Bennett et al.* (2020)
Wind direction	θ_{wind}	115	∘	Comparative study
Peak wave height	H_{max}	8.66	m	*Bennett et al.* (2020)
Maximum wave period	T_{max}	6.82	s	*Bennett et al.* (2020)
Wave direction	θ_{wave}	225	∘	*Bennett et al.* (2020)
Peak water level	h_{max}	5.51	m	*Bennett et al.* (2020)
River discharge	Q_r	60	m^3/s	*Ishak* (1997)
Storm duration	T_{storm}	75	h	*Bennett et al.* (2020)
Vegetation height	h_v	231 – 590	mm	Based on scenarios
Vegetation diameter	b_v	0.74 – 3.33	mm	Based on scenarios
Vegetation density	n_v	214 – 36000	$stems/m^2$	Based on scenarios
Vegetation flexural rigidity	EI_v	1.9×10^{-5} – 2.6×10^{-2}	Nm^2	Based on scenarios
Current drag coefficient	C_{Dc}	1.0	-	*Tanino and Nepf* (2008)
Wave drag coefficient	C_{Dw}	$(730/Re)^{1.37}$ +1.04	-	*Hu et al.* (2014)
Water density	ρ	1025	kg/m^3	Well-mixed estuary
Bed roughness	C_b	65	$m^{1/2}/s$	*Marciano et al.* (2005)
Horizontal eddy viscosity	K	1	m^2/s	*Mariotti and Canestrelli* (2017)
Wind drag coefficient	C_w	$(63+6.6u_{wind})$ $\times 10^{-5}$	-	*Smith and Banke* (1975)
Time step D-FLOW	Δt_{flow}	3	s	Sensitivity analysis
Time step D-WAVE	Δt_{wave}	900	s	Sensitivity analysis
Spin-up time	t_{ini}	6.25	h	Sensitivity analysis
Grid resolution	d_{grid}	5 – 300	m	Sensitivity analysis

This is particularly pronounced during the peak high waters when a successive bin is not reached.

Validation of flow velocity

A single point current meter was deployed in the main channel upstream of Laugharne Castle Marsh (see Fig. 7.10, D2) between 1 pm on 28 November 2017 and 2:45 pm on 30 November 2017. Comparison of modelled flow velocities at the location of deployment with modelled results show reasonable agreement (Fig. 7.9b). The coefficient of correlation $r^2 = 0.68$, the Nash-Sutcliffe efficiency coefficient $NSE = 0.48$ (*Nash and Sutcliffe*, 1970), and the root-mean-square-error $RMSE = 0.25$ m/s indicate that the model predicts flow velocities adequately for an estuary with a significant tidal asymmetry. The flood dominance of the estuary is particularly well reproduced by the model. The phase and amplitude of the flood tidal currents match well with the measured current velocities. The initial stage of the ebb tidal currents is also modelled correctly, but the measured ebb currents have a stronger maximum velocity, and the ebb tide is of shorter duration. This could be due to grounding of the meter on one of the tidal flats next to the channel. The current meter was free to move around the anchor point and could have travelled onto the flats, as it was fixed to a rope. This is supported by model results of a grid point in close proximity but on a tidal flat. Unlike the main channel, the tidal flat dries and contributes to drainage of the estuary over a short period only. Indeed, Figure 7.9c shows that the ebb tide corresponds better with measurements for such a location and the goodness-of-fit indicators have all improved with $r^2 = 0.72$, $NSE = 0.62$, and $RMSE = 0.21$ m/s.

7.4 Vegetation scenarios

We select six vegetation scenarios to investigate the coastal protection provided by salt marsh vegetation against coastal flooding. The scenarios have been selected to represent contrasting vegetation types that differ in flexibility and dimensions.

S1 No vegetatation: This is the reference scenario with no vegetation present on the salt marshes.

S2 Rigid vegetation: This scenario represents a uniform cover of rigid cylinders ($EI_v = \infty$). The vegetation dimensions are set equal to *A. Portulacoides* as the dominant vegetation species in the Taf Estuary.

S3 *A. Portulacoides* vegetation: This scenario exhibits a uniform cover of the semi-flexible woody shrub *A. Portulacoides*. It is the dominant species in the Taf Estuary and most commonly found on the middle marshes.

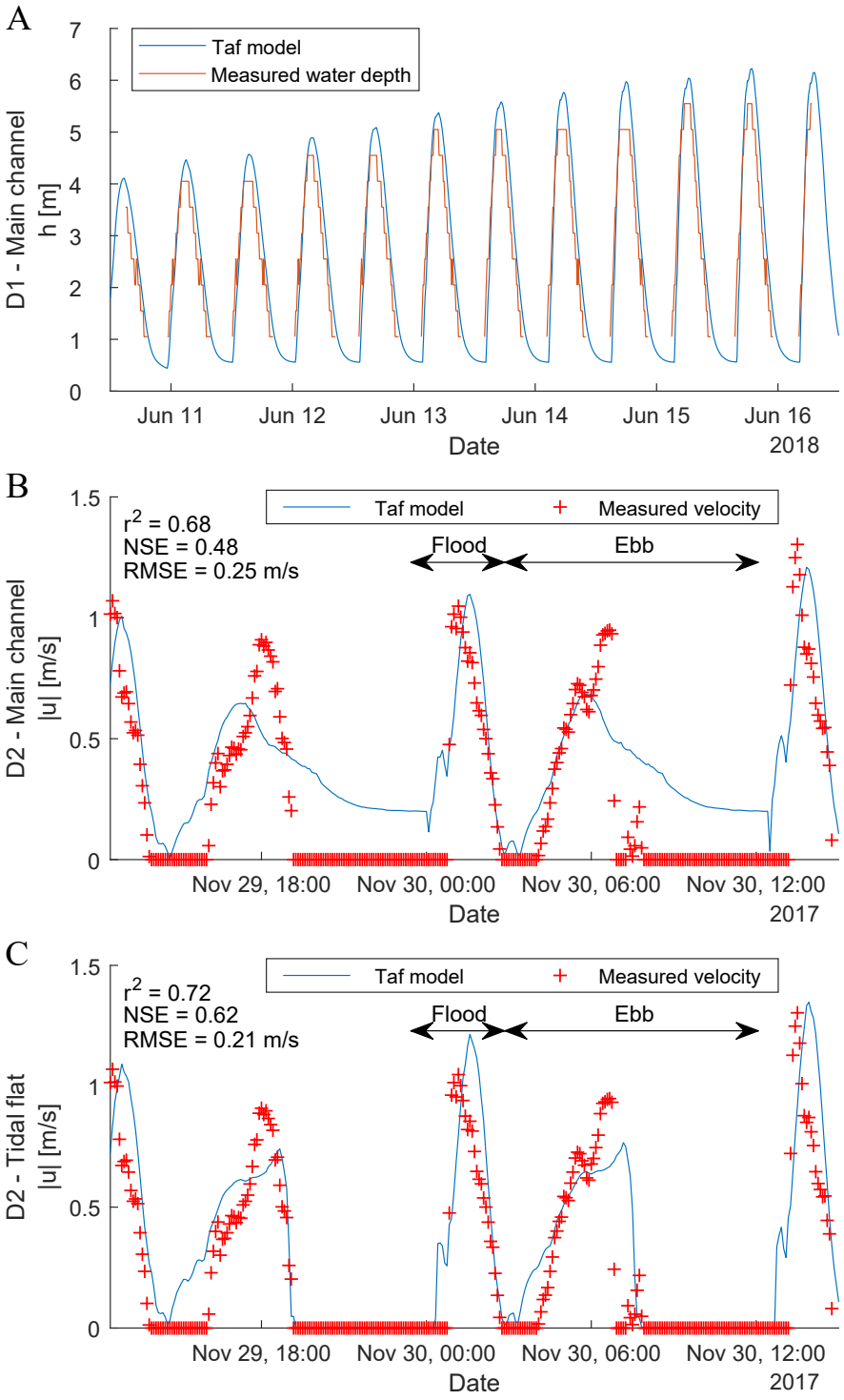

Figure 7.9: Model validation of (a) the water depth and (b and c) the current velocity. In all plots, the blue line denotes the modelled hydrodynamics and the red line / red + signs denote measured quantities. The measurement locations D1 and D2 are shown on the map of Fig. 7.10.

S4 *S. Anglica* vegetation: This scenario features a uniform cover of the flexible tall grass *S. Anglica* . It is the second most widespread species in the Taf Estuary and most commonly found on the lower marshes.

S5 *P. Maritima* vegetation: This scenario considers a uniform cover of the very flexible grass *P. Maritima*. It is the fourth-most widespread species in the Taf Estuary and most commonly found on the higher marshes.

S6 Mixed vegetation: This scenario features the five dominant vegetation species (*A. Portulacoides*, *S. Anglica*, *F. Rubra*, *P. Maritima*, *A. Tripolium*) simultaneously along with their spatial distribution.

The six scenarios can be grouped into three categories. S1 is a baseline scenario without vegetation that acts as a reference to quantify the effect of vegetation in the other scenarios. The impact of vegetation on the bathymetry is not considered such that the bed level is identical across all scenarios.

Scenarios S2-S5 are designed identify the hydrodynamic response to individual vegetation types. *P. Maritima* has been selected over *F. Rubra* to represent flexible grasses on the higher marshes, because its height and density (Table 7.2) are closer to that of *A. Portulacoides* as the primary focus of this study is on plant flexibility. Following the focus on plant flexibility, the stem density of scenarios S4 and S5 is adjusted such that all scenarios have an identical frontal area ($\lambda_f = 1.96$). The stem density of *S. Anglica* (S4) is increased from $n_v = 720$ to $n_v = 999$ stems/m^2 and the density of *P. Maritima* (S4) is increased from $n_v = 3444$ to $n_v = 6888$ stems/m^2.

Scenario S6 is designed to provide the most realistic estimate of the flood risk for Laugharne. The five vegetation species are distributed following the vegetation maps obtained for the Taf Estuary (Fig. 7.2) with the species distribution per NVC type given by Table 7.1. 12% of the salt marsh cover is populated by other vegetation species. This share has been proportionally distributed across the five dominant vegetation types. The vegetation properties match those listed in Table 7.2. Finally, SWAN is restricted to a single vegetation type. Therefore, the energy dissipation by each species was projected on proxy vegetation with $h_v = 100$ mm and $b_v = 10$ mm. The proxy height and diameter served as input in Eq. 7.1. The vegetation module in D-FLOW accepts multiple vegetation types such that proxy vegetation was not required.

A summary of the vegetation scenarios is provided in Table 7.5.

Table 7.5: List of vegetation scenarios with vegetation parameters and implementation in D-FLOW and SWAN/D-WAVE. EX: explicit implementation of plant parameters, CD: implemented with corrected density (Eq. 7.5), PR: implemented with proxy vegetation and corrected density

Scenario	h_v [mm]	b_v [mm]	EI_v [Nm^2]	n_v [m^{-2}]	λ_f	**FLOW**	**SWAN**
S1	-	-	-	-	-	-	-
S2	334	2.58	∞	2275	1.96	EX	CD
S3	334	2.58	1.6×10^{-3}	2275	1.96	EX	CD
S4	590	3.33	8.4×10^{-4}	999	1.96	EX	CD
S5	335	0.85	1.9×10^{-5}	6887	1.96	EX	CD
S6	Mixed: Tab. 7.2	Mixed: Tab. 7.2	Mixed: Tab. 7.2	Mixed: Tab. 7.2	2.17*	EX	PR

* represents a weighted average of all salt marshes.

7.5 Results

The contribution of salt marshes to coastal protection is considered through the hydrodynamic parameters water depth (h), depth-averaged current velocity (u) and significant wave height (H_s). The water depth is important for flood damage (*Smith*, 1994) and pressure on coastal defence structures (*Reeve et al.*, 2012). The flow velocity controls coastal erosion during storms through elevated bed shear stresses (*Fredsoe and Deigaard*, 1992). The wave height is an important indicator for hydrodynamic loading on coastal defence structures (*Vuik et al.*, 2016, 2019). The flood risk correlates positively with each of these parameters. Salt marshes contribute to coastal protection when they successfully lower one or more of these hydrodynamic parameters. The water depth and wave height are considered at peak high water conditions when the water level and wave height are at their maximum. The current velocities are considered during flood tide at 1 hour and 45 minutes before peak high water. At this time, current velocities were significant, and the water level was sufficient for flow over salt marshes to occur.

The model is run for the six vegetation scenarios (S1-S6) selected in Section 7.4. The results are presented on the scale of the full Taf Estuary and on the scale of Laugharne Castle Marsh, which is most critical for the protection of Laugharne (Fig. 7.10). Additionally, the propagation of wave height is studied along three transects: T1, T2, and T3. The three transects have been selected to compare the wave damping capacity of salt marshes over contrasting bathymetries. Tran-

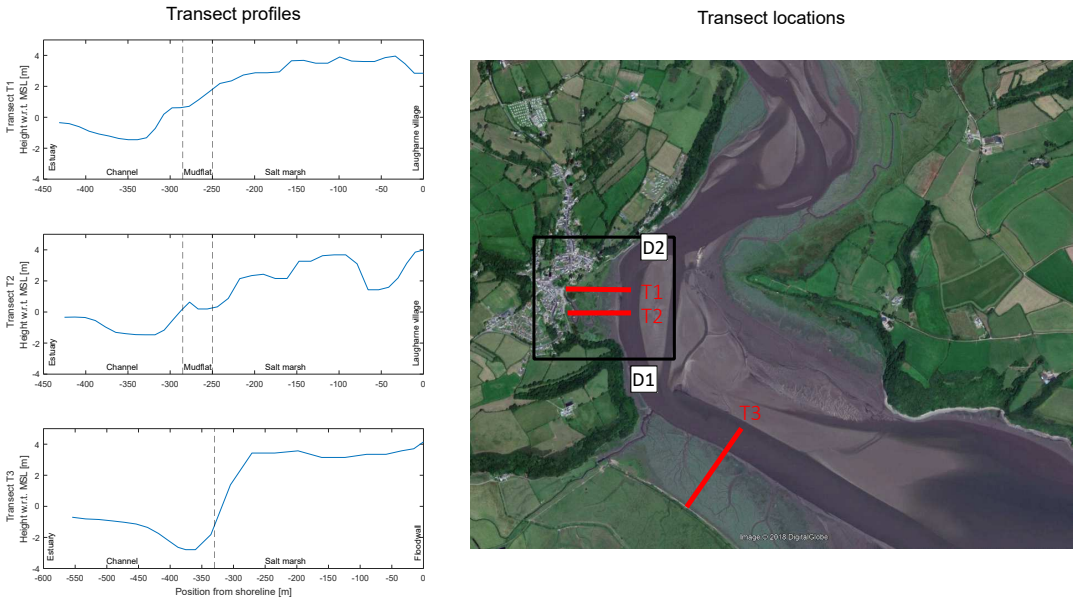

Figure 7.10: Bottom profile and location of transects T1, T2 and T3 which are used to compare wave height evolution. The dashed lines on the transects (left) mark the boundaries between the estuary channel, mudflat and salt marsh. The black box in on the map (right) corresponds to the hydrodynamic maps that are presented on the scale of Laugharne Castle Marsh. D1 and D2 mark the locations of the ADCP and the flow velocity meter respectively. Source satellite image: *Google Earth* (2018).

sects T1 and T2 are located on Laugharne Castle Marsh and in the predominant direction of wave propagation. T1 is located over a marsh section with vegetation only, whereas T2 represents a transect that coincides with a creek (river Coran). Transect T3 is located on Laugharne South Marsh and is in a direction perpendicular to the dominant wave propagation.

7.5.1 Impact of salt marshes on water depth

Deep water is observed across the Taf Estuary and over Laugharne Castle Marsh under all vegetation scenarios. The modelled peak water depth under scenarios S1-S6 is shown in Fig. 7.11. This figure shows the absolute water depth under each vegetation scenario for the whole Taf Estuary (left column) and Laugharne Castle Marsh (right column). Each row corresponds to a scenario with S1 on the top row and S6 on the bottom row. The water depth is denoted by a colour scale with the deepest water having a red shade and the shallowest water having a blue

shade.

The water depth correlates strongly to the bathymetry at the estuary scale with water depths up to 10 m in the main channel under all vegetation scenarios. The water depth on Laugharne Castle Marsh ranges from 2 m near the coastline up to 6 m in the river Coran. Like the water depths on the estuary scale, the variations in water depths on the marsh correlate to the elevation of its substrate. These results are found to be consistent across all six vegetation scenarios.

The relative difference in the water depth of each scenario with vegetation (S2-S6) with respect to the no vegetation reference scenario (S1) is displayed in Fig. 7.12. The top row shows the reference water depth under scenario S1. This row is identical to the top row of Fig. 7.11. The second to bottom rows depict the relative difference of the respective scenario compared to scenario S1, i.e. a relative difference of 0.1 denotes a 10% increase in water depth relative to the water depth in scenario S1. A green colour denotes no change, a red colour represents an increase in water depth, and blue colour shows a decrease in water depth.

The vegetation can reduce the water depth at the higher sections of a salt marsh, but its overall effect is found to be small. The water depth appears to be mostly unaffected by the presence of vegetation, but the water depth is reduced by up to 5% on the higher parts of Black Scar marsh under all scenarios. The 5% reduction corresponds to a 50 mm reduction of the absolute water depth. The water depth on Laugharne Castle Marsh is unaffected by the presence of vegetation under all vegetation scenarios. Also, Laugharne South Marsh and Laugharne North Marsh do not show an attenuation of water depth. The water level differences are again consistent across all scenarios.

The difference between Blackscar and the other marshes suggests that size, elevation and location are important marsh characteristics that control the attenuation of water depth. Blackscar Marsh is much larger than Laugharne Castle and Laugharne North. It can dissipate and store water over a larger area. Additionally, Blackscar is further from the main estuary channel, more upstream in the estuary, and at a higher elevation than the other marshes. These characteristics result in reduced current velocities over the marsh. As a result, the vegetation drag will be compensated by water depth attenuation instead of current attenuation. The attenuation capacity of Blackscar Marsh with respect to marsh width is 200 mm/km. The observed attenuation agrees with reviews by *Stark et al.* (2015) and *Paquier et al.* (2017) who found that salt marshes have an attenuation capacity of 0-700 mm/km with significant variation between individual study sites. The observations in this study may partially explain this variation.

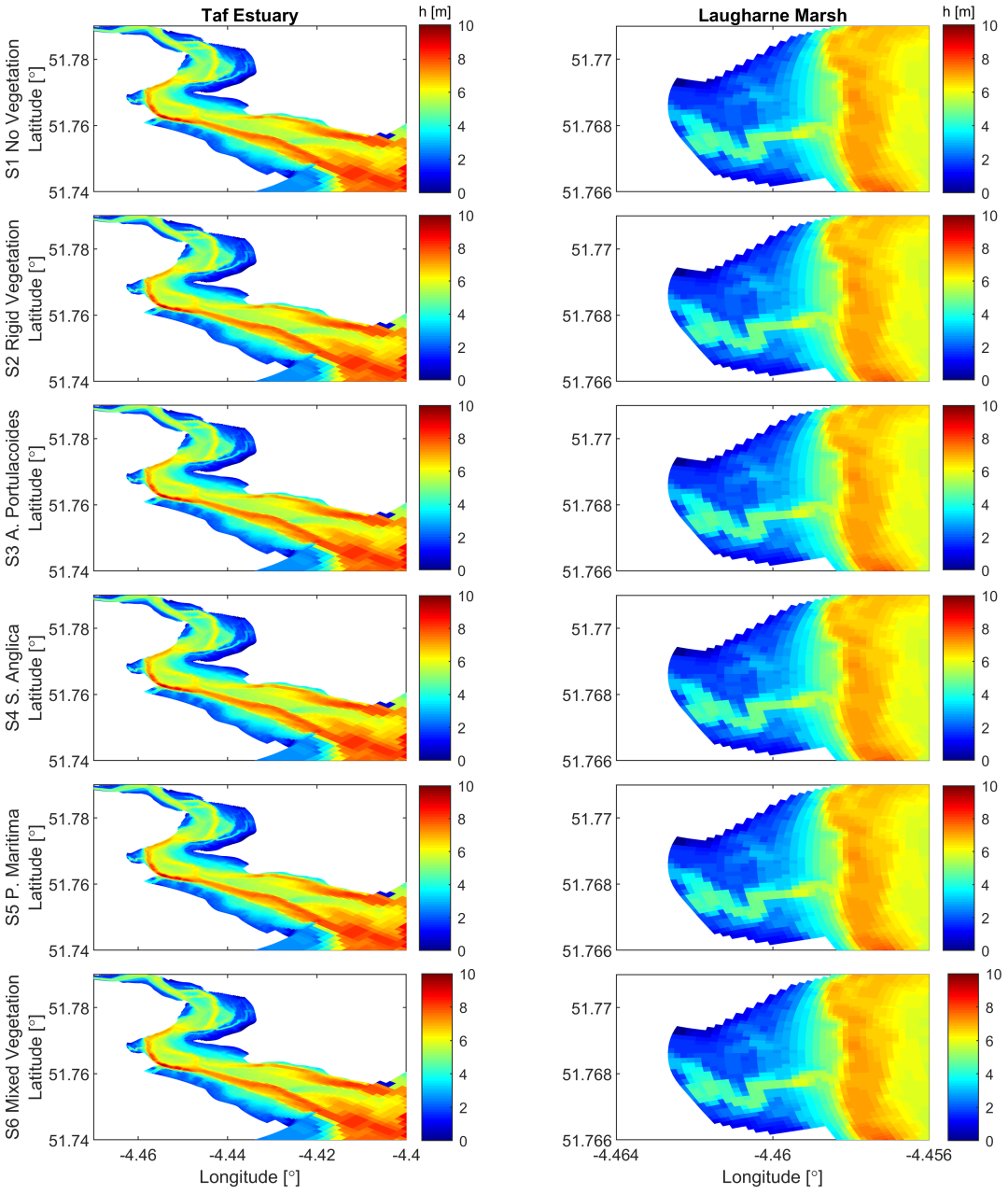

Figure 7.11: Modelled water depths in the Taf Estuary under six scenarios: S1 No vegetation (top row); S2 Rigid vegetation (second row); S3 *A. Portulacoides* vegetation (third row); S4 *S. Anglica* vegetation (fourth row); S5 *P. Maritima* vegetation (fifth row); S6 Mixed vegetation (bottom row). The water depth is shown on full estuary scale (left column) and as a close-up on Laugharne Castle Marsh (right column).

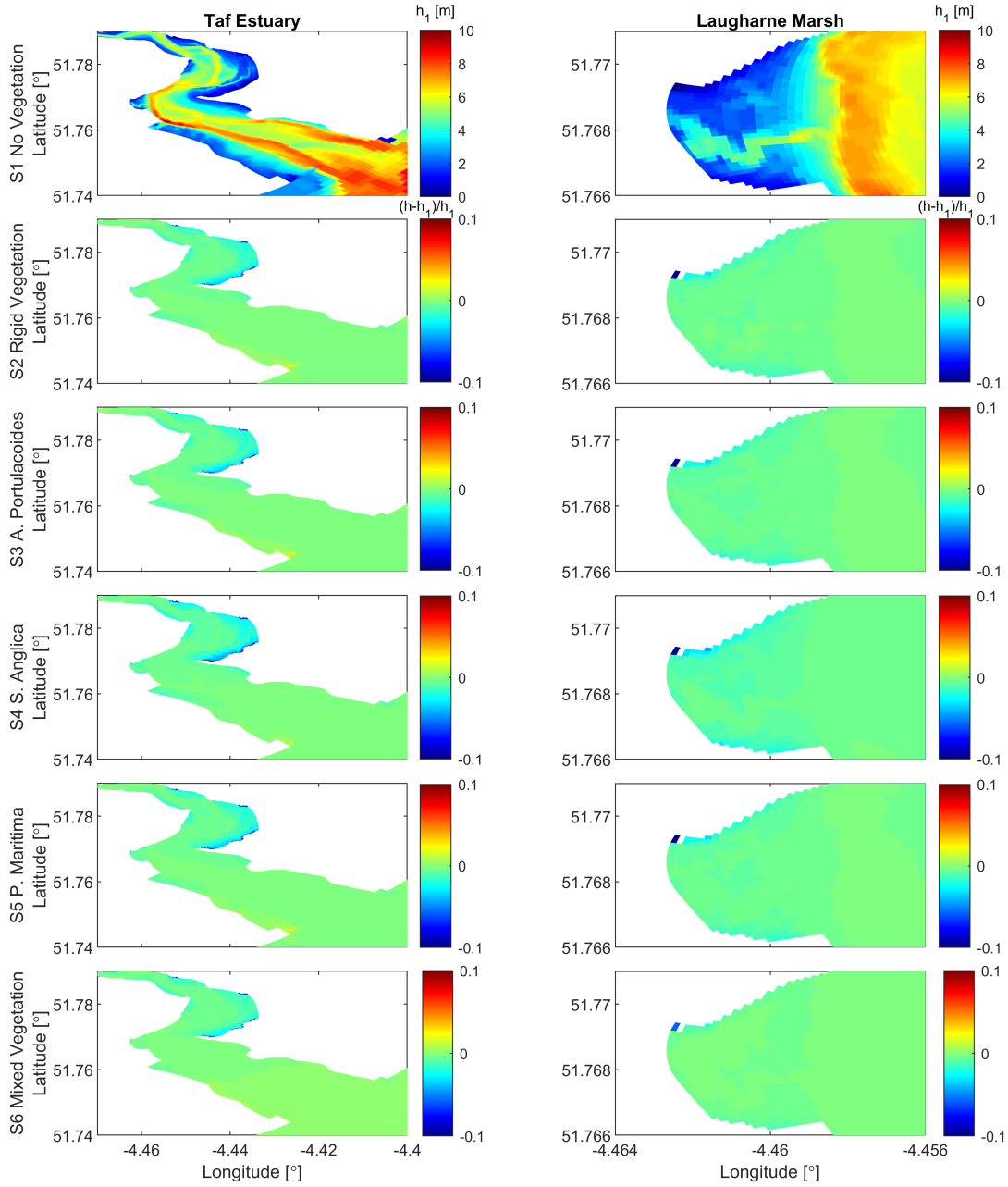

Figure 7.12: Modelled water depths relative to the no vegetation scenario. The reference water depth is displayed on the top row. The other rows denote the change in water depth by rigid vegetation (second row), *A. Portulacoides* vegetation (third row), *S. Anglica* vegetation (fourth row), *P. Maritima* vegetation (fifth row), and mixed vegetation (bottom row). The water depth is shown on full estuary scale (left column) and as a close-up on Laugharne Castle Marsh (right column).

7.5.2 Impact of salt marshes on currents

The presence of salt marsh vegetation constrains flood currents to the main estuary channel. The current fields (Fig. 7.13) show current velocities between 0.6 and 1.0 m/s in the main estuary under all vegetation scenarios. The maximum velocities are attained in the estuary channels with lower velocities on the shallower tidal flats. The velocities on the salt marshes are up to 0.4 m/s on Laugharne South and Blackscar under scenario S1 but are less than 0.1 m/s when salt marsh vegetation is present under scenarios S2-S5. The velocity vectors reveal that the predominant flow direction on Laugharne South under scenario S1 is parallel to the main estuary channel. The along-channel flow disappears when vegetation is present. Scenario S6 damps the currents significantly, but a reduced along-channel flow remains. The flow velocities on Laugharne Castle Marsh are low (< 0.2 m/s) even when no vegetation is present as it is a narrow extension in a direction perpendicular to the main current direction.

The relative difference plots (Fig. 7.14) reveal that the currents are almost fully dissipated on salt marshes due to the drag exerted by vegetation. The reduction over Laugharne Castle Marsh is nearly 100% for the vegetation scenarios S2-S5 but is only around 50% under scenario S6. The difference could be due to the strong presence of *F. Rubra* on this salt marsh. *F. Rubra* is the shortest of the five vegetation species considered with $h_v = 0.23$ m. Therefore, the height of the free flow layer over the vegetation is larger than under the other scenarios, which can lead to a smaller reduction in the current velocities.

Furthermore, the current velocities increase over the bare parts of the estuary such as the salt marsh creeks and the main estuary channel. The velocities more than double in the salt marsh creeks when vegetation is present on the adjacent platforms. The velocities increase up to 20% in the main estuary. The ratio vegetated to bare land appears to be a key predictor for the increase in current velocities with the highest increases in velocity occurring when the ratio of vegetated to bare land is high. This is the case in salt marsh creeks and in the estuary channel when it is constrained by salt marshes on both sides.

The Taf model results agree with the channelling effects observed in our analysis of the current-vegetation interaction in the idealised estuary presented in Chapter 3, and with models of currents over salt marshes in the Scheldt Estuary (*Temmerman et al.*, 2005) and the macro-tidal Bay of Fundy (*Ashall et al.*, 2016).

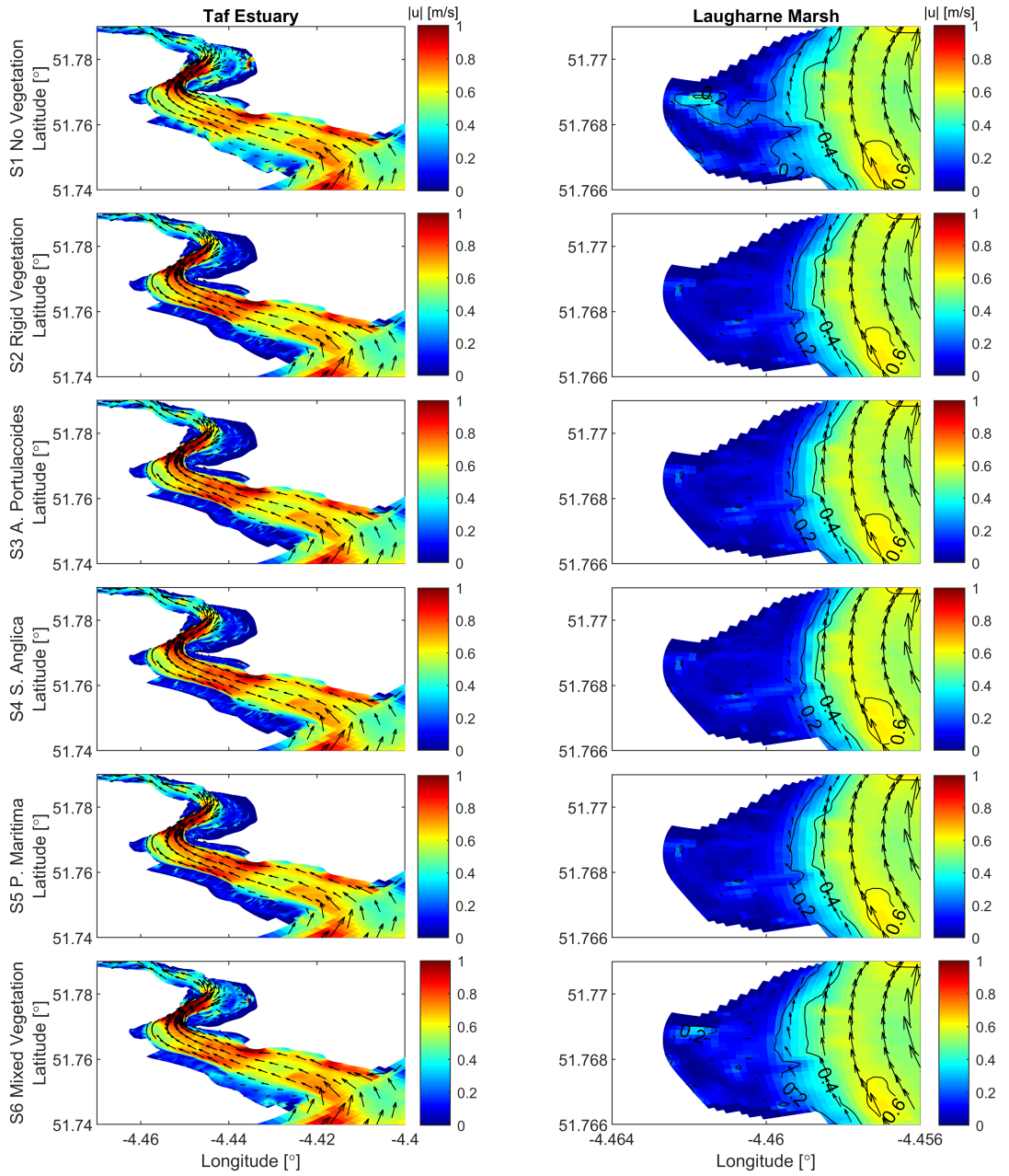

Figure 7.13: Modelled current velocities in the Taf Estuary under six scenarios: S1 No vegetation (top row); S2 Rigid vegetation (second row); S3 *A. Portulacoides* vegetation (third row); S4 *S. Anglica* vegetation (fourth row); S5 *P. Maritima* vegetation (fifth row); S6 Mixed vegetation (bottom row). The shading signals the magnitude of the current velocity and the arrows denote current direction. The arrows are plotted at reduced resolution for visibility. The currents are shown on full estuary scale (left column) and as a close-up on Laugharne Castle Marsh (right column).

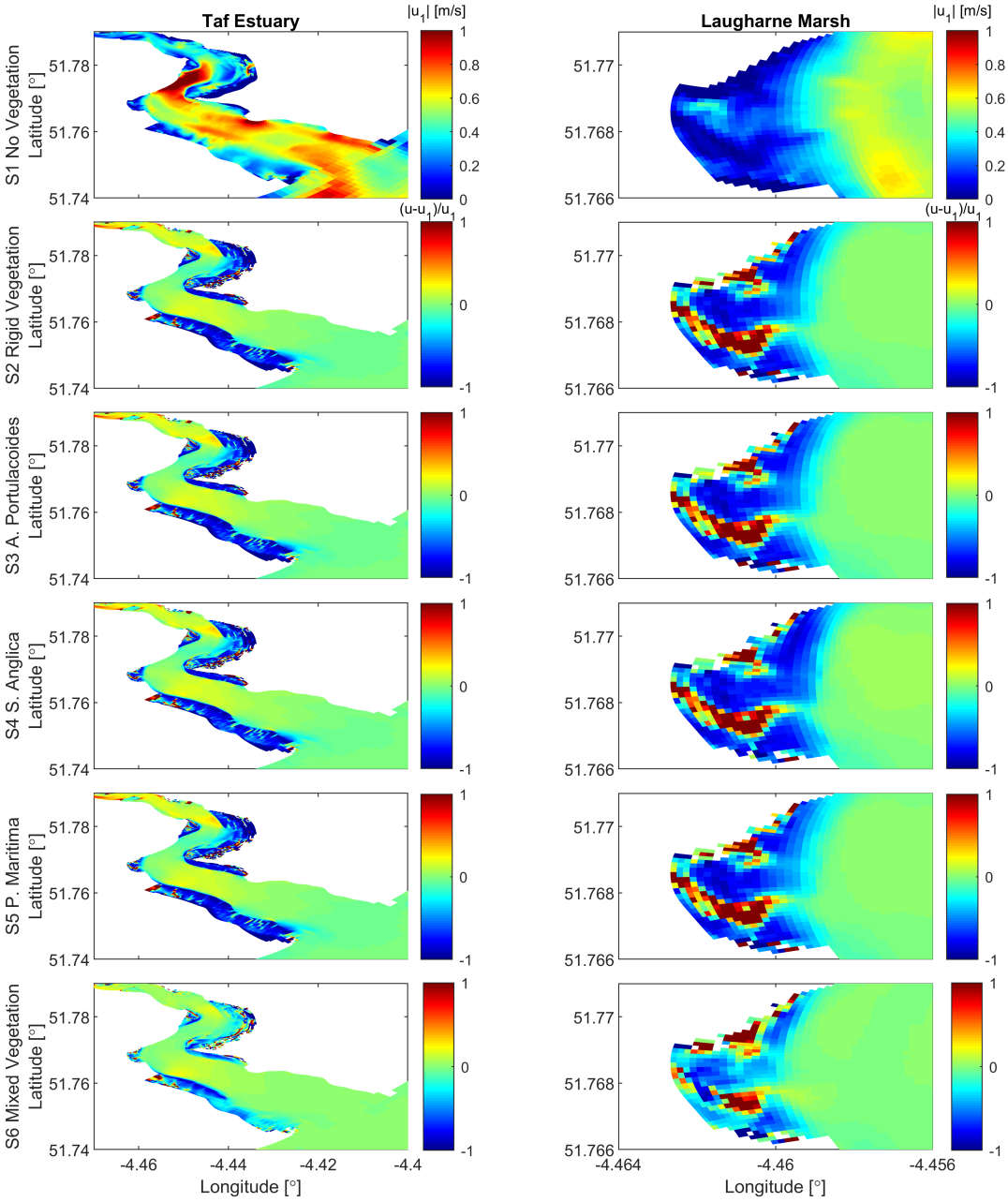

Figure 7.14: Modelled current velocity magnitudes relative to the no vegetation scenario. The reference current velocity is displayed on the top row. The other rows denote the change in water depth by rigid vegetation (second row), *A. Portulacoides* vegetation (third row), *S. Anglica* vegetation (fourth row), *P. Maritima* vegetation (fifth row), and mixed vegetation (bottom row). The current velocities are shown on full estuary scale (left column) and as a close-up on Laugharne Castle Marsh (right column).

7.5.3 Impact of salt marshes on waves

The vegetation on salt marshes dampens incoming wave heights under all vegetation scenarios. The significant wave height at the seaward edge of Laugharne South Marsh and Laugharne Castle Marsh ranges between 0.7 and 0.8 m under all vegetation scenarios (Fig. 7.15). Without vegetation (Scenario S1), the wave height reduces to 0.5-0.6 m over the bare platforms due to bottom friction and wave breaking. With vegetation (Scenario S2-S6), the wave heights reduce to approximately 0.2 m depending on location and scenario. The wave height at the coastline appears to be a balance between vegetation-induced decay and wind-driven growth. The comparison between the unvegetated and vegetated scenarios shows that vegetation lowers the wave heights up to 70% more (Fig. 7.16). The upper estuary is sheltered from wave propagation by the sinuous shape of the estuary, such that the wave height upstream of Laugharne does not exceed 0.4 m.

The wave damping capacity of vegetation is most effective over the 100 metres nearest to the seaward edge, but wide creeks may locally lower the wave damping capacity. The wave heights reduce by 25-50% relative to the incident wave height over the first 50 metres of marshland and up to 75% over the first 100 metres (Fig. 7.17). Transects T1 and T3 show that after the wave heights have reduced to a height of 0.2 m (a reduction of approximately 75%) an equilibrium between wave dissipation and growth is reached and no further damping will occur. This equilibrium is reached at 150 m from the marsh edge. In fact, the wave height slightly increases over transect T1 near the coastline under the mixed vegetation scenario. This is attributed to a reduction in stem density at the end of the transect, which reduces the magnitude of the vegetation-induced damping relative to the wind-driven growth. Alternatively, waves are only attenuated by 50% over a length of 250 metres along transect T2. This transect coincides with the river Coran which does not exhibit vegetation. The damping along this transect remains moderate despite significant damping on both sides of the creek. This observation shows that wide creeks can locally reduce the wave damping capacity of salt marshes.

The difference in wave damping between the vegetation scenarios is significant. The strongest damping is provided by mixed vegetation with a 72% reduction in wave height compared to the no vegetation reference case after 150 m salt marsh along transect T1, i.e. from -250 to -100 m relative to the coastline (Fig. 7.17). The strong damping is caused by a dense patch of *F. Rubra* between -190 to -100 m relative to the coastline. Its frontal area ($\lambda_f = 6.08$) is much higher than in scenarios S2-S5 ($\lambda_f = 1.96$). Out of the scenarios with equal frontal area, the largest damping is provided with by rigid vegetation with a 63% reduction in wave height compared to no vegetation. Conversely, the lowest damping is

provided by *S. Anglica* with only a 28% reduction.

The results suggest that plant flexibility is an important parameter for wave damping over salt marshes, but vegetation diameter and density also affect the wave damping. The wave damping reduces as the scaled flexibility Q increase for scenarios S2-S4 (Table 7.2). The tall semi-flexible species *S. Anglica* (S4) provides 56% less wave damping than rigid vegetation (S1) along transect T1. However, scenario S5 (*P. Maritima*) does not follow this relation. The wave damping by *P. Maritima* exceeds that of the stiffer species *S. Anglica* and *A. Portulacoides*. Although *P. Maritima* is the most flexible specie, it is also significantly thinner ($b_v = 0.85$ mm) and denser ($n_v = 6888$) than the other vegetation species. Thin stems are associated with low Re and, consequently, high C_{Dw}. Therefore, the motion of *P. Maritima* may be higher than that of more rigid species, but the higher drag coefficient and stem density compensate for its flexibility.

Finally, salt marsh vegetation prevents wave growth in addition to wave damping. The wave heights in the estuary channel east of Blackscar Marsh are reduced by 30% when salt marsh vegetation is present on Blackscar Marsh for each of the scenarios S2-S6 (Fig. 7.16). The wave field in the upper estuary is strongly controlled by the local wind field as the bend in the lower estuary prevents wave propagation from the lower estuary. Therefore, the reduction in wave height must be due to a reduction in wave growth over Blackscar Marsh.

7.6 Comparison against the full flexible model

The wave damping over Laugharne as simulated by the Taf model is compared against predictions by the full flexible model (Chapter 6) to investigate the impact of additional physical processes that are included in the Taf model but not in the full flexible model. These processes include a spatially varying bed level and additional wave dynamics, such as diffraction, depth-induced breaking and wind-driven growth. The full flexible model was run using the incident wave conditions $h = 2$ m, $H_{rms} = 0.53$ m, and $T_p = 3$ s at the edge of the salt marsh. The predicted damping coefficients for each scenario were $\beta = 0.033$ m^{-1} for S2, $\beta = 0.022$ m^{-1} for S3, $\beta = 0.009$ m^{-1} for S4, $\beta = 0.022$ m^{-1} for S5. A single damping coefficient cannot be defined for scenario S6 due to the spatial variations in the vegetation cover.

The wave damping simulated by the Taf model is lower than predicted by the full flexible model. A comparison along transect T1 between the two models shows that the wave heights simulated by the Taf model are consistently higher than predicted by the full flexible model (Fig. 7.18). The simulated wave height by the Taf model is 35 to 110% larger than predicted by the full flexible model in the 150 m of Laugharne Castle Marsh closest to the estuary, and between 80

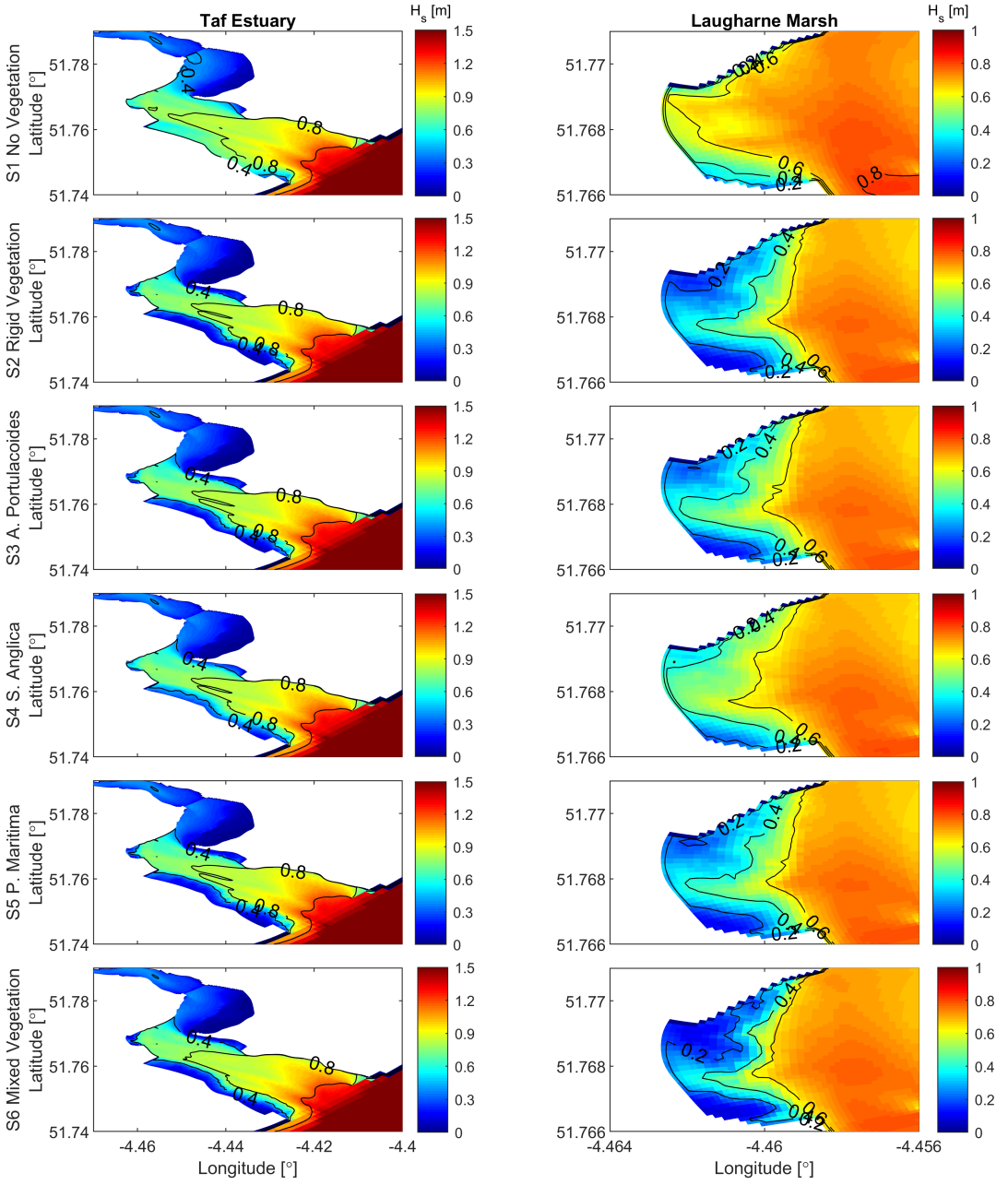

Figure 7.15: Modelled significant wave height in the Taf Estuary under six scenarios: S1 No vegetation (top row); S2 Rigid vegetation (second row); S3 *A. Portulacoides* vegetation (third row); S4 *S. Anglica* vegetation (fourth row); S5 *P. Maritima* vegetation (fifth row); S6 Mixed vegetation (bottom row). The significant wave height is shown on full estuary scale (left column) and as a close-up on Laugharne Castle Marsh (right column).

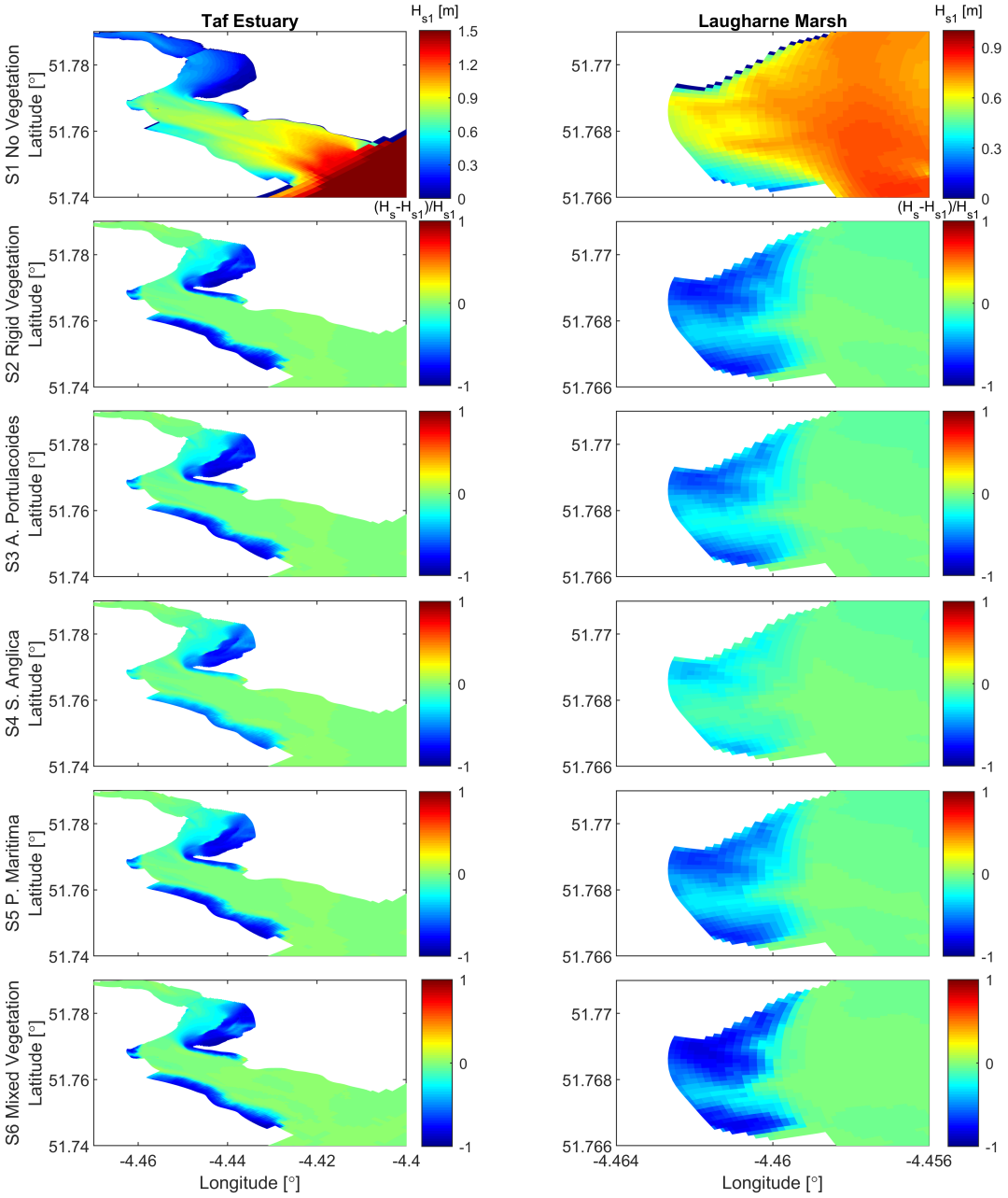

Figure 7.16: Modelled significant wave height relative to the no vegetation scenario. The reference wave height is displayed on the top row. The other rows denote the change in water depth by rigid vegetation (second row), *A. Portulacoides* vegetation (third row), *S. Anglica* vegetation (fourth row), *P. Maritima* vegetation (fifth row), and mixed vegetation (bottom row). The wave height is shown on full estuary scale (left column) and as a close-up on Laugharne Castle Marsh (right column).

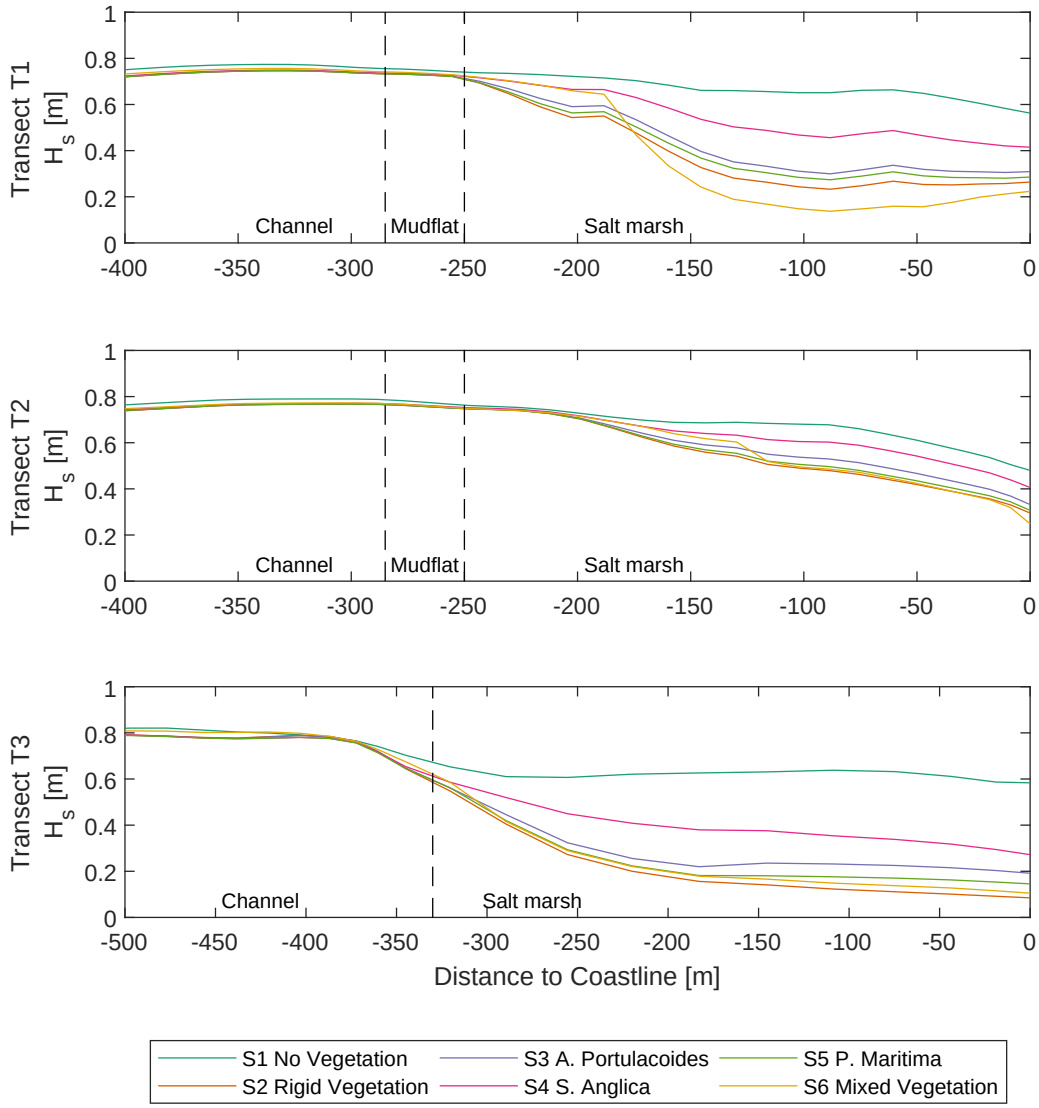

Figure 7.17: Comparison of the wave damping capacity of salt marshes along three transects under six vegetation scenarios. The transects are T1 (top row), T2 (middle row), and T3 (bottom row). The location of transects is shown in Figure 7.10.

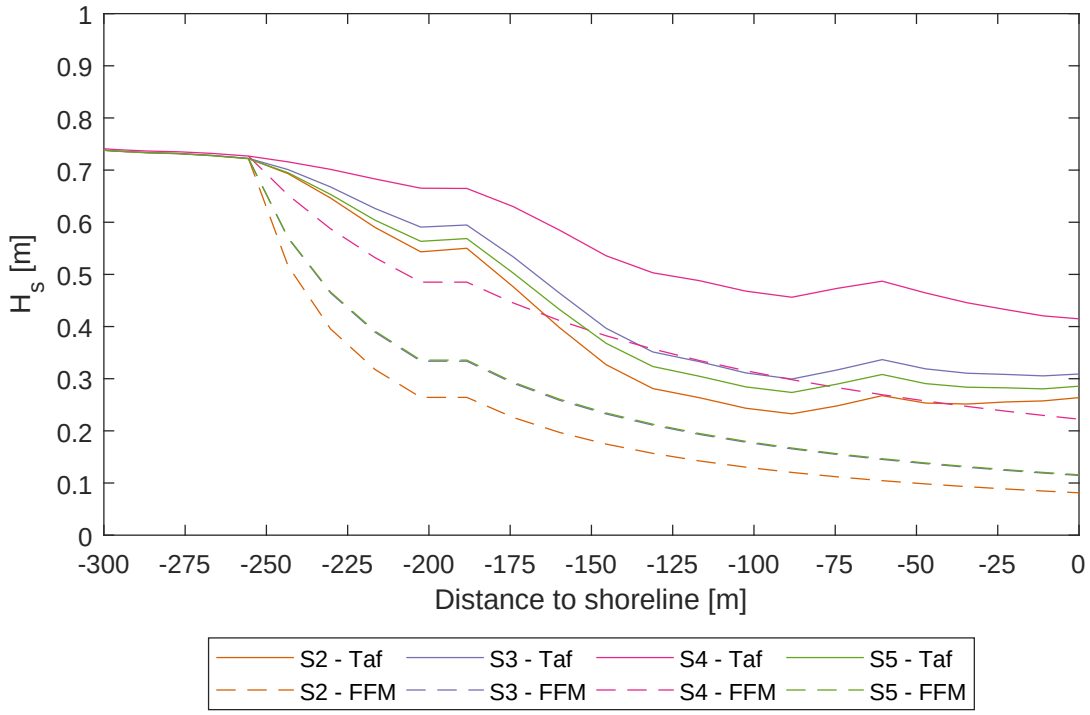

Figure 7.18: Comparison between the modelled wave attenuation along transect T1 of the Taf model (solid lines) and the theoretical full flexible model (FFM, dashed lines). The full flexible model predictions of scenarios S3 and S5 overlap.

and 200% larger in the 100 m closest to the coastline (Table 7.6).

The higher waves in the Taf model may be the result of wind growth, which is included in the Taf model but not in the full flexible model. Wind-driven growth is significant due to the high wind speeds in the direction of wave propagation. The presence of wind also explains why the relative difference between the two models increases closer to the coastline. The energy dissipation by vegetation reduces in landward direction as $\hat{\epsilon}_v \propto H_{rms}^3$ (Eq. 7.2). This results in continuous wave damping at an increasingly slower rate in the full flexible model. Alternatively, an equilibrium wave height is observed in the Taf model when the wind growth term equals the reducing dissipation term. The relative difference between the two models will increase in the landward direction from the location that an equilibrium is reached. In addition to wind growth, SWAN also includes energy source terms for whitecapping, depth-induced breaking, bottom friction, and wave-wave interactions (*Booij et al.*, 1999), but none of these source terms increases the spectral wave energy.

To further investigate the role of wind on wave damping over salt marshes, the Taf model has been run without wind on the Laugharne Castle Marsh subdo-

Table 7.6: Modelled significant wave height H_s in metres along transect T1 by the full flexible model (FFM) and the Taf model. The relative increase in wave height of the Taf model relative to the FFM model is also given.

	Distance to coastline [m]					
Scenario	**-250**	**-200**	**-150**	**-100**	**-50**	**0**
S2 - FFM	0.72	0.26	0.17	0.13	0.1	0.08
S2 - Taf	0.72	0.54	0.33	0.24	0.25	0.23
S2 - increase	0%	108%	94%	85%	150%	188%
S3 - FFM	0.72	0.34	0.23	0.18	0.14	0.12
S3 - Taf	0.72	0.59	0.4	0.3	0.32	0.31
S3 - increase	0%	74%	74%	67%	129%	158%
S4 - FFM	0.73	0.49	0.38	0.32	0.26	0.22
S4 - Taf	0.73	0.67	0.54	0.47	0.47	0.41
S4 - increase	0%	37%	42%	47%	81%	86%
S5 - FFM	0.72	0.34	0.23	0.18	0.14	0.12
S5 - Taf	0.72	0.56	0.37	0.28	0.29	0.29
S5 - increase	0%	65%	61%	56%	107%	142%

main (Fig. 7.19). The wind has remained in place on the other subdomains. The difference between the Taf model and the full flexible model has reduced significantly. The waves damp continuously over the whole marsh without reaching an equilibrium when the wind forcing is removed, which is consistent with the full flexible model predictions. As a result, the difference in simulated wave height between the two models has reduced by approximately 50% at the shoreline under each scenario. However, the Taf model still predicts significantly higher waves near the marsh edge. This suggests that edge effects are important in addition to wind growth. These include the advection of the wave energy flux, which may be enhanced at the edge by higher waves, currents in the main channel, and momentum that arise from wave breaking. Also, the salt marsh edge in the Taf Estuary is not straight and normal to the direction of wave propagation as assumed in the flexible model.

Furthermore, the difference between the Taf model and the full flexible model is the smallest for the most flexible species. The scaled flexibility Q decreases when the wave height reduces in the landward direction. Therefore, vegetation flexibility is most important at the seaward edge of a salt marsh, whereas flexible and rigid vegetation will impact waves more similarly near the coastline. This effect is included in the Taf model but not in the full flexible model, which assumes

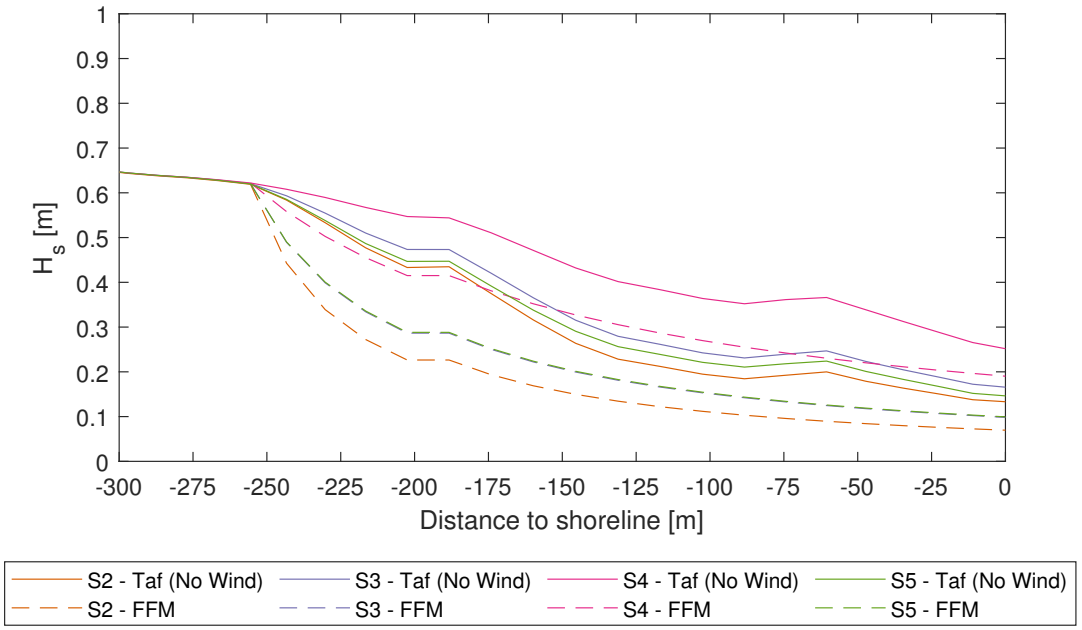

Figure 7.19: Comparison between the modelled wave attenuation along transect T1 of the Taf model without wind on the Laugharne Castle Marsh subdomain (solid lines) and the theoretical full flexible model (FFM, dashed lines).

that the wave-vegetation interaction remains constant over the marsh width. The reduction in scaled flexibility in the Taf model increases wave damping near the coastline. This mitigates the effect of the wind-driven wave growth, which reduces the difference in simulated wave height between the two models.

The differences in wave damping between the Taf model and the full flexible model follow from additional physics that are included in the Taf model. They highlight that the observed wave field follows from a complex interplay between wave dynamics and vegetation. Wind-driven wave growth by and the reduction in scaled flexibility of vegetation across a salt marsh appear to be important mechanisms, but cannot explain the full difference between the Taf model and the full flexible model. The difference is particularly large at the edge, which suggests that edge effects such as advection and complex topography may also play a part. Additional research is required to quantify the contribution of these processes.

7.7 Conclusions

We have created a new current-wave-vegetation model to investigate the coastal protection function of salt marshes in the Taf Estuary. Vegetation flexibility and spatial variations in the drag coefficient have been included for the first time in a large-scale hydrodynamic model. Six scenarios with contrasting vegetation species have been modelled to investigate their impact on the water level, current velocities and wave height as flood risk indicators.

Our results show that salt marshes contribute significantly to coastal protection. Their vegetation attenuates flood currents and lowers wave heights. The current velocities over salt marshes at peak flood are less than 0.1 m/s when vegetation is present. Furthermore, the wave heights reduce by up to 70% compared to the non-vegetated reference case on Laugharne Castle and Laugharne South Marsh. The wave damping potential of salt marshes lowers in the landward direction as the magnitude of the vegetation-induced energy dissipation reduces relative to the wind-driven growth term until an equilibrium wave height is reached. Additionally, salt marsh vegetation dampens wind-driven wave growth when the wave propagation is in the seaward direction. A reduction in water level was only observed over Blackscar Marsh.

The vegetation scenarios show that the wave damping strongly depends on the vegetation cover. We have identified that plant flexibility, plant dimensions, and the spatial distribution of vegetation affect wave damping. Tall semi-flexible species provide 50% less wave damping than rigid vegetation. The impact of vegetation flexibility decreases over longer salt marshes, as the wave heights lower and the scaled flexibility Q approaches its rigid limit for all species. Alternatively, the wave damping increases for thin and dense species due to the higher drag coefficient and the number of stems over which wave energy is dissipated. Furthermore, the wave damping can locally increase or decrease based on the spatial distribution of vegetation and the presence of salt marsh creeks. Finally, the flood current velocities were the least affected by mixed vegetation on Laugharne Castle Marsh, although the current attenuation remained significant at approximately 50%.

Our results highlight that all vegetation characteristics must be included in computational models in order to accurately simulate the wave field over salt marshes. Here we have investigated the impact of five contrasting vegetation species, including woody shrubs and grasses, across six scenarios. These species are found to interact very differently with waves. The model presented here can be adapted to investigate the contribution of salt marshes across a wider range of coastlines and vegetation species.

Chapter 8

Conclusions

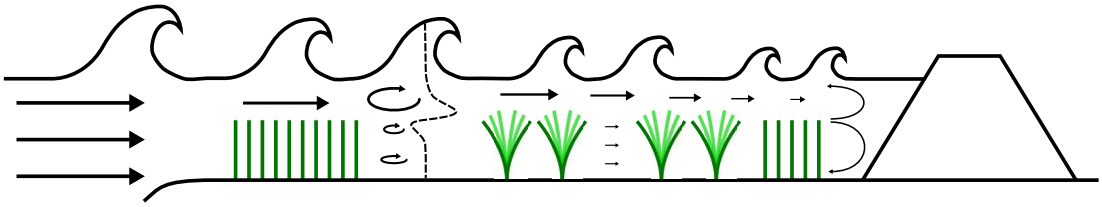

8.1 Synthesis

The main objective of this research is to better understand how salt marshes with a flexible vegetation cover contribute to coastal protection under storm conditions with surge and wave components, and how the vegetation cover affects the level of protection that is provided. I reached this objective by modelling the current-vegetation and wave-vegetation interactions. Four current-vegetation parameterisations were implemented in a Delft3D model of an idealised estuary to compare the uncertainty of the hydrodynamics due to model parameterisations. Then, the impact of vegetation flexibility on the wave-vegetation interaction was tested in the Swansea University wave flume. Wave heights, velocity fields and plant motion were measured simultaneously for the first time during these experiments to identify the key physics that control the wave-vegetation interaction. Based on the key physics, I developed a novel wave damping model for flexible coastal vegetation which predicts wave damping over the canopy using only wave and vegetation parameters. I combined the selected current-vegetation parameterisation and my novel wave damping model with Delft3D to set up a coupled current-wave-vegetation model of the Taf estuary. This model was successfully applied to study the effect of six contrasting vegetation scenarios on the water level, current velocities and wave heights under a storm surge in combination with waves. By studying the current-vegetation and wave-vegetation interactions in idealised models, in experiments, and in a case study, I was able to develop a thorough understanding of how salt marshes and their vegetation contribute to coastal protection in response to storm surges and waves.

8.2 Main outcomes

1. **Salt marshes contribute to coastal protection by constraining flood currents to the main estuary channel and attenuating incoming waves.**

Salt marsh vegetation induces drag resistance to water motion, which reduces the current velocities and manipulates the current direction. Significant longshore currents were observed over salt marshes during peak flood in our idealised estuary model and Taf model without vegetation. When vegetation was added to the salt marshes, the currents disappeared in both models. Only a small current in a direction perpendicular to the estuary or nearest creek remained. At the same time, the flow velocities in the main estuary channel increased due to the absence of longshore currents over salt marshes with vegetation. However, my results also

suggest that vegetation-induced drag on currents slows the drainage of flooded areas, which increases their inundation period.

Furthermore, the salt marsh vegetation attenuates wave heights, as has been shown experimentally and using computational models for idealised and field conditions. Experiments with artificial rigid and flexible vegetation have demonstrated the capacity of vegetation with varying flexibility to attenuate incoming waves. The experimentally observed wave damping was successfully reproduced in a novel wave damping model for regular and random waves. When the wave damping model was coupled with Delft3D into a large-scale current-wave-vegetation model, the salt marshes in the Taf estuary were found to damp wave heights by up to 70% depending on vegetation conditions. My results support prior field (e.g. *Jadhav et al.*, 2013) and experimental (e.g *Möller et al.*, 2014) evidence across a broader range of vegetation species and quantify the effect of plant flexibility on wave damping.

The attenuation of current velocities and waves contributes to coastal protection by preventing erosion and mitigating the loading on flood defence structures. The reduced current and orbital velocities mitigate the bed shear stresses on salt marshes, which lowers the probability of erosion during storm events (*Fredsoe and Deigaard*, 1992). Additionally, the loading on coastal defence structures is mitigated due to wave attenuation (*Vuik et al.*, 2016).

2. **Modelling the current-vegetation interaction by a momentum sink term parameterisation best resembles the literature and prior experimental studies.**

By comparing four current-vegetation parameterisations, I found that the vertical structure of horizontal velocity, the turbulent intensity, the water level and the bed shear stress are sensitive to the parameterisation of the current-vegetation interaction. Parameterisations via an elevated bottom roughness predicted higher bed shear stresses and the trachytope model produced a parabolic velocity profile for which no evidence was found in the literature. The momentum sink term parameterisation best resembles the vertical variation in the horizontal velocity profile with a region of dampened velocities within the vegetation and a region of free flow over the canopy (resembling *Baptist et al.*, 2007). It produces maximum turbulent intensity at the top of the canopy (resembling *Nepf*, 2012b) and leads to a reduction in bed shear stress, which agrees with the reduction in near-bed current velocities. Alternatively, no qualitative differences between the four parameterisations were observed in the modelled depth-averaged current velocity and direction.

3. **Vegetation flexibility is a key plant parameter that controls wave**

damping and the wave-induced velocity structure around vegetation.

My novel experimental results show that wave damping and the wave-induced velocity structure differ significantly between artificial rigid and flexible vegetation. Both vegetation types damp incoming waves, but the damping by flexible vegetation is 70% lower than by rigid vegetation under laboratory conditions. Thus, a salt marsh with a rigid vegetation species could be 70% narrower than a salt marsh with a flexible vegetation species while providing equivalent wave damping. The difference between the two vegetation types will often be smaller under field conditions due to wind-driven wave growth and a reduction in scaled vegetation flexibility over long salt marshes. My simulations of wave damping in the Taf estuary showed that the most flexible species provided 50% less wave damping than the most rigid species when these processes were included.

Furthermore, rigid vegetation strongly impacts the wave-driven velocity structure, whereas flexible vegetation does not. Specifically, the interaction between waves and rigid vegetation induces a current in the direction of wave propagation through the top of the canopy. This current propagates above and below the canopy in phase with the water surface. For submerged vegetation, this results in amplified horizontal particle velocities above the canopy and reduced velocities within the canopy. The magnitude of the current and the amplification depend on the submergence ratio. A stronger current and amplification develop for higher submergence ratios. Finally, a return current develops high in the water column when the vegetation is sufficiently submerged or, otherwise, through the meadow.

Based on the strong impact of vegetation flexibility on wave damping and velocity structure, I find that rigid vegetation controls the wave dynamics and flexible vegetation follows the wave dynamics.

4. **Wave damping over flexible coastal vegetation is controlled by the velocity transfer from water to stem motion in the upright bottom section of a stem.**

The wave-vegetation interaction is a reciprocal system where the drag force and plant motion depend on each other. Based on the combined experimental observations of wave damping, water particle velocities and plant motion, I have identified three key mechanisms in the wave-vegetation interaction that control wave damping over flexible vegetation: (i) the drag force is the dominant force at the bottom section of a flexible stem; (ii) wave energy is dissipated in the bottom section of a flexible stem; (iii) wave energy dissipation is controlled by the velocity difference between water and stem rather than the reconfiguration of stem posture. The three key mechanisms indicate that the velocity transfer in the bottom upright section of flexible coastal vegetation controls wave damping.

5. **The wave damping capacity of salt marshes can be predicted based on wave and vegetation parameters without calibration of a drag coefficient.**

I developed a novel wave damping model which predicts the wave damping coefficient of flexible coastal vegetation as a function of wave and vegetation parameters. The wave parameters are the water depth, wave height and wave period. The vegetation parameters are the vegetation height, vegetation diameter, vegetation density and flexural rigidity. Vegetation is modelled as near-vertical flexible rods. The velocity transfer from water to vegetation motion is solved via the Euler-Bernoulli beam equations. The impact of vegetation motion on wave damping is included in the model via a new work factor. The work factor describes the reduction in wave dissipation relative to rigid vegetation due to plant motion and follows directly from the computed velocity transfer. My model can predict the damping capacity of salt marshes under regular and random wave conditions. The random wave conditions are restricted to a Rayleigh distribution. The model has been successfully validated against observed wave damping over five vegetation species that differ in flexibility and under a range of regular and random wave conditions.

My new wave damping model is computationally efficient for large-scale coastal areas, does not require plant-specific calibration, and can be applied to salt marshes with a mixed vegetation cover. The model has been successfully applied to the Taf estuary, which covers a large area and exhibits extensive salt marshes with a diverse vegetation cover. Unlike prior models, my model does not rely on the plant-specific calibration of a drag coefficient as plant motion is explicitly included. It can be applied to any vegetation species when its geometry can be represented as a cylinder, and its height exceeds the water particle excursion length. The model can be adapted to non-cylindrical vegetation when appropriate relations for the drag coefficient and Cauchy number are used. Therefore, the model is particularly suited to areas with spatiotemporal variations in wave and vegetation conditions, or when interventions such as managed realignment, grazing, and the introduction of new species are considered.

6. **A coupled current-wave-vegetation model is a powerful tool to simulate flood risk under combined surge and wave conditions over salt marshes with mixed vegetation cover.**

The effect of salt marshes on storm surges and waves has traditionally been studied separately. Here I have combined the selected current-vegetation parameterisation with a new wave-vegetation model to simulate a storm event in the Taf estuary where the surge and wave components are both important. I show

that a coupled current-wave-vegetation model successfully simulates the water depth, current velocities and wave heights across the estuary. The coupled model is a powerful tool to quantify the impact of different vegetation scenarios, including salt marshes with mixed vegetation cover, on flood risk by storm surges and waves.

Although all model components have been validated individually, the coupled model could only be validated against water depth and velocity measurements under calm weather conditions. Setting up a full-scale field campaign during storm conditions was not possible. However, the current-vegetation model has been successfully validated against field measurements in prior studies (*Temmerman et al.*, 2005; *Ashall et al.*, 2016). Furthermore, the modelled water depths and flow velocities from a run with salt marsh vegetation present were validated against measurements taken at the Taf estuary, and the wave damping model has been extensively validated against observations for a wide range of vegetation and wave conditions which include real vegetation species under storm conditions. These individual validations provide reasonable confidence in the coupled model.

7. **The coastal protection provided by salt marshes depends on their vegetation cover.**

The vegetation cover of salt marshes strongly impacts the flood risk on the scale of the whole estuary and locally, as shown by my modelling results in the Taf estuary. Six scenarios with vegetation that differed in flexibility and dimensions were modelled. On the scale of an estuary, the vegetation cover primarily controls wave height. An increasingly flexible vegetation cover reduces the capacity of salt marshes to dampen waves, which agrees with my experimental results. Furthermore, I find that thin and dense vegetation better damps incoming waves than thick vegetation with an equal frontal area due to the higher drag coefficient of thin vegetation. The current velocities and water depth were insensitive to variations in vegetation cover. The currents over salt marshes were eliminated by all vegetation scenarios with a uniform plant cover, and no vegetation scenario significantly affected the water depth.

Salt marsh creeks and spatial variations in vegetation density can locally increase or decrease the attenuation of waves and currents. The presence of salt marsh creeks reduced the wave damping capacity significantly despite vegetation on either side of the creek. The average reduction in wave height over a salt marsh creek was 50% over 250 m compared to 75% over 100 m for an equivalent transect away from the creek. Alternatively, dense patches of vegetation were found to locally increase the wave damping capacity of salt marshes. Although the salt marsh vegetation attenuated flood currents over the platforms, current

velocities increased in the creeks due to the channelling effect of vegetation.

My results demonstrate that salt marshes contribute to coastal protection by attenuating currents and waves, but the protection provided strongly depends on the properties of its vegetation. Variations in the vegetation cover can strongly affect the wave attenuation by salt marshes. In particular, vegetation flexibility is a parameter that was previously omitted but is now found to significantly impact the wave-vegetation interaction. It is recommended that the biomechanical properties of vegetation, including flexibility, are considered when modelling the flood risk on coastlines with salt marshes. I have developed and tested a new modelling framework to quantify wave-current fields around coastal vegetation with application across plant species. Therefore, this thesis provides evidence and tools to further support the ongoing uptake of salt marshes as nature-based coastal defences.

8.3 Visual summary

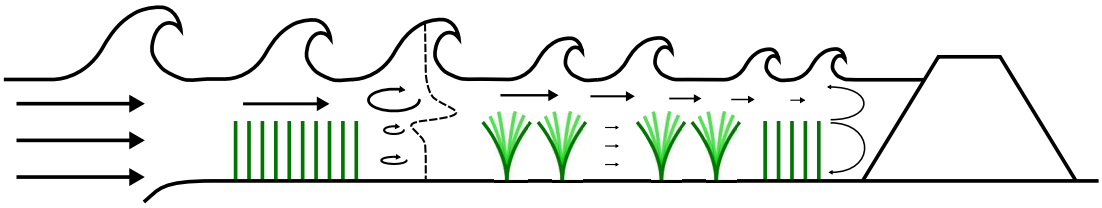

Figure 8.1: Visual summary of selected outcomes. Rigid and flexible vegetation both contribute to wave damping. Although rigid plants are more effective due to the swaying of flexible vegetation. The horizontal component of the orbital velocity is amplified above a rigid vegetation canopy and preferentially damped directly below the top of the canopy. This is denoted by the orbital velocity paths and the dashed line in the upstream gap in the vegetation field. Additionally, rigid vegetation can induce wave-averaged currents through the top of the canopy, which can result in circulations in closed environments. This is denoted by curved arrows near the levee. Finally, vegetation can attenuate unidirectional currents with the strongest attenuation within the canopy. Unidirectional currents are denoted by straight arrows. The vertical variation in the velocity is shown in the middle gap of the vegetation field.

8.4 Suggested improvements in methodology

In addition to the outcomes, this thesis has also provided insights into the methodology with possible improvements for future work. The combination of experiments and computational models has been very valuable to address the impact of vegetation on coastal protection from two complementary perspectives. The experimental work has provided new insights into the small-scale physical interactions between waves and currents, while the computational modelling work enabled me to scale up to large coastal zones. Yet, certain challenges that were encountered in both branches can be overcome when the methodology is improved in future work.

The main improvements in the experimental methodology lie in its set up. A major limitation was the presence of significant wave reflection at the back end of the flume. This restricted the length of the vegetation patch and the permissible wave conditions. This limitation can be overcome by investing in a strong wave damping mechanism at the back end of the flume. TA parabolic wave damper of reticulated foam as successfully used in *Sánchez-González et al.* (2011) was despite best efforts insufficient in this study. Possible alternatives are a long sandy beach under a low incline *Koftis et al.* (2013) or a rubber horsehair beach (*Augustin et al.*, 2009). Furthermore, ideally a larger range of KC, Re, and L should be tested to verify the proposed relations in this thesis over a wider range of hydrodynamic conditions. The gap within the vegetation was successful for measuring velocities within a rigid canopy, but did serve its purpose for flexible vegetation due to the swaying of vegetation. Finally, this thesis builds on few experiments under random waves. Future work can increase the number of random wave conditions to increase confidence in my new wave damping model for random waves.

The main improvements in the computational modelling methodology lie in the validation. The idealised estuary model (Ch. 3) lacked a benchmark solution. Hence, it was more difficult to compare the performance of the four selected parameterisations. The Taf model (Ch. 7) is validated for its modelled current velocities and water levels, but not its wave field. This would require an extensive measurement setup with multiple wave gauges along a single transect over a long period during which a major storm hopefully arrives (*Jadhav et al.*, 2013; *Vuik et al.*, 2016). This would have been a major undertaking beyond the resources available to this study. Furthermore, the Taf model can be improved by implementing my new wave damping model directly in SWAN.

8.5 Future Research

Wave-current interaction

Although the current-vegetation and wave-vegetation interactions have been coupled in this thesis, the impact of currents on the wave-vegetation interaction is not considered. *Losada et al.* (2016) showed that wave damping reduces in case of currents in the direction of wave propagation and increases in case of opposing currents. Therefore, my model may overpredict the wave damping during flood tide and with incoming surge flow, and underpredict the wave damping during ebb tide and outgoing surge flow. The most extreme wave conditions in the Taf estuary occurred during peak high water when current velocities were negligible, but the impacts of currents may be relevant to other coastal environments (e.g. *Garzon et al.*, 2019a). Currents manipulate the force balance that controls the wave-vegetation interaction, such that a new solution of the velocity transfer function is required. In addition to currents driven by tides, surges and rivers, wave-induced currents may also be included in the force balance. I have identified that wave-induced currents depend on vegetation flexibility, but I have not developed a relation between them. However, *Luhar et al.* (2010) and *Abdolahpour et al.* (2017) have provided theoretical models to predict the magnitude of wave-induced current velocities of rigid and flexible vegetation. These could form the basis of a wave-vegetation interaction model that includes the effect of currents. Such new wave-current-vegetation interaction model can be readily implemented in computational models such as Delft3D, as the wave-current interactions that do not involve vegetation are already implemented in computational models.

Sediment transport

This thesis has focussed on the hydrodynamic contributions of salt marshes to coastal protection. Yet, it is well-accepted that part of the contribution lies in the capacity of salt marshes to stabilise shorelines (*Bouma et al.*, 2014) and to adapt to sea level rise (*French*, 1993). These adaptive capabilities are particularly useful under the ongoing climate emergency which will significantly elevate the sea level and worsen the hydrodynamic conditions at the coast (*IPCC*, 2019). Recent morphodynamic modelling studies (*Temmerman et al.*, 2005; *Mariotti and Canestrelli*, 2017; *Best et al.*, 2018) have explored the impacts of geology and local sea level on the sediment budgets of vegetated seashores, but the underlying vegetation-induced physics have been greatly simplified in those models. The hydrodynamic model presented here can support the development of new morphodynamic models that are based on more sophisticated current-wave-vegetation interactions. New current-wave-vegetation-sediment models can potentially im-

prove estimates of sediment erosion and accretion under current and future storm conditions.

Based on the successful application in this thesis, it is advised to investigate sediment transport concurrently via experimental and computational studies. The small-scale interactions between sediments, waves, currents and vegetation such as sediment uptake and deposition are likely best studied in the controlled environment of a wave flume. Alternatively, the impact of vegetation on the coastal scale is best studied using computational models, where the impact of vegetation can be modelled in the context of real topographies and other coastal processes. The sediment-vegetation parameterisations in the computational models can be based on the experimental results such that the two studies are complementary. Ultimately, the computational model should aim to improve predictions of coastal evolution of salt marsh environments as well as the coastal protection provided by them, building on the the work presented in this thesis.

Appendix A

Data collection in South Wales estuaries

A.1 Plant Data

Salt marshes in South Wales are generally sheltered and exhibit a mix of shrubby and grassy species, among which *Atriplex Portulacoides*, *Spartina Anglica*, *Festuca Rubra*, *Puccinellia Maritima* and *Aster Tripolium* are most common. Data for these species has been obtained from field campaigns in the Taf (August 2017) and Neath (April 2018) estuaries. These two estuaries are typical of small, macro-tidal estuaries found in Wales, UK, which contain a substantial expanse of salt marshes. Plant density was measured in the field and at least 9 samples of each species were brought to the lab for further analysis from both sites (Table A.1).

The samples were pressed against a lightbox and photographed to obtain plant morphology, which was used to derive stem height, stem diameter, and the number of stems per plant. The mean values of stem height ranged from 231 mm (*F. Rubra*) to 590 mm (*S. Anglica*) and stem-averaged diameters from 0.74 mm (*F. Rubra*) to 5.50 mm (*A. Tripolium*). Furthermore, the number of stems per plant was multiplied by plant density to obtain stem density values. These ranged from 214 stems/m^2 (*A. Tripolium*) to 36000 stems/m^2 (*F. Rubra*). The corresponding frontal area λ_f varied between 0.57 m^2 (*A. Tripolium*) and 6.08 m^2 (*F. Rubra*) per m^2 ground area.

Furthermore, plant flexural rigidities were obtained via bending tests, following *Miler et al.* (2012) and *Paul et al.* (2014). *A. Portulacoides*, *P. Maritima* and *F. Rubra* were subjected to a three-point bending test, while a four-point bending test was applied to *S. Anglica* and *A. Tripolium* to avoid stem denting. However, only 4 samples of *S. Anglica* and *A. Tripolium* were viable. A mixture of top, middle and bottom stem sections were tested for all species. Ultimately, Young's

Table A.1: Plant data as measured on South Wales salt marshes. The number of samples n is given separately for geometrical and mechanical tests. Standard deviation σ is given for key parameter E.

Specie	h_v **(mm)**	b_v **(mm)**	n_v **(m^{-2})**	λ_f	**n**	E **(MPa)**	σ **(MPa)**	EI_v **(Nm2)**	**n**
A. Portulacoides	334	2.58	2275	1.96	72	745	355	1.62×10^{-3}	10
S. Anglica	590	3.33	720	1.42	72	139	71	8.38×10^{-4}	4
P. Maritima	335	0.85	3444	0.98	27	757	382	1.94×10^{-5}	15
F. Rubra	231	0.74	36000	6.08	9	2343	2006	3.45×10^{-5}	11
A. Tripolium	487	5.50	214	0.57	24	572	469	2.57×10^{-2}	4

moduli E ranged from 139 MPa (*S. Anglica*) to 2343 MPa (*F. Rubra*) and corresponding flexural rigidities EI ranged from 2.57×10^{-2} Nm^2 (*A. Tripolium*) to 1.94×10^{-5} Nm^2 (*P. Maritima*).

A.2 Wave Properties

Wave conditions were determined by numerical modelling of wave penetration into a sheltered macro-tidal estuary, which is typical of South Wales (*Bennett et al.*, 2019). Results for moderate storm conditions are used, because these occur more frequently and have a larger impact on salt marsh deterioration (*Leonardi et al.*, 2016). Typical wave parameters for these conditions are the significant wave height $H_s = 0.1$–0.2 m, peak period $T_p = 2$ s and water depth $h = 0$–0.6 m.

Appendix B

Linear velocity estimation

Linear velocity amplitude u_0 is derived from linear wave theory, using the water surface elevation harmonics from WG2 at the centre of the vegetation patch. The three primary water surface harmonics are used, which is consistent with PIV-derived velocity signals. Following linear wave theory, the orbital velocities can be expressed as

$$u_{00}(z,t) = \sum_{n=0}^{2} \left(\frac{\eta_{amp,n} g k_n}{\omega_n} \frac{\cosh\left[k_n(h+z)\right]}{\cosh(k_n h)} \cos(\omega_n t + \phi_n) \right), \tag{B.1}$$

where subscript n denotes the order of the harmonic of each parameter. $n = 0$ denotes the natural frequency and $n = 1, 2$ refers to the first and second order harmonics respectively. u_{00} is the reference horizontal velocity profile at WG2. Furthermore, η_{amp} is the amplitude of the water surface motion, $\omega = 2\pi/T$ is the wave frequency and ϕ is the wave phase. Like the PIV velocity signals, the velocity amplitude can now be obtained via the maximum and minimum of the time series at each point in the water column, expressed as $u_{00,amp}(z) = (\max u_{00} - \min u_{00})/2$.

However, WG2 is located at the centre of the vegetation patch and wave attenuation continues downstream. Therefore, the reference velocities are corrected with respect to along-patch coordinate x (see Section 4.2 for details), according to

$$u_0(x,z) = \frac{u_{00,amp}}{1 + \beta\left[\min(x, L_v) - x_{WG2}\right]}. \tag{B.2}$$

Herein, u_0 is a spatially varying reference velocities corrected for wave attenuation. We iterate that $x = 0$ depicts the upstream edge of the vegetation. Furthermore, $x_{WG2} = 0.75$ m is the position of WG2 and $x = L_v$ is the downstream edge of the vegetation, beyond which waves do not further attenuate.

We now define non-dimensional velocity $U^* = u_{amp}/u_0$. It should be noted that they closely resemble attenuation parameter α_w in *Lowe et al.* (2005). However, U^* also includes higher order harmonics and the impact of wave attenuation.

Appendix C

Derivation of plant motion

Plant posture is the position of the stem over time and describes plant motion. Rigid stems are fully upright over the wave cycle. For flexible stems, plant posture is obtained from the PIV-images that were taken during our experiments. Images were shot at a rate of 50 Hz for a continuous period of 15 seconds per run. This amounts to 750 images total for each experiment. It was found that waves and plant motion were still developing during the first 4 seconds of a run. Therefore, the plant motion time series were curtailed to 11 seconds or 550 images. At least five full wave cycles fitted within the measurement period and each wave condition was run three times. The same images were used to derive water particle velocities (Section 4.3.5), such that plant position and velocity data are in phase.

Any algorithm for plant posture should adequately resolve plant frontal area and stem velocity. Plant frontal area is important for area on the drag force exerts work (*Paul et al.*, 2016) and the stem velocity is required to obtain relative velocities between plant and water, which affects both drag and inertia forces (*Zeller et al.*, 2014). Following *Zeller et al.* (2014), stretching of flexible vegetation is considered negligible, such that the vegetation length is constant and the plant frontal area is a function of plant position only.

We apply a simple model that predicts the stem posture from the root and tip positions (Fig. C.1). It assumes that the stem is straight or forms a circular arc between root and tip. Which shape is fit, depends on vegetation height h_v and the chord length between root and tip d. When the chord length equals the vegetation height, $d = h_v$, the stem is straight with length h_v and rotation θ_v. The stem originates at the root and is in the direction of the tip. In mathematical terms, the stem position is expressed as

$$X(s,t) = se^{i(\frac{1}{2}\pi - \theta_v)}. \tag{C.1}$$

We reiterate that X is the complex plant coordinate with its root $X(0,t) = 0$ at the origin of the coordinate system.

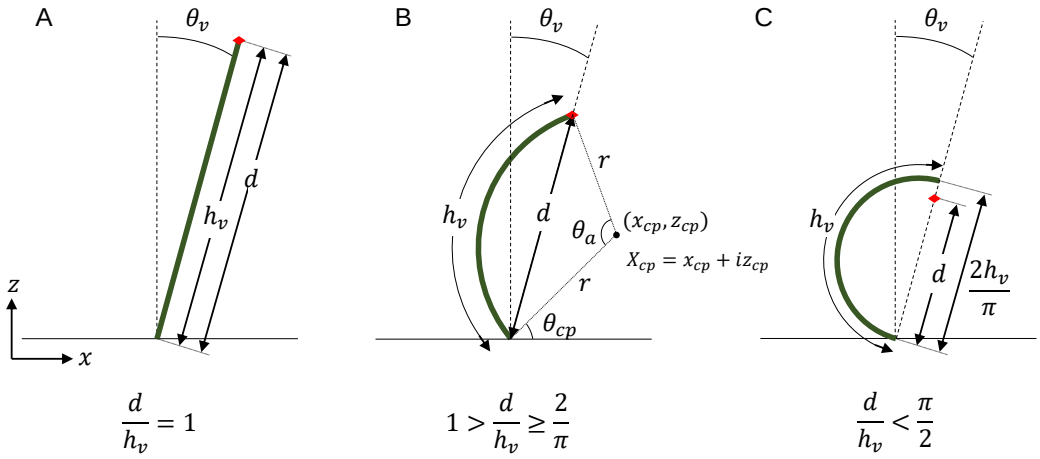

Figure C.1: Plant posture model that calculates plant position using the tip position (red diamond), plant length h_v and chord length d. θ_v is the vegetation rotation. Three cases are considered: (a) the plant is straight; (b) a circular arc with length h_v can be fitted between root and tip; (c) no circular arc with length h_v can be fitted. Therefore, the smallest semicircle with length h_v is fitted instead.

When the direct distance between root and tip is smaller than the stem length, $d < h$, a circular arc between root and tip with length h_v is fit. The radius r and angle θ_a of the arc are related to the arc length, according to

$$\theta_a = \frac{h_v}{r}, \tag{C.2}$$

and chord length, according to

$$\sin \frac{1}{2}\theta_a = \frac{d}{2r}. \tag{C.3}$$

Substituting Equation C.2 in Equation C.3 leads to

$$\sin\left(\frac{h_v}{2r}\right) = \frac{d}{2r}, \tag{C.4}$$

where r is the only unknown. Equation C.4 has a unique solution in the domain $1 > \frac{d}{h_v} \geq \frac{2}{\pi}$, which is obtained numerically.

The circle of which the arc is part, is constructed from root and tip positions and radius r. Specifically, two circles can be constructed from two given points and a radius: one with the centre point upstream and one with the centre point downstream of the stem. The downstream centre point is used, because this is the

dominant direction for plant bending of very flexible vegetation (*Luhar and Nepf*, 2016; *Rupprecht et al.*, 2017). We define the complex coordinate of the centre point $X_{cp} = x_{cp} + iz_{cp} = re^{i\theta_{cp}}$ with respect to the stem root. $\theta_{cp} = \frac{1}{2}\pi - \theta_v - \frac{1}{2}\theta_a$ is obtained from a simple trigonometric summation at the root. Then, the plant position is given by

$$X(s,t) = X_{cp} + re^{i[\pi+\theta_{cp}-(s/h_v)\theta_a]}. \tag{C.5}$$

As the fit is repeated for each frame, d, r, θ_v, θ_a and θ_{cp} are all functions of time. Complex plant position X is a function of both time and along-stem coordinate s.

The third and final case is that of extreme bending, such that no arc with length h_v can be fit between root and tip (Fig. C.1c). Equation C.4 has no solution when $\frac{d}{h_v} < \frac{2}{\pi}$, i.e. chord length d is too small to construct an arc with length h_v around. The limiting case is $\frac{d}{h_v} = \frac{2}{\pi}$ when the chord is the diameter of semicircle with circumference h_v. It is important to obtain a continuous solution for X. Therefore, the limiting case is used to fit plant positions under extreme bending. The methodology of bending stems is followed, but with chord length $d = 2\frac{h_v}{\pi}$ instead of direct distance between root and tip. It follows from Eq. C.4 that $r = \frac{h_v}{\pi}$. The plant position under extreme bending is

$$X(s,t) = X_{cp} + \frac{h_v}{\pi} e^{i[\pi+\theta_{cp}-(s/h_v)\theta_a]}. \tag{C.6}$$

This solution implies that the frontal height and area may be overestimated. Our experiments show that stems fold over under extreme bending. The height in the middle of the stem is significantly higher than at the tip, which is consistent with our correction.

The three equations for plant position (Eq. C.1, C.5, C.6) can be combined into a single case-based equation

$$X(s,t) = \begin{cases} se^{i(\frac{1}{2}\pi-\theta_v)} & \text{if } \frac{d}{h_v}=1 \\ re^{i(\frac{1}{2}\pi-\theta_v-\frac{1}{2}\theta_a)} + re^{i[\pi+\theta_{cp}-(s/h_v)\theta_a]} & \text{if } 1 > \frac{d}{h_v} \geq \frac{2}{\pi} \\ \frac{h_v}{\pi}e^{i(\frac{1}{2}\pi-\theta_v-\frac{1}{2}\theta_a)} + \frac{h_v}{\pi}e^{i[\pi+\theta_{cp}-(s/h_v)\theta_a]} & \text{if } \frac{d}{h_v} < \frac{2}{\pi}. \end{cases} \tag{C.7}$$

The stem root and tip positions are selected manually in the PIV-frames taken during the experiments. The root is constant over a run and is selected in the first frame. The tip is identified for each frame separately by two independent controllers. The final tip position results from the average of two selected d and θ_v. Examples of our methodology are provided for small bending under wave conditions R11 ($H = 0.15$ m, $T = 1.4$ s, $h = 0.40$ m, Fig. C.2) and strong bending under wave conditions R23 ($H = 0.10$ m, $T = 1.8$ s, $h = 0.30$ m, Fig. C.3). The derived stem postures over the full wave run are shown in Fig. C.4.

Vegetation velocity $U_{veg} = u_{veg} + iw_{veg}$ is obtained in two steps. First, velocity is calculated directly from the stem position via a central difference scheme, according to

$$U_{veg,n} = \frac{X_{n+1} - X_{n-1}}{2\Delta t}. \tag{C.8}$$

Herein, subscript n is the frame for which the vegetation velocity is calculated and $\Delta t = 0.02$ s is the time between two consecutive frames. The first and last frame are resolved using forward difference and backward difference respectively. Then, a Fourier filter is applied to remove the high frequency noise in the velocity signal. Only the natural frequency and the first order higher harmonic are retained.

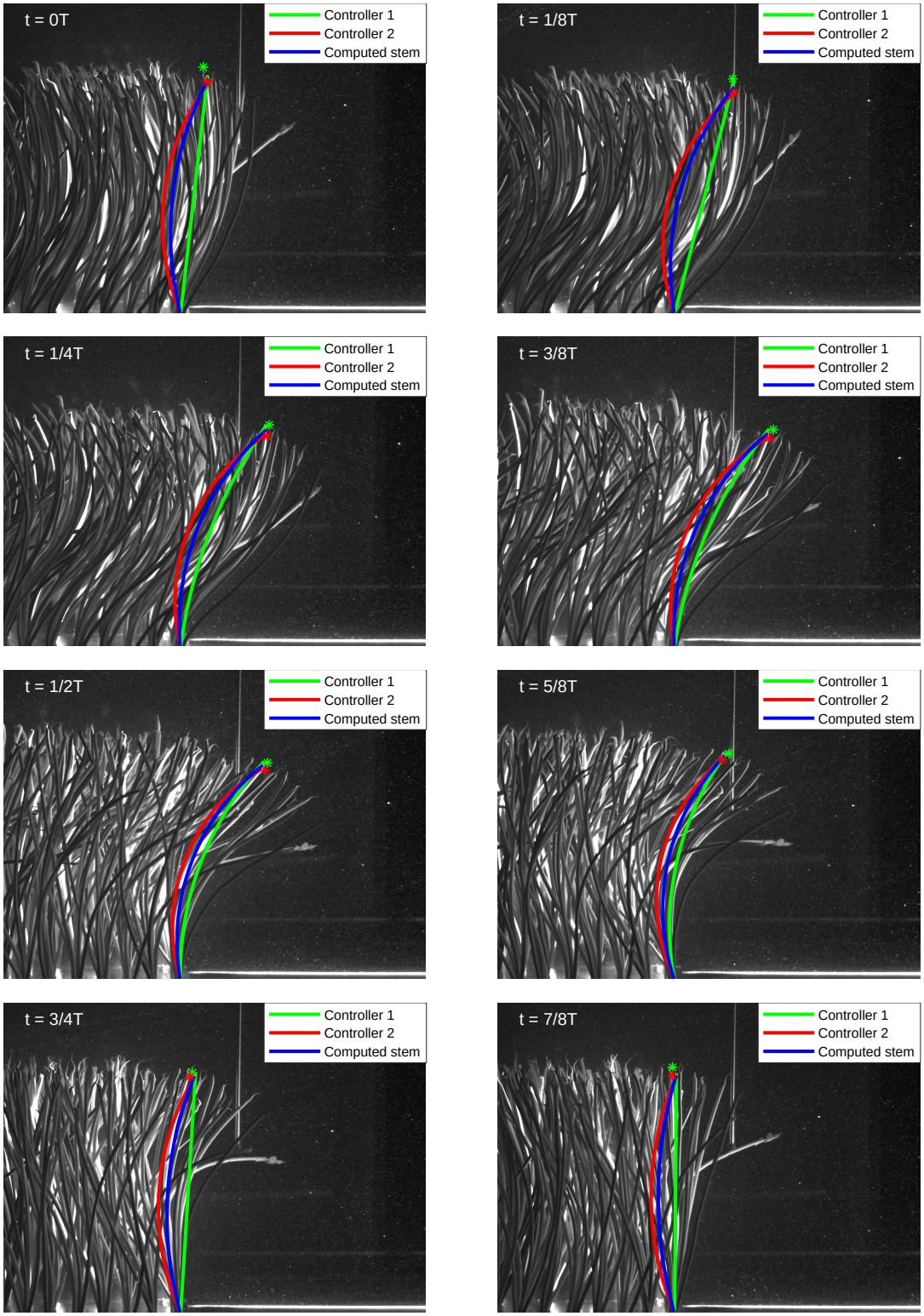

Figure C.2: Flexible stem identification under wave condition R11. The green and red lines are stem postures, which are derived independently by two independent controllers. The asterisks denote their respective tip selection. The blue line is the selected stem posture, which is derived from the average chord length and plant rotation.

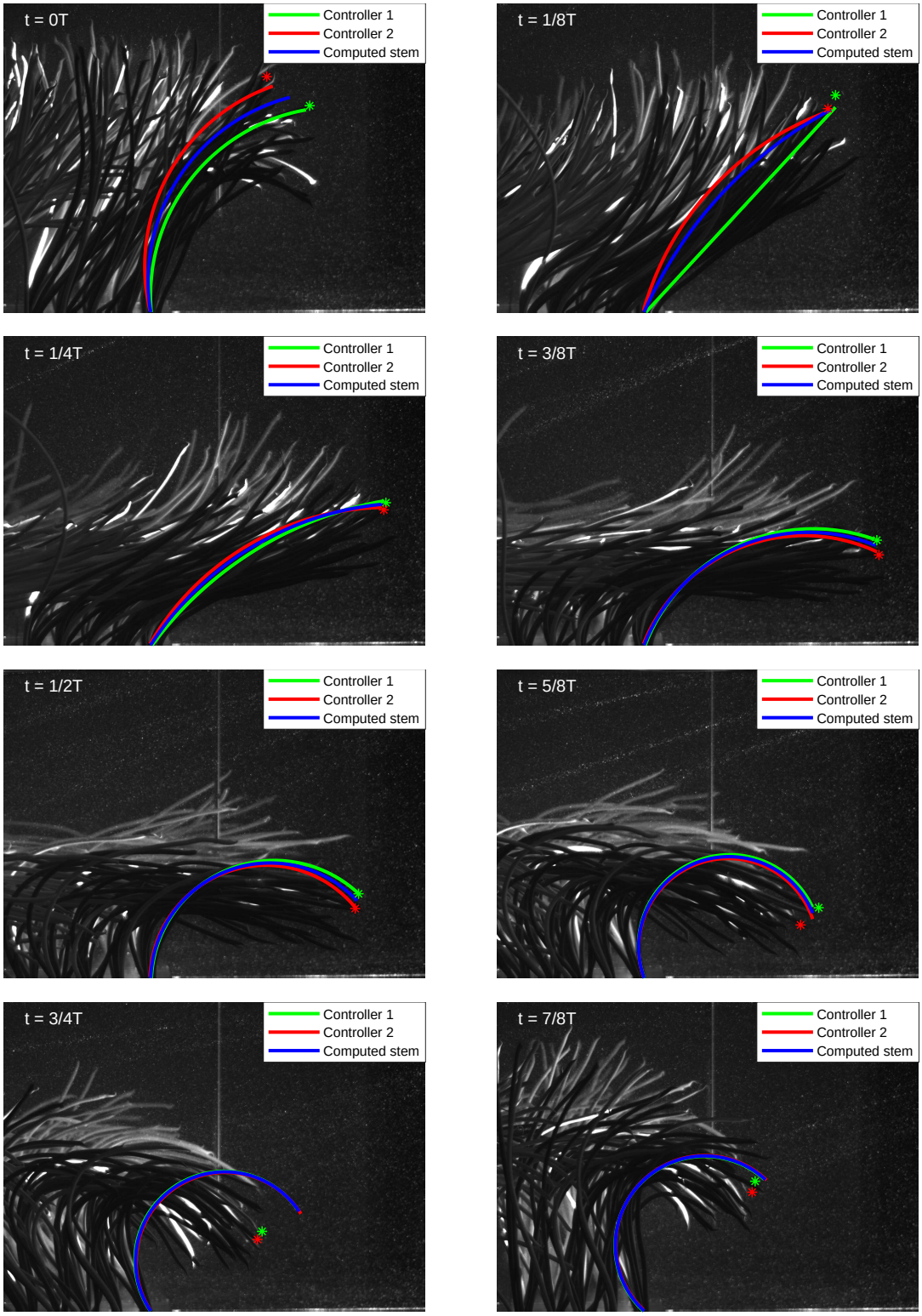

Figure C.3: Flexible stem identification under wave condition R23. The green and red lines are stem postures, which are derived independently by two independent controllers. The asterisks denote their respective tip selection. The blue line is the selected stem posture, which is derived from the average chord length and plant rotation.

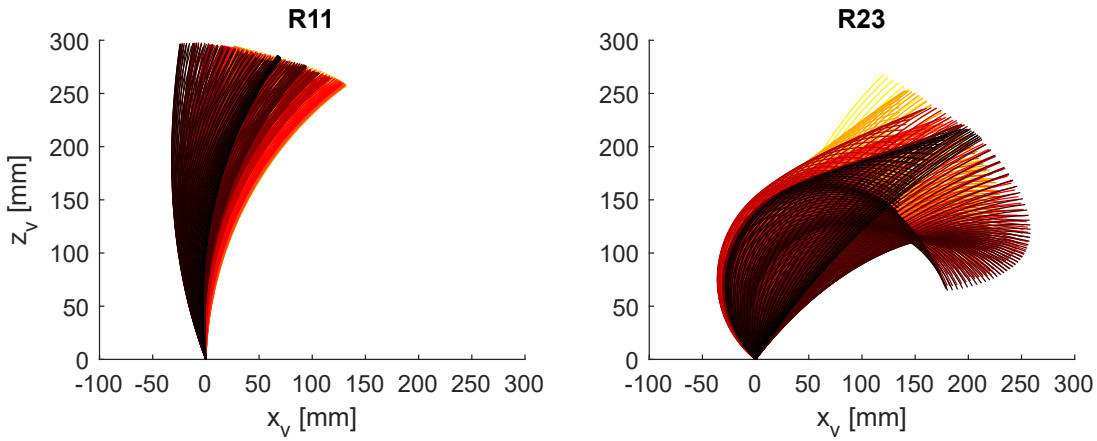

Figure C.4: The stem posture of flexible vegetation over time under conditions R11 and R23. The temporal variation is shown by colouring. The colours changes from yellow at the start of the experiment to black at the end. The root is at (0,0) for every stem.

Appendix D

Description of the spatial modes

The orthogonal spatial modes of the plant and water motion are given by

$$\psi_n(z_{v*}) = (\cosh \alpha_n z_{v*} - \cos \alpha_n z_{v*}) + \frac{\cos \alpha_n + \cosh \alpha_n}{\sin \alpha_n + \sinh \alpha_n} (\sin \alpha_n z_{v*} - \sinh \alpha_n z_{v*}) \tag{D.1}$$

where eigenvalues α_n satisfy

$$\cosh(\alpha_n) \cos(\alpha_n) - 1 = 0. \tag{D.2}$$

The first three roots of Eq. D.2 are given by $\alpha_1 = 0.5969\pi$, $\alpha_2 = 1.4942\pi$, $\alpha_3 = 2.5002\pi$, and are approximated by $\alpha_n = (n - 0.5)\pi$ thereafter. The spatial modes satisfy Eq. 5.11 and their spatial derivative is given by

$$\frac{\partial \psi_n}{\partial z_{v*}} = \alpha_n \psi_n. \tag{D.3}$$

The four lowest order modes are shown in Fig. D.1a. The weights of the complex spatiotemporal coefficients of the water motion are obtained by solving the linear system

$$\psi_n U_n = U_f \tag{D.4}$$

where $U_f(z_{v*})$ are the temporal coefficients of the water motion along the stem. To solve Eq. D.4, the wave motion along the stem is discretised following the number of modes considered, which is set at 10 in this study. A sample decomposition of a velocity profile based on linear wave theory by 10 spatial modes is plotted in Fig. D.1b. Furthermore, the resulting vegetation velocity profile of an artificial flexible stem under the sample forcing is shown in Fig. D.1c. While additional higher order modes will better represent the input velocity profile near the bottom, their effect on the resulting vegetation velocity is negligible due to their high eigenvalues (α_n) which damp velocity transfer in Eq. 5.23.

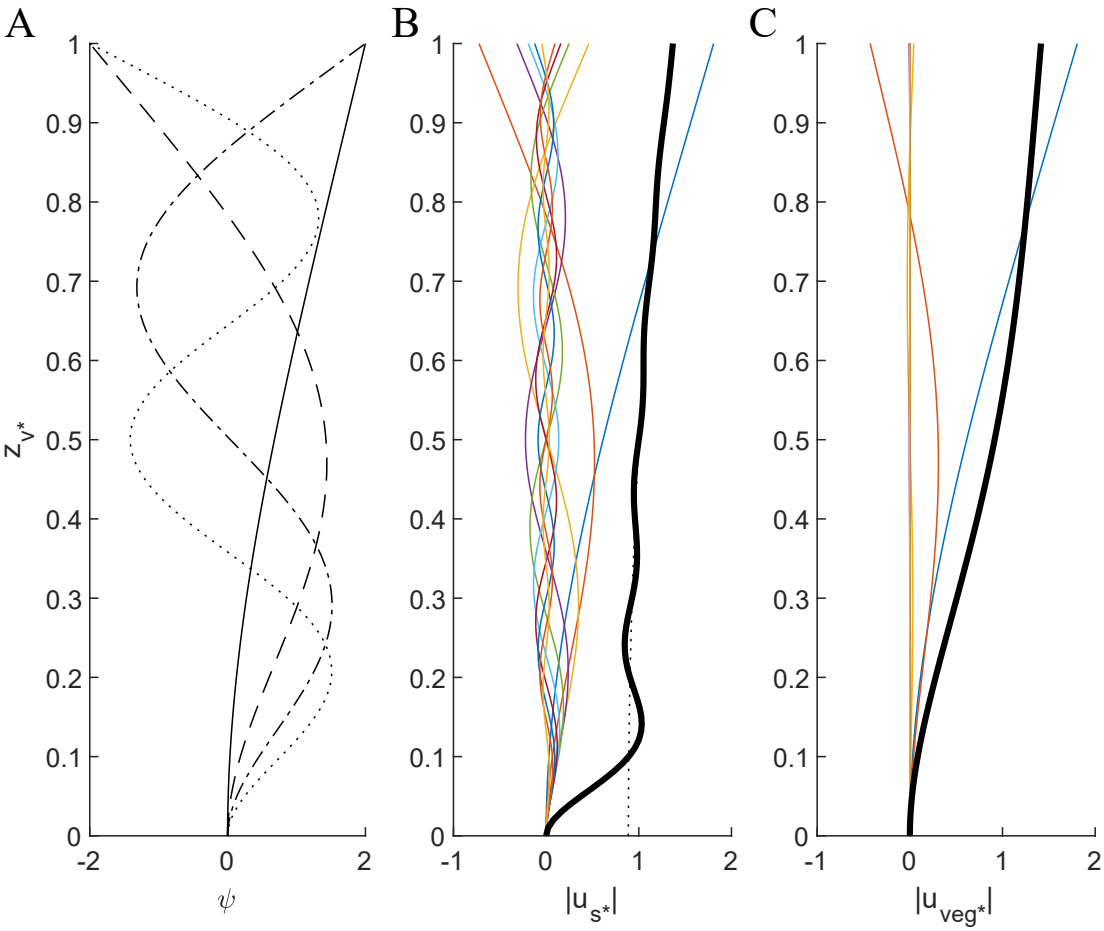

Figure D.1: (a) The first four spatial modes ψ_n (Eq. D.1); (b) decomposition of a velocity field given by linear wave theory using 10 spatial modes. The thin coloured solid lines denote the weighted spatial modes, the dotted black line denotes the input velocity profile and the thick black line denotes the sum of all spatial modes; (c) resulting vegetation velocity profile under artificial flexible vegetation using 10 spatial modes.

Appendix E

Proof of a unique solution of the velocity transfer function

We substitute Eq. 5.22 and $Q = \frac{4}{3\pi} C_{Dw} CaL \int_0^1 (a_u - a_v) ds_*$ in Eq. 5.23. Furthermore, we consider the stem-averaged magnitude of both sides of Eq. 5.23 to obtain an expression for the stem-averaged vegetation velocity according to

$$\int_0^1 a_v dz_{v*} = \int_0^1 \left| \sum \left(\frac{U_n \psi_n}{1 - \frac{i\alpha_n^4}{\frac{4}{3\pi} C_{Dw} CaL \left(\int_0^1 a_u dz_{v*} - \int_0^1 a_v dz_{v*} \right)}} \right) \right| dz_{v*}. \tag{E.1}$$

The stem-averaged magnitude of the vegetation velocity $\int_0^1 a_v ds_*$ is bound by $[0, \int_0^1 a_u ds_*]$. The lower bound denotes no vegetation motion and the upper bound represents full velocity transfer from water to vegetation motion. The left-hand side monotonically increases and the right-hand side monotonically decreases for increasing $\int_0^1 a_v ds_*$ within its range. Therefore, there is at most one solution of Eq. E.1.

We evaluate $\int_0^1 a_v ds_*$ at its lower and upper bound. If $\int_0^1 a_v ds_* = 0$, the left-hand side is smaller than the right-hand side of Eq. E.1. If $\int_0^1 a_v ds_* = \int_0^1 a_u ds_*$, then $Q = 0$ and the right-hand side of Eq. E.1 approaches 0. Yet $\int_0^1 a_v ds_* > 0$ at its upper bound when wave forcing is present. Then, the left-hand side is larger than the right-hand side if $\int_0^1 a_v ds_* = \int_0^1 a_u ds_*$. As both sides of Eq. E.1 are continuous functions of $\int_0^1 a_v ds_*$, there is at least one solution of Eq. E.1. As we showed before that there is at most one solution, there must be exactly one solution of Eq. E.1 and Eq. 5.23.

Appendix F

Flexible model validation data

The tables in this appendix support the validation of the regular wave damping model over flexible vegetation as developed in Chapter 5. They include stem density (n_v), water depth (h), incident wave height (H_0), wave period (T), velocity scale (u_c), Cauchy number (Ca), Excursion ratio (L), scaled flexibility (Q) at first iteration with $a_v = 0$, model type, experimentally derived damping coefficient (β_{exp}), and modelled damping coefficient (β_{model}). The model types are the general model with a full velocity profile (Full, Section 5.4.4) and the model under the assumption of linear wave theory (Lin., Section 5.4.5). The tables are organised with respect to vegetation species: Rigid Mimics (RM, Table F.1), Flexible Mimics (FM, Table F.2), *Puccinellia Maritima* (PM, Table F.3), *Spartina Anglica* (SA, Table F.4), and *Elymus Athericus* (EA, Table F.5).

Table F.1: Validation data rigid mimics.

Case	n_v [m^{-2}]	h [m]	H_0 [m]	T [s]	u_c [m/s]	Ca [-]	L [-]	Q [-]	Type	β_{exp} [10^{-3}/m]	β_{model} [10^{-3}/m]
RM1	1111	0.60	0.15	1.4	0.13	0.02	11	0.25	Full	42	26
RM2	1111	0.60	0.15	1.6	0.15	0.04	7.6	0.23	Full	38	38
RM3	1111	0.60	0.15	1.8	0.17	0.04	6.3	0.21	Full	49	38
RM4	1111	0.60	0.15	2.0	0.18	0.05	5.3	0.19	Full	42	39
RM5	1111	0.60	0.10	1.8	0.11	0.02	9.2	0.19	Full	39	33
RM6	1111	0.60	0.20	1.8	0.21	0.07	4.9	0.23	Full	63	39
RM7	1111	0.50	0.15	1.4	0.17	0.04	7.9	0.27	Full	72	55
RM8	1111	0.50	0.15	1.6	0.20	0.06	6.0	0.25	Full	67	70
RM9	1111	0.50	0.15	1.8	0.20	0.06	5.2	0.23	Full	80	68
RM10	1111	0.50	0.15	2.0	0.22	0.08	4.2	0.21	Full	70	80
RM11	1111	0.50	0.10	1.8	0.14	0.03	7.4	0.20	Full	59	61
RM12	1111	0.50	0.20	1.8	0.26	0.10	4.1	0.26	Full	94	67
RM13	1111	0.40	0.15	1.4	0.20	0.06	6.9	0.29	Full	145	99
RM14	1111	0.40	0.15	1.6	0.21	0.07	5.5	0.26	Full	125	111
RM15	1111	0.40	0.15	1.8	0.22	0.07	4.8	0.24	Full	138	99
RM16	1111	0.40	0.15	2.0	0.23	0.08	4.1	0.22	Full	108	104
RM17	1111	0.40	0.10	1.8	0.16	0.04	6.7	0.20	Full	97	112
RM18	1111	0.40	0.12	1.8	0.18	0.05	5.8	0.22	Full	116	105
RM19	1111	0.30	0.10	1.4	0.16	0.04	8.6	0.26	Full	210	134
RM20	1111	0.30	0.10	1.6	0.16	0.04	7.3	0.23	Full	219	128
RM21	1111	0.30	0.10	1.8	0.18	0.05	5.9	0.21	Full	197	151
RM22	1111	0.30	0.10	2.0	0.17	0.04	5.6	0.19	Full	195	107
RM23	1111	0.30	0.08	1.8	0.14	0.03	7.5	0.20	Full	169	130
RM24	1111	0.30	0.12	1.8	0.20	0.06	5.3	0.22	Full	219	118

Table F.2: Validation data flexible mimics.

Case	n_v [m^{-2}]	h [m]	H_0 [m]	T [s]	u_c [m/s]	Ca [-]	L [-]	Q [-]	Type	β_{exp} [10^{-3}/m]	β_{model} [10^{-3}/m]
FM1	1111	0.60	0.15	1.4	0.15	178	8.9	1343	Full	20	6
FM2	1111	0.60	0.15	1.6	0.19	278	6.2	1284	Full	16	10
FM3	1111	0.60	0.15	1.8	0.20	326	5.1	1184	Full	23	12
FM4	1111	0.60	0.15	2.0	0.22	390	4.2	1115	Full	15	15
FM5	1111	0.60	0.10	1.8	0.14	146	7.6	1013	Full	20	10
FM6	1111	0.60	0.20	1.8	0.25	498	4.1	1325	Full	26	14
FM7	1111	0.50	0.15	1.4	0.19	271	7.2	1459	Full	21	12
FM8	1111	0.50	0.15	1.6	0.21	352	5.5	1358	Full	17	16
FM9	1111	0.50	0.15	1.8	0.23	411	4.6	1256	Full	32	18
FM10	1111	0.50	0.15	2.0	0.25	472	3.8	1174	Full	24	22
FM11	1111	0.50	0.10	1.8	0.16	191	6.7	1058	Full	26	15
FM12	1111	0.50	0.20	1.8	0.30	692	3.5	1463	Full	25	21
FM13	1111	0.40	0.15	1.4	0.23	397	6.0	1601	Full	27	19
FM14	1111	0.40	0.15	1.6	0.25	507	4.6	1498	Full	28	26
FM15	1111	0.40	0.15	1.8	0.27	556	3.9	1368	Full	22	29
FM16	1111	0.40	0.15	2.0	0.25	498	3.7	1192	Full	48	26
FM17	1111	0.40	0.10	1.8	0.18	240	6.0	1106	Full	22	24
FM18	1111	0.40	0.12	1.8	0.21	355	4.9	1209	Full	32	25
FM19	1111	0.30	0.10	1.4	0.18	266	7.3	1453	Full	56	29
FM20	1111	0.30	0.10	1.6	0.20	309	5.9	1315	Full	68	37
FM21	1111	0.30	0.10	1.8	0.21	333	5.1	1191	Full	62	41
FM22	1111	0.30	0.10	2.0	0.20	325	4.6	1065	Full	62	39
FM23	1111	0.30	0.08	1.8	0.17	238	6.0	1104	Full	51	40
FM24	1111	0.30	0.12	1.8	0.24	444	4.4	1283	Full	40	41

Table F.3: Validation data *P. Maritima*. Source β_{exp}: *Maza et al.* (2015); *Lara et al.* (2016); *Losada et al.* (2016)

Case	n_v [m^{-2}]	h [m]	H_0 [m]	T [s]	u_c [m/s]	Ca [-]	L [-]	Q [-]	Type	β_{exp} [10^{-3}/m]	β_{model} [10^{-3}/m]
PM1	2436	0.40	0.15	2.0	0.19	128	7.9	1067	Lin.	286	187
PM2	2436	0.40	0.20	2.0	0.27	262	5.5	1184	Lin.	243	190
PM3	2436	0.40	0.20	1.2	0.29	318	8.4	2050	Lin.	124	89
PM4	2436	0.40	0.20	1.7	0.23	195	7.6	1325	Lin.	317	185
PM5	2436	0.40	0.20	2.2	0.34	418	4.0	1189	Lin.	129	174
PM6	2436	0.60	0.15	2.0	0.16	96	9.2	1041	Lin.	193	82
PM7	2436	0.60	0.20	2.0	0.23	186	6.6	1119	Lin.	170	83
PM8	2436	0.60	0.20	1.2	0.19	131	13	1784	Lin.	70	27
PM9	2436	0.60	0.20	1.7	0.20	147	8.7	1275	Lin.	192	73
PM10	2436	0.60	0.20	2.2	0.33	390	4.1	1170	Lin.	26	71
PM11	1389	0.40	0.15	2.0	0.19	137	7.7	1076	Lin.	264	104
PM12	1389	0.40	0.20	1.2	0.36	467	6.9	2240	Lin.	44	45
PM13	1389	0.60	0.15	2.0	0.16	99	9.0	1043	Lin.	185	46
PM14	1389	0.60	0.20	1.2	0.19	135	13	1789	Lin.	64	15
PM15	877	0.40	0.15	2.0	0.22	172	6.9	1106	Lin.	201	60
PM16	877	0.40	0.20	1.2	0.38	530	6.5	2314	Lin.	21	27
PM17	877	0.60	0.15	2.0	0.17	103	8.8	1047	Lin.	174	28
PM18	877	0.60	0.20	1.2	0.20	147	12	1806	Lin.	48	9

Table F.4: Validation data *S. Anglica*. Source β_{exp}: *Maza et al.* (2015); *Lara et al.* (2016); *Losada et al.* (2016)

Case	n_v [m^{-2}]	h [m]	H_0 [m]	T [s]	u_c [m/s]	Ca [-]	L [-]	Q [-]	Type	β_{exp} [10^{-3}/m]	β_{model} [10^{-3}/m]
SA1	729	0.40	0.15	2.0	0.19	0.28	4.7	0.89	Lin.	248	174
SA2	729	0.40	0.20	2.0	0.26	0.52	3.5	1.07	Lin.	236	204
SA3	729	0.40	0.20	1.2	0.31	0.75	4.8	2.02	Lin.	37	143
SA4	729	0.40	0.20	1.7	0.22	0.39	4.7	1.15	Lin.	298	205
SA5	729	0.40	0.20	2.2	0.33	0.84	2.5	1.15	Lin.	125	194
SA6	729	0.60	0.15	2.0	0.16	0.20	5.6	0.82	Lin.	182	71
SA7	729	0.60	0.20	2.0	0.22	0.38	4.1	0.97	Lin.	166	81
SA8	729	0.60	0.20	1.2	0.17	0.24	8.6	1.42	Lin.	50	37
SA9	729	0.60	0.20	1.7	0.21	0.35	5.0	1.11	Lin.	140	71
SA10	729	0.60	0.20	2.2	0.29	0.67	2.8	1.06	Lin.	56	77
SA11	430	0.40	0.15	2.0	0.20	0.32	4.4	0.92	Lin.	213	100
SA12	430	0.40	0.20	1.2	0.30	0.69	5.0	1.96	Lin.	51	85
SA13	430	0.60	0.15	2.0	0.16	0.20	5.6	0.82	Lin.	178	42
SA14	430	0.60	0.20	1.2	0.19	0.27	8.0	1.47	Lin.	24	21

Table F.5: Validation data *E. Athericus*. Source β_{exp}: *Möller et al.* (2014); *Rupprecht et al.* (2017)

Case	n_v [m^{-2}]	h [m]	H_0 [m]	T [s]	u_c [m/s]	Ca [-]	L [-]	Q [-]	Type	β_{exp} [10^{-3}/m]	β_{model} [10^{-3}/m]
EA1	1225	2.00	0.19	2.1	0.09	11	24	1656	Lin.	2.7	3.4
EA2	1225	2.00	0.19	2.9	0.13	26	11	1082	Lin.	5.0	6.6
EA3	1225	2.00	0.20	2.9	0.14	28	11	1071	Lin.	5.0	6.5
EA4	1225	2.00	0.28	2.5	0.17	40	11	1204	Lin.	4.8	5.1
EA5	1225	2.00	0.30	3.6	0.24	82	5.2	805	Lin.	6.0	7.5
EA6	1086	2.00	0.38	2.9	0.26	101	5.8	996	Lin.	5.4	5.5
EA7	1086	2.00	0.41	4.1	0.35	179	3.1	711	Lin.	4.9	7.0
EA8	1086	2.00	0.59	3.6	0.48	343	2.5	854	Lin.	4.0	6.8
EA9	1086	2.00	0.70	5.1	0.63	577	1.4	654	Lin.	5.6	8.5
EA10	666	2.00	0.89	4.1	0.75	824	1.4	872	Lin.	5.6	5.2

Appendix G

Research outcomes

This appendix provides an overview of the journal publications, conference publications and conference presentations during this thesis. The publications marked with * were prepared and submitted during the thesis, but the research content is independent from the work presented in this thesis.

G.1 Journal publications

van Veelen, T.J., Fairchild, T.P., Reeve, D.E., Karunarathna, H. (2020) Experimental study on vegetation flexibility as control parameter for wave damping and velocity structure. *Coastal Engineering*, 157, 103648. https://doi.org/10.1016/j.coastaleng.2020.103648.

Bennett, W.G., **van Veelen, T.J.**, Fairchild, T.P., Griffin, J.N., Karunarathna, H. (2020) Computational modelling of the impacts of salt marsh management interventions on hydrodynamics of a small macro-tidal estuary. *Journal of Marine Science and Engineering*, 8(5), 373. https://doi.org/10.3390/jmse8050373.

van Veelen, T.J., Roos, P.C., Hulscher, S.J.M.H. (2018) Process-based modelling of bank-breaking mechanisms of tidal sandbanks. *Continental Shelf Research*, 167, 139-152. https://doi.org/10.1016/j.csr.2018.04.007.*

van Veelen, T.J., Karunarathna, H., Reeve, D.E. (*submitted to Coastal Engineering*) Modelling wave attenuation by flexible coastal vegetation. (*submitted to Coastal Engineering*).

G.2 Conference papers

van Veelen, T.J., Karunarathna, H., Reeve, D.E. (2019) Sensitivity of estuary hydrodynamics to vegetation parameterisation. In *4th IMA International Conference On Flood Risk*.

Bennett, W.G., **van Veelen, T.J.**, Fairchild, T.P., Griffin, J.N., Karunarathna, H. (2019) Computational Modelling of the Impact of Salt Marsh Management Interventions on Coastal Flooding. In *4th IMA International Conference On Flood Risk*.

van Veelen, T.J., Roos, P.C., Hulscher, S.J.M.H. (2019) On shapes and breaks: modelling the transient evolution of tidal sandbanks. In *MARID VI*, pp. 239-242.* (awarded best abstract).

van Veelen, T.J., Karunarathna, H., Fairchild, T.P., Bennett, W.G., Griffin, J.N., Reeve, D.E. (2018) Improving predictive modelling of coastal protection by salt marshes. In *Coastal Engineering Proceedings* (ed. P.J. Lynett), 1(36), pp. risk.95. https://doi.org/10.9753/icce.v36.risk.95.

G.3 Conference presentations

van Veelen, T.J., Karunarathna, H., Bennett, W.G., Fairchild, T.P., Reeve, D.E. (2020) Nature-Based Coastal Protection: Wave Damping by Flexible Salt Marsh vegetation. *37th International Conference on Coastal Engineering*. (Abstract accepted for oral presentation, conference postponed due to Covid-19).

van Veelen, T.J., Karunarathna, H., Reeve, D.E. (2020) Modelling wave damping by flexible salt marsh vegetation. *NCK days 2020*. (Abstract accepted for oral presentation, conference cancelled due to Covid-19).

van Veelen, T.J., Karunarathna, H., Reeve, D.E. (2019) Coastal Protection by Salt Marshes in Wales. *Marine evidence Wales*.

van Veelen, T.J., Karunarathna, H., Fairchild, T.P., Reeve, D.E. (2018) Effect of salt marsh vegetation formulation on estuarine morphodynamics. *14th UK Young Coastal Scientists and Engineers Conference*.

van Veelen, T.J., Karunarathna, H., Reeve, D.E. (2017) Stability Of Salt Marshes In Response To Storm Surges. *13th UK Young Coastal Scientists and*

Engineers Conference, pp. A44.

Bibliography

Abdelrhman, M. A. (2007), Modeling coupling between eelgrass Zostera marina and water flow, *Marine Ecology Progress Series*, *338*, 81–96, doi:10.3354/meps338081.

Abdolahpour, M., M. Hambleton, and M. Ghisalberti (2017), The wave-driven current in coastal canopies, *Journal of Geophysical Research: Oceans*, *122*(5), 3660–3674, doi:10.1002/2016JC012446.

Aberle, J., and J. Järvelä (2013), Flow resistance of emergent rigid and flexible floodplain vegetation, *Journal of Hydraulic Research*, *51*(1), 33–45, doi:10.1080/00221686.2012.754795.

Al-Asadi, K., and J. G. Duan (2017), Assessing methods for estimating roughness coefficient in a vegetated marsh area using Delft3D, *Journal of Hydroinformatics*, *19*(5), 766–783, doi:10.2166/hydro.2017.064.

Albayrak, I., V. Nikora, O. Miler, and M. O'Hare (2012), Flow-plant interactions at a leaf scale: effects of leaf shape, serration, roughness and flexural rigidity, *Aquatic Sciences*, *74*(2), 267–286, doi:10.1007/s00027-011-0220-9.

Allen, J. R. L. (2000), Morphodynamics of Holocene salt marshes: a review sketch from the Atlantic and Southern North Sea coasts of Europe, *Quaternary Science Reviews*, *19*(12), 1155–1231, doi:10.1016/S0277-3791(99)00034-7.

Anderson, C. M., and M. Treshow (1980), A review of environmental and genetic factors that affect height inSpartina alterniflora loisel. (Salt marsh cord grass), *Estuaries*, *3*(3), 168–176, doi:10.2307/1352066.

Anderson, M. E., and J. M. Smith (2014), Wave Attenuation by Flexible, Idealized Salt Marsh Vegetation, *Coastal Engineering*, *83*, 82–92, doi:10.1016/j.coastaleng.2013.10.004.

Anderson, M. E., and J. M. Smith (2015), Implementation of wave dissipation by vegetation in STWAVE, *Tech. Rep. ADA613773*, ENGINEER RESEARCH

AND DEVELOPMENT CENTER VICKSBURG MS COASTAL AND HYDRAULICS LAB.

Asano, T., S. Tsutsui, and T. Sakai (1988), Wave damping characteristics due to seaweed, in *Proceedings of the 35th conference on coastal engineering*, pp. 138–142, Matsuyama.

Ashall, L. M., R. P. Mulligan, D. van Proosdij, and E. Poirier (2016), Application and Validation of a Three-Dimensional Hydrodynamic Model of a Macrotidal Salt Marsh, *Coastal Engineering*, *114*, 35–46, doi:10.1016/j.coastaleng.2016.04.005.

Augustin, L. N., J. L. Irish, and P. Lynett (2009), Laboratory and Numerical Studies of Wave Damping by Emergent and Near-Emergent Wetland Vegetation, *Coastal Engineering*, *56*(3), 332–340, doi:10.1016/j.coastaleng.2008.09.004.

Baptist, M., V. Babovic, J. Rodríguez Uthurburu, M. Keijzer, R. Uittenbogaard, A. Mynett, and A. Verwey (2007), On Inducing Equations for Vegetation Resistance, *Journal of Hydraulic Research*, *45*(4), 435–450, doi:10.1080/00221686.2007.9521778.

Barbier, E. B., I. Y. Georgiou, B. Enchelmeyer, and D. J. Reed (2013), The Value of Wetlands in Protecting Southeast Louisiana from Hurricane Storm Surges, *PLOS ONE*, *8*(3), e58,715, doi:10.1371/journal.pone.0058715.

Bennett, W. G., T. J. Van Veelen, T. P. Fairchild, J. N. Griffin, and H. Karunarathna (2019), Computational Modelling of the Impact of Salt Marsh Management Interventions on Coastal Flooding, in *Proceedings of the 4th IMA conference on flood Risk*, p. 10, Swansea, UK.

Bennett, W. G., T. J. van Veelen, T. P. Fairchild, J. N. Griffin, and H. Karunarathna (2020), Computational Modelling of the Impacts of Saltmarsh Management Interventions on Hydrodynamics of a Small Macro-Tidal Estuary, *Journal of Marine Science and Engineering*, *8*(5), 373, doi:10.3390/jmse8050373, number: 5 Publisher: Multidisciplinary Digital Publishing Institute.

Best, Ü. S. N., M. Van der Wegen, J. Dijkstra, P. W. J. M. Willemsen, B. W. Borsje, and D. J. A. Roelvink (2018), Do salt marshes survive sea level rise? Modelling wave action, morphodynamics and vegetation dynamics, *Environmental Modelling & Software*, *109*, 152–166, doi:10.1016/j.envsoft.2018.08.004.

Beudin, A., T. S. Kalra, N. K. Ganju, and J. C. Warner (2017), Development of a Coupled Wave-Flow-Vegetation Interaction Model, *Computers & Geosciences*, *100*, 76–86, doi:10.1016/j.cageo.2016.12.010.

Booij, N., R. C. Ris, and L. H. Holthuijsen (1999), A Third-Generation Wave Model for Coastal Regions: 1. Model Description and Validation, *Journal of Geophysical Research: Oceans*, *104*(C4), 7649–7666, doi:10.1029/98JC02622.

Borsje, B. W., B. K. van Wesenbeeck, F. Dekker, P. Paalvast, T. J. Bouma, M. M. van Katwijk, and M. B. de Vries (2011), How Ecological Engineering Can Serve in Coastal Protection, *Ecological Engineering*, *37*(2), 113–122, doi:10.1016/j.ecoleng.2010.11.027.

Bouma, T. J., et al. (2013), Organism traits determine the strength of scale-dependent bio-geomorphic feedbacks: A flume study on three intertidal plant species, *Geomorphology*, *180-181*, 57–65, doi:10.1016/j.geomorph.2012.09.005.

Bouma, T. J., et al. (2014), Identifying Knowledge Gaps Hampering Application of Intertidal Habitats in Coastal Protection: Opportunities & Steps to Take, *Coastal Engineering*, *87*, 147–157, doi:10.1016/j.coastaleng.2013.11.014.

Bradley, K., and C. Houser (2009), Relative velocity of seagrass blades: Implications for wave attenuation in low-energy environments, *Journal of Geophysical Research: Earth Surface*, *114*(F1), doi:10.1029/2007JF000951.

Bristow, C. R., and J. Pile (2003), South Wales Estuaries Camarthen Bay: Evolution of Estuarine Morphology and Consequences for SAC Management, *Tech. rep.*, CCW, Bangor.

Bullock, G. N., A. R. Crawford, P. J. Hewson, M. J. A. Walkden, and P. A. D. Bird (2001), The influence of air and scale on wave impact pressures, *Coastal Engineering*, *42*(4), 291–312, doi:10.1016/S0378-3839(00)00065-X.

Camfield, F. E. (1983), Wind-Wave Growth with High Friction, *Journal of Waterway, Port, Coastal, and Ocean Engineering*, *109*(1), 115–117, doi:10.1061/(ASCE)0733-950X(1983)109:1(115).

Chakrabarti, A., S. R. Brandt, Q. Chen, and F. Shi (2017), Boussinesq modeling of wave-induced hydrodynamics in coastal wetlands, *Journal of Geophysical Research: Oceans*, *122*(5), 3861–3883, doi:10.1002/2016JC012093.

Chatagnier, J. (2012), The Biomechanics of Salt Marsh Vegetation Applied to Wave and Surge Attenuation, Master's thesis, Louisiana State University, Baton Rouge, LA.

Chen, H., and Q.-P. Zou (2019), Eulerian-Lagrangian flow-vegetation interaction model using immersed boundary method and OpenFOAM, *Advances in Water Resources*, *126*, 176–192, doi:10.1016/j.advwatres.2019.02.006.

Chen, H., X. Liu, and Q.-P. Zou (2019), Wave-driven flow induced by suspended and submerged canopies, *Advances in Water Resources*, *123*, 160–172, doi:10.1016/j.advwatres.2018.11.009.

Chen, H., et al. (2018), Deriving vegetation drag coefficients in combined wave-current flows by calibration and direct measurement methods, *Advances in Water Resources*, *122*, 217–227, doi:10.1016/j.advwatres.2018.10.008.

Chen, Q., and H. Zhao (2012), Theoretical Models for Wave Energy Dissipation Caused by Vegetation, *Journal of Engineering Mechanics*, *138*(2), 221–229, doi:10.1061/(ASCE)EM.1943-7889.0000318.

Chmura, G. (2009), Tidal Salt Marshes and Mangroves Swamps, in *Coastal zone and estuaries*, edited by F. Isla and O. Iribarne, pp. 379–393, EOLSS Publications.

Christiansen, T., P. L. Wiberg, and T. G. Milligan (2000), Flow and Sediment Transport on a Tidal Salt Marsh Surface, *Estuarine, Coastal and Shelf Science*, *50*(3), 315–331, doi:10.1006/ecss.2000.0548.

Coceal, O., and S. E. Belcher (2004), A canopy model of mean winds through urban areas, *Quarterly Journal of the Royal Meteorological Society*, *130*(599), 1349–1372, doi:10.1256/qj.03.40.

D'Alpaos, A., S. Lanzoni, S. M. Mudd, and S. Fagherazzi (2006), Modeling the Influence of Hydroperiod and Vegetation on the Cross-Sectional Formation of Tidal Channels, *Estuarine, Coastal and Shelf Science*, *69*(3–4), 311–324, doi:10.1016/j.ecss.2006.05.002.

D'Alpaos, A., S. Lanzoni, A. Rinaldo, and M. Marani (2009), Intertidal Eco-Geomorphological Dynamics and Hydrodynamic Circulation, in *Coastal Wetlands: An Integrated Ecosystem Approach*, edited by G. M. E. Perillo, E. Wolanski, D. R. Cahoon, and M. M. Brinson, pp. 1–46, Elsevier, doi:10.1142/9789813231283_0001.

Dalrymple, R. A., J. T. Kirby, and P. A. Hwang (1984), Wave Diffraction Due to Areas of Energy Dissipation, *Journal of Waterway, Port, Coastal, and Ocean Engineering*, *110*(1), 67–79, doi:10.1061/(ASCE)0733-950X(1984)110:1(67).

Davidson, K. E., M. S. Fowler, M. W. Skov, S. H. Doerr, N. Beaumont, and J. N. Griffin (2017), Livestock grazing alters multiple ecosystem properties and services in salt marshes: a meta-analysis, *Journal of Applied Ecology*, *54*(5), 1395–1405, doi:10.1111/1365-2664.12892.

De Battisti, D., M. S. Fowler, S. R. Jenkins, M. W. Skov, M. Rossi, T. J. Bouma, P. J. Neyland, and J. N. Griffin (2019), Intraspecific Root Trait Variability Along Environmental Gradients Affects Salt Marsh Resistance to Lateral Erosion, *Frontiers in Ecology and Evolution*, *7*, 150, doi:10.3389/fevo.2019.00150.

Dean, R. G., and R. A. Dalrymple (1991), *Water Wave Mechanics for Engineers and Scientists*, *Advanced series on ocean mechanics*, vol. 2, World Scientific Publishing Company, Singapore.

Deltares (2018), Delft3D-FLOW Simulation of multi-dimensional hydrodynamic flows and transport phenomena, including sediments: User Manual Hydro-Morphodynamics. Version 3.15, *Tech. rep.*, Deltares, Delft, The Netherlands.

Dijkstra, J., and R. Uittenbogaard (2010), Modeling the Interaction between Flow and Highly Flexible Aquatic Vegetation, *Water Resources Research*, *46*(12), doi:10.1029/2010WR009246.

Dubi, A. M. (1997), Damping of water waves by submerged vegetation: A case study on Laminaria hyperborea., PhD Thesis, University of Trondheim, Trondheim, Norway.

Environment Agency (2018), Managing flood and coastal erosion risks in England: 1 April 2011 to 31 March 2017, *Tech. rep.*, Environment Agency, Bristol.

Eusebius, M. (2015), ModifiedMZerocross: Zerocrossing Method. A MATLAB file.

Fagherazzi, S., and D. J. Furbish (2001), On the Shape and Widening of Salt Marsh Creeks, *Journal of Geophysical Research: Oceans*, *106*(C1), 991–1003, doi:10.1029/1999JC000115.

Fagherazzi, S., et al. (2012), Numerical Models of Salt Marsh Evolution: Ecological, Geomorphic, and Climatic Factors, *Reviews of Geophysics*, *50*(1), RG1002, doi:10.1029/2011RG000359.

Fauria, K. E., R. E. Kerwin, D. Nover, and S. G. Schladow (2015), Suspended particle capture by synthetic vegetation in a laboratory flume, *Water Resources Research*, *51*(11), 9112–9126, doi:10.1002/2014WR016481.

Feagin, R. A., J. L. Irish, I. Möller, A. M. Williams, R. J. Colón-Rivera, and M. E. Mousavi (2011), Short Communication: Engineering Properties of Wetland Plants with Application to Wave Attenuation, *Coastal Engineering*, *58*(3), 251–255, doi:10.1016/j.coastaleng.2010.10.003.

Foster, N. M., M. D. Hudson, S. Bray, and R. J. Nicholls (2013), Intertidal Mudflat and Saltmarsh Conservation and Sustainable Use in the UK: A Review, *Journal of Environmental Management*, *126*, 96–104, doi:10.1016/j.jenvman.2013.04.015.

Foster-Martinez, M. R., J. R. Lacy, M. C. Ferner, and E. A. Variano (2018), Wave attenuation across a tidal marsh in San Francisco Bay, *Coastal Engineering*, *136*, 26–40, doi:10.1016/j.coastaleng.2018.02.001.

Fredsoe, J., and R. Deigaard (1992), *Mechanics of Coastal Sediment Transport*, *Advanced Series on Ocean Engineering*, vol. 3, World Scientific, doi:10.1142/1546.

French, J. R. (1993), Numerical Simulation of Vertical Marsh Growth and Adjustment to Accelerated Sea-Level Rise, North Norfolk, U.K., *Earth Surface Processes and Landforms*, *18*(1), 63–81, doi:10.1002/esp.3290180105.

Furukawa, K., and E. Wolanski (1996), Sedimentation in Mangrove Forests, *Mangroves and Salt Marshes*, *1*(1), 3–10, doi:10.1023/A:1025973426404.

Furukawa, K., E. Wolanski, and H. Mueller (1997), Currents and Sediment Transport in Mangrove Forests, *Estuarine, Coastal and Shelf Science*, *44*(3), 301–310, doi:10.1006/ecss.1996.0120.

Galland, J.-C., N. Goutal, and J.-M. Hervouet (1991), TELEMAC: A new numerical model for solving shallow water equations, *Advances in Water Resources*, *14*(3), 138–148.

Garzon, J. L., M. Maza, C. M. Ferreira, J. L. Lara, and I. J. Losada (2019a), Wave Attenuation by Spartina Saltmarshes in the Chesapeake Bay Under Storm Surge Conditions, *Journal of Geophysical Research: Oceans*, *124*(7), 5220–5243, doi:10.1029/2018JC014865.

Garzon, J. L., T. Miesse, and C. M. Ferreira (2019b), Field-based numerical model investigation of wave propagation across marshes in the Chesapeake Bay under storm conditions, *Coastal Engineering*, *146*, 32–46, doi:10.1016/j.coastaleng.2018.11.001.

Google Earth (2018), Satellite Imagery of the Taf Estuary and the Three Rivers Estuary.

Haddad, J., S. Lawler, and C. M. Ferreira (2016), Assessing the relevance of wetlands for storm surge protection: a coupled hydrodynamic and geospatial framework, *Natural Hazards*, *80*(2), 839–861, doi:10.1007/s11069-015-2000-7.

Halcrow Group Ltd. (2012), Lavernock Point to St. Ann's Head Shoreline Management Plan SMP2, *Tech. rep.*, Halcrow Group Ltd., Swindon.

Hasselmann, K., et al. (1973), Measurements of Wind Wave Growth and Swell Decay during the Joint North Sea Wave Project (JONSWAP), *Ergänzungsheft zur Deutschen Hydrographischen Zeitschrift Reihe*, *8*(12), 95.

Hellerick (2013), Blank topographic map of the British Isles.

Henderson, S. M. (2019), Motion of buoyant, flexible aquatic vegetation under waves: Simple theoretical models and parameterization of wave dissipation, *Coastal Engineering*, *152*, 103,497, doi:10.1016/j.coastaleng.2019.04.009.

Hu, K., Q. Chen, and H. Wang (2015), A Numerical Study of Vegetation Impact on Reducing Storm Surge by Wetlands in a Semi-Enclosed Estuary, *Coastal Engineering*, *95*, 66–76, doi:10.1016/j.coastaleng.2014.09.008.

Hu, K., Q. Chen, H. Wang, E. K. Hartig, and P. M. Orton (2018), Numerical Modeling of Salt Marsh Morphological Change Induced by Hurricane Sandy, *Coastal Engineering*, *132*, 63–81.

Hu, Z., T. Suzuki, T. Zitman, W. Uittewaal, and M. Stive (2014), Laboratory Study on Wave Dissipation by Vegetation in Combined Current–Wave Flow, *Coastal Engineering*, *88*, 131–142, doi:10.1016/j.coastaleng.2014.02.009.

IPCC (2019), *IPCC Special Report on the Ocean and Cryosphere in a Changing Climate*, Intergovernmental Panel on Climate Change, Geneva, Switzerland.

Ishak, A. K. (1997), Suspended Sediment Dynamics and Flux in the Macrotidal Taf Estuary, PhD Thesis, University of Wales, Bangor.

Jadhav, R. S., Q. Chen, and J. M. Smith (2013), Spectral distribution of wave energy dissipation by salt marsh vegetation, *Coastal Engineering*, *77*, 99–107, doi:10.1016/j.coastaleng.2013.02.013.

Jago, C. F. (1980), Contemporary Accumulation of Marine Sand in a Macrotidal Estuary, Southwest Wales, *Sedimentary Geology*, *26*(1), 21–49, doi:10.1016/0037-0738(80)90004-4.

Keulegan, G. H., and L. H. Carpenter (1958), Forces on cylinders and plates in an oscillating fluid, *Journal of Research of the National Bureau of Standards Research Paper*, *2857*, 423–440.

Kobayashi, N., A. W. Raichle, and T. Asano (1993), Wave Attenuation by Vegetation, *Journal of Waterway, Port, Coastal, and Ocean Engineering*, *119*(1), 30–48, doi:10.1061/(ASCE)0733-950X(1993)119:1(30).

Koftis, T., P. Prinos, and V. Stratigaki (2013), Wave Damping over Artificial Posidonia Oceanica Meadow: A Large-Scale Experimental Study, *Coastal Engineering*, *73*, 71–83, doi:10.1016/j.coastaleng.2012.10.007.

Lara, J. L., M. Maza, B. Ondiviela, J. Trinogga, I. J. Losada, T. J. Bouma, and N. Gordejuela (2016), Large-Scale 3-D Experiments of Wave and Current Interaction with Real Vegetation. Part 1: Guidelines for Physical Modeling, *Coastal Engineering*, *107*, 70–83, doi:10.1016/j.coastaleng.2015.09.012.

Le Méhauté, B. (1976), *An Introduction to Hydrodynamics and Water Waves*, 1 ed., Springer-Verlag, Berlin Heidelberg.

Leclercq, T., and E. de Langre (2018), Reconfiguration of elastic blades in oscillatory flow, *Journal of Fluid Mechanics*, *838*, 606–630, doi:10.1017/jfm.2017.910.

Lei, J., and H. Nepf (2019), Wave damping by flexible vegetation: Connecting individual blade dynamics to the meadow scale, *Coastal Engineering*, *147*, 138–148, doi:10.1016/j.coastaleng.2019.01.008.

Leonardi, N., N. K. Ganju, and S. Fagherazzi (2016), A Linear Relationship between Wave Power and Erosion Determines Salt-Marsh Resilience to Violent Storms and Hurricanes, *PNAS*, *113*(1), 64–68, doi:10.1073/pnas.1510095112.

Leonardi, N., I. Carnacina, C. Donatelli, N. K. Ganju, A. Plater, M. Schuerch, and S. Temmerman (2018), Dynamic interactions between coastal storms and salt marshes: A review, *Geomorphology*, *301*, 92–107, doi:10.1016/j.geomorph.2017.11.001.

Lesser, G. R., J. A. Roelvink, J. A. T. M. van Kester, and G. S. Stelling (2004), Development and Validation of a Three-Dimensional Morphological Model, *Coastal Engineering*, *51*(8–9), 883–915, doi:10.1016/j.coastaleng.2004.07.014.

Liu, P. L.-F. (1995), Model equations for wave propagations from deep to shallow water, in *Advances in Coastal and Ocean Engineering*, vol. 1, edited by P. L.-F. Liu, pp. 125–157, World Scientific.

Loder, N. M., J. L. Irish, M. A. Cialone, and T. V. Wamsley (2009), Sensitivity of hurricane surge to morphological parameters of coastal wetlands, *Estuarine, Coastal and Shelf Science*, *84*(4), 625–636, doi:10.1016/j.ecss.2009.07.036.

Longuet-Higgins, M. S. (1983), On the joint distribution of wave periods and amplitudes in a random wave field, *Proceedings of the Royal Society of London. A. Mathematical and Physical Sciences*, *389*(1797), 241–258, doi:10.1098/rspa.1983.0107.

Losada, I. J., M. Maza, and J. L. Lara (2016), A New Formulation for Vegetation-Induced Damping under Combined Waves and Currents, *Coastal Engineering*, *107*, 1–13, doi:10.1016/j.coastaleng.2015.09.011.

Lowe, R. J., J. R. Koseff, and S. G. Monismith (2005), Oscillatory Flow through Submerged Canopies: 1. Velocity Structure, *Journal of Geophysical Research: Oceans*, *110*(C10), doi:10.1029/2004JC002788.

Luettich, R. A., J. J. Westerink, and N. W. Scheffner (1992), ADCIRC: An Advanced Three-Dimensional Circulation Model for Shelves, Coasts, and Estuaries. Report 1. Theory and Methodology of ADCIRC-2DDI and ADCIRC-3DL., *Tech. Rep. ADA261608*, US Army Corps of Engineers, Washington.

Luhar, M., and H. M. Nepf (2011), Flow-induced Reconfiguration of Buoyant and Flexible Aquatic Vegetation, *Limnology and Oceanography*, *56*(6), 2003–2017, doi:10.4319/lo.2011.56.6.2003.

Luhar, M., and H. M. Nepf (2016), Wave-Induced Dynamics of Flexible Blades, *Journal of Fluids and Structures*, *61*, 20–41, doi:10.1016/j.jfluidstructs.2015.11.007.

Luhar, M., S. Coutu, E. Infantes, S. Fox, and H. M. Nepf (2010), Wave-induced Velocities inside a Model Seagrass Bed, *Journal of Geophysical Research: Oceans*, *115*(C12), doi:10.1029/2010JC006345.

Luhar, M., E. Infantes, and H. Nepf (2017), Seagrass blade motion under waves and its impact on wave decay, *Journal of Geophysical Research: Oceans*, *122*(5), 3736–3752, doi:10.1002/2017JC012731.

Marani, M., E. Belluco, A. D'Alpaos, A. Defina, S. Lanzoni, and A. Rinaldo (2003), On the Drainage Density of Tidal Networks, *Water Resources Research*, *39*(2), 1040, doi:10.1029/2001WR001051.

Marciano, R., Z. B. Wang, A. Hibma, H. J. de Vriend, and A. Defina (2005), Modeling of Channel Patterns in Short Tidal Basins, *Journal of Geophysical Research: Earth Surface*, *110*(F1), F01,001, doi:10.1029/2003JF000092.

Mariotti, G., and A. Canestrelli (2017), Long-Term Morphodynamics of Muddy Backbarrier Basins: Fill in or Empty Out?, *Water Resources Research*, *53*(8), 7029–7054, doi:10.1002/2017WR020461.

Marsooli, R., P. M. Orton, N. Georgas, and A. F. Blumberg (2016), Three-dimensional hydrodynamic modeling of coastal flood mitigation by wetlands, *Coastal Engineering*, *111*, 83–94, doi:10.1016/j.coastaleng.2016.01.012.

Marsooli, R., P. M. Orton, and G. Mellor (2017), Modeling wave attenuation by salt marshes in Jamaica Bay, New York, using a new rapid wave model, *Journal of Geophysical Research: Oceans*, *122*(7), 5689–5707, doi:10.1002/2016JC012546.

Maza, M., J. L. Lara, and I. J. Losada (2013), A Coupled Model of Submerged Vegetation under Oscillatory Flow Using Navier–Stokes Equations, *Coastal Engineering*, *80*, 16–34, doi:10.1016/j.coastaleng.2013.04.009.

Maza, M., J. L. Lara, I. J. Losada, B. Ondiviela, J. Trinogga, and T. J. Bouma (2015), Large-Scale 3-D Experiments of Wave and Current Interaction with Real Vegetation. Part 2: Experimental Analysis, *Coastal Engineering*, *106*, 73–86, doi:10.1016/j.coastaleng.2015.09.010.

McMillan, A., C. Batstone, D. Worth, J. Tawn, K. Horsburgh, and M. Lawless (2011), Coastal flood boundary conditions for UK mainland and islands. Project SC060064/TR2: Design sea levels.

Mcowen, C., et al. (2017), A global map of saltmarshes, *Biodiversity Data Journal*, *5*, e11,764, doi:10.3897/BDJ.5.e11764.

Mendez, F. J., and I. J. Losada (2004), An Empirical Model to Estimate the Propagation of Random Breaking and Nonbreaking Waves over Vegetation Fields, *Coastal Engineering*, *51*(2), 103–118, doi:10.1016/j.coastaleng.2003.11.003.

Méndez, F. J., I. J. Losada, and M. A. Losada (1999), Hydrodynamics induced by wind waves in a vegetation field, *Journal of Geophysical Research: Oceans*, *104*(C8), 18,383–18,396, doi:10.1029/1999JC900119.

Miler, O., I. Albayrak, V. Nikora, and M. O'Hare (2012), Biomechanical Properties of Aquatic Plants and Their Effects on Plant–Flow Interactions in Streams and Rivers, *Aquatic Sciences*, *74*(1), 31–44, doi:10.1007/s00027-011-0188-5.

Möller, I., et al. (2014), Wave Attenuation over Coastal Salt Marshes under Storm Surge Conditions, *Nature Geoscience*, *7*(10), 727–731, doi:10.1038/ngeo2251.

Morison, J. R., J. W. Johnson, and S. A. Schaaf (1950), The Force Exerted by Surface Waves on Piles, *Journal of Petroleum Technology*, *2*(05), 149–154, doi:10.2118/950149-G.

Mork, M. (1996), Wave Attenuation due to Bottom Vegetation, in *Waves and Nonlinear Processes in Hydrodynamics*, edited by J. Grue, B. Gjevik, and J. E. Weber, pp. 371–382, Springer Netherlands, Dordrecht, doi:10.1007/978-94-009-0253-4_30.

Mudd, S. M., A. D'Alpaos, and J. T. Morris (2010), How does vegetation affect sedimentation on tidal marshes? Investigating particle capture and hydrodynamic controls on biologically mediated sedimentation, *Journal of Geophysical Research: Earth Surface*, *115*(F3), F03,029, doi:10.1029/2009JF001566.

Mullarney, J. C., and S. M. Henderson (2010), Wave-Forced Motion of Submerged Single-Stem Vegetation, *Journal of Geophysical Research: Oceans*, *115*(C12), doi:10.1029/2010JC006448.

Mullarney, J. C., and S. M. Henderson (2018), Flows Within Marine Vegetation Canopies, in *Advances in Coastal Hydraulics*, edited by V. Panchang and J. Kaihatu, pp. 1–46, World Scientific, doi:10.1142/9789813231283_0001.

Nash, J. E., and J. V. Sutcliffe (1970), River Flow Forecasting through Conceptual Models Part I — A Discussion of Principles, *Journal of Hydrology*, *10*(3), 282–290, doi:10.1016/0022-1694(70)90255-6.

Nepf, H. (2012a), Flow over and through biota, in *Treatise on estuarine and coastal science*, vol. 2, edited by E. Wolanski and D. McLusky, pp. 267–288, Elsevier, San Diego, CA.

Nepf, H. M. (1999), Drag, Turbulence, and Diffusion in Flow through Emergent Vegetation, *Water Resources Research*, *35*(2), 479–489, doi:10.1029/1998WR900069.

Nepf, H. M. (2012b), Flow and Transport in Regions with Aquatic Vegetation, *Annual Review of Fluid Mechanics*, *44*(1), 123–142, doi:10.1146/annurev-fluid-120710-101048.

Nordstrom, K. (2014), Living with shore protection structures: A review, *Estuarine, Coastal and Shelf Science*, *150*(part A), 11–23, doi:10.1016/j.ecss.2013.11.003.

Ozeren, Y., D. G. Wren, and W. Wu (2014), Experimental Investigation of Wave Attenuation through Model and Live Vegetation, *Journal of Waterway, Port,*

Coastal, and Ocean Engineering, *140*(5), 04014,019, doi:10.1061/(ASCE)WW.1943-5460.0000251.

Paquier, A.-E., J. Haddad, S. Lawler, and C. M. Ferreira (2017), Quantification of the Attenuation of Storm Surge Components by a Coastal Wetland of the US Mid Atlantic, *Estuaries and Coasts*, *40*(4), 930–946, doi:10.1007/s12237-016-0190-1.

Paul, M., and C. L. Amos (2011), Spatial and seasonal variation in wave attenuation over Zostera noltii, *Journal of Geophysical Research: Oceans*, *116*(C8), doi:10.1029/2010JC006797.

Paul, M., P. Y. T. Henry, and R. E. Thomas (2014), Geometrical and Mechanical Properties of Four Species of Northern European Brown Macroalgae, *Coastal Engineering*, *84*, 73–80, doi:10.1016/j.coastaleng.2013.11.007.

Paul, M., et al. (2016), Plant Stiffness and Biomass as Drivers for Drag Forces under Extreme Wave Loading: A Flume Study on Mimics, *Coastal Engineering*, *117*, 70–78, doi:10.1016/j.coastaleng.2016.07.004.

Pennings, S. C., and R. M. Callaway (1992), Salt Marsh Plant Zonation: The Relative Importance of Competition and Physical Factors, *Ecology*, *73*(2), 681–690, doi:10.2307/1940774.

Phan, K. L., M. J. F. Stive, M. Zijlema, H. S. Truong, and S. G. J. Aarninkhof (2019), The effects of wave non-linearity on wave attenuation by vegetation, *Coastal Engineering*, *147*, 63–74, doi:10.1016/j.coastaleng.2019.01.004.

Pigott, C. D., D. A. Ratcliffe, A. J. C. Malloch, H. J. B. Birks, and M. C. F. Proctor (2000), *British Plant Communities*, vol. 5, Cambridge University Press, Cambridge, doi:10.1017/CBO9780511541834.

Price, W. A., K. W. Tomlinson, and J. N. Hunt (1968), The Effect of Artificial Seaweed in Promoting the Build-Up of Beaches, in *Proceedings of 11th International Conference on Coastal Engineering*, vol. 1, pp. 570–578, doi:10.1061/9780872620131.036.

Pujol, D., T. Serra, J. Colomer, and X. Casamitjana (2013), Flow structure in canopy models dominated by progressive waves, *Journal of Hydrology*, *486*, 281–292, doi:10.1016/j.jhydrol.2013.01.024.

Pye, K., and S. J. Blott (2009), Coastal Processes and Shoreline Behaviour of Estuary Dominated Systems in Swansea Bay and Carmarthen Bay, *Tech. rep.*, K Pye associates, Berkshire.

Pye, K., and S. J. Blott (2014), The geomorphology of UK estuaries: The role of geological controls, antecedent conditions and human activities, *Estuarine, Coastal and Shelf Science*, *150*, 196–214, doi:10.1016/j.ecss.2014.05.014.

Reeve, D. E., A. Chadwick, and C. Fleming (2012), *Coastal Engineering: processes, theory and design practice*, second ed., Spon Press, Oxon, UK.

Riffe, K. C., S. M. Henderson, and J. C. Mullarney (2011), Wave dissipation by flexible vegetation, *Geophys Research Letters*, *38*(18), L18,607, doi:10.1029/2011GL048773.

Rinaldo, A., S. Fagherazzi, S. Lanzoni, M. Marani, and W. E. Dietrich (1999), Tidal Networks: 2. Watershed Delineation and Comparative Network Morphology, *Water Resource Research*, *35*(12), 3905–3917, doi:10.1029/1999WR900237.

Rupprecht, F., A. Wanner, M. Stock, and K. Jensen (2015), Succession in salt marshes – large-scale and long-term patterns after abandonment of grazing and drainage, *Applied Vegetation Science*, *18*(1), 86–98, doi:10.1111/avsc.12126.

Rupprecht, F., et al. (2017), Vegetation-Wave Interactions in Salt Marshes under Storm Surge Conditions, *Ecological Engineering*, *100*, 301–315, doi:10.1016/j.ecoleng.2016.12.030.

Sánchez-González, J. F., V. Sánchez-Rojas, and C. D. Memos (2011), Wave attenuation due to Posidonia oceanica meadows, *Journal of Hydraulic Research*, *49*(4), 503–514, doi:10.1080/00221686.2011.552464.

Schulze, D., F. Rupprecht, S. Nolte, and K. Jensen (2019), Seasonal and spatial within-marsh differences of biophysical plant properties: implications for wave attenuation capacity of salt marshes, *Aquatic Sciences*, *81*(4), 65, doi:10.1007/s00027-019-0660-1.

Siverd, C. G., S. C. Hagen, M. V. Bilskie, D. H. Braud, S. Gao, R. H. Peele, and R. R. Twilley (2019), Assessment of the temporal evolution of storm surge across coastal Louisiana, *Coastal Engineering*, *150*, 59–78, doi:10.1016/j.coastaleng.2019.04.010.

Smith, D. I. (1994), Flood damage estimation - A review of urban stage-damage curves and loss functions, *Water SA*, *20*(3), 231–238.

Smith, S. D., and E. G. Banke (1975), Variation of the sea surface drag coefficient with wind speed, *Quarterly Journal of the Royal Meteorological Society*, *101*(429), 665–673, doi:10.1002/qj.49710142920.

Smolders, S., Y. Plancke, S. Ides, P. Meire, and S. Temmerman (2015), Role of Intertidal Wetlands for Tidal and Storm Tide Attenuation along a Confined Estuary: A Model Study, *Natural Hazards and Earth System Sciences*, *15*(7), 1659–1675, doi:10.5194/nhess-15-1659-2015.

Stark, J., T. V. Oyen, P. Meire, and S. Temmerman (2015), Observations of tidal and storm surge attenuation in a large tidal marsh, *Limnology and Oceanography*, *60*(4), 1371–1381, doi:10.1002/lno.10104.

Stark, J., Y. Plancke, S. Ides, P. Meire, and S. Temmerman (2016), Coastal Flood Protection by a Combined Nature-Based and Engineering Approach: Modeling the Effects of Marsh Geometry and Surrounding Dikes, *Estuarine, Coastal and Shelf Science*, *175*, 34–45, doi:10.1016/j.ecss.2016.03.027.

Stratigaki, V., E. Manca, P. Prinos, I. J. Losada, J. L. Lara, M. Sclavo, C. L. Amos, I. Cáceres, and A. Sánchez-Arcilla (2011), Large-Scale Experiments on Wave Propagation over Posidonia Oceanica, *Journal of Hydraulic Research*, *49*(sup1), 31–43, doi:10.1080/00221686.2011.583388.

Sutton-Grier, A. E., K. Wowk, and H. Bamford (2015), Future of our coasts: The potential for natural and hybrid infrastructure to enhance the resilience of our coastal communities, economies and ecosystems, *Environmental Science & Policy*, *51*, 137–148, doi:10.1016/j.envsci.2015.04.006.

Suzuki, T., M. Zijlema, B. Burger, M. C. Meijer, and S. Narayan (2012), Wave dissipation by vegetation with layer schematization in SWAN, *Coastal Engineering*, *59*(1), 64–71, doi:10.1016/j.coastaleng.2011.07.006.

Suzuki, T., Z. Hu, K. Kumada, L. K. Phan, and M. Zijlema (2019), Non-hydrostatic modeling of drag, inertia and porous effects in wave propagation over dense vegetation fields, *Coastal Engineering*, *149*, 49–64, doi:10.1016/j.coastaleng.2019.03.011.

Tanino, Y., and H. M. Nepf (2008), Laboratory Investigation of Mean Drag in a Random Array of Rigid, Emergent Cylinders, *Journal of Hydraulic Research*, *134*(1), 34–41, doi:10.1080/00221686.2011.552464.

Temmerman, S., T. J. Bouma, G. Govers, Z. B. Wang, M. B. De Vries, and P. M. J. Herman (2005), Impact of Vegetation on Flow Routing and Sedimentation Patterns: Three-Dimensional Modeling for a Tidal Marsh, *Journal of Geophysical Research: Earth Surface*, *110*(F4), F04,019, doi:10.1029/2005JF000301.

Temmerman, S., T. J. Bouma, J. V. de Koppel, D. V. der Wal, M. B. D. Vries, and P. M. J. Herman (2007), Vegetation Causes Channel Erosion in a Tidal Landscape, *Geology*, *35*(7), 631–634, doi:10.1130/G23502A.1.

Temmerman, S., P. Meire, T. J. Bouma, P. M. J. Herman, T. Ysebaert, and H. J. De Vriend (2013), Ecosystem-based coastal defence in the face of global change, *Nature*, *504*(7478), 79–83, doi:10.1038/nature12859.

Tempest, J. A., I. Möller, and T. Spencer (2015), A Review of Plant-Flow Interactions on Salt Marshes: The Importance of Vegetation Structure and Plant Mechanical Characteristics, *WIREs Water*, *2*(6), 669–681, doi:10.1002/wat2.1103.

Uittenbogaard, R. E., and G. Klopman (2001), Numerical Simulation of Wave-Current Driven Sediment Transport, *Coastal Dynamics '01*, pp. 568–577, doi:10.1061/40566(260)58.

van Hulzen, J. B., J. van Soelen, and T. J. Bouma (2007), Morphological variation and habitat modification are strongly correlated for the autogenic ecosystem engineer Spartina anglica (common cordgrass), *Estuaries and Coasts: J ERF*, *30*(1), 3–11, doi:10.1007/BF02782962.

Van Rooijen, A., J. Van Thiel de Vries, R. McCall, A. Van Dongeren, J. Roelvink, and A. Reniers (2015), Modeling of wave attenuation by vegetation with XBeach, in *E-proceedings of the 36th IAHR world congress*, The Hague, Netherlands.

Van Rooijen, A., R. Lowe, D. P. Rijnsdorp, M. Ghisalberti, N. G. Jacobsen, and R. McCall (2020), Wave-Driven Mean Flow Dynamics in Submerged Canopies, *Journal of Geophysical Research: Oceans*, *125*(3), e2019JC015,935, doi:10.1029/2019JC015935, _eprint: https://agupubs.onlinelibrary.wiley.com/doi/pdf/10.1029/2019JC015935.

Verschoren, V., D. Meire, J. Schoelynck, K. Buis, K. D. Bal, P. Troch, P. Meire, and S. Temmerman (2016), Resistance and Reconfiguration of Natural Flexible Submerged Vegetation in Hydrodynamic River Modelling, *Environmental Fluid Mechanics*, *16*(1), 245–265, doi:10.1007/s10652-015-9432-1.

Vogel, S. (1996), *Life in Moving Fluids*, 2nd ed., Princeton University Press.

Vuik, V., S. N. Jonkman, B. W. Borsje, and T. Suzuki (2016), Nature-Based Flood Protection: The Efficiency of Vegetated Foreshores for Reducing Wave Loads on Coastal Dikes, *Coastal Engineering*, *116*, 42–56, doi:10.1016/j.coastaleng.2016.06.001.

Vuik, V., H. Y. S. Heo, Z. Zhu, B. W. Borsje, and S. N. Jonkman (2018a), Stem breakage of salt marsh vegetation under wave forcing: A field and model study, *Estuarine, Coastal and Shelf Science*, *200*, 41–58, doi:10.1016/j.ecss.2017.09.028.

Vuik, V., S. van Vuren, B. W. Borsje, B. K. van Wesenbeeck, and S. N. Jonkman (2018b), Assessing safety of nature-based flood defenses: Dealing with extremes and uncertainties, *Coastal Engineering*, *139*, 47–64, doi:10.1016/j.coastaleng.2018.05.002.

Vuik, V., B. W. Borsje, P. W. J. M. Willemsen, and S. N. Jonkman (2019), Salt marshes for flood risk reduction: Quantifying long-term effectiveness and life-cycle costs, *Ocean & Coastal Management*, *171*, 96–110, doi:10.1016/j.ocecoaman.2019.01.010.

Walley, S. S. (1996), Holocene Evolution of a Coastal Barrier Complex, Pendine Sands, PhD Thesis, University of Wales, Bangor, UK.

Wamsley, T. V., M. A. Cialone, J. M. Smith, B. A. Ebersole, and A. S. Grzegorzewski (2009), Influence of Landscape Restoration and Degradation on Storm Surge and Waves in Southern Louisiana, *Natural Hazards*, *51*(1), 207–224, doi:10.1007/s11069-009-9378-z.

Widdows, J., N. D. Pope, and M. D. Brinsley (2008), Effect of Spartina anglica stems on near-bed hydrodynamics, sediment erodability and morphological changes on an intertidal mudflat, *Marine Ecology Progress Series*, *362*, 45–57, doi:10.3354/meps07448.

Wu, G., H. Li, B. Liang, F. Shi, J. T. Kirby, and R. Mieras (2017), Subgrid Modeling of Salt Marsh Hydrodynamics with Effects of Vegetation and Vegetation Zonation, *Earth Surface Processes and Landforms*, *42*, 1755–1768, doi:10.1002/esp.4121.

Yang, Z., J. Tang, and Y. Shen (2018), Numerical study for vegetation effects on coastal wave propagation by using nonlinear Boussinesq model, *Applied Ocean Research*, *70*, 32–40, doi:10.1016/j.apor.2017.09.001.

Ysebaert, T., S.-L. Yang, L. Zhang, Q. He, T. J. Bouma, and P. M. J. Herman (2011), Wave Attenuation by Two Contrasting Ecosystem Engineering Salt Marsh Macrophytes in the Intertidal Pioneer Zone, *Wetlands*, *31*(6), 1043–1054, doi:10.1007/s13157-011-0240-1.

Zeller, R. B., J. S. Weitzman, M. E. Abbett, F. J. Zarama, O. B. Fringer, and J. R. Koseff (2014), Improved parameterization of seagrass blade dynamics and

wave attenuation based on numerical and laboratory experiments, *Limnology and Oceanography*, *59*(1), 251–266, doi:10.4319/lo.2014.59.1.0251.

Zhang, K., H. Liu, Y. Li, H. Xu, J. Shen, J. Rhome, and T. J. Smith (2012), The role of mangroves in attenuating storm surges, *Estuarine, Coastal and Shelf Science*, *102-103*, 11–23, doi:10.1016/j.ecss.2012.02.021.

Zimmerman, J. (1982), On the Lorentz linearization of a quadratically damped forced oscillator, *Physical Letters A*, *89*(3), 123–124, doi:10.1016/0375-9601(82)90871-4.